UNIVERSITY OF OKLAHOMA

GRADUATE COLLEGE

QUANTIFYING THE PHYSICS AND ENERGETICS OF IRON LOW-IONIZATION BROAD ABSORPTION-LINE QUASAR OUTFLOWS

A DISSERTATION

SUBMITTED TO THE GRADUATE FACULTY

in partial fulfillment of the requirements for the

Degree of

DOCTOR OF PHILOSOPHY

By

HYUNSEOP CHOI
Norman, Oklahoma
2022

QUANTIFYING THE PHYSICS AND ENERGETICS OF IRON LOW-IONIZATION BROAD ABSORPTION-LINE QUASAR OUTFLOWS

A DISSERTATION APPROVED FOR THE
HOMER L. DODGE DEPARTMENT OF PHYSICS AND ASTRONOMY

BY THE COMMITTEE CONSISTING OF

Dr. Karen M. Leighly, Chair

Dr. Phillip Gutierrez

Dr. Keri A. Kornelson

Dr. Bruce A. Mason

Dr. Leah K. Morabito

Dr. Donald M. Terndrup

Acknowledgements

I would like to express my sincere appreciation to my advisor Dr. Karen M. Leighly. Her unrelenting support and guidance allowed me to grow as a scientist and produce this work. Through her mentorship, I was able to develop a strong identity as an astrophysicist.

I would like to acknowledge my doctoral committee: Dr. Donald M. Terndrup, Dr. Leah K. Morabito, Dr. Bruce A. Mason, Dr. Phillip Gutierrez, and Dr. Keri A. Kornelson. I would like to extend special thanks to Dr. Terndrup, with whom I shared many exciting scientific discussions. I would like to thank Dr. Morabito for academic and career guidance. I would like to show my appreciation to Dr. Mason for helping me avoid a not-so-minor crisis in completing the Ph. D. Also, I would like to thank Dr. Jens-Kristian Krogager for useful scientific discussions and for helping me prepare for the post Ph. D. journey.

I would also like to acknowledge the past and current *SimBAL* group members: Francis MacInnis, Adam Marrs, Cassidy Wagner, Collin Dabbieri, Collin McLeod, Ryan Hazlett, Cora DeFrancesco, and Julianna Voelker. I had the privilege to spend the first summer in the group working with the talented student Collin Dabbieri and to mentor Ryan Hazlett, another brilliant student with whom I got to attend my first American Astronomical Society meeting.

Last, but not least, I need to acknowledge the members of *SimBAL* collaboration: Drs. Sarah C. Gallagher and Gordon T. Richards for their constructive feedback and

contribution to the work presented in this dissertation. I would also like to acknowledge my esteemed colleague Kaylie Green at the University of Western Ontario in Canada for sharing with me her outlook on life and how it is like to live in Canada.

The computing for this work was largely performed at the OU Supercomputing Center for Education & Research (OSCER) at the University of Oklahoma (OU). The funding for this work was provided by: National Science Foundation grant AST-1518382 and AST-2006771 to the University of Oklahoma; Homer L. Dodge Endowed Student Scholarship from the Homer L. Dodge Department of Physics and Astronomy at the University of Oklahoma; Bullard Dissertation Completion Fellowship from the Graduate College at the University of Oklahoma; Homer L. Dodge Department of Physics and Astronomy Bush Computational Grant awarded to Dr. Karen M. Leighly; and Hubble Space Telescope grant HST-AR-15035.001-A. A partial funding for the *SimBAL* computing resources was provided by the OU Research Council and the Homer L. Dodge Department of Physics and Astronomy.

I would also like to acknowledge the often-overlooked labor of the custodial, facilities, administrative, and IT staff in the Homer L. Dodge Department of Physics and Astronomy. The time and effort that they devote to keeping our buildings clean and operational is essential to the department's success. Ultimately, their work enables our work.

Long before the University of Oklahoma was established, the land on which the University now resides was the traditional home of the "Hasinais" Caddo Nation and "Kirikiris" Wichita & Affiliated Tribes. This land was also once part of the Muscogee

Creek and Seminole nations. We acknowledge this territory once also served as a hunting ground, trade exchange point, and migration route for the Apache, Comanche, Kiowa and Osage nations. Today, 39 federally-recognized Tribal nations dwell in what is now the State of Oklahoma as a result of settler colonial policies designed to assimilate Indigenous peoples. The University of Oklahoma recognizes the historical connection our university has with its Indigenous community. We acknowledge, honor and respect the diverse Indigenous peoples connected to this land. We fully recognize, support and advocate for the sovereign rights of all of Oklahoma's 39 tribal nations. This acknowledgement is aligned with our university's core value of creating a diverse and inclusive community. It is our institutional responsibility to recognize and acknowledge the people, culture and history that make up our entire university community.

Table of Contents

Abstract

Quasars are among the most luminous and massive objects in the universe. They host an actively accreting supermassive black hole (SMBH) at their centre that can power energetic phenomena that outshine the host galaxy. A substantial fraction ($\sim 20-40\%$) of quasars show broad absorption-line (BAL) features in their rest-ultraviolet (UV) spectra that show clear evidence for powerful outflows originating from the central SMBHs. These outflows can carry a significant amount of energy and mass from the central SMBHs to their host galaxies. Therefore, BAL quasars are prime targets for investigating luminous quasar feedback on galaxies by which the star formation rate and the evolution of the host galaxies are thought to be controlled.

SimBAL provides a novel method to study the complicated spectra of BAL quasars. Tens of thousands of BAL quasar spectra available in public archives were assumed to be impossible to analyze for more than five decades. The spectral synthesis code *SimBAL* our group developed can analyze even the most heavily absorbed BAL quasar spectra and provide constraints on the physical properties of the outflow as a function of velocity. Using this software, I discovered the most powerful BAL quasar outflow analyzed to date in SDSS J135246.37+423923.5. The spectral analysis showed that the outflow has the velocities reaching $\sim -38000\,\mathrm{km\,s^{-1}}$ and the outflowing gas is located near the dusty torus at ~ 10 pc from the central SMBH. The outflow has the log kinetic luminosity

$\log L_{KE} \sim 48.1$ [erg s^{-1}] which exceeds the bolometric luminosity of the quasar and is energetic enough to power feedback.

I performed the first systematic study of a large sample of low-redshift iron low-ionization broad absorption-line (FeLoBAL) quasars and characterized the general properties of the FeLoBAL outflows. The *SimBAL* analysis of 50 FeLoBAL quasar spectra revealed that the FeLoBAL gas is located at a wide range of distances ($0 \lesssim \log R \lesssim 4.4$ [pc]) and has a wide range of physical properties. We discovered a new type of FeLoBAL quasar, *loitering outflow* objects, that are characterized by low outflow velocities and high column density winds located at $\log R \lesssim 1$ [pc] from the central SMBH. Finally, I used *SimBAL* to analyze a spectroscopic variability for J164653.72+243942.2 that showed a variable BAL features from an extremely-high velocity outflow ($v \sim 0.17c$).

The series of work presented in this dissertation demonstrates only a small fraction of scientific discoveries that can be made with *SimBAL*. I briefly summarize the results from the series of publications led by *SimBAL* collaboration that make use of the properties of the low-redshift FeLoBAL quasar outflows constrained from the *SimBAL* analysis. Finally, some of the planned future work using *SimBAL* is outlined.

CHAPTER 1

Introduction

Quasars have been studied extensively in the past several decades since their first discovery (Schmidt, 1963). Astronomers are now able to measure the size scales of their structure and to understand the source of their broad band radiation and their special role in the universe. Some of the fundamental background information and current understanding of quasars is briefly reviewed in this section.

1.1. Quasar Components

Quasars are one of the most luminous and massive objects in the universe. A quasar is a galaxy with an active galactic nucleus (AGN) in its center. Most massive galaxies have super-massive black holes in the center, but only a few percent of the super-massive black holes have sufficient mass inflow to create accretion disks and become AGNs. The term quasar reflects the history of their discovery in the 1960s (3C 273, Schmidt, 1963). The unresolved light from the central AGN often dominates the light from the host galaxy so they appear as a star. In addition, a fraction of them are very bright radio sources. When they were first discovered people called the objects 'quasi-stellar radio sources'.

The unified model by Urry & Padovani (1995) in Figure 1.1 shows different components of AGN we infer but generally cannot resolve. The main spectral feature in the optical and ultraviolet (UV) part of the quasar spectrum is the radiation coming from an accretion disk in the shape of a continuum emission. Matter falling onto a black hole forms an accretion disk around the central super massive black hole and clouds of photoionized light-emitting sources located around the accretion disk emit broad lines or narrow lines depending on their distances from the black hole. Commonly used models approximate the accretion disk radiation as a sum of local blackbodies originating from different distances away from

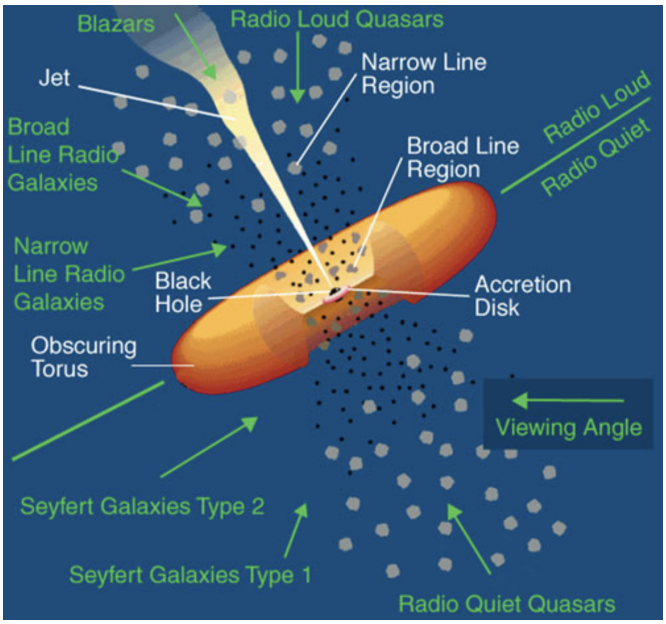

Figure 1.1: The plot was taken from Schneider (2015) Figure 5.12 (Credit: NASA) showing the unification model of Urry & Padovani (1995). The green arrows show different sight lines and the different types of quasar spectra we observe from these different angles. The thin white lines show different components of AGN. The figure is not to scale.

the center. The size scale (~ 0.01 pc) and the temperature profile of the disks have been probed by microlensing and reverberation mapping techniques (e.g., Blackburne et al., 2011).

In addition to the continuum emission from accretion disk, strong emission-lines, broad and narrow, from photoionized gas can be observed in the optical and UV part of the quasar spectrum. The temperatures of the emission line clouds are known to be only about T $\sim 10^4$ K, calculated from the ratios of the forbidden line strengths (e.g., Peterson, 1997). However, this temperature is too low to produce the large width of the emission lines or the high ionization lines (e.g. O VI, Ne VIII) seen in quasar spectra (e.g., Osterbrock, 1991). This strongly suggests that the photoionized gas clouds around the central black hole are travelling around the center at high velocities. The predominant motion of the light-emitting clouds is Keplerian motion in which the clouds orbit around the central black hole. We can see the velocities of the clouds from the widths of the lines by Doppler broadening

(e.g., Peterson & Wandel, 1999). Analysis from reverberation mapping observations suggest the location of the broad line clouds to be ~ 0.1 pc away from the central black hole (Bentz et al., 2009) and scale as the luminosity of the accretion disk (e.g., Greene & Ho, 2005; Bentz et al., 2013). The narrow lines are formed at much larger distances away ($\sim 10 - 1000$ pc) and in some cases narrow line emission is also found at much larger scales and can be resolved. For example, Hubble Space Telescope (HST) observations of nearby ($z < 0.12$ or a distance less than ~ 560 Mpc or $\sim 1.68 \times 10^{22}$ km away) luminous quasars showed resolved structures of the narrow lines extending out to several kiloparsecs ([O III] $\lambda\lambda 4959, 5007$ imaging; e.g., Fischer et al. 2018).

A dusty, obscuring torus is located at the outskirts of the accretion disk (~ 1 pc, by reverberation mapping (e.g., Kishimoto et al., 2007)) and it can also be resolved in some objects. Depending on the viewing angle, whether an observer is looking at the AGN nearly face on or edge on, the torus can block the observers from seeing the inside of the AGN, specifically the central engine and the broad line region. The torus emits a blackbody-like radiation in the infrared band from reprocessing of accretion disk photons, and some dust grains (e.g. silicates, polycyclic aromatic hydrocarbons (PAHs)) produce emission lines in near-infrared band. The torus has been discussed as possible origin of quasar winds. Observations using high-angular-resolution instruments and magneto-hydrodynamic simulations suggest a physical picture of 'dusty wind' coming off the torus structure (e.g., Elitzur & Shlosman, 2006; Gallagher et al., 2015; Hönig, 2019). The full spectral energy distribution (SED) of a typical quasar is shown in Figure 1.2. The accretion disk, torus and broad/narrow line clouds dominate the quasar spectral features in UV, optical and infrared.

In the high-energy region of quasar SED, continuum emission from the corona and the innermost (extension) part of the accretion disk is usually seen in the X-ray band, unless the emission is intrinsically weak or absorbed by X-ray absorbers ('compton thick absorption'). Figure 1.2 shows three main sources of X-ray emission and how they shape the SED. Moving to the low-energy part of the SED (not shown in Figure 1.2), some

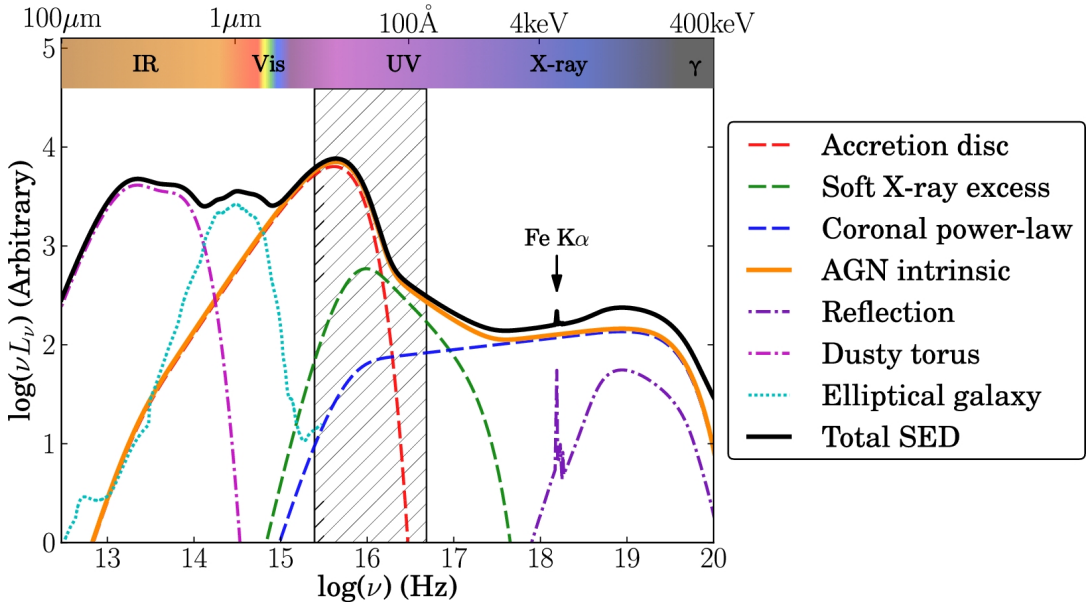

Figure 1.2: The plot, taken from Figure 1 of Collinson et al. (2017), shows how various components of the AGN contribute to the overall SED of a quasar. An elliptical galaxy template was used to show the galaxy starlight contribution, and for more detailed models, multiple starlight components can be used. In the case of luminous quasars, the contribution from the host galaxy is generally negligible and the torus and the accretion disk components dominate the shape of the SED from the infrared to UV. On this figure, none of the major optical/UV line emissions discussed in the text are plotted. The hatched region shows the part of the SED where most of the radiation gets severely attenuated by the interstellar medium (ISM). The origin of the soft X-ray excess is not well understood but currently the community believes that, in most cases, it originates from the extension of inner region of the accretion disk by thermal Comptonizations.

objects with jets exhibit radio emission from synchrotron radiation. Broad absorption-line (BAL) quasars are typically weak X-ray and radio emitters, so we do not discuss these components further.

1.2. Quasars in the Universe

The quasars are not very common objects. The total surface density of the quasars is 40 times less than the stars that are located near the sparsely populated Galactic poles (Peterson, 1997). However, the surface density, or the numbers of quasars from various surveys, is highly dependent on the survey bands and/or how deep the observations go. Quasars might not be found in every corner of the universe, but their role in the universe is quite important. On a smaller scale, 'AGN Feedback' is believed to regulate the star formation and the growth of the host bulge and on a bigger scale, AGNs are assumed to be partly responsible for reionizing of the universe at high redshift.

The growth and the evolution of the quasars have been studied using the quasar luminosity function (QLF). Redshift around $z \sim 2 - 3$ is often called the 'quasar epoch', when the quasars were most active and we see the peak of the QLF at this redshift range. Figure 1.3 shows the evolution of quasar activity. What is most interesting about the QLF is that people have found an evidence for 'cosmic downsizing' from analyzing QLF at different redshifts. Cosmic downsizing refers to the observational finding that the more massive black holes were formed in the early universe and the accretion activity of less massive objects happened during more recent past. QLF analysis by Richards et al. (2006a) also confirms this idea. Luminous quasars ($\log L_{quasar} \gtrsim 46$ [erg s^{-1}]) are located at the lower end of the QLF and are rare compared to overall quasar populations, but it is believed that the quasars with larger luminosities have stronger outflows (e.g., Fiore et al., 2017; Hamann et al., 2019a).

Observational evidence and galaxy evolution simulations call for the need of quasar feedback mechanism that can connect the AGNs to their host galaxies. Energy injection from the central supermassive black hole (SMBH) in a form of winds with energy ex-

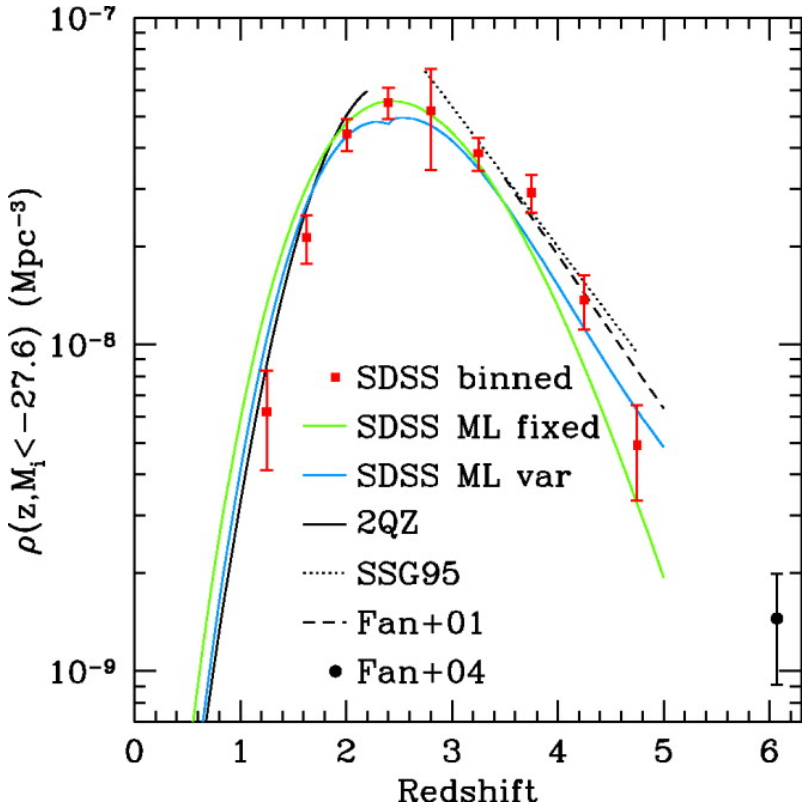

Figure 1.3: The plot, taken from Figure 20 of Richards et al. (2006a), shows the peak of the quasar activity at redshift ~ 2.5. The green and blue lines are the results from their work using different fitting mechanisms and the circle and other lines plotted in this figure are from other literature they used to compared their result.

ceeding 0.5%∼5% of the quasar luminosity (e.g., Scannapieco & Oh, 2004; Di Matteo et al., 2005; Hopkins & Elvis, 2010) are thought to be able to power AGN feedback. The tight correlation between the central black hole mass and the host bulge has been well known from the observations of quasars (e.g., Ferrarese & Merritt, 2000; Kormendy & Ho, 2013). Galaxy evolution simulations require some sort of quasar feedback that can regulate the growth of the black hole and the host galaxy in order to correctly produce the galaxy populations at current epoch (e.g., Choi et al., 2012). Brooks & Christensen (2016) briefly mentions the need for AGN feedback for bulge formation simulations. They point out that the AGN feedback can influence across the entire galaxy compared to stellar feedback and the strength of the AGN feedback does not directly depend on the mass of stars formed.

King & Pounds (2015) discuss the role of AGN outflows on feedback mechanisms in detail and further confirms the pivotal role they play. One form of such quasar feedback and energy transport signature can be found in radio jets which show clear evidence for a super massive black hole injecting energy and material onto nearby medium. However, such a highly collimated outflow maybe unlikely to be able to effectively influence the entire surrounding region, and a more of isotropic flow might be more likely to influence the host bulge. AGN outflowing winds, on the other hand, are thought to be wide angle and are more prevalent in quasars.

1.3. Broad Absorption-Line Quasars

The class of known objects known as BAL quasars which show broad blueshifted absorption features in their rest-UV spectra exhibit indisputable evidence for powerful winds (Weymann et al., 1991). The first BAL quasar was discovered by Lynds (1967) in the rest-UV spectrum of PHL 5200 with an absorption feature blueshift of $\sim 10000\,\mathrm{km\,s^{-1}}$. BAL quasars are found in 20%∼40% of the total quasar population (Foltz et al., 1990; Weymann et al., 1991; Tolea et al., 2002; Reichard et al., 2003; Trump et al., 2006; Dai et al., 2008; Knigge et al., 2008; Allen et al., 2011) once corrected for selection effects.

They are often easily identified by a blueshifted C IV$\lambda\lambda 1548, 1550$ absorption feature in ground based spectra in objects that have sufficiently high redshifts ($4 \gtrsim z \gtrsim 1.5$). A small number of BAL outflows have velocities of up to $\sim 0.2c$ or greater, which implies the presence of energetic outflows (e.g., Hamann et al., 2018; Rogerson et al., 2016). These outflows may be able to significantly impact their host galaxies and control star formation rates, and thus they are considered a potential driver of quasar feedback.

The BAL features originating from the quasar outflow gas are distinguished from the intervening absorption-lines (e.g., associated absorption-line) originating from a foreground gas that is not associated with the quasar by following spectroscopic and physical characteristics of the absorbing gas: (1) wider absorption lines, (2) partial coverage of the emission source and non-black saturation, (3) time variability of the absorption troughs, (4) higher ionization condition of the absorbing gas, (5) higher metallicity of the absorbing gas (e.g., Weymann et al., 1991; Hamann et al., 2001; Barlow et al., 1989; Barlow & Sargent, 1997; Ganguly & Brotherton, 2008). Unlike BAL gas clouds, foreground gas clouds do not typically show complex kinematic structures and thus they form narrow absorption lines. Foreground gas clouds are typically at large distances away from the background quasars. As a result, the gas clouds show complete coverage of the emission source because the angular sizes of the quasars the gas clouds see becomes very small. Moreover, these gas clouds are ionized by the UV extragalactic background radiation (e.g., Haardt & Madau, 1996), not by quasars, and have lower ionization condition compared to BAL gas clouds. Time variability and enhanced metallicity are only observed in BAL gas clouds because they result from the interactions between the central AGN and the surrounding environment where BAL gas clouds are found.

Although we did not impose a strict criteria for distinguishing BAL features from the intervening absorption-lines, most of the absorption features we studied have large widths that kept their classification unambiguous. Nonetheless, we were able to identify a small number of intervening absorption-line systems in the BAL spectra we analyzed by comparing the distribution of some of the properties mentioned above (Appendix 5.C).

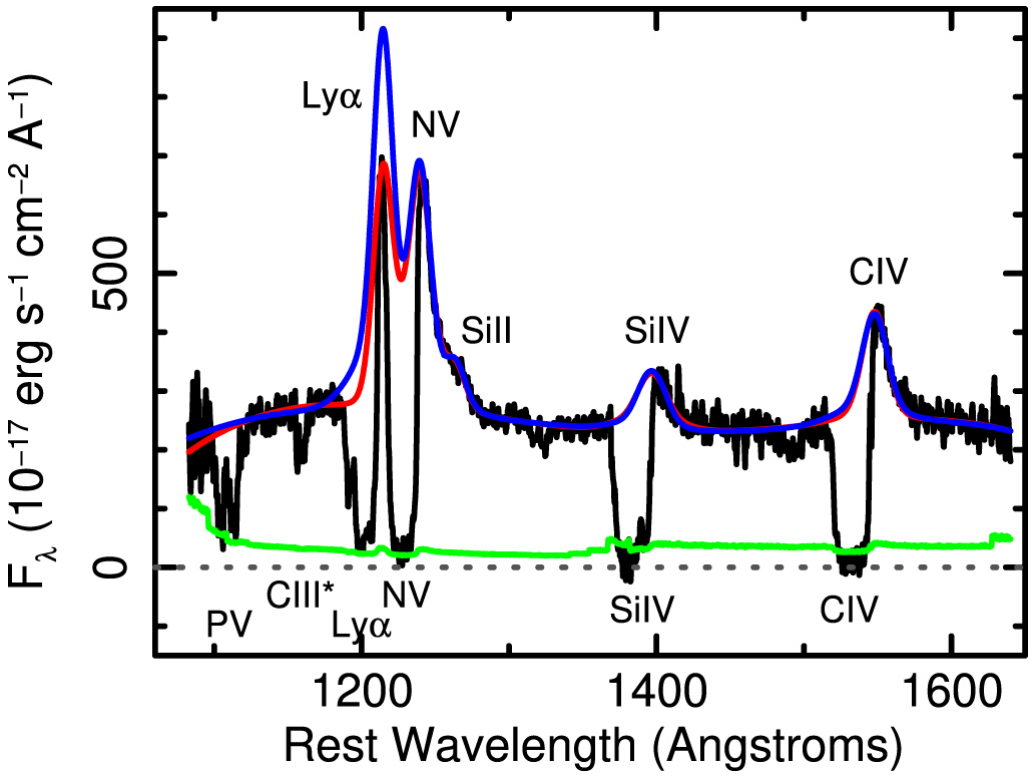

Figure 1.4: The plot, taken from Figure 1 of Leighly et al. (2018), shows the HST spectrum of SDSS J085053.12+445122.5. The solid blue and red lines are the continuum models used in their paper. The name of emission lines and the absorption lines are labelled above and below the spectrum, respectively. Here we can see some of the most common BAL transitions such as C IV and Si IV.

BAL quasars are further divided into subgroups based on their spectroscopic properties. High-ionization broad absorption-line (HiBAL) quasars show only the absorption transitions from highly ionized atoms (C IV, Si IV, N V, O VI), while low-ionization broad absorption-line (LoBAL) quasars show both the high-ionization transitions and absorption lines from lower-ionization ions (Mg II, Al II, Al III) in their rest-UV spectra. Figure 1.4 shows some of the most common absorption transitions seen in (Lo)BAL quasars in the rest-UV bandpass. There is also another class of rarer BAL quasars called iron low-ionization broad absorption-line (FeLoBAL) quasars that show Fe II absorption lines. These objects have large gas column densities, thick enough to extend beyond the hydrogen ionization front (Figure 1.5; Hazard et al., 1987). Although FeLoBAL quasars comprise less than $\sim 2\%$ of the observed quasar population (Dai et al., 2012), their outflows can have the highest column densities compared to other types of BAL outflows (Lucy et al., 2014). Some FeLoBAL objects with broad saturated troughs, where the troughs overlap to nearly completely absorb the continuum emission shortward of 2800 Å, are called 'overlapping trough' objects (e.g., Hall et al., 2002), and they are expected to have the largest hydrogen column densities ($\log N_H$) in their outflows.

In this dissertation I mainly focus on the study on FeLoBAL quasars. There are two main reasons why FeLoBAL quasars are attractive targets to study quasar outflows and quasar evolution. First, FeLoBAL outflowing gas has the highest column densities that can produce powerful and massive outflows. By studying these outflows, we will be able to further our understanding of the acceleration mechanisms that are responsible for powering massive winds to high velocities. Moreover, FeLoBAL quasars with energetic winds are excellent targets for investigating the potential mechanism of feedback on galaxies. Secondly, FeLoBAL quasars are known to have redder optical colors or found more frequently in optically red quasars (e.g., Urrutia et al., 2009), and they are sometimes observed to have high infrared luminosities (e.g., Farrah et al., 2005, 2007). These results suggest that FeLoBAL quasars may represent a short-lived stage in quasar evolution where the quasar blows out its cocoon of gas and dust ("blowout" phase; e.g., Sanders et al.,

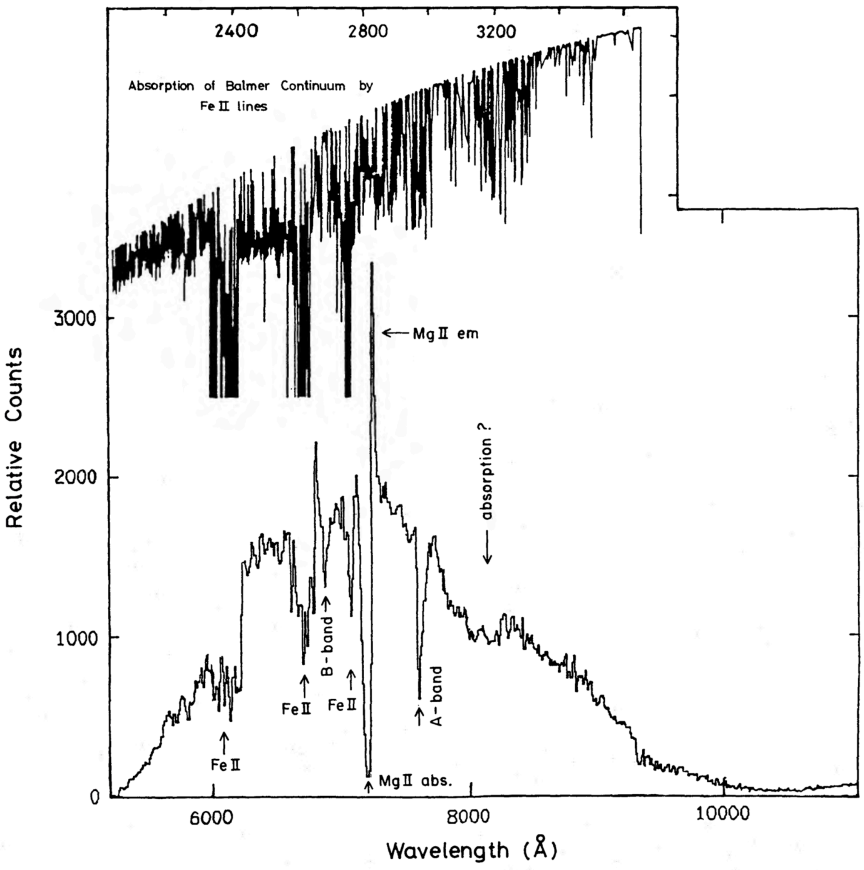

Figure 1.5: The discovery of an FeLoBAL quasar QSO 0059-2735. The figure showing the uncorrected spectrum was directly taken from Figure 4 in Hazard et al. (1987). A and B-bands annotated below the spectrum are from the Earth's atmosphere and not intrinsic to the quasar.

1988a; Farrah et al., 2012) transitioning from the ultraluminous infrared galaxy (ULIRG) phase. In addition to these scientific advantages of studying FeLoBAL quasars, the spectra of these objects show a significantly more number of absorption line transitions compared to other type of BAL quasars. This allows us to test the performance of our group's spectral analysis software *SimBAL*, and the wealth of information can be extracted from the plethora of absorption lines with which we can use to constrain the physical properties of the outflowing gas.

The wide range of ionization, which is not observed in collisionally ionized gas, and a behavior that BAL variability is coordinated with the changes in the continuum flux (e.g., Wang et al., 2015) suggest that the BAL clouds are photoionized. In order to understand the BAL phenomenon, it is crucial that we understand the physical conditions of the outflowing winds. The absorption features are coming from the outflowing photoionized clouds/winds and detailed photoionization modelling is required to fully assess the energetics of the outflowing winds.

Although the BAL phenomenon was discovered more than five decades ago, very little progress has been made on our understanding of quasar winds observed in these objects and detailed physical properties of BAL outflows and their role in feedback remains elusive. Despite the availability of tens of thousands of BAL quasar spectra publicly available in the archive, only a small number of them have been studied in detail, because their spectra are extremely challenging to analyze and perform detailed photoionization modelling of a complex outflowing gas system with currently available tools. In particular, the use of commonly used analysis methods, further discussed in Chapter 2 (§ 3.2), becomes nearly impossible when BAL quasar spectra show broad and blended absorption lines, spectral features commonly found in FeLoBAL quasars.

Our group has developed the novel spectral synthesis code *SimBAL* (Leighly et al., 2018) which is used to analyze BAL quasar spectra by creating synthetic spectra using photoionization calculations (*Cloudy*; Ferland et al., 2017) and comparing them with the observed spectra using a Bayesian model calibration method. *SimBAL* models absorption

lines in terms of the physical conditions in the outflow and thereby constrains the location and the energetics of BAL outflows. With *SimBAL*, we can also constrain the acceleration processes responsible for quasar winds. The software enables us to not only analyze extreme cases and a wide variety of quasar outflows but also to investigate large samples of BAL quasars, and for the first time, to perform a systematic study of the properties of quasar outflows. As one of the principal developers of *SimBAL*, I have contributed to the group's ongoing efforts to update the software, to improve the software's speed and versatility, and to prepare for eventual public release. Most of the work included in this dissertation used *SimBAL* to perform the spectral analysis and the detailed notes on the spectral modeling using *SimBAL* can be found in each corresponding chapter (Chapters 4, 5, and 6).

I present our efforts to advance our knowledge of BAL quasar outflows with an emphasis on the detailed analyses of rest-UV spectra of FeLoBAL quasars. Firstly, I briefly provide a detail of the observational facilities and instruments used to take the data used in this dissertation in Chapter 2. In Chapter 3, I introduce *SimBAL* and discuss in detail how the software is used to analyze BAL quasar spectra using photoionization modeling and machine learning methods. Then, in Chapter 4, I present the discovery of the most energetic BAL outflow analyzed to date in a FeLoBAL quasar SDSS J135246.37+423923.5. In Chapter 5, I present the results from the first systematic study of a large sample of low-redshift FeLoBAL quasars and describe the general properties of the FeLoBAL outflows observed in the sample. Finally, in Chapter 6, I report the results from the *SimBAL* analysis of a BAL quasar, J164653.72+243942.2, that has an extremely high-velocity outflow. The chapter summaries and planned future work can be found in Chapter 7, the final Chapter of the dissertation.

CHAPTER 2

Facilities and Instruments

Most of the data used in the analyses included in this dissertation are obtained from the Sloan Digital Sky Survey (SDSS) public archive. Additional data have been obtained from remote observing or queue observing performed with the Apache Point Observatory (APO) 3.5-meter and Gemini Observatory 8.1-meter Gemini North telescopes. All of the computational work was done at the University of Oklahoma. Here I present a summary of the facilities and instruments used in the work presented in this dissertation.

2.1. Sloan Digital Sky Survey

The SDSS uses a 2.5-meter telescope (the Sloan Foundation 2.5-meter telescope) located at Apache Point Observatory in south-east New Mexico in the Sacramento Mountains. The telescope is a modified Ritchey-Chrétien wide-field altitude-azimuth telescope with charge-coupled device (CCD) cameras (Gunn et al., 2006). It was had first light in May of 1998 and started its survey operations in 2000.

The SDSS began its operations as both imaging and spectroscopy surveys. A large-format mosaic CCD camera with five broadband filters (name and central wavelength): u 3551 Å, g 4686 Å, r 6166 Å, i 7480 Å, and z 8932 Å (Gunn et al., 1998) was used for the imaging survey. The imaging survey concluded on November 18, 2009 after imaging 31,637 square degrees of the sky (total area $\sim 41,252.96$ square degrees) and the full imaging survey data were published in the Data Release 8 (DR8; Aihara et al., 2011). The imaging camera is currently stored at the Smithsonian Museum in Washington, D.C.

The spectroscopic exposures were collected using 640 3″-fibers that are positioned by an aluminum plate (a "plug plate") located on the telescope focal plane. The optical fibres carry the light from the focal plane to the dual-channel (blue and red) spectrographs (York

et al., 2000). The two SDSS spectrographs cover $3800 - 6150$ Å in blue and $5800 - 9200$ Å in red with a pixel size of ~ 69 kms^{-1}. The spectra are processed by the pipeline (including flux calibration) and stored in the SDSS archive for public releases.

2.1.1. Baryon Oscillation Spectroscopic Survey

The Baryon Oscillation Spectroscopic Survey (BOSS) spectrographs were rebuilt from the SDSS spectrographs as successors and to conduct the eponymous BOSS project, an SDSS-III spectroscopic survey, and began operations in Fall 2009 (Aihara et al., 2011). The new instrument follows the same dual-channel design with two cameras on each blue and red side and a dichroic at ~ 6000 Å. The upgrade allowed the BOSS spectrographs a broader wavelengths coverage: the blue side covers $3600 - 6350$ Å and the red side covers $5650 - 10000$ Å, providing the total wavelength coverage of $3600 - 10,400$ Å. The spectral resolution is $R = 1560 - 2270$ in the blue channel, $R = 1850 - 2650$ in the red channel ($R = 2000$ roughly corresponds to resolving power of ~ 150 kms^{-1}) with the same SDSS spectrograph pixel size of ~ 69 kms^{-1}. The new plug plate for the BOSS holds 1000 $2''$-fibers, each fiber positioned at the locations of astronomical objects, such as quasars, standard stars, or a random blank area on the sky for calibration purposes.

The BOSS spectrographs are still currently in use at the 2.5-meter telescope The upcoming SDSS-V survey (Kollmeier et al., 2017) will make use of the BOSS spectrographs for its spectroscopic surveys. In preparation for the survey, the BOSS spectrographs have given new updates to its focal plane system. The SDSS-V has installed the new robotic fibre positioner to locate the optical fibers and thus eliminating the needs for manual plugging of optical fibers into the aluminum plates each night (Pogge et al., 2020).

The most recent data release from the SDSS is the Data Release 17 (Abdurro'uf et al., 2022) which is the fifth and final release from the SDSS-IV. The work presented throughout the dissertation used data obtained from either or both the SDSS and BOSS spectrographs. Detailed information on the data used can be found in each chapter.

2.2. Apache Point Observatory

The Apache Point Observatory is located in Sunspot, New Mexico, and it is owned and operated by the Astrophysical Research Consortium. The consortium has three telescopes: the 3.5-meter telescope, the Sloan Foundation 2.5-meter telescope (§ 2.1), and the 0.5-meter Small Aperture Telescope. The University of Oklahoma is a member of the consortium with a 6.5% of the observing time. The telescope currently hosts 7 different imaging and spectroscopic instruments both in the near-infrared and optical bands. The observers can either perform the observation in-person at the observatory or conduct a remote observing.

2.2.1. TripleSpec

TripleSpec is a cross-dispersed spectrograph that provides a wavelength coverage of $0.95 - 2.46$ microns (Wilson et al., 2004). The instrument is mounted at the Nasmyth 2 (NA2) focus of the 3.5-meter telescope and has a default configuration of a spectral resolution $R \sim 3500$ (or ~ 86 kms^{-1}) with a 1.1″slit. The five spectral orders are imaged by a 2048x1024 pixel HAWAII-II detector and a separate imager performs as a guider/slitviewer that allows the observers an easy target acquisition. TripleSpec is an excellent instrument to study the rest frame optical spectra of high-redshift ($z \gtrsim 2$) quasars. The effective limiting magnitude for signal-to-noise ratio (SNR) > 10 is $H \sim 15.5$

We limited a single exposure time to be less than 240 seconds in order to avoid the spectrograph array saturation by the airglow but also to limit the effect of changing atmospheric opacity. We performed dithering with the telescope user interface (TUI), a software used to control the telescope, that has an automated script that allows for an ABBA nod sequence exposures in which the telescope is nodded back and forth along the slit. The nod sequence exposures are needed for near-infrared observations so that the airglow and the atmospheric emission-lines can be easily subtracted from the target image. We used the Fowler sampling of $N = 8$ to reduce the read noise. This step is needed for (near)-infrared observations, because infrared detectors have significantly higher read noise than optical detectors. A standard TripleSpec observation includes following exposure frames: science

targets, telluric standard targets, and flat-fields with and without the telescope truss lamps.

The TripleSpec data can be reduced using a extraction software, `Triplespectool`, which is largely based on the `Spextool` reduction package (Cushing et al., 2004). The data obtained from TripleSpec observations were used in the analysis of SDSS J135246.37+423923.5 (Chapter 4).

2.3. Gemini Observatory

The Gemini Observatory consists of two identical 8.1-meter telescopes that are located in Hawai'i and Chile. The data used in the dissertation have been obtained from the Frederick C. Gillett Gemini North telescope. The telescope sits on top of Hawai'i's Mauna Kea at an elevation of $\sim 4,214$ meters which provides an ideal atmospheric conditions with low humidity that is crucial for ground-based observations. The Gemini telescopes are operated by international collaborations that include the United States, Canada, Chile, Brazil, Argentina, and Korea. The observations are mainly done in "Queue Schedueling" system that is designed to optimize the telescope operations and the Gemini staff members carry out the observations on behalf of the proposers.

2.3.1. Gemini Near-Infrared Spectrograph

The Gemini Near-Infrared Spectrograph (GNIRS) is a multi-function instrument with both imaging and spectroscopy capabilities (Elias et al., 2006a,b). It has long-slit and cross-dispersion modes with different wavelength coverages and resolving powers for spectroscopic observations. We chose cross-dispersion mode that provides a broad wavelength coverage of the near-infrared band, $0.85 - 2.5$ microns, which is needed for our science goals. It utilizes two prisms to perform the cross-dispersed spectroscopy and typical configurations include 32 l/mm grating and short blue camera or 10 l/mm grating and long blue camera with a resolving power of $R \sim 1800$. Spectral image is then captured by the Aladdin III InSb 1024x1022 pixels detector array. The data is stored and maintained at the Gemini Observatory Archive.

The GNIRS data can be reduced using a wide variety of softwares that includes Gemini

`IRAF` package[1] and `Pypeit`[2] (Prochaska et al., 2020a,b). The detector has several known issues and a preprocessing of the images are required before the data reduction procedures. The Gemini Observatory provides `cleanir.py`[3] python tool that can perform various tasks such as pattern noise cleaning and quadrant leveling. Once the images have been cleaned, one can follow the steps outlined on the GNIRS website[4] or use the semi-automatic reduction pipeline `Pypeit`.

The data obtained from the GNIRS were used in the analysis of SDSS J135246.37+423923.5 (Chapter 4). Detailed notes on observation configurations and reduction process can be found in § 4.2.1.

2.4. Computing Resources

SimBAL group at the University of Oklahoma (OU) owns three Linux servers each equipped with more than 60 threads (logical Processors) and condominium servers at the OU Supercomputing Center for Education & Research[5] (OSCER; 4 nodes with 80 threads each). The Linux servers are managed and hosted by the Homer L. Dodge Department of Physics and Astronomy, and they are housed in a server room on the basement of Nielsen Hall. `Condor`[6] cluster computing scheduler is installed on those servers to allow users to submit parallel computing jobs. The OSCER is a division of OU Information Technology[7] that serves undergraduates, grad students, faculty and staff at OU to learn and use advanced computing resources in their research. OSCER system uses the `Slurm` (or Simple Linux Utility for Resource Management)[8] for cluster management and job scheduling.

The biggest difference between running *SimBAL* on the Linux servers and the OSCER system is the use of the Message Passing Interface (MPI) which allows users to distribute

[1] https://www.gemini.edu/observing/phase-iii/understanding-and-processing-data/data-processing-software
[2] https://github.com/pypeit/PypeIt
[3] https://github.com/andrewwstephens/cleanir
[4] https://www.gemini.edu/instrumentation/gnirs/data-reduction
[5] https://www.ou.edu/oscer
[6] https://research.cs.wisc.edu/htcondor/
[7] https://www.ou.edu/ouit
[8] https://slurm.schedmd.com

calculations across processors on a number of machines. Multiprocessing is used for distributing a computing job across processors or threads on a single machine. On the Linux servers with `Condor`, we use multiprocessing to parallelize *SimBAL* across available threads in a single server ($\sim 60-80$ threads). In contrast, we typically use MPI on OSCER to request more than $\sim$ 100s of cpus for a single job. MPI allows the user to take advantage of a bigger cluster and to run the program on multiple machines. We used the `OpenMPI`[9] module available on OSCER to submit *SimBAL* jobs with MPI. In addition to running *SimBAL*, we also used OSCER to perform a large number of *Cloudy* (Ferland et al., 2017) photoionization simulations to generate grids of ionic column densities for *SimBAL* software (Chapter 3; § 3.2).

To optimize the usage of these two computing resources, we used the Linux servers for simpler *SimBAL* jobs, e.g., analysis of iron low-ionization broad absorption-line (FeLoBAL) quasar spectra with moderate absorption, that generally take less than a day to finish with < 100 threads(cpus). We used the OSCER for the analysis of more complicated and heavily absorbed FeLoBAL quasar spectra. Currently, the public normal node on the OSCER has a 24-hour limit; however, there is no time limit on condominium servers. The OSCER hosts regular help sessions where new users can get an one-on-one consultation during which the support provides answers to questions about the OSCER systems and useful tips on supercomptuer usage.

2.5. Acknowledgments

Funding for the SDSS-IV has been provided by the Alfred P. Sloan Foundation, the U.S. Department of Energy Office of Science, and the Participating Institutions. SDSS-IV acknowledges support and resources from the Center for High Performance Computing at the University of Utah. The SDSS website is www.sdss.org. SDSS-IV is managed by the Astrophysical Research Consortium for the Participating Institutions of the SDSS Collaboration including the Brazilian Participation Group, the Carnegie Institution for

[9] https://www.open-mpi.org

Science, Carnegie Mellon University, Center for Astrophysics — Harvard & Smithsonian, the Chilean Participation Group, the French Participation Group, Instituto de Astrofísica de Canarias, The Johns Hopkins University, Kavli Institute for the Physics and Mathematics of the Universe (IPMU) / University of Tokyo, the Korean Participation Group, Lawrence Berkeley National Laboratory, Leibniz Institut für Astrophysik Potsdam (AIP), Max-Planck-Institut für Astronomie (MPIA Heidelberg), Max-Planck-Institut für Astrophysik (MPA Garching), Max-Planck-Institut für Extraterrestrische Physik (MPE), National Astronomical Observatories of China, New Mexico State University, New York University, University of Notre Dame, Observatário Nacional / MCTI, The Ohio State University, Pennsylvania State University, Shanghai Astronomical Observatory, United Kingdom Participation Group, Universidad Nacional Autónoma de México, University of Arizona, University of Colorado Boulder, University of Oxford, University of Portsmouth, University of Utah, University of Virginia, University of Washington, University of Wisconsin, Vanderbilt University, and Yale University.

The Gemini Observatory is operated by the Association of Universities for Research in Astronomy, Inc., under a cooperative agreement with the National Science Foundation (NSF) on behalf of the Gemini partnership: the NSF (United States), National Science and Engineering Research Council (Canada), CONICYT (Chile), Ministerio de Ciencia, Tecnología e Innovación Productiva (Argentina), Ministério da Ciência, Tecnologia e Inovação (Brazil), and Korea Astronomy and Space Science Institute (Republic of Korea).

The Sloan Foundation 2.5-m Telescope and the Apache Point Observatory 3.5-meter telescope are located in the Sacramento Mountains in the stolen land of the Mescalero Apache tribe. I wish to recognize and acknowledge the very significant cultural role and reverence that the summit of Maunakea has always had within the indigenous Hawaiian community. We are most fortunate to have the opportunity to conduct observations from these mountains.

CHAPTER 3

SimBAL: a Spectral Synthesis Method for Modeling Broad Absorption-Line Quasar Spectra

Our group's proprietary software, *SimBAL*, played a crucial role in performing the majority of the spectral analysis presented in this thesis. *SimBAL* combines traditional photoionization analysis with novel machine learning methods and a forward modeling approach. Here, I briefly introduce the photoionization code used to calculate the column density grids used in our software and present a detailed discussion of *SimBAL*.

3.1. *Cloudy*

Cloudy (Ferland et al., 2017) is a software package developed to perform non-local thermodynamic equilibrium (n-LTE) photoionization calculations to simulate astrophysical environments and predict the conditions of interstellar matter. Photoionization is a physical process in which the interstellar medium (ISM) and circumstellar material (CSM) are being illuminated and ionized by electromagnetic radiation (photons) from an external source (e.g., star, accretion disk). Unlike thermal gas where LTE has been reached and the physical properties of the gas can be described by a single temperature, photoionized gas has complex ionization and temperature structures and thus it is difficult to obtain analytical solutions to describe their physical properties. The software calculates the atomic physics, chemistry, radiation transport, and (limited) dynamics problems simultaneously and self-consistently, based on individual atomic and molecular processes. Given a radiation source, *Cloudy* solves the microphysics within interstellar gas cloud and predicts the thermal, ionization, and chemical structure of the cloud. Users can run photoionization simulations under a broad range of conditions. The main physical conditions that need to be specified are: (1) the intensity as a function of frequency of the incident radiation, (2) the physical

and chemical condition of the gas clouds (e.g., metallicity and hydrogen density of the gas), and (3) the geometry of the gas. Additional properties (e.g., turbulence) can also be included as needed. Because an analytic solution cannot be obtained for the non-LTE gas, a numerical simulation is performed to solve the physical condition of the gas, and the process is iterated to obtain an accurate solution.

Cloudy solves the thermal and photoionization equilibrium equations as a function of depth into the illuminated gas slab. The software is exclusively designed for extreme non-LTE condition and it will fail when the gas becomes Compton-thick ($\log N_H \gtrsim 1.5 \times 24\ [\mathrm{cm}^{-2}] \sim \sigma_{\mathrm{T}}^{-1}$, σ_T: Thomson cross-section; $\tau_e \sim 1$). Highly optically thick environments such as stellar atmosphere require different software (e.g., `SYNOW`, Parrent et al. 2010; `PHOENIX`, Hauschildt & Baron 1999) that can numerically solve radiative transfer equations.

Cloudy is a mature code first developed in 1978 and it has been widely used in a variety of fields that use spectra to make physical measurements, including broad absorption-line (BAL) quasar science. There is a dedicated online user forum[1] and periodic instructional workshops for new users[2] organized by the developers of the software. *Cloudy* is an evolving code and new updates are released every couple of years. The latest version is C17 (Ferland et al., 2017) which was released in 2017. Throughout the thesis I note which version of *Cloudy* has been used with *SimBAL*.

3.2. *SimBAL*

It is not easy to determine the physical conditions of the outflowing gas from the observed spectrum. Depending on the physical conditions of the cloud, different absorption lines will appear. For example, a highly-ionized gas cloud will produce stronger high-ionization absorption lines (e.g., Si IV$\lambda\lambda$1402, 1393, C IV$\lambda\lambda$1548, 1550, O VI$\lambda\lambda$1032, 1038), while a cloud with a higher column density (thickness) will be able to produce stronger lines from all ions and also show transitions from rare ions because more gas is present

[1] https://cloudyastrophysics.groups.io/
[2] https://cloud9.pa.uky.edu/ gary/cloudy/CloudySummerSchool/

(detailed discussion in § 3.2.3). In addition, measuring the density of the absorbing gas is not straightforward. Generally, a special set of doublet or multiplet lines with one or more of the transitions occurring from a slightly excited state is needed to constrain a density of the absorbing gas. Because the excited state is populated by collisional excitation, a ratio between the strengths of the two doublet lines depends on the density. Even with the full understanding of the photoionization processes, constraining the physical conditions of the outflowing clouds can be very challenging due to line blending and the non-black saturation of absorption lines from partial coverage of the emission sources.

The standard method for analyzing BAL quasar spectra relies on the apparent optical depth (AOD) analysis (e.g., Arav et al., 2013). This method requires line identification and optical depth measurement of each absorption line. The optical depths are converted to ionic column densities and compared to the output from 1D photoionization simulations using *Cloudy* to find the physical conditions of the gas along the line of sight. Line blending makes this process particularly difficult for BAL quasar spectra and sometimes nearly impossible especially when the width of the lines is extremely large and a single giant trough is produced from dozens of blended absorption lines.

However, the AOD analysis can only provide lower limits for the column density estimates for the identified absorption lines and fails to provide accurate line ratios due to non-black saturation. Non-black saturation of BAL features is very common and is thought to originate from the BAL clouds not entirely covering the continuum source, i.e., accretion disk continuum and broad line emission features (e.g., Barlow & Sargent, 1997). For example, quantum mechanics predicts the ratio of the transition strengths of the doublet lines from sodium-like ions (e.g. C IV$\lambda\lambda 1548, 1550$) to be 1:2. However, this ratio is almost never seen in quasar spectra and the flux level rarely reaches 0 even at the bottom of the saturated absorption troughs. Because we are only seeing the part of the cloud that is occulting the background source, column densities calculated from the AOD can only serve as lower limit constraints. Obtaining accurate measurements of the density and the location of the gas with respect to the ionizing continuum source is difficult with

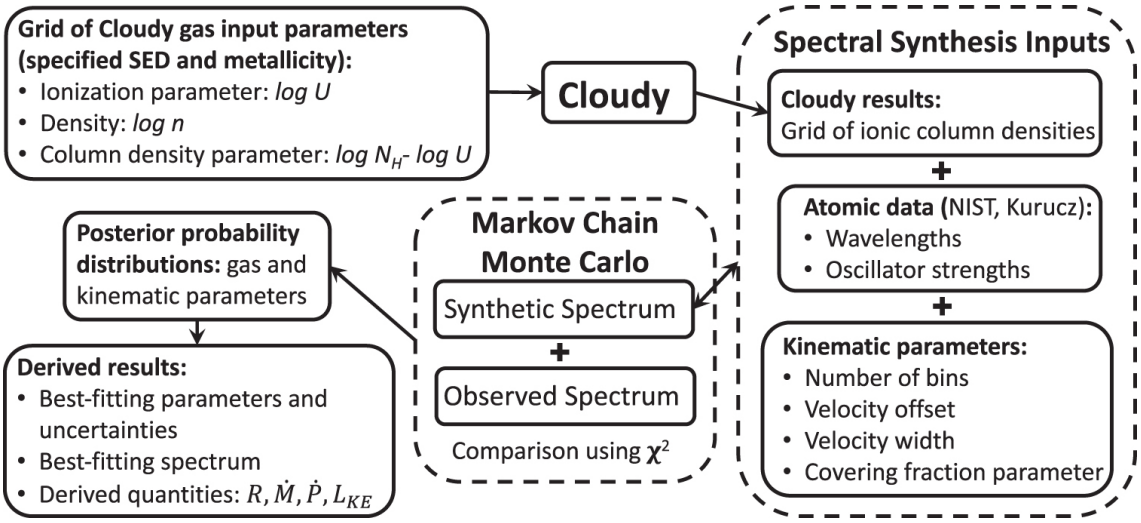

Figure 3.1: The plot is taken from Figure 2 of Leighly et al. (2018). Proceeding clockwise from the upper left, the flow chart shows how *SimBAL* uses the ionic column density information for the photoionized outflowing gas calculated from *Cloudy* simulations (Ferland et al., 2017) and other kinetic parameters to model the BAL features. The Markov Chain Monte Carlo (MCMC) method calibrates the model fitting procedures and provides the source of the posterior distributions of the fit parameters.

the AOD analysis method.

A revolutionary approach to studying BAL quasar spectra with the novel spectral synthesis code *SimBAL* was introduced by Leighly et al. (2018). *SimBAL* uses grids of ionic column densities calculated using the photoionization code *Cloudy* (Ferland et al., 2017) and a Bayesian model calibration method to model BAL quasar spectra. Because *SimBAL* employs a forward modeling technique and a sophisticated mathematical implementation of partial covering to model the absorption features (Leighly et al., 2019b), it can accurately reproduce the complex absorption features in BAL quasars and constrain the physical properties of the outflow as a function of velocity, thereby overcoming the limitations of the AOD analysis method. With a given set of parameters, *SimBAL* combines ionic column density information from the *Cloudy* grids, line transition strengths from atomic data (*Stout*, Lykins et al. 2015; *NIST*, Kramida & Ralchenko 2021; *Kurucz*, Kurucz & Bell 1995) and the parameterized kinematics of the outflow to create a synthetic spectrum. Figure 3.1 shows a flowchart describing the relationship of the components. A more

detailed discussion on how *SimBAL* operates can be found in § 3 of Leighly et al. (2018).

SimBAL uses the MCMC method `emcee`[3] (Foreman-Mackey et al., 2013) to compare the synthetic spectrum with the observed spectrum. MCMC methods explore the parameter space to sample the probability (of a data given the model parameters with their priors) and return Markov Chain with which the posterior probability density function for the parameters can be extracted. The software uses χ^2 to calculate the likelihood and a set of priors for the model parameters. For example, we used flat priors for the outflow physical parameters, to ensure that the solution stayed within bounds of the the computed *Cloudy* column density grid. If there exists prior knowledge for certain parameters (e.g., slope of the power law continuum, Krawczyk et al., 2015), we tuned the priors to match the known statistics. We checked that the posteriors of these parameters were always narrower than the priors to avoid priors from dominating the sampling. The Bayesian model calibration method used in *SimBAL* yields error estimates for the physical parameters that describe the gas in the outflow. From the converged chain of parameter values we construct posterior probability distributions for the fit parameters. The best-fitting model, the parameters, and their uncertainties are extracted from the posterior probability distributions.

Each absorption component is specified by 6 parameters: ionization parameter $\log U$, density $\log n\,[\mathrm{cm}^{-3}]$, thickness of the gas relative to the hydrogen ionization front (Figure 3.2) $\log N_H - \log U\,[\mathrm{cm}^{-2}]$, outflow velocity $v\,(\mathrm{km\,s}^{-1})$, velocity width $\sigma\,(\mathrm{km\,s}^{-1})$, and a covering fraction parameter $\log a$ (discussed further below). The first three parameters define the physical conditions of the outflowing gas in terms of the photoionization state and the last three parameters serve as an empirical description of the kinematics of the gas as well as the state of non-black saturation by modeling the partial coverage using the covering fraction parameter $\log a$. *SimBAL* can model a broad absorption feature with either one or multiple Gaussian opacity profiles or the "tophat accordion" model where a broad velocity profile is divided up into multiple velocity-adjacent "tophat" bins (Leighly et al., 2018), and the number of bins is specified for a given model. The procedure is very

[3] http://dan.iel.fm/emcee/current/

flexible and the outflow velocity and width parameter can be modified in many different ways depending on what kind of velocity profile is being used for the model. For example, each bin can have its own set of physical parameters (i.e., ionization parameter, density and $\log N_H - \log U$) and covering-fraction parameter. Alternatively, a single parameter may be fit for several velocity bins.

Several prescriptions have been proposed to model the partial coverage. The homogeneous partial covering model uses two parameters that describe the fraction of background source covered and a column density/opacity in front of the covered region. But recent studies have found that the homogeneous partial covering model falls short in describing the complex nature of partial covering in BAL systems. The inhomogeneous partial covering model was developed to produce more realistic quasar spectra (de Kool et al., 2002c; Arav et al., 2005). As discussed in detail in Leighly et al. (2019b), the inhomogeneous partial covering model in *SimBAL* uses a powerlaw distribution of opacity τ where $\tau = \tau_{max} x^a$ (Sabra & Hamann, 2005; Arav et al., 2005). The powerlaw slope can be thought to measure the degree of diffuseness of physical BAL gas cloudlets. For example, steep slopes (large values of a) correspond to peaked gas (opacity) distribution in which a low opacity is spread over a large spatial region, and a high opacity is concentrated in a small fraction. *SimBAL* uses log a to control the partial coverage and $x \in (0, 1)$ in the above equation is a normalized continuum source size scale. Full covering is achieved with low values of a close to 0, and low covering can be modeled with high values of a. Further discussion of inhomogeneous partial covering is given in Leighly et al. (2019b) and in § 3.2.2.

3.2.1. Updates to *SimBAL*

Since *SimBAL* was first introduced by Leighly et al. (2018), a number of updates has been applied the software. The first major update to *SimBAL* was reported in Choi et al. (2020) and the details of subsequent updates can be found in Choi et al. (2022a). As one of the key developers of *SimBAL*, I have made a significant contribution to the updates including inventing new models to be included in the software, facilitating the update of

the atomic data used within the code, and setting up supplemental guide materials for new users. I am currently in the process of developing a new user interface for *SimBAL*. In this section, I present the changes made to *SimBAL* since its debut that I facilitated with the collaborators.

In Choi et al. (2020), we introduced three major updates to *SimBAL*. The first update involves expanding the atomic data used in *SimBAL*. The version of *SimBAL* used in Leighly et al. (2018, 2019b) employed the 2013 version of *Cloudy*. After that analysis was initiated, the version C17 of *Cloudy* (Ferland et al., 2017) was released, which allowed more complete and accurate photoionization calculations with a significantly larger atomic database. Compared with Leighly et al. (2018), the ionic column density grids that have been calculated with version C17 of *Cloudy* include the column densities of Fe II ions with a greater number of excited state levels and multiple iron-peak element ions including Co and Zn at multiple ionization states. To illustrate the magnitude of the update I note the that the first version of *SimBAL* used a line list with 6267 transitions (78 ions; 179 counting the excited energy states); the updated line list includes 76488 transitions (281 ions; 997 counting the excited energy states).

A second update involved the grid sampling. The photoionization state of the gas changes dramatically near the hydrogen ionization front. This transition point is located and calculated at which the recombination rate of hydrogen, the most abundant atom, equals the ionization rate assuming that the hydrogen in the gas is totally ionized (also called Strömgren Sphere; Strömgren, 1939). On the illuminated side of a photoionized slab of gas, hydrogen is essentially fully ionized as expected. On the farther side beyond the hydrogen ionization front, hydrogen can be partially ionized. Gas clouds responsible for producing iron low-ionization broad absorption-line (FeLoBAL) features are typically thick enough to encompass the hydrogen ionization front within the cloud and have a stratified structure. Most of the Fe II opacity is produced near this boundary. Figure 3.2 illustrates the rapid change in physical properties of the gas across the hydrogen ionization front.

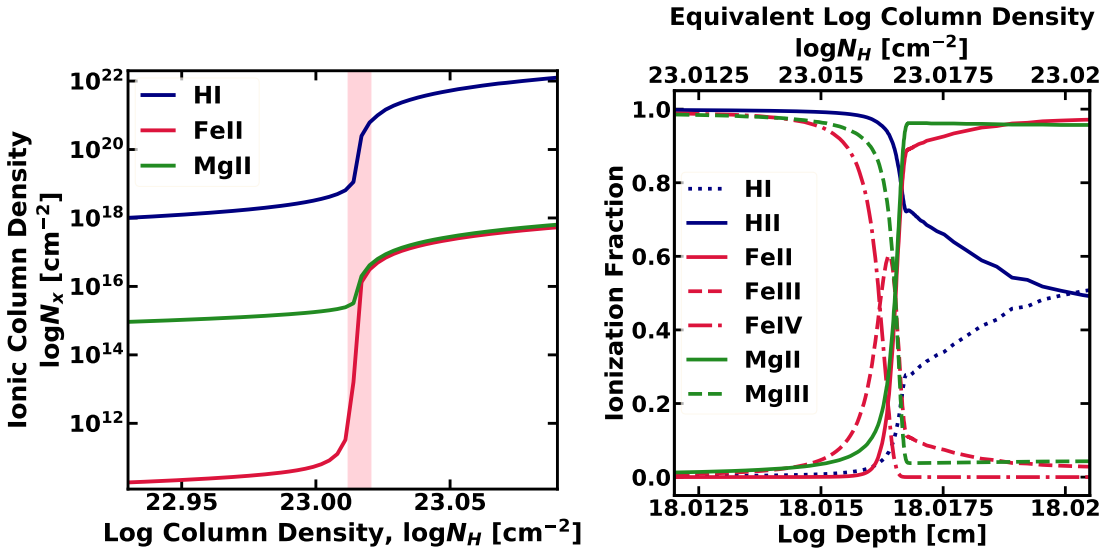

Figure 3.2: An illustration of the dramatic changes in the gas physical properties such as ionization fraction that occurs at the hydrogen ionization front. *Left panel*: once the gas becomes thick enough to include the hydrogen ionization front, highlighted in pink, the amount of Fe^{+} (Fe II) in the gas jumps by more than four orders of magnitude. The opacity of an absorption line is proportional to the ionic column density of the ion that is producing the line transition (Savage & Sembach, 1991). *Right panel*: the change in ionization fractions of select atoms in region where the hydrogen ionization front occurs is plotted as a function of cloud depth (0 at the illuminated side). Note that the dominant ionization states for hydrogen, iron, and magnesium abruptly changes from H^{+} (H II), Mg^{+2} (Mg III), and Fe^{+3} (Fe IV) to H (H I), Mg^{+} (Mg II), and Fe^{+} (Fe II) across the hydrogen ionization front.

A simple even sampling by a modest amount across the column density or the $\log N_H - \log U$ parameter is insufficient to characterize the rapid change of ionic column densities across the hydrogen ionization front. For example, the ionic column densities of some species that are mostly found in the partially ionized zone such as Fe II increase by more than 4 dex as the hydrogen ionization front is traversed (e.g., Lucy et al., 2014, their Figure 10). A finer sampling is needed to properly capture the steep increase in ionic column density around the hydrogen ionization front. However, the remainder of the hydrogen column density range does not need a finer sampling and a grid with much finer sampling requires a tremendous amount of calculation time as well as a large file size. Therefore we approached this problem by adopting a flexible indexing scheme where we identify the location of the hydrogen ionization front and apply the oversampling only around the region where the ionic column densities change very rapidly. In addition, the changes in physical conditions before and after the hydrogen ionization front becomes more dramatic with higher ionization parameter. We took into account this change in the "sharpness" of the hydrogen ionization front when calculating the indexing scheme by increasing the grid density of the oversampled regions for higher ionization parameters (total 619,721 grid points).

A third change involves continuum modeling of the spectra. In Leighly et al. (2018), continuum-normalized spectra were used for analysis, which means that they normalized (divided) the spectrum by a continuum emission model they developed to obtain spectrum that only has absorption line features. This method has two steps and the absorption modeling is performed independently after continuum fitting is completed. The issue is that the depth of the absorption feature can either be overestimated or underestimated depending on the continuum placement. Moreover, one needs to take into account for the additional systematic uncertainties due to the continuum emission model shape and placement. For instance, Leighly et al. (2018) performed absorption analysis multiple times using different continuum emission models to explore the systematic effects.

The new version of *SimBAL* models both the synthetic continuum model and the

absorption model simultaneously, producing the full synthetic spectrum. Thus *SimBAL* can fit both the emission features and the absorption features of the spectrum simultaneously to produce a more robust solution. This methodology allows more accurate measurement of the outflows. Moreover, simultaneous absorption and emission continuum modeling enables the fitting of heavily absorbed objects (e.g., overlapping trough objects) that have thick outflows and show very little residual continuum emission.

In Choi et al. (2020), we used an emission line template developed from an HST observation of Mrk 493 (Chapter 4; § 4.3.3) and fit the normalizations. In Choi et al. (2022a), *SimBAL* has been updated to include two substantial enhancements that facilitate the emission continuum modeling: (1) use of spectral eigenvectors for continuum fitting, (2) addition of anomalous reddening (Choi et al., 2020) as an option. The updated version of *SimBAL* uses spectral eigenvectors from spectral principal component analysis (PCA) to model the emission lines. These eigenvectors enable *SimBAL* to employ only a small number of parameters for the emission-line model. A detailed discussion of the construction of the eigenvectors used in this work is found in Appendix A of Choi et al. (2022a). The continuum emission is currently modelled with a power law for the continuum, and the Small Magellanic Cloud (SMC) reddening curve (Prevot et al., 1984) or a general reddening curve (Choi et al., 2020) to reproduce the reddening in the spectra depending on whether the object showed a typical continuum shape or anomalous reddening with a break.

Another update to *SimBAL* involves incorporating the instrument resolution into synthetic spectrum (MacInnis, 2018). The spectrum data file from the Sloan Digital Sky Survey (SDSS) includes information about the wavelength dispersion at each pixel. *SimBAL* uses this information to create a resolution matrix and performs a convolution of synthetic spectrum with the matrix. The process is precisely analogous to the "Response Matrix Function" matrix used for forward modeling in X-ray spectral fitting. The spectrograph has a finite resolution, effectively convolving the source spectrum with a kernel width corresponding to the detector resolution (e.g., $\sim 150\ \mathrm{kms}^{-1}$ for SDSS, § 2.1 in Chapter2).

The principal effect is that the absorption lines with intrinsically narrow widths become noticeably shallower and wider in the spectra once the instrument resolution has been taken into account (MacInnis, 2018). The other effect is aesthetic; the steps in the step-function opacity (from the tophat accordion model) appear smoothed out when the resolution has been taken into account. Without the resolution convolution, *SimBAL* would modify the fit parameters to mimic the effect of the instrument resolution, resembling a larger measured value of the partial covering parameter $\log a$, corresponding to a lower covering fraction, and a larger measured BAL width. This incorporation of wavelength-dependent instrument resolution into the synthetic spectrum generation not only helps *SimBAL* to create a more realistic spectrum that more closely matches the data, but also provides more accurate properties of the outflowing gas when the lines are very narrow.

3.2.2. *Cloudy* and the Partial-Covering Power Law Parameterization[4]

As discussed by Sabra & Hamann (2005), the power-law opacity profile $\tau(x) = \tau_{max} x^a$ yields the following residual intensity equation

$$I(\lambda) = \frac{1}{a} \frac{1}{\tau_{max}^{1/a}} \Gamma(1/a) P(1/a, \tau_{max})$$

where Γ and P are the complete and incomplete Gamma functions, respectively. This is the equation that is used in *SimBAL*.

Cloudy computes photoionization equilibrium in a slab of gas; there is no provision in the software for partial covering. How the ionic column densities produced by the *Cloudy* simulations map to the power-law opacity profile is a matter of interpretation. There are at least two possibilities: the opacity of an ion calculated using *Cloudy* corresponds to the *average* opacity across the continuum emission region (i.e., $N_{ion} \Rightarrow \bar{\tau}$, where $\bar{\tau} = \int_0^1 \tau_{max} x^a dx = \tau_{max}/(1+a)$), or the opacity of the ion maps to the maximum opacity (i.e., $N_{ion} \Rightarrow \tau_{max}$). These two methods produce indistinguishable results when the covering fraction is high (a is low), but lead to somewhat different interpretations of

[4]This subsection is reproduced from § 5.1.1 in Leighly et al. (2019b) with permission.

partial covering, somewhat different implementations in *SimBAL*, and different line profile behaviors, as we discuss below.

For the $N_{ion} \Rightarrow \bar{\tau}$ case, we must first obtain τ_{max} using $\tau_{max} = \bar{\tau}(1 + a)$. Thus, the opacity of an ion computed by *Cloudy* is multiplied by $1 + a$ *before* the spectrum is computed in *SimBAL*. For the $N_{ion} \Rightarrow \tau_{max}$ case, the opacity computed by *Cloudy* is used directly as τ_{max} by *SimBAL* to compute the spectrum, and the fitted column density is then corrected for the portion that is not covered by dividing by $1 + a$ *after* the *SimBAL* computation (referred to as the covering-fraction-weighted column density here and in Leighly et al. 2018). There is no difference when a is small, simply because $\bar{\tau}$ approaches τ_{max}. But when a is large, $\bar{\tau}$ is much less than τ_{max}.

If the proportions of ions were uniform as a function of column density of the *Cloudy* slab, it might seem that there would be no difference between the two interpretations: either the average opacity is scaled up by $1 + a$ before the spectrum is constructed, or the inferred column density is corrected by dividing by $1 + a$ after the spectrum is constructed. The proportionally of the ionic populations is the assumption that is implicitly made by the $N_{ion} \Rightarrow \bar{\tau}$ method, since it assumes that the optically thickest part of the inhomogeneous partial covering is adequately modeled by $\tau_{max} = (1 + a)\bar{\tau}$. However, it is readily apparent that the ionic column densities do not increase in proportion with the hydrogen column density (Figure 3.2). As ionizing photons are removed from the photoionizing continuum by transmission through the gas, the proportions of different types of ions change. This is especially true when approaching the hydrogen ionization front where low-ionization ions such as Mg^+ start to become common. These low-ionization lines can be very important in constraining the column density. In SDSS J0850+4451, a low-ionization broad absorption-line (LoBAL) quasar, it is the C III* that constrains the $\log N_H - \log U$ of the simulation (see Figure 10 in Leighly et al., 2018, in particular, see the accompanying animation). For large a, it is more important to model the ionic proportions in the high-column density centers of the "clouds," which is done by the $N_{ion} \Rightarrow \tau_{max}$ method, but not the $N_{ion} \Rightarrow \bar{\tau}$ method.

Further tests show subtle but significant differences in behavior that lead us to reject the $N_{ion} \Rightarrow \bar{\tau}$ interpretation. We created a mock line list to test the differences between the two methods. The mock line list includes a strong line, a weak line, and a blend of four weak lines (Figure 3.3). The weak lines all have the same line strength (i.e., same $\lambda f_{ik} N_{ion}$), and the strong line is a factor 20 times larger. Thus, the total opacity of the blend is 5 times smaller than that of the strong line. The left panel shows the synthetic line profiles for a range of $\log a$ values for the $N_{ion} \Rightarrow \bar{\tau}$ method (top panel) and the $N_{ion} \Rightarrow \tau_{max}$ method (bottom panel). The right panel shows the depth of each feature as a function of $\log a$. As expected, the depths of all features decrease with the increase of $\log a$. The difference is seen in the relative change in the features for the two methods. For the $N_{ion} \Rightarrow \tau_{max}$ method, the depths of the lines decrease together, maintaining the order of the total opacity. That is, the strong line is always deeper than the blend, which is always deeper than the weak line. This makes sense, because the total opacity of the strong line is 5 times that of the blend, which is in turn 4 times that of the weak line. However, for the $N_{ion} \Rightarrow \bar{\tau}$ case and $\log a > 0.7$, the depth of the blend is larger than the depth of the strong line. This is unphysical, since the total opacity of the blend is smaller than the opacity of the strong line. This result occurs because, as mentioned above, in this method, opacities from *Cloudy* are multiplied by $1 + a$ to obtain τ_{max} before the spectrum is made, and the $1 + a$ factor dominates over the actual opacity of the lines for sufficiently high a. The same result is obtained if line equivalent width is measured instead of line depth. This problem is most noticeable when modeling overlapping-trough FeLoBALs, where a large $\log a$ means that blends of iron multiplets that are predicted to have low opacity still produce significant optical depth due to the dominance of the $1 + a$ factor.

SimBAL uses the second method, i.e., $N_{ion} \Rightarrow \tau_{max}$. We have run a few tests using $N_{ion} \Rightarrow \bar{\tau}$ on Hubble Space Telescope (HST) spectrum of SDSS J0850+4451, and we obtained commensurate total column densities (so the derived parameters do not change significantly), but slightly lower log likelihoods (worse fits). This preference for the $N_{ion} \Rightarrow \tau_{max}$ method makes sense for SDSS J0850+4451, as the high opacity cores of

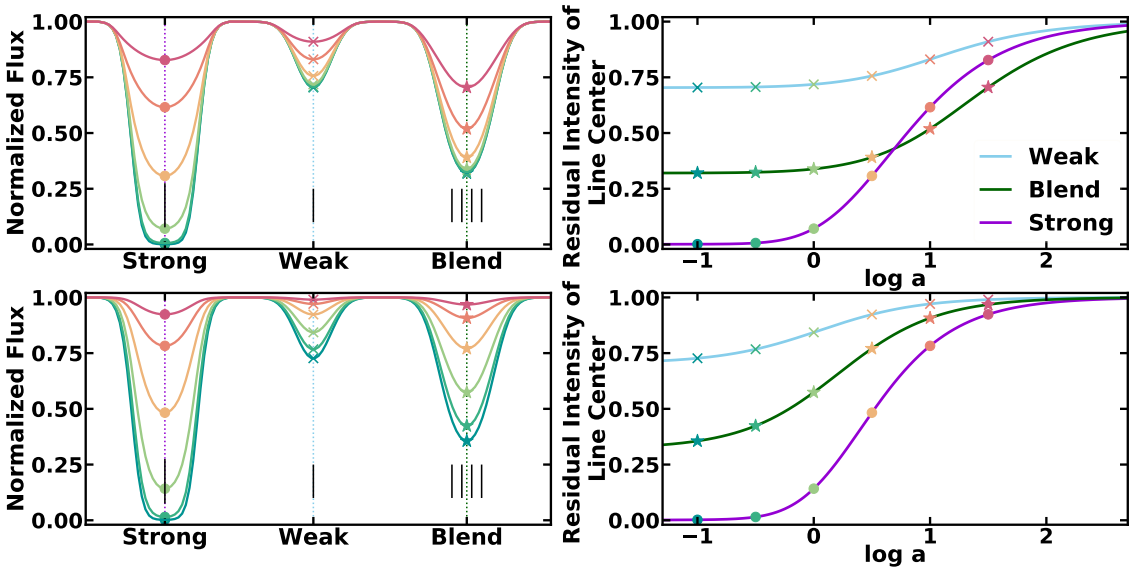

Figure 3.3: The influence of the choice of mapping of *Cloudy* output results to the power law partial covering parameters. The top panel shows the results for $N_{ion} \Rightarrow \bar{\tau}$ method, and the lower panel shows the $N_{ion} \Rightarrow \tau_{max}$ method, the method currently used in *SimBAL*. *Left:* A strong, a weak, and a blend of four weak lines were simulated for a range of covering fraction parameters $\log a$, where the total opacity of the strong line is 20 times that of the weak line. *Right:* the depth at the lowest point for the simulated lines shown in the left panel. For the $N_{ion} \Rightarrow \tau_{max}$ case (lower panel), the line depth tracks the total opacity. That is, as $\log a$ is increased (covering fraction decreased), all lines become shallower, but the blended line is always shallower than the strong line. For the $N_{ion} \Rightarrow \tau_{max}$ case (upper panel), the blended line is deeper than the strong line for $\log a > 0.7$, even though the total opacity for the blend is five times smaller than for the strong line. This is unphysical, and therefore we reject the $N_{ion} \Rightarrow \bar{\tau}$ mapping.

the clouds that yield sufficient opacity in weak lines such as C III* strongly constrain the $\log N_H - \log U$ best fit. But given the unphysical results produced by the $N_{ion} \Rightarrow \bar{\tau}$ method for blended lines as discussed above, we found no reason to investigate this method further.

3.2.3. *SimBAL* Parameter Sensitivity

How does *SimBAL* constrain its model parameters and how do the changes in the absorption parameter manifest in the synthetic spectra? As mentioned in § 3.2, *SimBAL* uses six parameters to control each absorption component. The first three parameters ($\log U$, $\log n$, and $\log N_H - \log U$) define the physical photoionization condition of the gas and the other three parameters explain the kinematics of the outflowing gas (outflow velocity and width) and the level of partial coverage ($\log a$). The latter three parameters control the spectra in a more direct manner and thus their impact on shaping the synthetic spectra is easier to explain. For instance, the change in outflow velocity parameter shifts the absorption features in wavelength and the width parameter controls the widths of absorption lines without having any influence on their relative strengths. The dimensionless covering fraction parameter ($\log a$) controls the overall depths of the absorption lines as discussed in § 3.2.2. However, it is often difficult to predict how the change in $\log U$, $\log n$, or $\log N_H - \log U$ impacts the absorption lines present (or not) in the bandpass without considering various photoionization properties of the individual line transitions. In order to demonstrate how these parameters are constrained by *SimBAL*, I created a set of synthetic spectra and varied each parameter to show the change in absorption lines. I chose physical condition of $\log U = -0.75$, $\log n = 5.5$ [cm^{-3}], and $\log N_H - \log U = 23.04$ [cm^{-2}] to create an FeLoBAL synthetic spectrum with $v_{off} = 0$ km s^{-1}, $v_{width} = 400$ km s^{-1}, and $\log a = 0$. Only the absorption lines in $2300 \lesssim \lambda \lesssim 3200$ Å are examined in this exercise for simplicity. The behavior in other regions of the spectrum where there are more strong high-ionization lines will be somewhat different. A more detailed explanation of various absorption lines observed in an FeLoBAL quasar spectrum can be found in Chapter 5

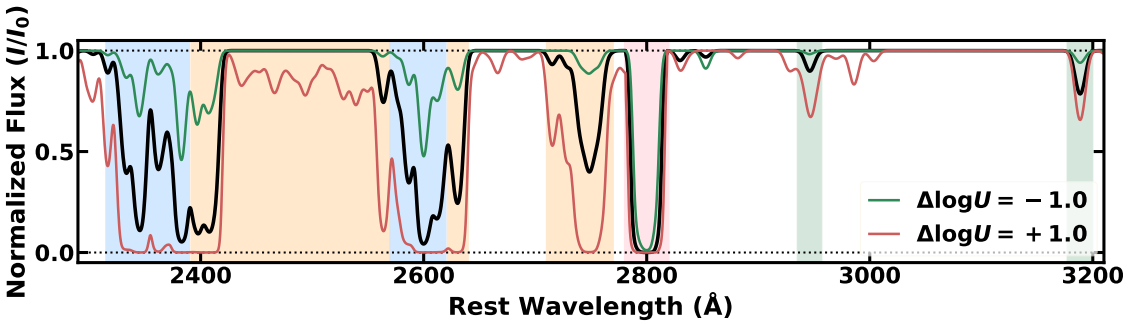

Figure 3.4: Change in BALs as a function of ionization parameter ($\log U$). Comparison synthetic spectrum is plotted in black. The strengths of all absorption lines present in the bandpass increase (decrease) with increasing (decreasing) $\log U$. A higher-$\log U$ (red) also produces excited-state Fe II absorption lines especially near 2500 Å. Major absorption-line transitions are highlighted: blue, ground state and low-excitation Fe II; orange, excited-state Fe II; red, Mg II$\lambda\lambda 2796, 2803$; green, He I* absorption lines at 2945 and 3188 Å. Mg II lines are saturated even for lowest $\log U$ and thus they change very little.

(§ 5.5.1.2; Figure 5.3).

Figure 3.4 shows how the change in ionization parameter influences the strengths of the BALs. We see that all the absorption lines are influenced by the change in ionization parameter and their depths follow the change in $\log U$. Two changes occur with the change in $\log U$: (1) column density ($\log N_H$), a measure that represents how much gas is present in the cloud, increases with $\log U$, given that $\log N_H - \log U$ is fixed and (2) as the name suggests, higher $\log U$ means the gas is more highly ionized. For example, we observe deeper absorption lines with higher $\log U$ because an increase in $\log N_H$ means more material in the gas cloud along the line of sight and thus more absorption occurs.

For example, the impact of the change in the ionization state of the gas cloud can be uniquely witnessed from the change in the strengths of He I* absorption lines (highlighted in orange in Figure 3.4). In order to create observable He I* absorption lines, a gas cloud needs to have a significant population of metastable He I* ions. These ions are formed by recombination onto singly-ionized helium (He^+ or He II) which means a gas cloud should have a significant fraction of He^+ ions to populate metastable He I* ions (Leighly et al., 2011). The ionization potential of He is ~ 24.59 eV, much greater than that of hydrogen

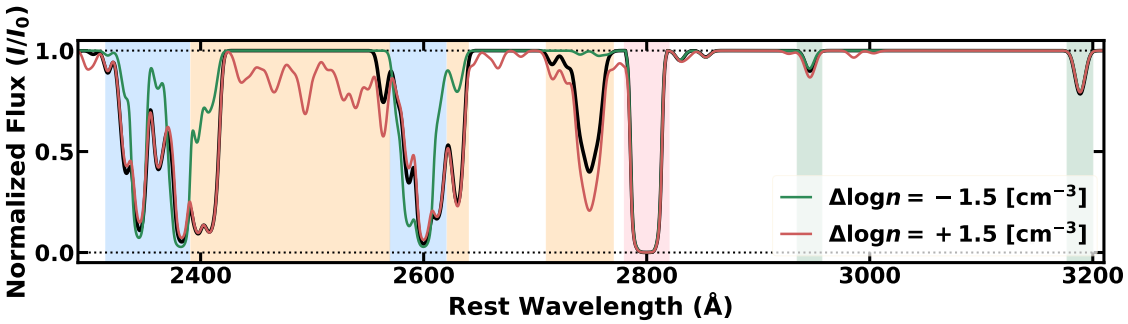

Figure 3.5: Change in BALs with density ($\log n$). Only the excited-state Fe II absorption lines change with density. The synthetic spectrum for lower-$\log n$ (green) shows absence of excited-state Fe II absorption lines. This plot follows the same format as Figure 3.4.

($\sim$ 13.6 eV), and thus more highly-ionized condition (higher-$\log U$) is required for a gas cloud to populate metastable He I* ions.

Figure 3.5 shows how the change in density ($\log n$) appears in synthetic spectra. Unlike Figure 3.4 in which the change in ionization parameter varied the depths of all the absorption lines, density only varied the strengths of the excited-state Fe II absorption lines. In low-$\log n$ synthetic spectrum, no excited-state Fe II absorption lines are observed and the spectrum in this bandpass is dominated by the ground-state Fe II and Mg II absorption lines. Fe II ions have a large number of excited states and they can be populated by collisional excitation. The rate of collisional excitation is governed by density. In other words, the level population ratios between the excited states and the ground state will increase with density up to a critical density at which the ratios approximately become the ratios of the levels' degeneracies. Therefore the excited-state Fe II absorption lines are highly sensitive to the change in density and are often used to measure the density in BAL gas as one of the most useful density diagnostic absorption lines. While the critical density is different for different excited states, many high-opacity Fe II transitions that we observe have critical densities of $\log n_{crit.} \sim 6\,[\mathrm{cm}^{-3}]$ (e.g., Lucy et al., 2014, Figure 13).

A combination parameter ($\log N_H - \log U$) measures the depth of the cloud relative to the hydrogen ionization front. Much of the Fe II opacity is mainly produced in a thin layer near the hydrogen ionization front which means a small change in $\log N_H - \log U$

can cause the strengths of the Fe II absorption lines to vary rapidly (e.g., Wampler et al., 1995; de Kool et al., 2001). Absorption lines from rarer atoms (e.g., Mn, Cr) and those with lower oscillator strengths can continue to get stronger beyond the hydrogen ionization front with increasing $\log N_H - \log U$ (Lucy et al., 2014). In Figure 3.6, we can see how even a small change in $\log N_H - \log U$ impacts the Fe II absorption lines. Notably, we can see that with lowering $\log N_H - \log U$ by 0.1 the Fe II absorption lines completely disappear and the synthetic spectrum changes from an FeLoBAL to a LoBAL spectrum. This is because the depth (or the thickness) of gas became too shallow for the gas cloud to produce the layer where Fe II ions are produced; the iron atoms in such a slab of gas have a higher ionization state. An increase in $\log N_H - \log U$ creates deeper Fe II absorption lines because it corresponds to an increase in gas thickness and the gas cloud will include a larger region where Fe II is populated.

In summary, various absorption lines react differently to the changes in physical parameters ($\log U$, $\log n$, and $\log N_H - \log U$). The ionization parameter can vary the strengths of all the absorption lines whereas the density only controls the strengths of the excited-state Fe II absorption lines. The depths of the He I* absorption lines are only sensitive to the change in $\log U$. The strengths of the Fe II absorption lines are highly dependent on $\log N_H - \log U$. *SimBAL* uses the information from the whole spectrum provided by both absent and present absorption lines with forward modeling approach. A combination of absorption lines with different diagnostic powers allows *SimBAL* to constrain the parameters in spectral models.

3.2.4. *SimBAL* Usage

SimBAL is written in Python and the software makes use of a number of widely used Python packages (e.g., numpy, scipy). The code can be run on both Python 2 and Python 3; however, we recommend that the users use Python 3. The software performs the spectral synthesis using the Python programs my collaborators and I authored. It then use `emcee` (Foreman-Mackey et al., 2013), a pure-Python implementation of Affine Invariant MCMC

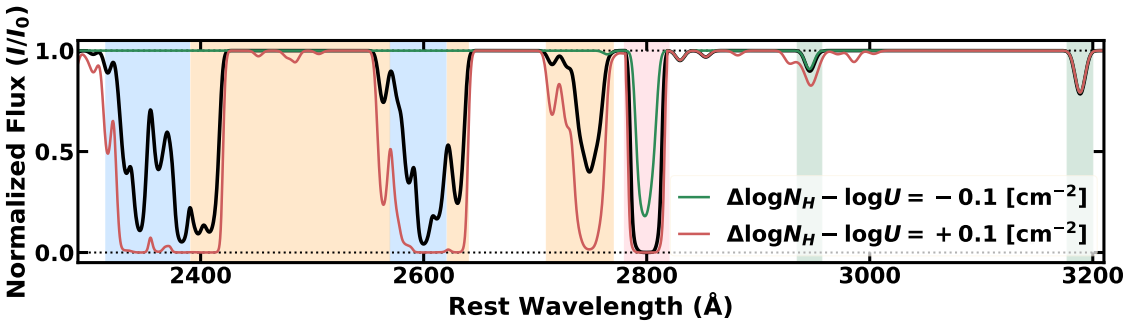

Figure 3.6: Change in BALs with column density parameter ($\log N_H - \log U$). The majority of the variations can be found in Fe II absorption lines. Note that no Fe II opacity is observed for $\Delta \log N_H - \log U = -0.1$ (green). This plot follows the same format as Figure 3.4.

Ensemble sampler (Goodman & Weare, 2010), for model calibration. As mentioned in § 3.2, the spectral synthesis is performed using grids of ionic column densities calculated using the photoionization code *Cloudy*. There are four main ionic column density grids currently available in the software:

1. C13 grid: ionic column densities calculated using the c13.03 version of *Cloudy* (Ferland et al., 2013)

2. C17 grid: ionic column densities calculated using the c17.01 version of *Cloudy* (Ferland et al., 2017); includes finer sampling (§ 3.2.1)

3. hard spectral energy distribution (SED) grid: ionic column densities calculated using the c13.03 version of *Cloudy* (Ferland et al., 2013) with a relatively hard SED (Korista et al., 1997) illuminating the slab of gas

4. Z = 3 $Z_\odot$ grid: ionic column densities calculated for a gas that has higher metallicity (Leighly et al., 2018); also calculated with c13.03 version of *Cloudy*.

All the grids were calculated using a relatively soft SED that may be characteristic of typical quasars (Hamann et al., 2013) unless specified otherwise (hard SED grid). The C17 grid and its accompanying atomic data contain a significantly larger number of absorption

line transitions compared to the C13 grid. Because *SimBAL* has to calculate a larger number of absorption lines, it takes longer to generate a synthetic spectrum using the C17 grid. However, the C17 grid is necessary to model FeLoBAL quasar spectra that have a large number of excited-state absorption lines. The grids calculated with the c13.03 version of *Cloudy* (C13 grid, hard SED grid, and Z = 3 $Z_{\odot}$ grid) are useful for analyzing high-ionization broad absorption-line (HiBAL) quasar spectra as they have significantly fewer absorption lines (Green et al., in preparation). Therefore, depending on the object and the objectives of the experiment, users may select the most appropriate grid for their *SimBAL* analysis.

While it is not a requirement to run *SimBAL*, an access to high-performance servers or super computing resources is highly recommended. The program execution time depends on the number of walkers and simulations. It may take several hours for the MCMC solver with ~ 300 walkers and ~ 5000 simulations to explore the parameter space and converge for a relatively simple spectral model with a single Gaussian opacity profile absorber when run with a multiprocessing setting with $\sim 60 - 80$ threads. In other words, if the same run was executed without multiprocessing it would take $\sim 60 - 80$ longer for the program to complete. *SimBAL* uses `emcee` (version 3) which is optimized for parallel computing and it employees the `multiprocessing` module in the Python standard library or the `schwimmbad` package[5] (Price-Whelan & Foreman-Mackey, 2017).

I used the Linux servers owned by *SimBAL* group and a set of private condominium servers, also owned by the group, and public compute nodes available on the OU Supercomputing Center for Education & Research[6] (OSCER; Chapter 2; § 2.4). In particular, *SimBAL* runs for some of the heavily absorbed FeLoBAL quasar spectra often require a substantially long computation time because of a large number of absorption line transitions *SimBAL* has to calculate for the synthetic spectrum. I utilized the condominium nodes, 320 threads total, on OSCER to run *SimBAL* to analyze the spectra of "overlapping

[5]https://github.com/adrn/schwimmbad
[6]https://www.ou.edu/oscer

trough" objects (§ 5.6.4). *SimBAL* model fitting using a complicated spectral model for a heavily absorbed FeLoBAL quasar spectrum can take multiple days even with 100s of CPU threads.

The use of `emcee` requires a small number of user configuration. An exhaustive review and a thorough guide can be found in Foreman-Mackey et al. (2013) and on their website[7]. Here, I briefly describe some key techniques most relevant for *SimBAL*. One of the key features of the ensemble sampler is walkers which are the members of the ensemble (Goodman & Weare, 2010). A user needs to specify the number of walkers to be used in the `emcee` process in *SimBAL*. A reasonable rule of thumb is that a greater number of walkers is generally better for `emcee` to produce a well sampled posterior distributions for model parameters. However, memory usage and *SimBAL* (`emcee`) runtime linearly increase with the number of walkers and thus one needs to find a good balance. We found that a *SimBAL* model with a single Gaussian opacity profile BAL (total ~ 15 model parameters) requires about ~ 300 walkers for optimal performance. Tophat accordion models that use a significantly larger number of model parameters require a larger number of walkers of about $\gtrsim 500$ in order for `emcee` to be able to robustly explore the large dimensional parameter space.

The simplest indicator that measures the `emcee` performance is the acceptance fraction. The `emcee` manual suggests the acceptance fraction should be between 0.2 and 0.5. With *SimBAL*, the values of acceptance fraction often stay close to the lower end of the optimal range (or even lower) due to the nature of complex spectral model with a large number of fit parameters. One can increase the acceptance fraction by increasing the number of walkers and/or decreasing the a parameter (default, $a = 2$), an adjustable scale parameter that effectively controls the step size of the walkers. While it may be recommended to monitor the autocorrelation time to check the MCMC performance, we did not find this metric to be useful for *SimBAL*.

[7] https://emcee.readthedocs.io/en/stable/

3.3. Emission Line Modeling Using Spectral Principal Component Analysis Eigenvectors

Accurately measuring the strengths of the absorption lines is crucial for constraining the physical properties of BAL outflowing gas. The absorption line strengths depend on the continuum placement and it becomes challenging and more important when analyzing BAL spectra that show heavy absorption from blended absorption lines or shallow BAL features. In order to obtain a more robust solution, *SimBAL* has been updated to simultaneously model both the emission line and absorption line features (§ 3.2.1).

In Choi et al. (2020), I used a set of emission line templates extracted from Mrk 493 to model the emission lines. Although this commonly-used method produced an excellent result, the use of templates has various disadvantages. The template model requires a large number of fit parameters in order to reproduce a wide range of spectral features and line ratios. And when the parameters are not properly controlled, one could end up with an emission line model that is unphysical. In Choi et al. (2022a), I used the updated version of *SimBAL* that uses spectral eigenvectors from spectral PCA to model the emission lines (Appendix A of Choi et al. (2022a)). These eigenvectors enabled *SimBAL* to require only a small number of parameters to successfully model various line ratios and emission line morphologies observed in BAL quasars. These eigenvector sets provided wavelength coverage from 1675 Å to 3050 Å, suitable for the analysis of the near-ultraviolet (UV) bandpass of FeLoBAL quasar spectra where the main Fe II absorption lines are observed. However, the majority of BAL quasars are HiBAL quasars which have absorption lines in the rest-UV (e.g., Si IV$\lambda\lambda1402, 1393$, C IV$\lambda\lambda1548, 1550$, O VI$\lambda\lambda1032, 1038$). Moreover, there are several important diagnostic absorption lines in the far-UV bandpass (e.g., Arav et al., 2013). For example, C III*$\lambda1175$ multiplets and S IV$\lambda\lambda1072, 1062$ doublet transitions can be used as density diagnostics (e.g., Gabel et al., 2006). In addition, the P V$\lambda\lambda1118, 1128$ doublet can be used to constrain the ionization parameter and column density of the gas (Leighly et al., 2009, 2018). In order to use *SimBAL* to extract information from these transitions with robust model fits, we need a

good method to model the emission lines at rest-UV wavelengths.

I created a set of spectral PCA eigenvectors to model the rest-UV emission lines from $\sim$ 1020 Å to $\sim$ 2000 Å. Performing spectral PCA in this bandpass is particularly challenging because of the presence of Lyman-α forest features that contaminate the spectra. Lyman-α forest absorption-lines are created by gas clouds located between the observer and the distant quasar background continuum source. The Lyman-α forest pattern is frequently seen in the spectra of high-redshift quasars (e.g., Gunn & Peterson, 1965) where the absorbing gas is the intergalactic medium (IGM) and the quasars act as an background light source, creating 1215.67 Å Lyman-α absorption lines from neutral gas at various redshifts. Therefore, careful continuum reconstruction to remove the Lyman-α forest feature is required for the analysis of rest-UV quasar spectra. There are publicly available spectral PCA eigenvectors for the rest-UV bandpass (e.g., Suzuki et al., 2005; Suzuki, 2006; Pâris et al., 2011). However, none of these specifically modeled the Lyman-α forest features to obtain an accurate reproduction of the continuum. Also, they did not subtract the power-law continuum emission from the spectra when performing PCA and thus their eigenvectors include variance from both line emission and continuum emission. The spectral PCA eigenvectors described below improve upon the existing rest-UV spectral PCA eigenvectors by including Lyman-α absorption line modeling, continuum emission subtraction, and the use of a PCA solver that can properly handle noisy data (Weighted Expectation Maximization Principal Component Analysis; Bailey, 2012). In this section, I describe the steps taken to produce the rest-UV spectral PCA eigenvectors.

3.3.1. Data and Methods

The quasar sample was drawn from Pâris et al. (2011). They selected objects in the redshift range from 2.82 to 3.00 and excluded objects that showed strong absorption features from damped Lyman-α systems (DLAs) or BAL in the spectra. 78 high signal-to-noise ratio (SNR) quasar spectra from SDSS-DR7 were chosen for principal component analysis (PCA) and the resulting spectral PCA eigenvectors were made available to the

public.

The first step of the analysis involves preparing the data by modeling out Lyman-α absorption lines. This procedure is composed of a two-stage iterative process: (a) Lyman-α absorption line identification, and (b) spectral fitting using `emcee`. At the start of each iteration, a normalized spectrum is calculated by dividing the data by the continuum model that is either extracted from the previous iteration or produced using the eigenvector coefficients calculated from the analytic equation for the first iteration. The Lyman-α absorption lines are identified by first defining the regions of Lyman-α absorption to be where the value of normalized flux dips below 0.9 (or below 1 minus the normalized error) and locating the lowest point in each region as the center of absorption line. This identification procedure is done automatically and one example of the result is shown in Figure 3.7.

Then a spectral model is configured based on the result of the line identification with Gaussian opacity profiles for Lyman-α absorption lines, one for each identification, and the ten spectral PCA eigenvectors from Pâris et al. (2011). The eigenvector coefficients and the absorption line locations are allowed to vary, but the widths of the lines are kept the same for all absorption lines. This is because the intrinsic widths of Lyman-α absorption line is about $\sim 10 - 45$ km s^{-1} (Rauch, 1998) which is significantly less then the SDSS detector resolution (~ 150 km s^{-1}). Thus the absorption lines are mainly shaped by the instrument resolution. I used `emcee` to fit the model to the data.

The two-stage iteration continues until no new Lyman-α absorption lines are identified (i.e., no change to the spectral model). Figure 3.8 shows the result of the iterative model fitting for one of the 78 objects. Using this iterative method, I was able to obtain spectral models that included Lyman-α absorption lines as well as the continuum models for all 78 objects. The Lyman-α absorption line models were extracted from the best-fitting models and Lyman-α forest features were modeled out by dividing the spectra by the absorption line models. A small number of absorption lines created residual spike features due to the absorption model not completely matching the data. These flux points were identified and

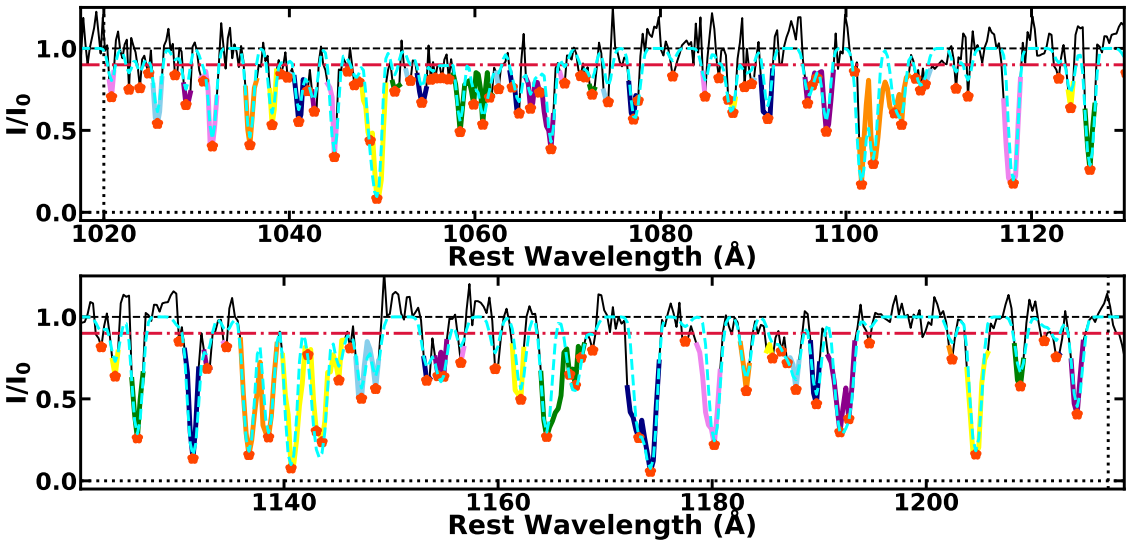

Figure 3.7: The continuum normalized spectrum (I/I_0) and the results of the automatic absorption line identification and initial fit. Each segment of the normalized spectrum marked with a different color represents a region affected by Lyman-α absorption lines. Red stars represent the locations of the absorption lines. Line identification is performed in the bandpass between 1020 Å and 1217 Å. The number of absorption lines identified by the algorithm is used to configure a spectral model that is used to fit the data. The locations of the lines identified by the algorithm are used as initial starting points for the spectral model. The cyan dashed line shows the automatically generated initial model fit. The model calibration is done using the MCMC method.

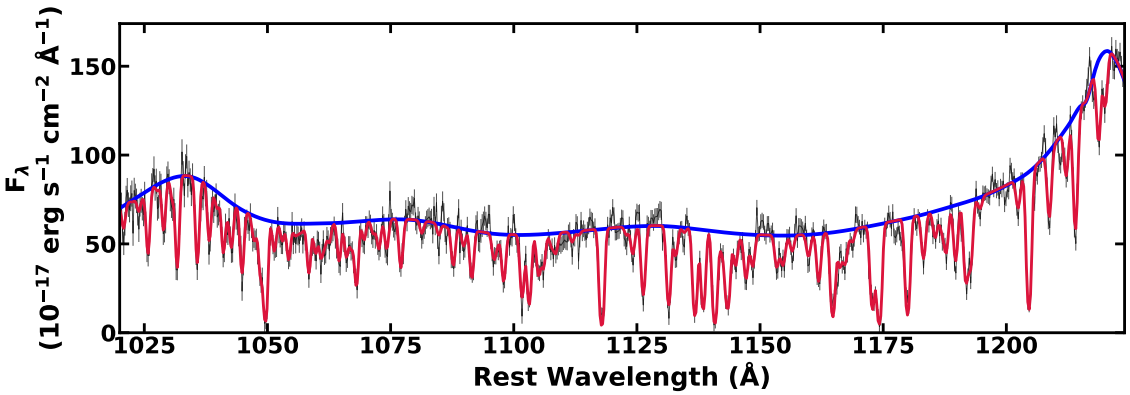

Figure 3.8: Best-fitting spectral model for one of objects included in the sample. The data is plotted in black and the spectral (continuum) model is plotted in red (blue).

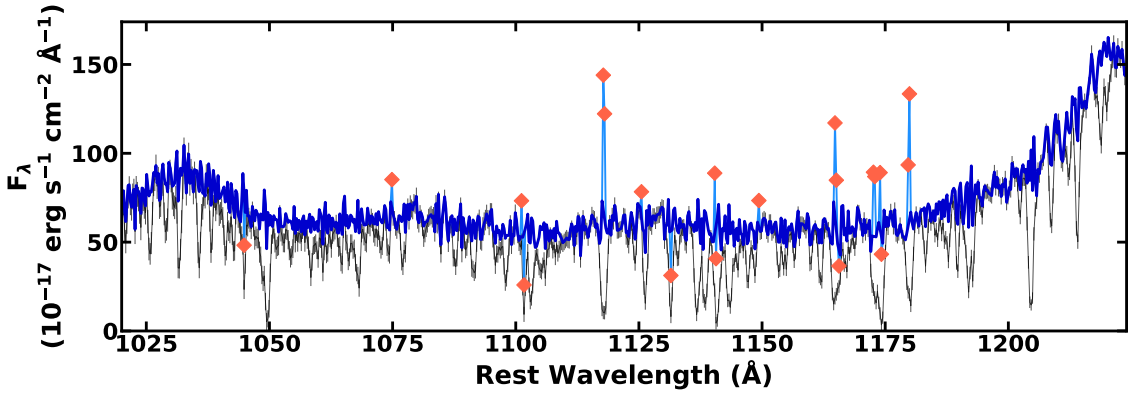

Figure 3.9: Spectra showing the result of the absorption line removal procedure. The absorption lines have been modeled out using the absorption line model extracted from the best-fitting model. The red diamonds represent the flux points that have been flagged as affected by the imperfect match between the data and the absorption line model (see text). The unprocessed original spectrum is plotted in black.

flagged using a sigma clipping method where I compared the spectrum with its smoothed version to find the data points that deviated significantly. Figure 3.9 shows the end result of absorption line removal. Some spectra showed IGM absorption lines redward of ~ 1216 Å and these features were flagged in a similar fashion.

The final step in correcting for the intergalactic Lyman-α absorption lines is calibrating the mean flux values of continuum normalized spectra. Lyman-α forest features can mimic a continuum depression because the individual Lyman-α absorption lines are mostly unresolved and blended at the SDSS resolution. Therefore modeling out the observed Lyman-α absorption lines alone may not be sufficient. The evolution of intergalactic Lyman-α optical depth over cosmic time is well known (e.g., $\tau_{eff} = 0.0018(1+z)^{3.92}$, Faucher-Giguère et al., 2008). I calculated the mean flux values for three redshift bins ($2.3-2.5$,$2.5-2.7$, and $2.7-2.9$) and compared with the values calculated from the equation given in Faucher-Giguère et al. (2008). I used a quadratic fitting function blueward of $\lambda = 1280$ Å to correct for the small difference: $C_{corrected}(\lambda) = C_{uncorrected}(\lambda) \times (1 + a\lambda + b\lambda^2)$, similar to the method used in Lee et al. (2012). Because of our relatively low redshift range, the required correction was less than $\sim 5\%$.

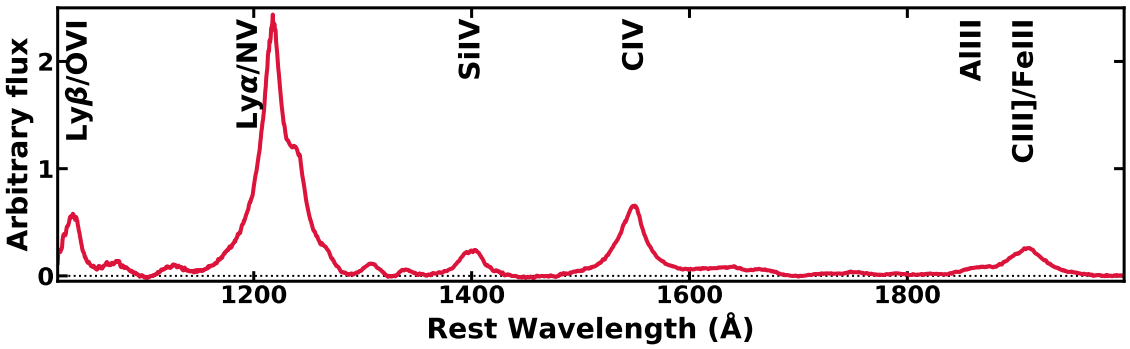

Figure 3.10: The weighted-mean spectrum generated from 78 continuum subtracted and normalized spectra. The principal quasar emission lines are labeled above the spectrum.

After the Lyman-α absorption features have been corrected in all the 78 spectra, I performed a power-law continuum fitting using the relatively emission line-free regions near 1100 Å, 1290 Å, 1450 Å, 1700 Å, and 2000 Å. I subtracted the continua from the spectra and they were then normalized near 1280 Å. The weighted-mean spectrum was generated using the continuum subtracted and normalized spectra (Figure 3.10). I used `EMPCA`[8] (Bailey, 2012) to compute PCA. This program uses an expectation-maximization algorithm and takes into account the weights associated with data points. In other words, it can handle noisy or missing data properly. In our case, I assigned the weights of each spectrum according to the inverse variance of the original spectrum. Zero weights were given to the points affected by imperfect absorption line modeling or IGM absorbers, so that such points are ignored in the computation of PCA. The weighted-mean spectrum was subtracted from each spectrum before executing `EMPCA`.

3.3.2. Results

Figure 3.11 shows the first eight spectral PCA eigenvectors calculated from `EMPCA`. The output of `EMPCA` includes the fraction of data variance explained by the model and the amount of variance explained by each eigenvector. The first eigenvector resembles the weighted-mean spectrum and it explains the most of the variance observed in the data.

[8] https://github.com/sbailey/empca

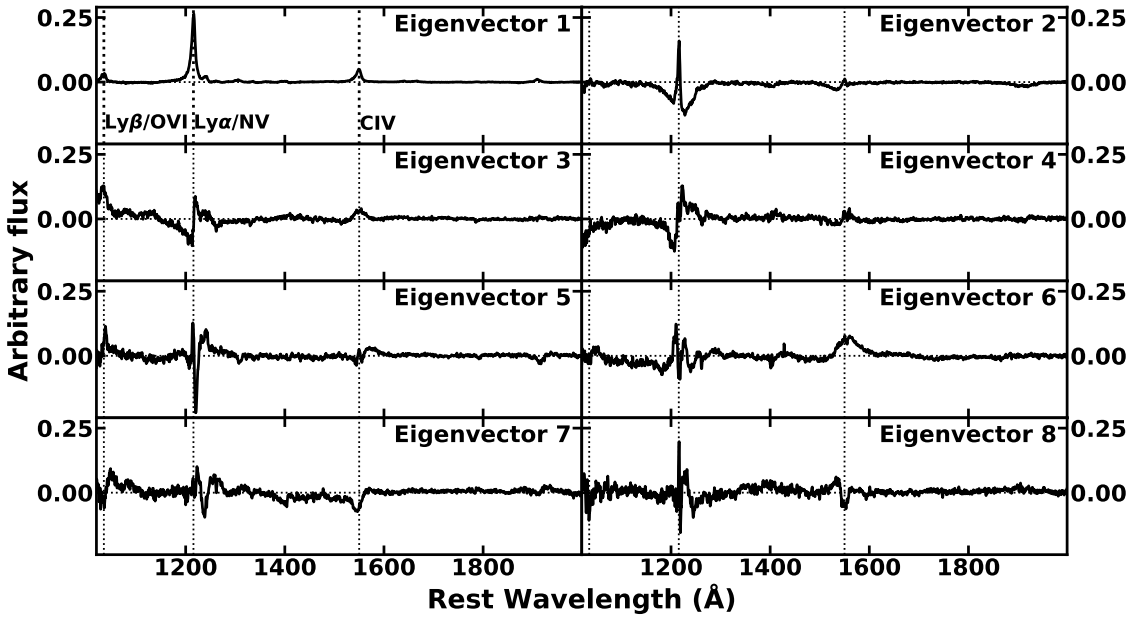

Figure 3.11: The panels show first eight spectral eigenvectors calculated from EMPCA. The first four spectral eigenvectors can reproduce $\sim 90\%$ of the variance observed in our sample. The vertical dotted lines and their identifications represent the major emission lines observed in the bandpass.

It shows the strongest quasar emission lines observed in the bandpass such as Lyman emission lines (α, β) and high-ionization lines (C IV$\lambda\lambda 1548, 1550$, N V$\lambda\lambda 1238, 1242$). The subsequent eigenvectors play a role in shaping the emission line profiles (e.g., blueshift, width). For example, a "P Cygni" profile, e.g., Eigenvector 3, in the eigenvector shifts the center of the emission line profile, and a "w"-shaped feature such as seen in Eigenvector 2 either makes the emission line broader or narrower.

The importance of the eigenvectors, or the amount of variance explained by each eigenvector, monotonically decreases after the first eigenvector. We found that the first four eigenvectors are capable of reproducing $\sim 90\%$ of the variance observed in the sample. Inclusion of the fifth eigenvector only improved this percentage by $\sim 1.2\%$. Therefore, we conclude that keeping only the first four eigenvectors is generally sufficient to model various emission line morphologies seen in the rest-UV spectra of luminous quasars. Inclusion of additional eigenvectors may only yield a minuscule improvement in

the emission line modeling and may not be statistically justifiable since each of the the extra eigenvector will add extra fitting parameter to the model.

This set of new rest-UV emission line spectral eigenvectors have been used to perform *SimBAL* analysis of a high-redshift BAL quasar with an extremely high-velocity outflow, J164653.72+243942.2. The result of the continuum modeling that used this set of eigenvectors to model the rest-UV emission lines can be found in Chapter 6 (§ 6.3.1). While the eigenvectors produced excellent model fits to the data so far, there are a couple of planned future improvements. We plan to include a larger number of objects to calculate PCA so that eigenvectors can model a wider variety of emission line shapes. Moreover, we intend to perform a clustering analysis of the sample spectra prior to calculating PCA. For example, high-ionization emission lines such as C IV emission lines observed in the rest-UV are known to show significant blueshift relative to the quasar rest frame (e.g., Gaskell, 1982; Wilkes, 1984). Preliminary analysis using two sets of eigenvectors, calculated from two groups of spectra classified based on C IV emission line blueshift, showed promising results (Hazlett, R., the University of Oklahoma undergraduate capstone thesis, 2020).

CHAPTER 4

Discovery of a Remarkably Powerful Broad Absorption Line Quasar Outflow in SDSS J135246.37+423923.5[1]

4.1. Introduction

Broad absorption-line (BAL) quasars (BALQs) have been studied extensively in the past several decades since their discovery (Lynds, 1967), and their distinctive blueshifted BAL features provide clear evidence for quasar outflows (e.g., Weymann et al., 1991). Outflowing winds with energy exceeding 0.5%∼5% of the quasar luminosity (e.g., Scannapieco & Oh, 2004; Di Matteo et al., 2005; Hopkins & Elvis, 2010) are thought to be able to effectively cause active galactic nucleus (AGN) feedback. Outflow energies depend on the amount of material ($\log N_H$) that is being carried by the wind, and more importantly, the velocity of the outflow through $\dot{E}_k = 4\pi\mu m_p \Omega R N_H v^3$ (Dunn et al., 2010). The combination of large column density ($\log N_H$) and high velocity produce energetic outflows.

A few discoveries of high-velocity high-ionization broad absorption-line (HiBAL) outflows ($v \sim$ 0.1c–0.3c) have been made. For example, Rodríguez Hidalgo (2009) discussed a $v \sim$ 0.2c BAL outflow in PG0935+417 and Hamann et al. (2018) suggested that there is a C IV BAL feature at $v \sim$ 0.3c in PDS 456. Rogerson et al. (2016) reported BAL features at $v \sim$ 0.2c and 0.1c in the variable HiBAL quasar SDSS 0230+0059. In the cases mentioned above, the physical properties of the outflows were not sufficiently constrained to estimate the outflow energy because those HiBAL quasars only showed prominent C IV absorption lines (and Si IV or N V lines in some cases) and lacked diagnostic lines to probe the density of the outflow. Moreover, HiBAL quasars are not

[1]This chapter is reproduced from Choi et al. (2020) with permission.

expected to have the highest $\log N_H$ because the lack of low-ionization lines such as Mg II$\lambda\lambda 2796, 2803$ or Fe II multiplets means that the gas is not as thick as that observed in iron low-ionization broad absorption-line (FeLoBAL) quasars (Chapter 3, § 3.2.3).

Low-ionization broad absorption-line (LoBAL) quasars and FeLoBAL quasars have significantly higher column densities, and therefore, high-velocity outflows in these objects may yield produce the most energetic outflows. Borguet et al. (2013) and Chamberlain et al. (2015) analyzed the rest-UV spectra of LoBAL quasars SDSS J1106+1939 and SDSS J0831+0354, respectively. They found high-velocity LoBAL outflows with high energies and constrained their physical properties ($\sim -8000\,\mathrm{km\,s^{-1}}$ and $\sim -10000\,\mathrm{km\,s^{-1}}$, respectively; see § 4.5). Although the FeLoBALs are expected to have thick (highest log N_H) and massive outflows, potentially harboring energetic outflows, only a few FeLoBAL objects have been analyzed to determine the physical properties of their outflows (de Kool et al., 2001, 2002a,b; Dunn et al., 2010; Bautista et al., 2010; Lucy et al., 2014). Because the common method (e.g., Arav et al., 2013) used to analyze BAL troughs involves individual line identification, it becomes extremely challenging to extract physical properties of an outflow that has a large number of Fe II absorption features that are blended together.

SimBAL was first introduced by Leighly et al. (2018) as a novel spectral synthesis code developed to analyze BAL outflows. Because *SimBAL* uses forward modeling with spectral synthesis, the code can be used to analyze even the most complex BAL spectroscopic features with significant line blending. The code has produced an excellent fit to SDSS J0850+4451 (Leighly et al., 2018), a LoBAL object; moreover its sophisticated treatment of modeling the partial coverage of BAL absorbers led to further understanding of the geometry and the structure of the outflow (Leighly et al., 2019b).

For thick BAL outflows, part of the radiation can be significantly absorbed by gas closer to the central engine before reaching the gas further away producing a phenomenon called "radiation filtering or shielding" (e.g., Leighly, 2004; Leighly et al., 2007, for the case of emission lines). The question of whether or not the radiation filtering is important in outflows has gained some recent attention. Leighly et al. (2018) recently explored the

possibility of radiation filtering in their *SimBAL* models and found no evidence supporting the phenomenon in SDSS J0850+4451. Miller et al. (2018) suggested a potential two-phase photoionization condition arising from radiation filtering in LBQS 1206+1052. Despite the effort to understand the radiation filtering, no definitive observational evidence has been found.

Not only do BAL quasars show interesting outflow signatures, they also are known to show stronger reddening and a higher scattering fraction (e.g., Sprayberry & Foltz, 1992; Brotherton et al., 1997; DiPompeo et al., 2011; Krawczyk et al., 2015). Some extragalactic objects are known to show "anomalous reddening", where their reddening curves do not resemble any of the commonly used reddening curves derived from the Milky Way galaxy (e.g., Cardelli et al., 1989) or the Magellanic Clouds (e.g., Prevot et al., 1984), possibly due to a particular dust composition near the quasar (Hall et al., 2002; Leighly et al., 2009; Jiang et al., 2013; Fynbo et al., 2013; Zhang et al., 2015a; Krogager et al., 2015; Meusinger et al., 2016). The nature of the strong reddening observed in BAL quasars may offer clues to the physical conditions and geometry of the outflows in these objects. Moreover, the dust has significantly larger scattering cross-section than the ions and can provide significant acceleration to the outflows (e.g., Fabian et al., 2008, 2018). Dusty outflows are able to harness the radiation pressure more efficiently and could potentially explain the acceleration mechanism of some of the BAL outflows with the highest velocities.

In this chapter, we report the discovery of the most energetic BAL outflow analyzed to date. SDSS J135246.37+423923.5, hereafter referred to as SDSS 1352+4239, is an overlapping trough object that was initially observed by the Sloan Digital Sky Survey (SDSS). This object has all the fascinating BAL characteristics in its spectrum, including a wide overlapping trough, anomalous reddening and a substantial scattered light signature. With new near-infrared observations of SDSS 1352+4239, we measured an accurate redshift, $z = 2.26$, from the Balmer emission lines. From the correct redshift we were able to identify the fastest FeLoBAL outflow ever observed ($v \sim -38000\,\mathrm{km\,s^{-1}}$). We performed detailed analysis with *SimBAL* to determine the physical conditions of the

outflowing cloud and constrain the energetics of the outflow. We were able to not only characterize the main BAL outflow but we also found evidence for radiation shielding in the zero-velocity BAL system. In § 4.2, we describe the new observation and data reduction done for SDSS 1352+4239. We introduce a general reddening curve used to model the unusual continuum shape in § 4.3 and we describe the spectral model used with *SimBAL* to analyze SDSS 1352+4239 in § 4.4. We report the energetics derived from the *SimBAL* fit of the outflow in § 4.5 and compare our result with other quasar objects known to have powerful outflows. Implications of our findings and a summary can be found in § 4.6 and § 4.7.

4.2. Observations and Analysis

The observations of SDSS 1352+4239 discussed in this work are listed in Table 4.1.

4.2.1. Gemini Gemini Near-Infrared Spectrograph Observation

SDSS 1352+4239 was observed using the Gemini Near-Infrared Spectrograph (GNIRS)[2] on the Gillett Gemini (North) Telescope using a standard cross-dispersed mode (the SXD camera with the $31.7 \mathrm{l/mm}$ grating) and a $0\farcs45$ slit. Eight 200-second exposures were made on 7 February 2015 in an ABBA dither pattern. Four 1-second exposures were made of the A0 star HIP 61471 at a similar airmass for telluric correction. The data were reduced using the IRAF *Gemini* package, coupled with the GNIRS XD reduction scripts, in the standard manner for near-infrared spectra, through the spectral extraction step. For telluric correction, the *Gemini* spectra of the source and the telluric standard star were converted to a format that resembled IRTF SpeX data sufficiently that the Spextool `xtellcor` package (Cushing et al., 2004; Vacca et al., 2003) could be used.

4.2.2. Apache Point Observatory Triplespec Observation

SDSS J1352+4239 was observed using Triplespec[3] (Wilson et al., 2004) on the Apache Point Observatory Astrophysical Research Consortium 3.5-meter telescope on 25 February

[2] http://www.gemini.edu/sciops/instruments/gnirs
[3] https://www.apo.nmsu.edu/arc35m/Instruments/TRIPLESPEC/

Table 4.1. Observations of SDSS J1352+4239

Observatory and Instrument	Date	Exposure (s)	Observed Frame Band Pass (Å)	Resolution
SDSS	2003 June 24	6300.0	3810–9189	$100\,\mathrm{km\,s^{-1}}$
Gemini (GNIRS)	2015 February 7	1600.0	8263–25208	$240\,\mathrm{km\,s^{-1}}$
BOSS	2016 April 5	8100.0	3628–10387	$89\,\mathrm{km\,s^{-1}}$
APO (Triplespec)	2018 February 25	5280.0	9097–24704	$80\,\mathrm{km\,s^{-1}}$

2018 under photometric conditions. The 240-second observations were made in a standard ABBA dither pattern and split into two segments of 10 and 12 exposures. Twenty 20-second exposures of the A0 star HIP 61471 were made before the first segment, and twelve 20-second exposures of the A0 star HIP 71172 were made after the second segment. The $1\farcs1$ slit was used. The resolution was measured using the night sky lines to be $80\,\mathrm{km\,s^{-1}}$ near 1.5 microns.

The spectra were extracted in a standard manner using TripleSpecTool, a modification of SpexTool (Cushing et al., 2004; Vacca et al., 2003). TripleSpecTool uses the airglow emission lines for wavelength calibration. To account for a very small amount of flexure, wavelength calibration solutions were computed for each AB dither pair sequence of exposures. The telluric correction was performed using the adjacent observation of the A0 star (Vacca et al., 2003).

The spectra were combined with the Gemini spectrum using a flux-weighted average, where the variance was based on the deviations of the spectrum around a best-fitting linear model to 21-pixel bins, after first down-sampling the APO spectra to the Gemini resolution. The combined spectrum is shown on the right panel in Figure 4.1.

4.2.3. The SDSS and BOSS Observations and Merging the Spectra

SDSS J1352+4239 was observed by SDSS and by the Baryon Oscillation Spectroscopic Survey (BOSS) program. We did not find any measurable flux offset or any strong evidence

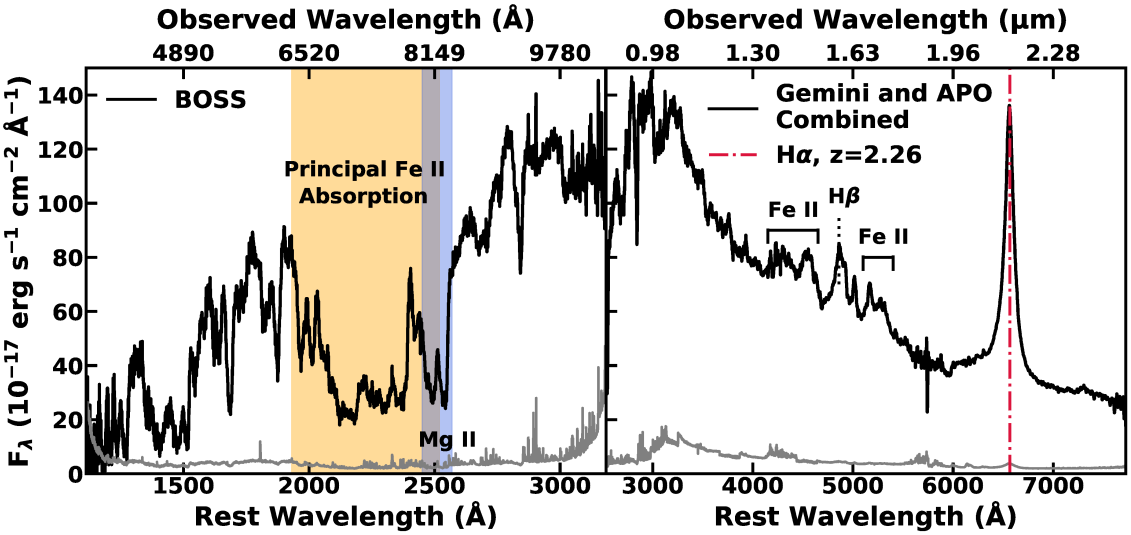

Figure 4.1: The BOSS spectrum on the left shows an "overlapping trough" feature from the Fe II absorption lines. The main iron trough and Mg II absorption features are marked on the left panel. BOSS spectrum showed no strong emission features that could be used to estimate the redshift. Therefore we used Hα in the combined GNIRS+APO spectrum (right) to measure the redshift for SDSS J1352+4239. The flux level for the Gemini and APO combined spectrum has been corrected to match BOSS flux density. The grey lines below the spectra show the uncertainties associated with the data.

for spectral variability in the two spectra. We chose to use the BOSS optical data from the SDSS archive because the data were taken closer to our near-infrared observations and the spectrum provides larger wavelength range coverage than the SDSS spectrum. The Baryon Oscillation Spectroscopic Survey (BOSS) and combined near-infrared Gemini and APO spectra are shown in Figure 4.1. We used the flux density of Baryon Oscillation Spectroscopic Survey (BOSS) spectrum and the wavelength range between rest frame $\sim$ 3000 to $\sim$ 3100 Å to match and merge the optical Baryon Oscillation Spectroscopic Survey (BOSS) and near-infrared Gemini and Apache Point Observatory (APO) spectra.

4.2.4. The Redshift

SDSS 1352+4239 was first cataloged in the SDSS Third Data Release catalog (Schneider et al., 2005), where the redshift was listed as 2.0385. Other published redshifts range from 2.000 (Meusinger et al., 2012a) to 2.049184 (Hewett & Wild, 2010). The difficulty

in estimating the redshift occurs because there are no strong emission lines in the SDSS spectrum. A broad bump just longward of the Mg II absorption was identified as Mg II emission by Trump et al. (2006, their Fig. 10). On the other hand, the redshift of the absorption features is fairly obvious ($z = 1.954$), based on the characteristic pattern of Mg II and Fe II absorption lines (e.g., Lucy et al., 2014, Fig. 12).

The redshift of SDSS 1352+4239 can be measured unambiguously from the infrared spectrum. We use Hα because there are no prominent [O III] lines and Hβ is blended with Fe II emission. The line appears slightly asymmetric due to Fe II emission so we fit it with two Lorentzian profiles. The peak of the narrower one yields a redshift of 2.2639 ± 0.0008, $\sim 11\%$ larger than any of the previous estimated values, implying that the outflow has a much larger velocity than previously suspected.

4.2.5. The Black Hole Mass

We estimated the black hole mass using the Hβ emission line. Strong Fe II emission is apparent throughout the rest-frame optical spectrum, and especially around Hβ. We constrain the shape of Hβ by simultaneously fitting Lorenzian profiles to each of Hα, Hβ, and Hγ, and constraining their widths to be the same and their relative central wavelengths based on known wavelengths of these lines. We used `Sherpa` for spectral fitting [4] (Freeman et al., 2001). The strong Fe II emission was modeled using the catalog of Fe II emission lines obtained from I Zw 1 (Véron-Cetty et al., 2004). No obvious [O III] lines are visible in the spectrum, but they are included with a fixed width of $1500\,\mathrm{km\,s^{-1}}$ and variable position and flux, with the 4960Å component constrained to have the same width and fixed relative flux with respect to the 5008Å component. The best-fitting model is shown in Figure 4.2.

To determine the radius of the broad line region, we refer to Bentz et al. (2013), who find that $\log(R_{BLR}) = K + \alpha \log[\lambda L_\lambda(5100)/10^{44}\,\mathrm{erg\,s^{-1}}]$. The continuum flux density at 5100Å was estimated from the combined Gemini and APO spectrum to be

[4] http://github.com/sherpa/sherpa/, http://cxc.harvard.edu/sherpa/

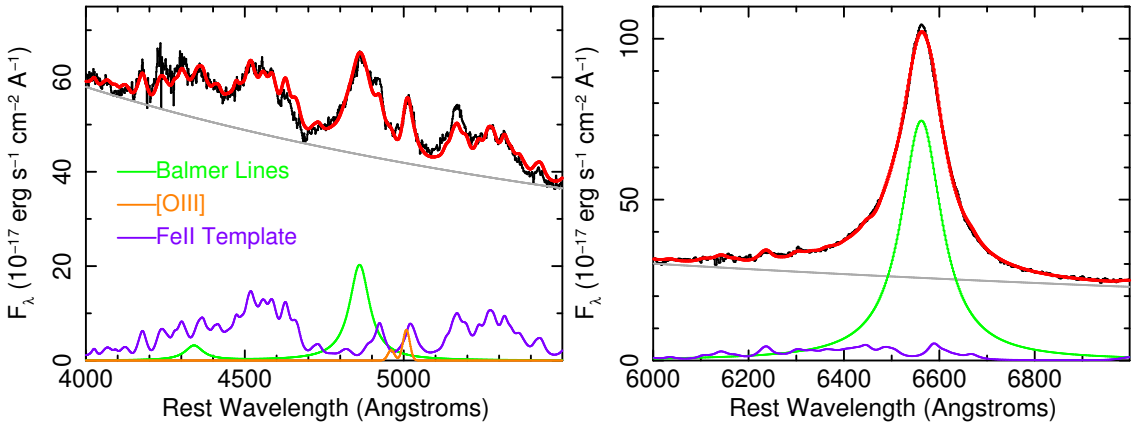

Figure 4.2: The model fits to the combined Gemini and APO spectrum. The left panel shows the bandpass that includes Hβ, and the right panel shows the bandpass that includes Hα. The strong Fe II emission obscures the Hβ line, so the two regions of the spectrum were fitted simultaneously, requiring that the FWHM of the Balmer lines to be equal.

$F_{5100} = 48.71 \times 10^{-17}\,\mathrm{ergs\,s^{-1}\,cm^{-2}\AA^{-1}}$. With the cosmological parameters used by Bentz et al. (2013) ($H_0 = 72\,\mathrm{km/s/Mpc}$, $\Omega_M = 0.27$, and $\Omega_\Lambda = 0.73$), we obtain a luminosity distance $D_L = 18074\,\mathrm{Mpc}$. Using $K = 1.527^{+0.031}_{-0.031}$ and $\alpha = 0.533^{+0.035}_{-0.033}$, we obtain an estimate of the radius of the Hβ emitting broad-line region of 1315^{+480}_{-340} light days corresponding to $1.1^{+0.4}_{-0.3}$ parsec. For reference, we also calculated the location of the C IV emitting region using the equation given by Lira et al. (2018, Equation (1)). We estimated the continuum flux density at 1345Å to be $F_{1345} = 343.2 \times 10^{-17}\,\mathrm{ergs\,s^{-1}\,cm^{-2}\AA^{-1}}$ after scaling the composite spectral energy distribution (SED) (Richards et al., 2006b) to match the near-infrared (rest-optical) photometry (§ 4.3.1) and calculated the location of the C IV emitting region of 199^{+436}_{-150} light days or $0.17^{+0.37}_{-0.13}$ parsec.

The model fit yields a full width at half maximum (FWHM) of the Balmer lines of $4720\,\mathrm{km\,s^{-1}}$ for a Lorentzian profile. We estimated the black hole mass in the usual way. We refer to Collin et al. (2006), who provide line-shape-based correction factors based on the ratio of the FWHM to σ_{line}, where σ_{line} is the line dispersion. For a Lorentzian profile, $FWHM/\sigma_{line} \Rightarrow 0$, and therefore $f = 1.5$. We estimate that the black hole mass is $8.6 \times 10^9\,\mathrm{M_\odot}$.

4.3. Continuum Modeling and Spectral Energy Distribution

4.3.1. The Long-Wavelength Spectrum

SDSS J1352+4239 shows a peculiar continuum shape compared to a typical quasar spectrum. We used the composite quasar SED from Richards et al. (2006b) and the composite spectrum from Francis et al. (1991) to analyze the shape of the underlying AGN continuum of the object using both the spectrum and the photometry from SDSS, Two Micron All Sky Survey (2MASS) and Wide-field Infrared Survey Explorer (WISE) (Figure 4.3). In Figure 4.3, compared with the composite spectrum (Francis et al., 1991), the spectrum of SDSS J1352+4239 is similar to a typical unreddened quasar at wavelengths longward of $\sim$ 3000 Å. In the infrared region, the shape of the SED of SDSS J1352+4239 also resembles the mean quasar mid-infrared SED shape. Because the continuum bluewards of the break shows a large difference in the slope, we analyzed the reddening and the slope of the continuum in the long wavelength region separately from the short-wavelength region.

Krawczyk et al. (2015) found that BAL quasars are redder than the non-BAL quasars, and that the Small Magellanic Cloud (SMC) reddening curve (extinction curve derived from the SMC) fits BAL quasars well in most cases. Therefore we used the SMC reddening law to measure the reddening in SDSS J1352+4239. We used the Markov Chain Monte Carlo (MCMC) code `emcee`[5] (Foreman-Mackey et al., 2013) to fit the SMC (Prevot et al., 1984) reddened composite SED to the rest frame optical / near-infrared photometry points and found no evidence for reddening in the optical / near-infrared region of the spectrum ($E(B-V) < 0.002$).

We also fit the optical / near-infrared part of the continuum using an SMC-reddened power law to get an estimate of the slope and reddening. We measured a power law slope of $-1.82\,(\pm 0.02)$, consistent with a mean spectral slope value for BAL quasars (-1.83, Krawczyk et al. 2015), and no reddening ($E(B-V) < 0.03$) for the continuum

[5] http://dan.iel.fm/emcee/current/

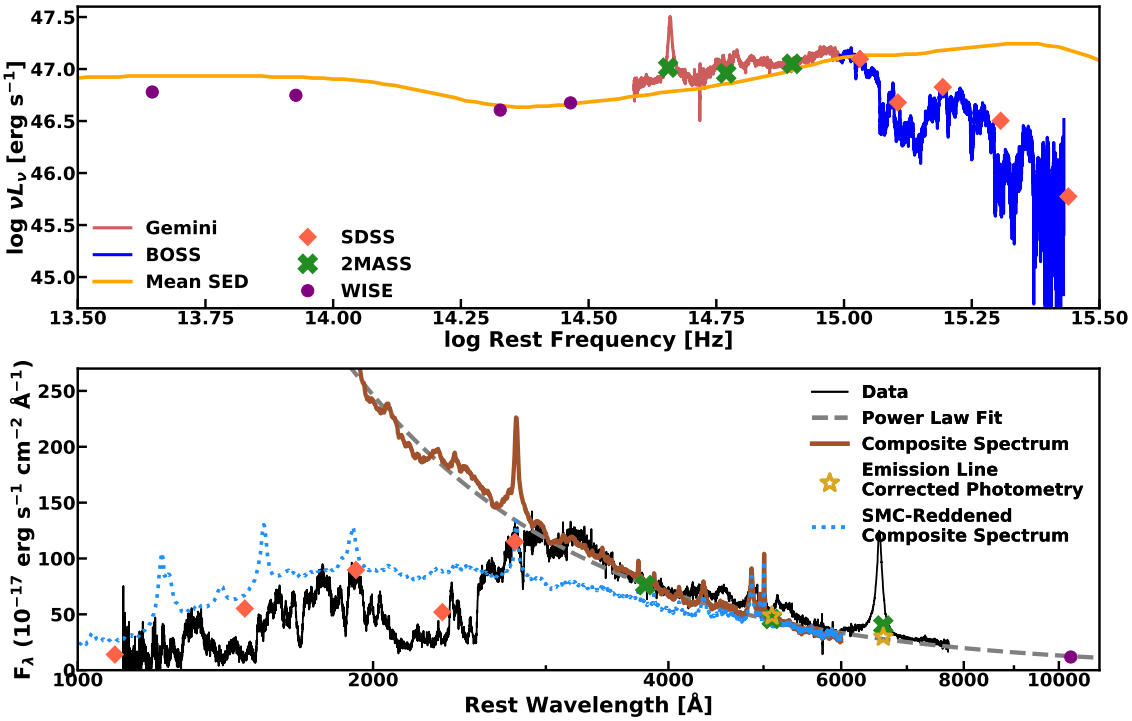

Figure 4.3: SDSS J1352+4239 is plotted with the mean SED from Richards et al. (2006b) in the upper panel. The lower panel shows the power law continuum fit to long wavelengths ($\lambda >$ 3000 Å) and the composite spectrum from Francis et al. (1991). The H and K band photometry points have been corrected for the hydrogen line emission and iron emission using 2MASS filter functions (Cohen et al., 2003) and iron emission templates created from the decomposition of the I Zw 1 spectrum (Véron-Cetty et al., 2004). The SMC-reddened composite spectrum with $E(B-V)$=0.17, plotted in dotted blue in the lower panel, demonstrates that the SMC reddening curve fails to reproduce the continuum shape of SDSS 1352+4239. While the observed and composite continuum shapes are similar longward of $\sim$ 3000 Å, SDSS 1352+4239 diverges significantly at shorter wavelengths. Because of the dramatic change in the SDSS 1352+4239 continuum shape at $\sim$ 3000 Å, we use a non-traditional reddening curve to model the continuum emission (§ 4.3.2).

from 1.4 μm to 3788 Å. Thus the object has a typical value of spectral slope and no evidence for reddening in the long wavelength region, despite significant reddening at shorter wavelengths.

To estimate the bolometric luminosity, we used the bolometric correction factor (BC) from Gallagher et al. (2007) who provide bolometric corrections for monochromatic luminosity at two different wavelengths. The strong reddening in the spectrum is only seen at wavelengths shortward of $\sim$ 3000 Å. Therefore we used the monochromatic luminosity at 5100Å of SDSS J1352+4239 (§ 4.2.5) and obtained the log bolometric luminosity of 48.0 ± 0.2 [erg s^{-1}], with the uncertainties estimated from the uncertainties associated with the bolometric correction factor ($\mathrm{BC} = 10.47 \pm 4.14$).

SDSS J1352+4239 is among the most luminous quasars observed and it is considered a hyper-luminous quasar (i.e., quasars with $L_{\mathrm{Bol}} > 10^{47}$ erg s^{-1}). The bolometric luminosity of SDSS J1352+4239 is comparable to the objects in the WISSH quasar sample (Bischetti et al., 2017) where they focused on a sample of WISE/SDSS selected hyper-luminous quasars to study the power and the effect of the AGN feedback. The mass accretion calculated from the bolometric luminosity, assuming the energy conversion efficiency (η) of 0.1, is 176 $\mathrm{M}_{\odot}$ per year. Compared with the black hole mass of $8.6 \times 10^{9}\,\mathrm{M}_{\odot}$, SDSS J1352+4239 is radiating at about 93% of the Eddington limit.

4.3.2. Anomalous Reddening

As can be seen from Figure 4.3, the shape of the continuum for SDSS J1352+4239 is quite peculiar, but it is not unprecedented. Among other BAL objects with anomalous reddening, Mrk 231 shows steep reddening in the near-UV to optical part of the continuum (e.g., Smith et al., 1995; Veilleux et al., 2013a). Leighly et al. (2014) fit the continuum in Mrk 231 and concluded that a Type Ia supernovae reddening curve (Goobar, 2008) best describes the reddening behavior of Mrk 231. Jiang et al. (2013) derived a reddening curve from IRAS 14026+4341 by comparing the object to a quasar composite spectrum and found that their reddening curve could be explained by a particular distribution of dust

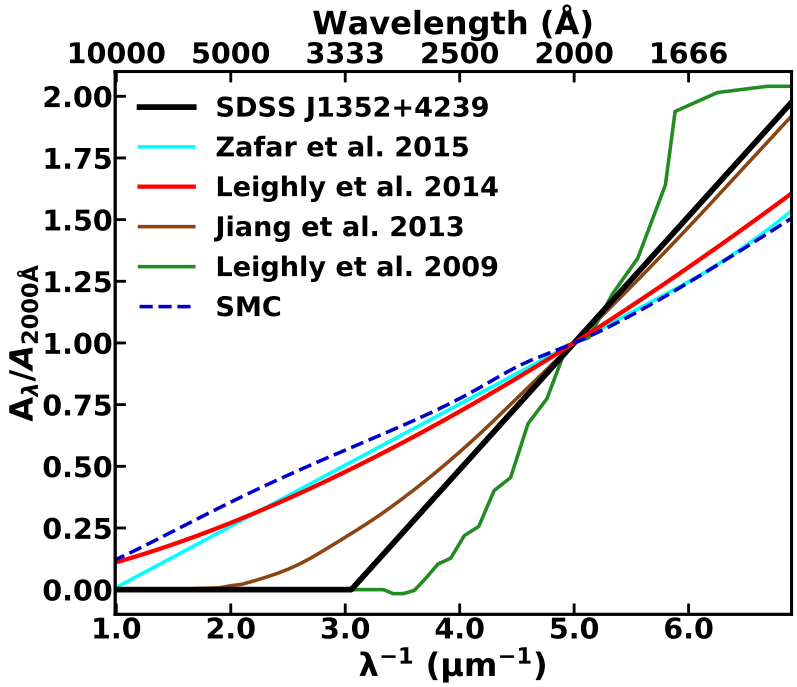

Figure 4.4: The reddening curve for SDSS J1352+4239 found from *SimBAL* fits using our model ($p = 0.57 \pm 0.003,\ \lambda_{Break} = 0.328 \pm 0.001$ (μm)) compared with other reddening curves developed for anomalous reddening. The reddening curves have been normalized to A_λ at 2000 Å. Anomalous reddening curves by Leighly et al. (2009) and Jiang et al. (2013) show different break wavelengths and slopes. The SMC reddening curve and an empirical reddening curve derived from a sample of reddened quasars by Zafar et al. (2015) is also plotted (A_V = 0.51) for comparison.

grain sizes (one lacking large grains, $a_{max} = 70$ nm). However, in the case of WPVS 007 (Leighly et al., 2009), no particular grain distribution was able to model their anomalous reddening curve.

We tried using the reddening templates developed with WPVS 007 (Leighly et al., 2009) and IRAS 14026+4341 (Jiang et al., 2013) as well as the reddening model used for Mrk 231 (Leighly et al., 2014) to model the break in the continuum shape. However, none of the anomalous reddening models were able to appropriately model the continuum shape of SDSS J1352+4239 because their slopes and the locations of sharp reddening increase did not match the continuum shape of SDSS J1352+4239.

Therefore, we developed a general anomalous reddening curve. Using the general

reddening equation A(λ) $= 2.5 \log\{C(\lambda)/S(\lambda)\}$ where S(λ) is the reddened spectrum and C(λ) is the intrinsic spectrum, our general reddening curve has the form of a power law.

$$A(\lambda\ (\mu\mathrm{m})) = \begin{cases} p(\frac{1}{\lambda} - \frac{1}{\lambda_{Break}}),\ (p > 0) & \text{if } \lambda \leq \lambda_{Break} \\ 0 & \text{if } \lambda > \lambda_{Break} \end{cases}$$

Our anomalous reddening curve generates reddening from a specified wavelength (λ_{Break}) to shorter wavelengths with A(λ) gradually increasing from zero, and therefore there is no reddening in the wavelength region as required. The reddening equation requires two parameters: the slope of the curve (p) and a reddening starting wavelength (λ_{Break}). Figure 4.4 illustrates various reddening curves. Our general reddening model provides excellent fits for other anomalously reddened BAL quasar spectra as well (Choi et al., 2022a).

To fit the shorter wavelength spectrum, we fixed the power law spectral slope to the value we found from the optical / near-infrared photometry fit, and only varied the two anomalous reddening parameters and the power law normalization to model the continuum with *SimBAL*.

4.3.3. Modeling the Line Emission

Visual inspection of SDSS J1352+4239 revealed that the object potentially has a weaker Mg II emission and stronger iron emission compared with the typical AGN spectrum. It is not possible to model the individual emission lines due to the heavy absorption features seen throughout the bandpass. Instead, we constructed a set of broadband emission templates to model the emission lines. It is well known that the ratio between the strengths of the prominent emission lines (e.g. Mg II, C IV) and the strength of the iron emission differs from object to object (e.g., Sulentic et al., 2000). Therefore, we created separate emission line templates for the iron emission and several other emission line templates for other emission lines so that our model can create the iron emission independently from other emission lines. Mrk 493 is a narrow-line Seyfert with a strong Fe II emission,

making it a suitable target for AGN emission-line analysis. It was observed by Hubble Space Telescope (HST)[6] to create a high resolution and good signal-to-noise ratio Fe II template. From this Mrk 493 spectrum, we derived empirical emission templates for the iron emission (the Fe II pseudo-continuum) and for other emission lines (e.g. Ly α, Si IV, C IV, C III], Mg II, Balmer lines) separately and used the extracted templates to model the emission features of SDSS J1352+4239.

In order to separate the Fe II emission from the other emission lines in the Mrk 493 spectrum, we used `Sherpa` to model the spectrum using a power law, existing Fe II templates (Véron-Cetty et al. (2004): 4000 Å $\lesssim \lambda_{rest} \lesssim$ 7000 Å, Leighly & Moore (2006): 2000 Å $\lesssim \lambda_{rest} \lesssim$ 3000 Å and Leighly et al. (2011): 3000 Å $\lesssim \lambda_{rest} \lesssim$ 4000 Å) and Gaussian line profiles for all other emission lines present in the spectrum. We obtained the Fe II emission templates from the Mrk 493 spectrum by subtracting the emission-line models consisting of only the non-Fe II emission lines and power law continuum from the data. Separate emission templates for other major emission lines were made from the non-Fe II emission line component of the same model. We merged the resulting Fe II emission templates together to create a single broadband emission template (1500 Å $\lesssim \lambda \lesssim$ 7500 Å). We did not attempt to do the same for the non-Fe II emission line templates to allow *SimBAL* more flexibility in fitting the major emission-line features so that each templates could be scaled to their own independent normalization coefficients. The final emission-line templates consist of a single full wavelength range template for Fe II emission lines and 4 emission templates divided in wavelength sections mentioned above for the non-Fe II AGN emission lines.

4.4. Best-Fitting Model

We created a complex spectral model for SDSS J1352+4239 to extract the physical properties of the outflow. Our best-fitting model is made of 4 major components including two absorbing components. The continuum and line emission were modeled by a power

[6]PI: Park, "A Definitive UV−Optical Template for Iron Emission in Active Galactic Nuclei", program number 14744

law and emission line templates described in § 4.3.3. A scattered non-absorbed continuum emission component was added to the model to produce the peculiar non-black saturation shape under the iron trough. Reddening was applied to all components using the anomalous reddening model discussed in § 4.3.2. We first discuss the main blueshifted absorption-line component in § 4.4.1, then explore the necessity of the scattered light component in § 4.4.2 and a zero-velocity absorption component in § 4.4.3. The results are summarized in Table 4.2.

The model is given by:

$$f_{model} = Reddening \times \{(f_{Continuum} + f_{LineEmission}) \times I_{High-Velocity} \times I_{Zero-Velocity} + f_{Scattered\,Flux}\}$$

where $f(\lambda)$ is the flux from each component and the final model and $I(\lambda)$ is the normalized flux (I/I_0) from each absorption component. Figure 4.5 shows the best fit model of SDSS J1352+4239.

Depending on the geometry and the angular size scale of the BAL outflowing cloud, the covering fraction for the accretion disk and the line-emitting gas (broad line region, BLR) can be different. Leighly et al. (2019b) demonstrated how *SimBAL* can be used to test the scenarios where the outflowing cloud has multiple covering fractions for different AGN components. We tested both two-covering models where the covering-fraction parameters for the line emission and the continuum emission were allowed to differ and single-covering models and concluded that there is no strong evidence for a different covering fraction for emission lines and continuum emission in SDSS J1352+4239. Therefore we used a model with a single covering fraction for both emission components.

The tophat accordion model provided an exceptional fit of the complex velocity structures of the trough in SDSS J1352+4239, and yielded the physical parameters of the outflows as a function of velocity (Figure 4.6). We fit the high-velocity troughs with a 10-bin tophat model with an additional 7-bin tophat model for the zero-velocity absorption

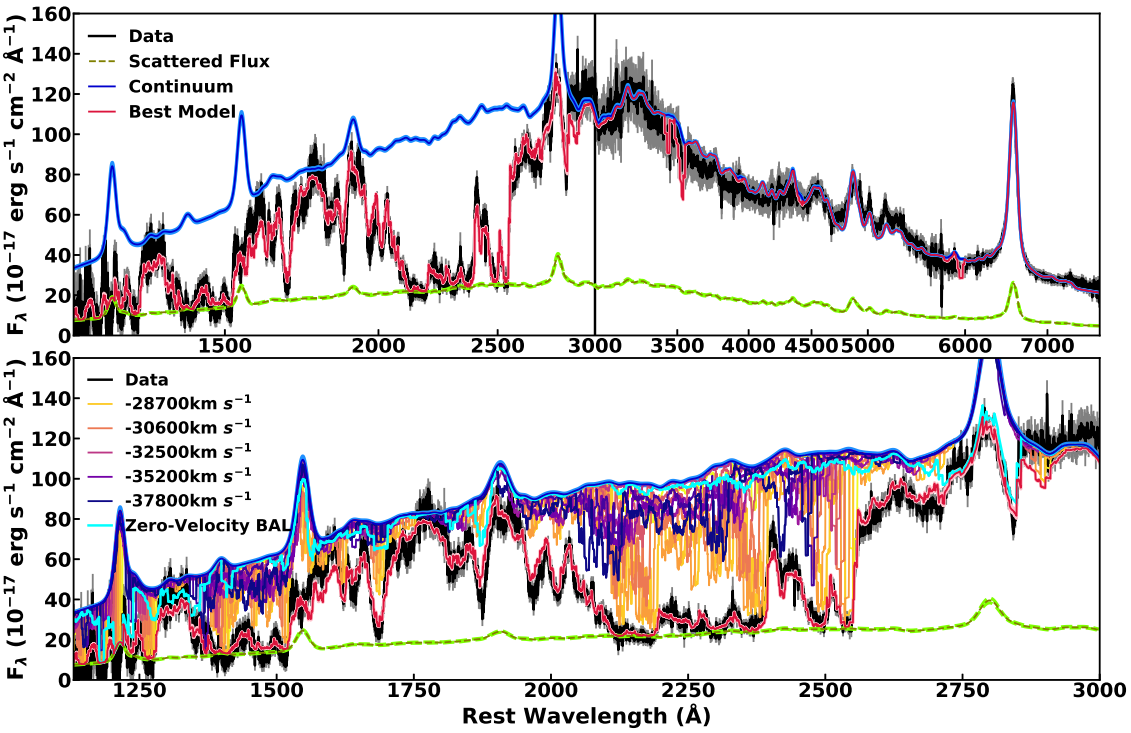

Figure 4.5: Upper panel: Our best fitting model described in § 4.4. Lower panel: Decomposition of ten tophat bins is shown in different colors (from yellow to navy); the zero-velocity BAL component is plotted in cyan. The velocities of five of the ten tophat bins for the main complex are labeled on the figure. Each bin in the absorption complex creates an absorption feature at a different velocity. The combination of 10 bins create the full trough and we harvest the information about the physical parameters of the outflow as a function of velocity.

feature we identify near the Mg II emission lines (§ 4.4.3). Leighly et al. (2018) explored the dependence on number of bins and concluded that the number of bins does not change the result of the fit except when too few bins were used, and that there were no significant differences between the results obtained with models with different number of bins. We experimented with 7, 10 and 15-bin tophat accordion models and found that 10 bins were sufficient to model the complex. Ten bins span a velocity range from $\sim -38000\,\mathrm{km\,s^{-1}}$ to $\sim -28000\,\mathrm{km\,s^{-1}}$ with the total velocity width of $\sim 10000\,\mathrm{km\,s^{-1}}$ (Figure 4.5).

The physical parameters and the derived outflow properties for the high velocity trough and zero-velocity component (§ 4.4.3) as well as for each group are reported in Table 4.2. The main blueshifted trough in SDSS J1352+4239 was modeled with a 10-bin tophat accordion model where the bins were divided into two groups with a single ionization parameter and density for all bins in each group as described in § 4.4.1. The values for $\log U$, $\log n\,[\mathrm{cm^{-3}}]$, $\log N_H - \log U\,[\mathrm{cm^{-2}}]$ and $\log a$ were directly taken from the the physical fit parameters of the best-fitting model. The hydrogen column density values that have been corrected for the partial coverage with $\log a$ and the outflow properties (e.g., $\log \dot{M}$, $\log\ L_{KE}$) have been calculated from the aforementioned fit parameters. For $\log N_H - \log U\,[\mathrm{cm^{-2}}]$, $\log a$ and $\log N_H\,[\mathrm{cm^{-2}}]$, the ranges reflect the values we found for the individual bins. Total $\log N_H$ for the groups are also reported. Uncertainties for each parameter were calculated from the posterior probability distributions of the MCMC chain. We did not attempt to model the posterior distribution (e.g., Gaussian distribution), instead we calculated the median, 1σ, 2σ and 3σ values directly from the posteriors. The uncertainties reported in the Table 4.2 represents 95% confidence regions. A global covering fraction (Ω) of 0.2 was used for the calculations and further discussion of this parameter can be found in § 4.5.

4.4.1. The High-Velocity Component

The 10 bins for the main high-velocity trough were grouped into two sets with each group having a single density and ionization parameter. Our initial investigation with

Table 4.2. Physical Parameters and Derived Outflow Properties from the Best-Fitting *SimBAL* Model

Outflow Properties	Higher Velocity Group	Lower Velocity Group	High-Velocity Total[a]	Zero-Velocity Component
		Physical Parameters		
$v_{outflow}$ (km s^{-1})[b]	-38000 to -33000	-33000 to -28000	-38000 to -28000	-8900 to 6700
$\log U$	$0.82^{+0.07}_{-0.12}$	$-0.56^{+0.07}_{-0.08}$	-	-2.8 to 1.8[b]
$\log n$ [cm^{-3}]	$6.12^{+0.12}_{-0.07}$	$7.43^{+0.09}_{-0.07}$	-	< 5.0[e]
$\log N_H - \log U$ [cm^{-2}][b]	23.0–23.16	23.13–23.17	-	21.9–23.0
$\log a$[b]	0.91–1.9	0.38–1.13	-	-0.58 to 1.92
		Derived Outflow Properties		
$\log N_H$ [cm^{-2}], per bin[b]	22.03–22.85	21.41–22.06	-	18.31–21.82
$\log N_H$ [cm^{-2}], total[d]	$23.11^{+0.07}_{-0.06}$	$22.57^{+0.06}_{-0.07}$	23.22 ± 0.05	$21.85^{+0.05}_{-0.06}$
$\log R$ [pc]	$0.97^{+0.05}_{-0.04}$	1.0 ± 0.02	0.93–1.02	> 1.0[e]
$\log \dot{M}$ [M$_\odot$ yr^{-1}][f]	$3.41^{+0.04}_{-0.05}$	$2.81^{+0.06}_{-0.07}$	3.51 ± 0.04	-
$\log \dot{P}$ [dyne][f]	$38.77^{+0.04}_{-0.05}$	$38.08^{+0.06}_{-0.07}$	38.85 ± 0.04	-
$\log L_{KE}$ [erg s^{-1}][f]	$48.04^{+0.04}_{-0.05}$	$47.25^{+0.06}_{-0.07}$	48.1 ± 0.04	-

[a]The values are the combined result of the left two columns.

[b]The range of values estimated from the multiple bins is reported.

[c]Large value of $\log a$ corresponds to small covering fraction

[d]Covering fraction weighted values are reported (§ 4.4.1).

[e]Zero-velocity component is located at a larger distance than the main high velocity component (§ 4.6.1).

[f]The global covering fraction $\Omega = 0.2$ was used (e.g., Hewett & Foltz, 2003), and further discussion of Ω can be found in § 4.5.

SimBAL models revealed that the bins at higher velocities and at lower velocities have clear differences in their physical parameters, primarily in their densities. Subsequently, we found that the two density groups also had different characteristic ionization parameters. Therefore, we assigned a single ionization parameter and density to each group.

Fe II has a plethora of excited state levels, ranging from low level excited states (0-0.12 eV) as well as high levels (>2.89 eV), making the strengths of the excited state Fe II lines very density sensitive (e.g., Lucy et al., 2014). Fe II ions are populated deep in the photoionized cloud away from the incoming radiation because the ionization potentials to create Fe II ions is relatively low (7.9 eV). Therefore Fe II ions require a large column density to be significant (column density reaching beyond hydrogen ionization front), otherwise most of the iron atoms will be in a higher ionization state than Fe II. Thus the presence of the excited state Fe II lines along with other low ionization lines (e.g., Mg II) helps *SimBAL* to constrain both the density and the thickness of the outflowing gas. We see in Figure 4.5 not only how all 10 bins model the trough together in combination but also how each tophat bin creates a large number of absorption lines. Together the physical parameters at each velocity can be constrained.

Figure 4.6 shows the outflow physical parameters as a function of velocity. We found the high velocity part of the outflow has lower density ($\log n \sim 6.12$ [cm^{-3}]) and higher ionization ($\log U \sim 0.82$) than the lower velocity group ($\log n \sim 7.43$ [cm^{-3}], $\log U \sim -0.56$). The large combination parameter ($\log N_H - \log U$) of ~ 23.1 [cm^{-2}] reflects the significant opacity from Fe II ions that we see in the data. The covering fraction parameter ($\log a$) changes strongly with the velocity and the bottom panel in Figure 4.7 shows how the shape of the opacity profile of the absorber closely follows the shape of $\log a$. Moreover, the large covering fraction (low $\log a$) and high $\log N_H - \log U$ parameter found near ~ -29000 $\mathrm{km\,s}^{-1}$ indicates that a large amount of opacity is concentrated around that velocity region in the outflow. Similarly, Leighly et al. (2018) also found a "concentration" region in their *SimBAL* model of SDSS J0850+4451, i.e., an enhancement in column density for a few of the bins in their 11-bin tophat model. By summing the

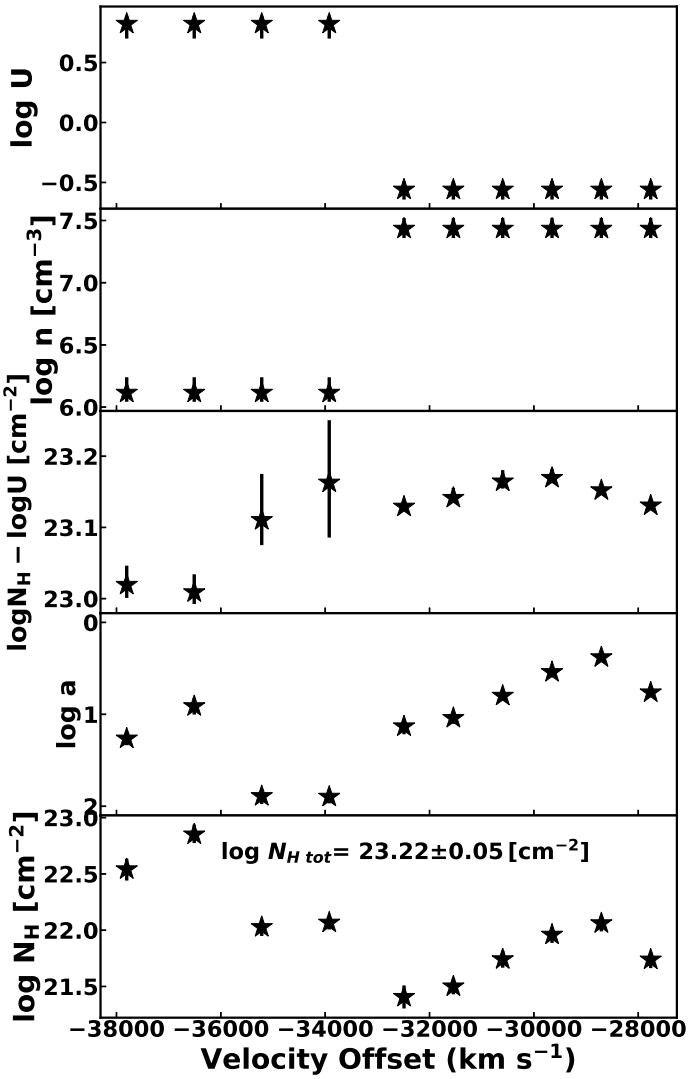

Figure 4.6: Physical parameters as a function of velocity with error bars representing 95% confidence regions. The parameters plotted in the top 4 panels were directly fitted with *SimBAL* and in the bottom panel, the hydrogen column density values (log N_H), corrected for the covering fraction from each bin, were calculated from log U, $\log N_H - \log U$ and log a. The total log N_H value for the outflow, calculated from adding the hydrogen column density values from all 10 bins is also reported in the bottom panel. The two groups ($-38000 \sim -33000$ km s^{-1} and $-33000 \sim -28000$ km s^{-1}) are constrained to each have the same density and ionization parameter (top two panels), while the $\log N_H - \log U$ parameter and the covering fraction parameter (lower log a values indicate higher covering fraction) were allowed to vary independently for each bin. The highest covering fraction (lowest log a value) occurs around ~ -30000 km s^{-1} and the column density parameter $\log N_H - \log U$ also peaks around the same velocity. This shows that most of the opacity is generated near this velocity (see also Figure 4.7).

hydrogen column density values weighted by the covering fraction from all 10 bins, each calculated from the $\log U$ parameter, $\log N_H - \log U$ parameter, and covering-fraction parameter (log a) per bin ($\log N_H = (\log N_H - \log U) + \log U - \log(1 + 10^{\log a})$ Arav et al., 2005; Leighly et al., 2018, 2019b), we estimated a covering fraction weighted total hydrogen column density of $\log N_H = 23.22 \pm 0.05\,[\mathrm{cm}^{-2}]$ (95% confidence errors, bottom panel in Figure 4.6).

Figure 4.7 shows how the two tophat groups model the wide absorption feature. The higher velocity component contributes less opacity than the lower velocity component; however, the lower velocity component alone cannot produce the wide trough we see in the data. The lower velocity component has gaps between ~ 2450 Å and ~ 2600 Å, and near ~ 2100 Å where the Fe II and other iron peak ions in the high-excited states are expected to be the main source of the opacity. The problem is that the lower velocity component cannot produce enough opacity in those regions without creating a deep absorption feature near ~ 2600 Å that is not present in the spectrum. Therefore the higher velocity group (with distinct values for the density and ionization parameter) was needed to fill in the gaps in the trough where the lower velocity component did not produce enough opacity to complete the absorption feature (arrows in Figure 4.7).

In Figure 4.7, we also see that the concentration of opacity and strong absorption contribution from the lower velocity component, as expected from Figure 4.6, and the shape of the absorption profile for an individual transition (dark green and orange lines in the lower panel) closely follows the shape of the covering fraction parameter. The blended lines in the main trough are nearly saturated even with the partial covering; the flux at the bottom of the trough is mainly modeled by the scattered light component.

4.4.2. The Scattered Light Component

SDSS J1352+4239 shows an extreme case of non-black saturation in the main trough where the emission at the bottom of the trough increases as a function of wavelength and contains a significant amount of flux. Non-black saturation of BAL features is very

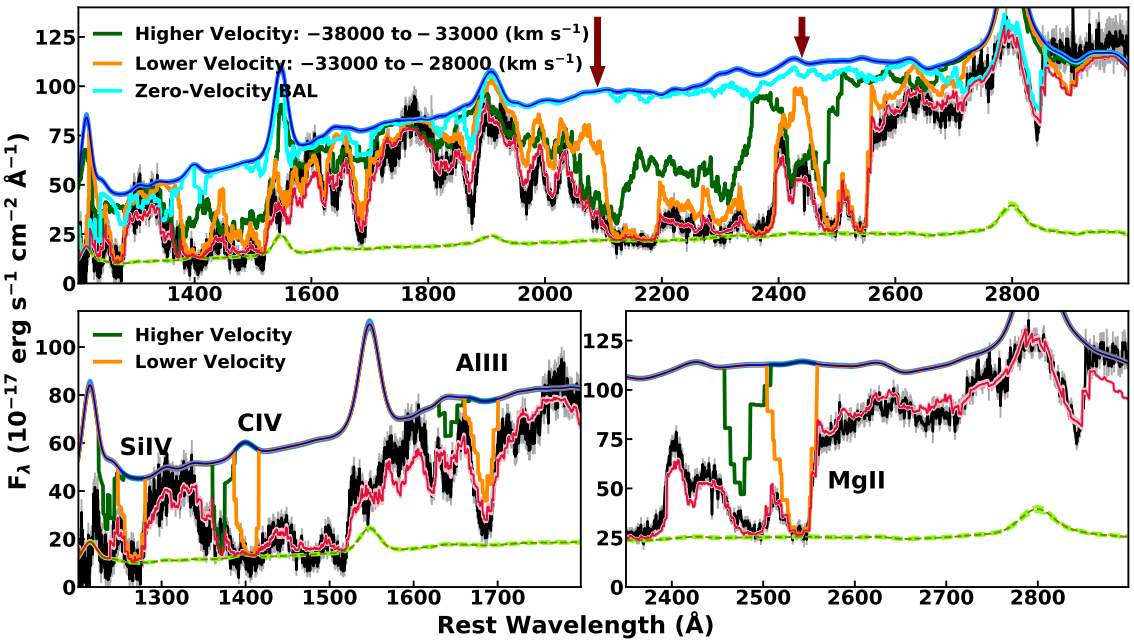

Figure 4.7: The top panel shows the two models generated from combining only the higher and lower velocity bins in dark green and orange, respectively. The regions where the higher velocity group plays a significant role in producing sufficient opacity to model the trough are marked with arrows in the top panel. The bottom two panels show how some of the common BAL absorption lines (Si IV, C IV, Al III, Mg II) have been modeled by the higher velocity group and the lower velocity group. The best-fitting model, continuum and the scattered flux component are plotted in same colors as Figure 4.5.

common and is thought to originate from the BAL outflow not entirely covering the continuum sources, which includes the accretion disk continuum and broad emission line features (e.g., Barlow & Sargent, 1997). Continuum scattering is not uncommon in BAL quasars, and it is known from spectropolarimetry that frequently the troughs are highly polarized indicating an origin in scattered light (e.g., Cohen et al., 1995; Ogle et al., 1999). The shape of the offset found under the trough in SDSS J1352+4239 suggests that this component is scattered light from the accretion disk continuum and line emission with the wavelength dependence created by the reddening. We modeled the scattered light component by multiplying the scattering fraction parameter by the emission model consisted of the sum of the reddened power law continuum and line emission and added this component to the absorbed emission model:

$$f_{Scattered\,Flux}(\lambda) = (f_{Continuum}(\lambda) + f_{LineEmission}(\lambda)) \times Scattering\,Fraction.$$

The reddening of the scattered flux is assumed to be the same as the continuum reddening, and we assume that the scattered light is not absorbed by the wind. Our best model creates the underlying emission feature with a scattering fraction of $\sim 29 \pm 0.5\%$. This value is large but comparable to the scattering fraction of $> 20\%$ found in IRAS 13349+2438 by Lee et al. (2013). A large scattering fraction suggests that SDSS J1352+4239 may be highly polarized. Considering the amount of polarization depends both on the geometry of the scattering source and the scattered fraction, SDSS J1352+4239 may exhibit polarization less than this value. Previous spectropolarimetry observations of BAL quasars revealed polarization reaching greater than $\sim 10\%$ in some objects (e.g., Brotherton et al., 1997; Ogle et al., 1999).

To test the necessity of the scattered flux component, we fit the data with a model that does not include it. The model fails to match the shape around $\sim 2100 - 2200$ Å, creating a deeper Fe II trough. Figure 4.8 shows the comparison between the best fitting model and the model without the scattered component. Further discussion of possible origins of the

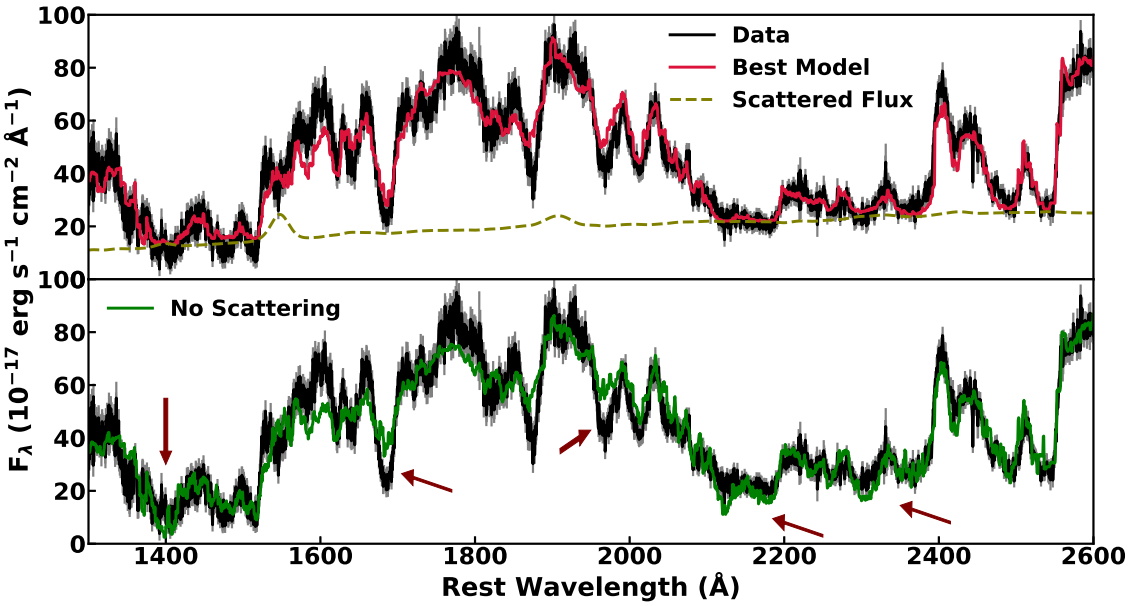

Figure 4.8: The top panel shows the data and the best fit model that has the scattered flux component in it. The bottom panel shows a model that does not have the scattered light component. The scattered light component is clearly necessary to create an appropriate trough shape.

scattered light is given in § 4.6.1.

4.4.3. The Zero-Velocity Component

We found a single prominent absorption feature between 2800Å and 2850Å that was not modeled with the blueshifted components (Figures 4.5 and 4.7). We identified this feature as Mg II$\lambda\lambda 2796, 2803$ lines with near zero velocity offset and modeled it with a separate group of tophats bins. Seven tophat bins for the zero-velocity component span a velocity range from $\sim -8900\,\mathrm{km\,s^{-1}}$ to $\sim 6700\,\mathrm{km\,s^{-1}}$ with the total velocity width of $\sim 15000\,\mathrm{km\,s^{-1}}$. The zero-velocity component seems to be most prominent in the Mg II lines and this doublet is the only feature that is not blended significantly with the high-velocity lines. Our model also found the low-ionization lines Al III$\lambda\lambda 1854, 1862$ and Al II$\lambda 1670$ from the zero-velocity component to be present as shallow features in the spectrum at ~ 1880 Å and ~ 1670 Å with the Al II line being the shallower of the two.

Notably, we find no strong evidence for high-ionization absorption lines such as

Si IV$\lambda\lambda 1402, 1393$ and C IV$\lambda\lambda 1548, 1550$ from the zero-velocity component in the data. That is, the high-velocity component alone produces enough opacity to match the data in the regions where the high-ionization lines from the zero-velocity component are expected to appear. This is very unusual since Al III and Mg II are always accompanied by high-ionization lines (e.g., Voit et al., 1993). Moreover, the high ionization conditions that produce larger Al III opacity than Al II opacity for the zero-velocity component also predicts significant high-ionization lines.

We suspect that the gas cloud for the zero-velocity component is illuminated by continuum that lacks the high-energy photons necessary to create such ions because it has been transmitted through the high-velocity part of the outflow. That is, in the presence of a multiple gas clouds along a line of sight, the gas cloud further from the radiation source may see an absorbed "filtered" SED from the back of the gas cloud that is located closer to the radiation source. This phenomenon has been investigated previously by Leighly et al. (2018), where they explored the potential possibilities for the radiation filtering with SDSS J0850+4451 by creating synthetic spectra using the filtered SEDs. Both the accelerating and decelerating outflow scenarios with radiation filtering produced features that are not seen in the spectra of SDSS J0850+4451 and they concluded that there was no support for the radiation shielding of outflowing gas in that object. Miller et al. (2018) tested this idea in their analysis of the BAL troughs in LBQS 1206+1052 and found no strong evidence supporting the radiation shielding. SDSS J1352+4239, on the other hand, seems to require an absorption component (zero-velocity component) originating from an absorbed SED to avoid creating the high-excitation ions at zero-velocity. The evidence is that we see several moderate to strong low-ionization absorption lines (e.g. Mg II, Al III) from the zero-velocity component but the high-ionization lines normally associated with those lines are completely absent from the spectrum.

To test the filtering model, we first tried using a modified line list to model the zero-velocity component. We removed the high-ionization ion transitions (ionization potential $>$ 24.6eV) to approximate such a condition. The results are not shown, but the success

from this approach led to modeling with filtered continuum constructed following Leighly et al. (2018) Appendix A.2. We started with an unabsorbed SED redshifted to match the outflow velocity of the starting bin (highest velocity bin and lowest velocity bin for the decelerating outflow and accelerating outflow, respectively). Then we created the first transmitted continuum from the starting bin with *Cloudy* and used the resulting transmitted continuum to illuminate the next adjacent bin for a subsequent *Cloudy* simulation to create the next transmitted continuum. The final filtered SED for the high-velocity trough was calculated from the transmitted continuum of the final bin. A more detailed description of the construction of the filtered SED can be found in Leighly et al. (2018) Appendix A.2. We used the filtered SED from the accelerating outflow calculation because we do not find a significant difference between the accelerating and the decelerating outflow scenarios. Figure 4.9 shows how the filtered SED differs from the unfiltered AGN SED and how the filtered SED for SDSS J1352+4239, an FeLoBAL, differs from that of SDSS J0850+4451, a LoBAL. A new ionic column density grid was calculated using the filtered SED for the zero-velocity component.

We fixed the emission and high-velocity trough components from the preliminary best-fitting model and fit only the zero-velocity component with the new column density grid from the filtered continuum. The physical parameters for the new grid were allowed to vary as fitting parameters. Figure 4.10 shows how the zero-velocity component from the filtered SED produces sufficient low-ionization lines to match the data without overproducing high-ionization lines. The ionization parameters for the bins ranged between -2.8 and 1.8 with the filtered SED (Table 4.2). The uncertainties associated with the fit parameters and the range of values from the bins for the zero-velocity component were large mainly because the absorption feature is shallow and only a small number of lines from that component are present in the spectrum.

In summary, the absorption feature centered around zero-velocity only showed absorption lines from low-ionization species. The zero-velocity component from an SED filtered by the high-velocity outflow provided a good fit by producing sufficient opacity

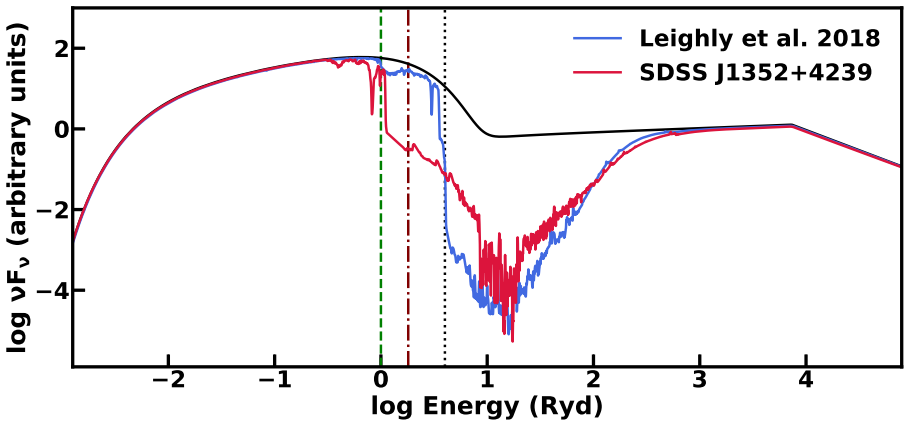

Figure 4.9: The unabsorbed AGN SED is plotted in black and the filtered SED generated from *Cloudy* with the physical parameters retrieved from the *SimBAL* fit of the blueshifted component is plotted in red. The filtered SED from SDSS J0850+4451 (Leighly et al., 2018) is plotted in blue as a comparison. The green dashed vertical line, brown dot-dashed vertical line and the black vertical dotted line show the ionizing potentials for H I, He I, and He II, respectively. SDSS J1352+4239 shows stronger attenuation in the Lyman continuum, as expected for high column density FeLoBAL, than the LoBAL SDSS J0850+4451 which has a thinner outflow that does not encompass the hydrogen ionization front.

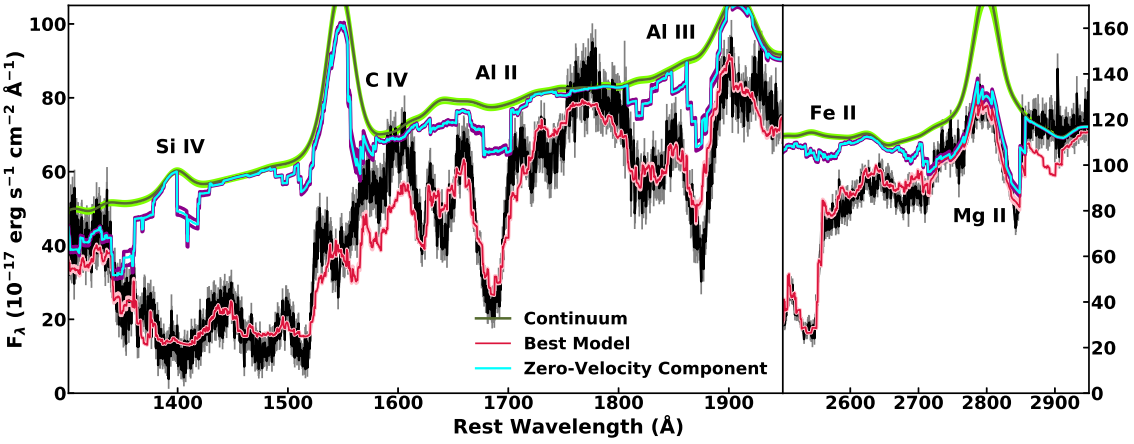

Figure 4.10: The cyan line represents the zero-velocity component model from the filtered grid. The filtered SED model produces sufficient opacity from the low-ionization ions (Mg II, Al III and Al II) while high-ionization lines (C IV and Si IV) are suppressed.

for the low-ionization transitions without producing deep high-ionization absorption lines. The distinction between this result and previous ones looking for evidence for filtering or shading (Miller et al., 2018) is that while the previous efforts found that the data were consistent with filtering, our data show the lack of high-ionization lines that must be the signature of this phenomenon, and therefore require a filtered continuum.

4.5. Derived Physical Properties of the Outflow

Using *SimBAL*, we can measure the physical parameters of the outflow and the uncertainties associated with those values. We extracted the radius of the outflow using the following relationship:

$$U = \frac{\phi}{nc} = \frac{Q}{4\pi R^2 nc},$$

where ϕ is the photoionizing flux in $\mathrm{photons\,s^{-1}\,cm^{-2}}$ and Q is the number of photoionizing photons per second emitted from the central engine. Therefore, with the density and ionization measurements from *SimBAL* we can calculate the location of the outflow R. The value of Q was estimated by scaling the *Cloudy* input SED to the observed quasar spectrum and integrating the scaled SED for energies greater than the hydrogen ionization potential of 13.6 eV. We estimate log Q = 57.3 - 57.4 [photons $\mathrm{s^{-1}}$] when scaled the flux density at 4000 Å ($F_{4000} = 72.58 \times 10^{-17}\,\mathrm{ergs\,s^{-1}\,cm^{-2}\AA^{-1}}$) and to the near-infrared (rest-optical) photometry, respectively. We derived the radius of each bin using the sets of physical parameters constrained by the tophat accordion model (Figure 4.11). We found that the location of the outflow is ~ 10 pc away from the center.

Once we know the radius of the outflow, we can further calculate the mass outflow rate of the outflow and the kinetic luminosity associated with it. We computed the outflow mass using the equation from Dunn et al. (2010)

$$\dot{M} = 8\pi\mu m_p \Omega R N_H v,$$

where the mean molecular weight is assumed to be $\mu = 1.4$, the global covering fraction

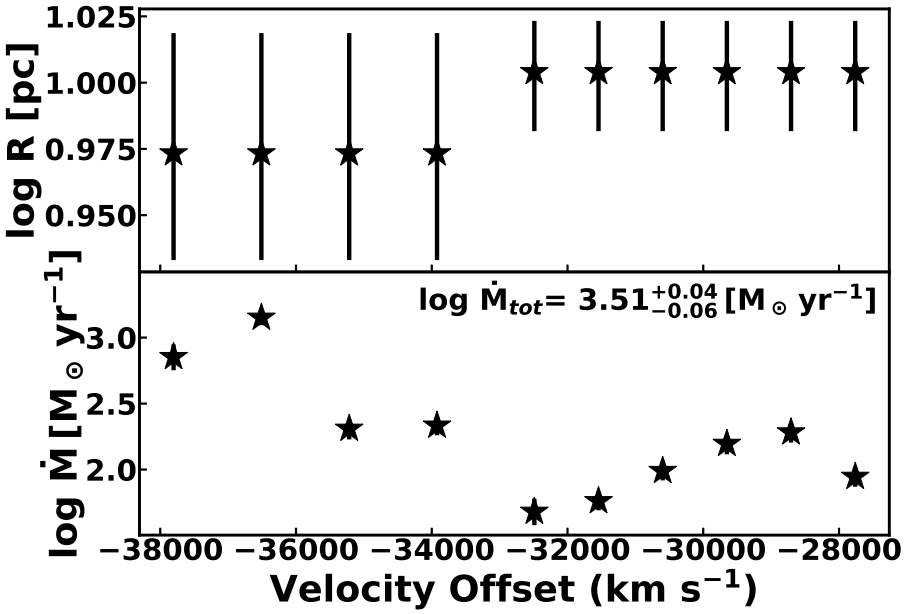

Figure 4.11: The radius and outflow mass estimates for each velocity bin. The outflowing wind is located ~ 10 pc away from the central engine. The $\log n$ and $\log U$ values for the bins in the higher and lower velocity groups were constrained to have the same value. The total outflowing mass of 3200 $(M_{\odot}\,\mathrm{yr}^{-1})$ is noted on the bottom panel.

is given by Ω, and R, N_H, and v are calculated from the best-fitting parameters from *SimBAL*. We calculated the mass outflow rate for each bin (Figure 4.11) and summed them to estimate the total mass outflow rate of $\log \dot{M} = 3.5 \pm 0.04\,[\mathrm{M}_{\odot}\,\mathrm{yr}^{-1}]$. The outflowing mass rate of 3210^{+270}_{-290} $(\mathrm{M}_{\odot}\,\mathrm{yr}^{-1})$ is about 18 times the mass accretion rate (§ 4.2.5) which suggests an extremely massive outflow. We use $\Omega = 0.2$ based on the fraction of BAL quasars in optically selected surveys (e.g., Hewett & Foltz, 2003), and further discussion of Ω is below.

Kinetic luminosity is one of the critical physical measures of the outflow strength. Cosmological simulations require the ratio between the kinetic luminosity and the bolometric luminosity to be 0.5% to 5% for effective quasar feedback that could reproduce the observed scaling relations between the host galaxy and the central black hole (e.g., Di Matteo et al., 2005; Hopkins & Elvis, 2010). Using the equation $\dot{E}_k = \dot{M}v^2/2$, we measured the log kinetic luminosity to be 48.1 ± 0.04 [erg s^{-1}] and L_{KE}/L_{Bol} of ~ 1. This

value of kinetic luminosity is the largest ever found from BAL quasars and sets a new record for the strength of the quasar outflowing wind. We compare with other large L_{KE} outflows in § 4.6.3.

In the above mass outflow and kinetic luminosity calculations we adopted the commonly used value of 0.2 for the global covering fraction (Ω) following Hewett & Foltz (2003) who found that 20% of optically-selected quasars have broad absorption lines (once selection effects were accounted for). Typical values for global covering factor, or the BAL fraction, range from 0.2 to 0.4 depending mainly on the sample selection criteria (e.g., Weymann et al., 1991; Trump et al., 2006; Allen et al., 2011; Dai et al., 2008; Knigge et al., 2008). One explanation for BALs is that they are present in all quasars, covering 20%$\sim$40% of the solid angle, and that the fraction of objects with BAL features reflect the amount of sky covered by the quasar outflows in an individual object. Supporting this view is the fact that (Hi)BAL quasars have similar broad band spectral energy distribution as the normal quasars (e.g., Gallagher et al., 2002, 2006, 2007). However, the above number is derived from HiBALs with C IV lines, and LoBAL fractions can be as low as $\sim$ 1% in a quasar sample (e.g., Trump et al., 2006; Dai et al., 2012). Assuming this is the case, we would infer the global covering fraction for (Fe)LoBALs to be as low as $\sim$ 0.01.

FeLoBALs can be difficult to identify in the general quasar population due to their lack of strong emission lines and their population fraction might not necessarily reflect the realistic sky coverage of the FeLoBAL wind. Dunn et al. (2010) discuss this particular issue in detail and concluded that a selection effect is the reason for the low LoBAL fraction. They used the value of (Hi)BAL fraction as the global covering fraction for FeLoBAL outflows. They assert that LoBALs and HiBALs are coming from the physically similar outflowing gas, but we observe LoBAL features from the gas because the line of sight (LOS) happens to pass through the edge of dusty torus. This not only explains the additional reddening in LoBALs (e.g., Sprayberry & Foltz, 1992; Reichard et al., 2003) but also the low LoBAL fraction because the LOS needs to be precisely at an angle where it passes through enough torus to produce low ionization lines but not obscure the broad

line region.

Finding the true value for BAL fraction or the global covering fraction is difficult and often uncertain. For example, a large BAL quasar fraction of about $\sim 40\%$ has been found from a luminous infrared selected sample (Dai et al., 2008). This value is about double of what Hewett & Foltz (2003) found from the optically selected sample but this discrepancy is not very surprising considering BAL quasars tend to be more frequently reddened than non-BAL quasars (Krawczyk et al., 2015). Therefore, in principle, one can adopt the value of global covering fraction as large as 0.4 for all BALs or as low as 0.01 for FeLoBALs depending on the assumption made to translate the statistical BAL fractions into global covering fractions.

Instead of using a single global covering fraction, we constructed a model to explore the idea that a single outflow exists in the vicinity of the central engine and multiple sightlines observe the outflowing gas as different types of BAL (e.g., HiBAL, LoBAL or FeLoBAL) depending on the viewing angle and the column density the sightline passes through (Figure 4.12). We estimated the mass outflow rate according to this scenario by gradually lowering the column densities of all the bins by the same small amount while keeping all other parameters fixed to mimic the effect of sightlines passing through less outflowing gas material. Specifically, we lowered the $\log N_H - \log U$ column density parameter and recorded the parameters when the model no longer produced Fe II absorption lines and transformed to a LoBAL. We continued lowering the $\log N_H - \log U$ column density parameter until the Mg II absorption lines disappeared to create a HiBAL. From this exercise we were able to estimate log N_H values for different sightlines that can produce different BAL spectral types of the same outflowing cloud reponsible for the trough in SDSS J1352+4239 ($N_{H\ HiBAL}$ and $N_{H\ LoBAL}$). We then modify the use of single global covering fraction with the following equation

$$\Omega N_H \Rightarrow \Omega_{HiBAL} N_{H\ HiBAL} + \Omega_{LoBAL} N_{H\ LoBAL} + \Omega_{FeLoBAL} N_{H\ FeLoBAL}.$$

Using the result from Dai et al. (2012), we set Ω_{HiBAL}, Ω_{LoBAL}, and $\Omega_{FeLoBAL}$ to be 0.14, 0.04, and 0.02. Figure 4.12 shows the result of our exercise with the changes in the column density noted on the illustration. We obtain log L_{KE} of $\sim$ 47.6 [erg s^{-1}] following the above interpretation. We conclude that the true value lies between 47.6 (computed using the scenario described here and in Figure 4.12) and 48.4 (computed using the maximum value Ω=0.4 from Dai et al. (2008)). Applying the same method, we obtain the range of mass outflow rate log $\dot{M}$ = 3.0 - 3.8 [$M_\odot\,yr^{-1}$]. We note that the current version of *SimBAL* that uses the grids calculated from the version C17 of *Cloudy* is only available for the solar metallicity. A higher metallicity grid would yield a smaller column density and therefore a smaller outflow rate (Leighly et al., 2018).

4.6. Discussion

4.6.1. A Plausible Geometry of the Outflows

In § 4.5 we found the radius of the outflow to be approximately 10 pc. Using the equation $R_{\tau k} = 0.47(6\nu L_\nu(V))/(10^{46}\,\mathrm{erg\,s^{-1}})$ from Kishimoto et al. (2007), derived from near-infrared reverberation monitoring, we estimated the distance to the innermost edge of the torus to be 3.5 pc. Furthermore, we estimated the dust sublimation radius $R_{sub} \simeq 2.0$ pc using the equation $R_{sub} = 0.2L_{46}^{1/2}$pc from Laor & Draine (1993). This indicates that the outflow is located in the vicinity of the dusty torus.

§ 4.4.3 describes the radiation shielding in the zero-velocity component and how this gas must be further from the central engine than the main high-velocity outflow gas. Considering both the kinematics and the peculiar ionization condition of the absorber, it is possible that the the zero-velocity absorption feature might be arising from an infalling gas cloud. Hall et al. (2013) analyzed a sample of objects that show redshifted C IV absorption features and suggested that such absorption signatures can originate from infalling clouds or rotating disk winds. SDSS J1352+4239, on the other hand, does not show any redshifted high-ionization lines like the sample Hall et al. (2013) studied, so it is not possible to use their interpretation of the phenomenon directly. Also, none of

the objects in their sample shows strong blueshifted troughs, therefore it is possible that the physical conditions in SDSS J1352+4239 are very different from their objects. We speculate that this potential infalling gas could originate from an earlier ejection episode and we are seeing the signature of the infalling remnant.

Figure 4.12 shows a physical picture of our spectral model. From analyzing the best-fitting spectral model, we know the location of the BAL outflow is near the torus. Both the absorbed spectrum and the scattered flux are reddened, so the dusty reddening source must lie at a larger radius. The zero-velocity component must be located between the main outflow and the reddening source as the reddening source would transmit too few ionizing photons. We constrained the ionization parameters for the zero-velocity component to be $\log U < 1.8$ and this implies that we can estimate the density of $\log n < 5.0$ $[\mathrm{cm}^{-3}]$ in order for the gas to be located further than the high velocity outflow gas. We do not have enough information from the spectrum to determine the exact geometry of the scattering cloud. Potential follow up spectropolarimetry observations may help us gain an insight into the geometry of some of the physical components in SDSS J1352+4239 we discussed throughout the chapter.

4.6.2. Acceleration Mechanisms

We calculated the momentum flux of the outflow from the equation $\dot{P} = \dot{M}v$ (e.g., Faucher-Giguère et al., 2012), and we found log $\dot{P}$ of 38.85$\pm$0.04 [dyne] (38.36 - 39.15 following the global covering fraction discussion in § 4.5 and Figure 4.12) with each individual bin having log $\dot{P}$ of 37 - 38.5. Compared to log L_{Bol}/c of 37.5, we find that the ratio between the momentum flux of the outflow and the photon flux is around 20. The ratio of 20 is far greater than the what is expected of the momentum conserving wind where the maximum momentum flux of the outflow for a single scattering is L_{Bol}/c or momentum flux ratio of $\sim$1 (e.g., Fiore et al., 2017). Two mechanisms have been proposed for objects with large log $\dot{P}$. In the energy conserving scenario the outflowing winds get an additional push by the shocks generated from ISM interactions (e.g., Faucher-

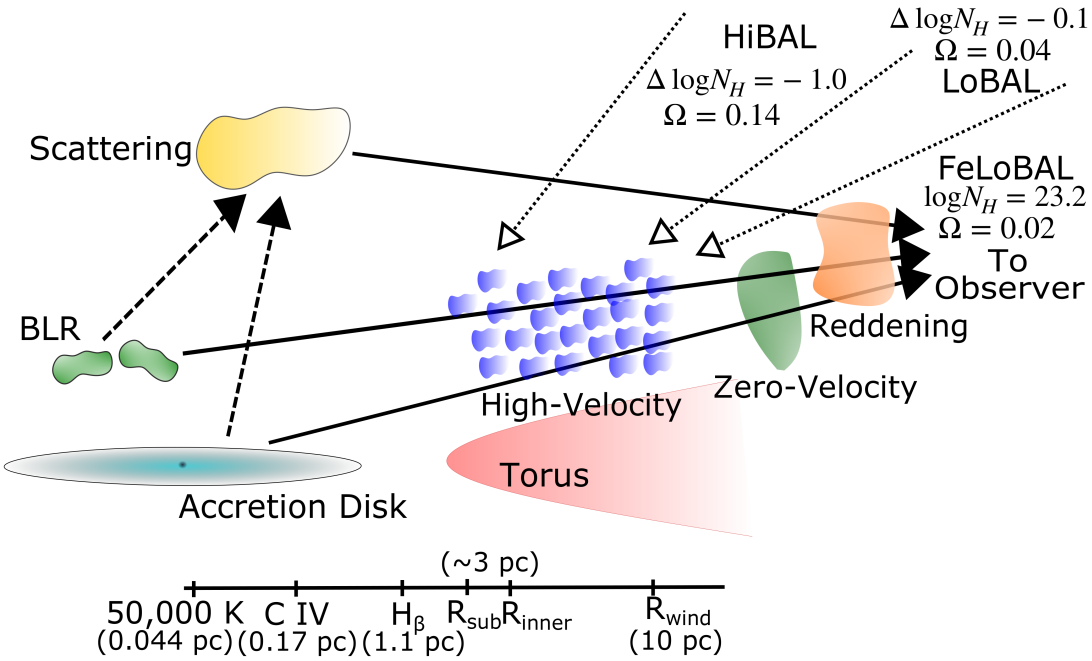

Figure 4.12: The cartoon illustrates how each spectral model component corresponds to different physical AGN components around the central black hole. The dashed lines represent the photons reaching the scattering medium to create the scattered flux and the solid lines represent the photons reaching the observer. The dotted lines represent different sightlines for HiBAL, LoBAL and FeLoBAL quasars (§ 4.5). The changes in column density (log N_H) required to transform the spectrum from FeLoBAL to the other types and the different global covering fractions (Ω) are labeled on the figure. The main BAL cloud is located slightly further away from the central engine than the innermost edge of the torus, and the zero-velocity cloud must be located between the main cloud and the reddening source. The horizontal bar at the bottom of the figure represents the location on the accretion disk where the temperature is about 50,000 K (§ 4.6.2), the locations of the C IV and Hβ emitting broad-line regions (§ 4.2.5), the distances to the torus and the outflowing wind (R_{inner}, R_{sub}, and R_{wind}; § 4.6.1).

Giguère & Quataert, 2012). Such a mechanism can generate a momentum boost and increase the momentum flux ratio between the outflowing gas and radiation by an order of magnitude. King & Pounds (2015) discuss various acceleration mechanisms for AGN outflows and compare the size scales of the energy conserving outflows and the momentum conserving outflows. An energy conserving mechanism mainly explains the $\sim$ kpc size scale outflows where the Compton cooling time-scale becomes greater than the flow time-scale and the full energy of the fast nuclear wind is communicated due to inefficient cooling (e.g., King et al., 2011). The Compton cooling time for SDSS J1352+4239 is $t_c \simeq 1.16 \times 10^5 R_{kpc}^2 \simeq 12$ yr (King et al., 2011, Equation (7)) and we can calculate the flow time $t_{flow} = \frac{R}{v} \simeq 330$ yr $(R \sim 10$ pc, $v \sim 0.1$c). It is unlikely for the outflow in SDSS J1352+4239 to be accelerated via energy conserving mechanism. The estimated cooling time-scale remains smaller than the flow time-scale for up to R $\sim$50 pc. The outflow in SDSS J1352+4239 is a compact torus scale outflow (R $\sim$ 10 pc) located in a region where the cooling is still assumed to be effective.

The other mechanism involves scattering by dust, which has a larger scattering cross-section than resonance scattering by ions (e.g., Fabian et al., 2008, 2018). Based on the size scale and the reddening observed in SDSS J1352+4239, it seems plausible that the outflow is a momentum conserving wind with the additional momentum being harnessed by the dust. Thompson et al. (2015) points out that if the effective infrared optical depth is significantly large at the cloud launch point, the outflowing gas can have momentum ratio greater 1 with the momentum conserving mechanism.

We further explored the acceleration mechanism responsible for the high-velocity outflow using force multiplier (FM) analysis. The FM is defined as the ratio of the total cross-section to the Thompson cross-section. We used the best fit parameters from the model and *Cloudy* to calculate the force multiplier values for each bin. Figure 4.13 shows the FM values as a function of velocity. In order for radiative driving of absorbers to occur, FM $\geqslant (L_{Edd} \ / \ L_{Bol})^{-1}$ is a necessary condition (e.g., Netzer, 2013). Leighly et al. (2018) calculated the FM values for their *SimBAL* model of LoBAL object SDSS J0850+4451 and

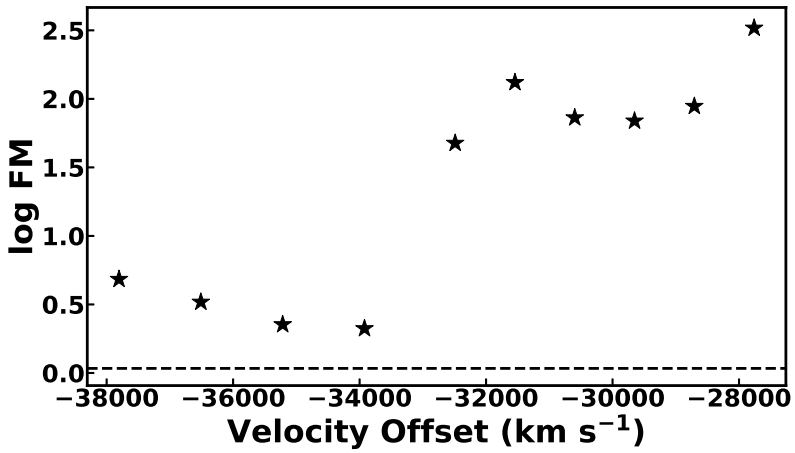

Figure 4.13: The force multiplier (FM) values computed for each bin using *Cloudy*. The horizontal dashed line represents FM = L_{Edd} / L_{Bol} above which the absorber can be radiatively driven. Because SDSS J1352+4239 is radiating at near Eddington limit, the FM threshold necessary for the radiative driving is low ($\sim$1) and the FM values for each bin are also rather higher due to lower ionization parameters. For comparison, see Fig. 17 in Leighly et al. (2018) for LoBAL object SDSS J0850+4451.

found that not all tophat bins satisfied the above condition and suggested that alternative driving mechanism might be necessary. However, SDSS J0850+4451 is radiating at only 6% L_{Edd}. SDSS J1352+4239, on the other hand, is radiating near the Eddington limit (log $(L_{Edd}\ /\ L_{Bol})\ \sim 0$). Therefore, even with lower FM values, the absorber can be radiatively driven as all 10 bins have FM values greater than $(L_{Edd}\ /\ L_{Bol})^{-1}$. This intuitively makes sense since the radiative driving relies on the power of radiation relative to the black hole mass. The FM values are smaller for the higher velocity bins because they have higher ionization parameter. Photoionized gas with higher ionization will have fewer ions that can provide UV line opacity and therefore have lower FM.

FM values alone do not fully explain how the main outflow in SDSS J1352+4239 was able to reach its high-velocity and large momentum ratio with a large outflow mass. Therefore we used the equation of motion to further probe how much radiative acceleration can be obtained with the given FM values we found for the main outflow in SDSS J1352+4239.

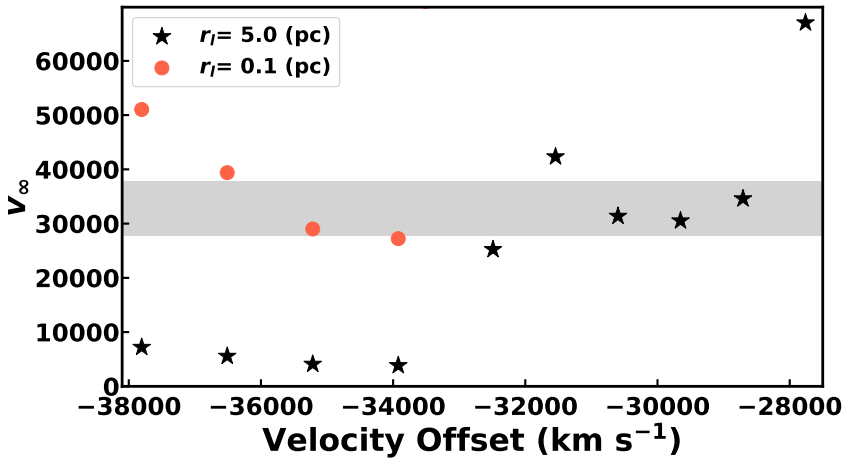

Figure 4.14: The wind terminal velocities for different inner wind radii ($r_l = 5.0$ and 0.1 pc in black stars and orange circles, respectively) have been calculated for each bin from the force multiplier (FM) values. The horizontal gray shaded region shows the actual outflow velocity range observed in SDSS J1352+4239. The lower velocity bins can get enough acceleration from large FM values and reach high outflow velocity that we see in the spectra even when launched at a large inner wind radius (5 pc) near the current location of the outflow; however, the higher velocity bins have small FM values (Figure 4.13) and can only reach high velocity with a smaller launch radius (0.1 pc).

We use the equation for acceleration,

$$v\frac{dv}{dR} \simeq \frac{M(R)\sigma_T L}{4\pi R^2 m_p c} - \frac{GM_{BH}}{R^2}$$

where the first term represents the radiative acceleration with the force multiplier ($M(R)$) and the second term is the force of gravity from the black hole. Integrating this equation assuming a constant force multiplier value (FM) we retrieve the following equation

$$v_\infty = 32,000 R_{0.1}^{-1/2}(6.69 \times 10^{-3} L_{46} FM - 0.008 M_8)^{1/2} \text{ km s}^{-1}$$

where v_∞ is the wind terminal velocity, $R_{0.1}$ is the inner wind radius or the launch radius in units of 0.1 pc, L_{46} is the luminosity of the quasar in the units of 10^{46} erg s^{-1} and M_8 is the black hole mass in the units of 10^8 M$_\odot$. Figure 4.14 shows the wind velocities calculated from the above equation. The wind velocities for the lower velocity bins can reach the

observed outflow velocities with the launch radius ($r_l \sim 5.0$ pc), similar to where we find the outflow ($r \sim 10$ pc). But the higher velocity bins require a much smaller launch radius ($r_l < 0.1$ pc) to match the outflow velocity seen in the spectra. At such a small radius we expect the gas to be more highly ionized and have smaller FM value, therefore if we compute the integral with FM as a function of radius then the lower velocity bins would need even smaller inner wind radius to be able to reach high outflow velocity. Note that the above FM values do not include the opacity from the dust. However with the presence of dust, the total opacity will increase significantly and as a consequence, the gas will be able to obtain extra acceleration. It will enable the lower velocity bins to potentially reach high velocities even at a larger radius.

Another useful size scale is the location of the UV emission of the accretion disk. The radiation-driven disk winds are thought to be accelerated by absorption of energetic photons from the UV radiation of the accretion disk (e.g., Proga & Kallman, 2004). The radius at which the disk radiation is mostly in the UV and the location on the accretion disk where the temperature is about 50,000 K is considered the outflow launch radius for such winds (e.g., Giustini & Proga, 2019). We calculated the location of 50,000 K emission of the accretion disk for SDSS J1352+4239 to be 0.044 parsec, using the equation $T(R) = (3GM\dot{M}/8\pi R^3\sigma)^{1/4}$ where σ is the Stefan-Boltzmann constant, M is the mass of the black hole and $\dot{M}$ is the accretion rate. This value is significantly smaller than the location of the outflow. Assuming constant outflow velocity of -30000 km s^{-1}, it would take about 320 years for the outflow to reach current location of 10 pc if the gas was launched at 50,000 K emission region of the accretion disk. The value is substantially larger than the rough estimate of the cloud dissipation time (e.g., Hamann et al., 2013, $t \sim \Delta R_{Cloud}/\Delta v \sim 10s$ yr for SDSS J1352+4239). Therefore, we suspect the outflow is being radiative driven by both the absorption lines and dust, launched near the torus at a large distance from the disk.

Czerny et al. (2017) discuss a failed radiatively accelerated dusty outflow (FRADO) model to understand the motion of the clouds within the broad line region. Their model is

for the broad line region but it is possible that some of the clouds elevated by radiation pressure from the disk or dust would be entrained into the outflow. These dusty gas clouds with high opacity can form an outflow that can potentially create BAL troughs.

4.6.3. Comparison with Other Known Energetic Quasar Outflows

We compared our results with other exceptionally energetic outflows in the literature (Table 4.3). Borguet et al. (2013) found an outflow with log L_{KE} of at least 46 [erg s^{-1}] in SDSS J1106+1939 and it was the most energetic BAL quasar outflow ever reported at the time of publication. SDSS J0831+0354 was also discovered to have a strong outflow with with log L_{KE} = 45.7 [erg s^{-1}] (Chamberlain et al., 2015). Since their discovery, several more BAL quasars with comparable energetics have been found. Fiore et al. (2017) collected a large sample of AGN outflow data and performed a quantitative analysis on the properties of the outflows. Some ultra-fast outflow (UFO) objects with absorption lines in the X-ray band have strong winds in their systems due to the high velocity of the outflows. APM 08279+5255 is a lensed quasar with an X-ray UFO feature that has a near-relativistic outflow with log L_{KE} = 46.85 [erg s^{-1}] (Chartas et al., 2009). The energy of the outflows we discovered in SDSS J1352+4239 is greater than even the most energetic UFO outflow known. Estimating the outflow radius is crucial in estimating the kinetic luminosity of the outflows and it is worth noting that the outflow radius calculation for UFOs are different from the BAL quasars. To estimate the radius, the density of the gas needs to be carefully constrained. For BAL spectra, the density of the gas can be directly constrained by analyzing the density sensitive absorption lines. On the other hand, UFOs and X-ray spectra rely on an indirect method where the density is estimated by interpreting the trough variability (e.g., Risaliti et al., 2002; Hemler et al., 2019). For example, if the variability is thought to be caused by the ionization variability in the outflowing gas then the density of the gas (and the location of the outflow) can be constrained by analyzing the recombination time scales of the ions producing the variable troughs (§ 6.4.1). Among the objects listed in Table 4.3, SDSS J1352+4239 is the only FeLoBAL object and the

Table 4.3. Comparison with Other BAL Quasar Outflows

Object	log L_{Bol} [erg s^{-1}]	log M_{BH} [$M_\odot$]	$\dot{M}$ ($M_\odot$ yr^{-1})	log L_{KE} [erg s^{-1}]	Ω	Reference
SDSS J1106+1939 (LoBAL)	47.2	8.9	390^{+300}_{-10}	$46.0^{+0.3}_{-0.1}$	0.08	Borguet et al. (2013)
SDSS J0831+0354 (LoBAL)	46.9	8.8	410^{+530}_{-220}	$45.7^{+0.3}_{-0.4}$	0.08	Chamberlain et al. (2015)
HE 0238-1904 (HiBAL)	47.2	-	69^{+50}_{-50}	$45.4^{+0.3}_{-0.6}$	0.5	Arav et al. (2013)
APM 08279+5255 (UFO)	47.45	10.0	11.2	46.9	-	Chartas et al. (2009); Fiore et al. (2017)
SDSS J1352+4239 (FeLoBAL)	48.0	9.9	1040–6460	47.6–48.4	see § 4.5	This work

Note. — The mass outflow rate and the kinetic luminosity of the outflow in SDSS J1352+4239 were estimated using multiple global fractions (§ 4.5).

most luminous. FeLoBAL objects are known to have higher column density relative to the hydrogen ionization front (Lucy et al., 2014) than the other BAL objects and it is possible that in a large FeLoBAL sample we might be able to find more BAL objects with comparable or more energetic outflows (Leighly et al., 2022; Dabbieri et al., in preparation).

4.6.4. How Special is SDSS J1352+4239?

SDSS J1352+4239 is a very luminous quasar with an energetic outflow and an impressive overlapping trough feature in the rest-UV spectrum. The quasar luminosity function shows that such luminous quasars are rare objects in the universe with space densities 1∼2 orders of magnitude lower than the less luminous quasars (Richards et al., 2006a). Moreover, fewer than half of quasars show BAL features (e.g., Hewett & Foltz 2003 ($\sim$ 20%); Dai et al. 2008 ($\sim$ 40%)) and among the BAL quasars, only a handful of objects show features of very powerful outflows (e.g., Fiore et al., 2017). This means one can find only about $2 \sim 4$ luminous BAL quasars that may potentially have strong outflows from a sample of 1000 quasars and a sample of at least tens of thousands quasars is needed to find one luminous quasar with such a high velocity FeLoBAL outflow. From these statistics, we can infer that SDSS J1352+4239 is indeed a rare and a special kind of object.

Observational survey programs and the pipelines they use have biases and observational limitations that would result in under-reporting of the BAL quasars with strong outflows or peculiar spectroscopic features (extreme BAL troughs, heavy reddening, and low luminosity and signal-to-noise ratio). BAL quasars with strong absorption from thick absorbing gas often do not show any strong emission features, making it difficult for survey pipelines to correctly categorize them as quasars. Strong reddening not only dims the object but can also make the spectra more difficult to analyze and classify. The implication is that more BAL objects similar to SDSS J1352+4239 may already be in the publicly available archives.

4.6.5. Implications for AGN Feedback and Evolution

Theoretical model calculations require outflows to have the kinetic luminosities of about 0.5∼5% of the bolometric luminosity to contribute to AGN feedback and influence the star formation in the host galaxies (e.g., Di Matteo et al., 2005; Scannapieco & Oh, 2004; Hopkins & Elvis, 2010). The energy in the outflow we discovered in SDSS J1352+4239 is roughly the same as the quasar bolometric luminosity and we can confidently conclude that the outflow has more than enough energy to influence the star formation in the host galaxy and provide feedback. The strength of the outflow (L_{KE}) is thought to scale with the bolometric luminosity of the quasar (e.g., Costa et al., 2014; Zubovas & King, 2012). SDSS J1352+4239 has a very high bolometric luminosity, greater than most of the quasars known to have extreme AGN luminosities (e.g., Bischetti et al., 2017, WISE/SDSS selected hyper-luminous (WISSH) quasars), and the observed energetic outflow (§ 4.5, § 4.2.5) which seems to support this conjecture.

Some extremely red quasars are also found to have high bolometric luminosities and a fraction of them are known to host strong outflows (e.g., Hamann et al., 2017; Zakamska et al., 2019). Urrutia et al. (2009) found an anomalously large fraction of BALs (LoBALs) in a sample of red quasars and argues that the LoBAL quasars represent quasars in their early evolutionary stage. They further suggest the idea that the BAL outflows occur just after the merger events during a "blow out" phase which suppresses the star formation in the host galaxy. Obscured quasars are expected to show a sign of ongoing merger activities and/or a signature of recent star burst episode (Sanders et al., 1988b); however, the observational evidence shows mixed evidence for merger activities or starbursts (e.g., Violino et al., 2016; Zakamska et al., 2019; Villforth et al., 2019).

SDSS J1352+4239 does not show a signatures of substantial star formation. Violino et al. (2016) used the Submillimetre Common-User Bolometer Array 2 (SCUBA-2) to investigate whether FeLoBALs represent an evolutionary step between ultraluminous infrared galaxies (ULIRGs) and unobscured quasars. They found no evidence for enhanced

star formation in FeLoBALs including SDSS J1352+4239. SDSS J1352+4239 was also observed by ESA Herschel Space Observatory (Pilbratt et al., 2010)[7] with Photodetector Array Camera and Spectrometer (PACS; Poglitsch et al., 2010) and Spectral and Photometric Imaging Receiver (SPIRE; Griffin et al., 2010), and was detected with PACS at 70 microns. We obtained the PACS data from the Herschel Science Archive[8]. The infrared data are plotted in Figure 4.15 along with composite quasar AGNs from Richards et al. (2006b), Elvis et al. (1994) and Netzer et al. (2007). No far-infrared excess is detected. Therefore the photometry data do not support the need for an extra SED component from a starbust.

4.7. Summary

In recent years, several discoveries of powerful AGN outflows have been made (e.g., Borguet et al., 2013; Fiore et al., 2017; Chartas et al., 2009). A number of such discoveries were made from the studies of X-ray observations or emission lines in the optical or mm bands. UV outflows from BAL quasars have received less attention even though their discovery predates the other channels by decades. There has not been a well-defined statistical analysis of the BAL absorbers primarily due the complex nature of the BAL spectra. *SimBAL* (Leighly et al., 2018) enables the first quantitative and systemic studies of UV BAL outflows and their potential for feedback. With *SimBAL*, we were able to analyze the complex absorption features in the overlapping trough quasar spectrum of SDSS J1352+4239 and discover the most energetic AGN wind discovered to date with log kinetic luminosity of 48.1 ± 0.04 [erg s^{-1}]. Our principal results are as follows:

1. In § 4.2.4, we used Hα to measure the true redshift of 2.2639 ± 0.0008, a value about $\Delta z \sim 0.25$ larger than the previously reported values for SDSS J1352+4239. The true redshift led to the discovery of the extreme velocity of the outflow.

2. The black hole mass calculated from the Hβ line is 8.6 $\times 10^9\, M_\odot$ and L_{Edd} for

[7]PI: Meisenheimer, "The Dusty Young Universe: Photometry and Spectroscopy of Quasars at z>2"
[8]http://archives.esac.esa.int/hsa/whsa

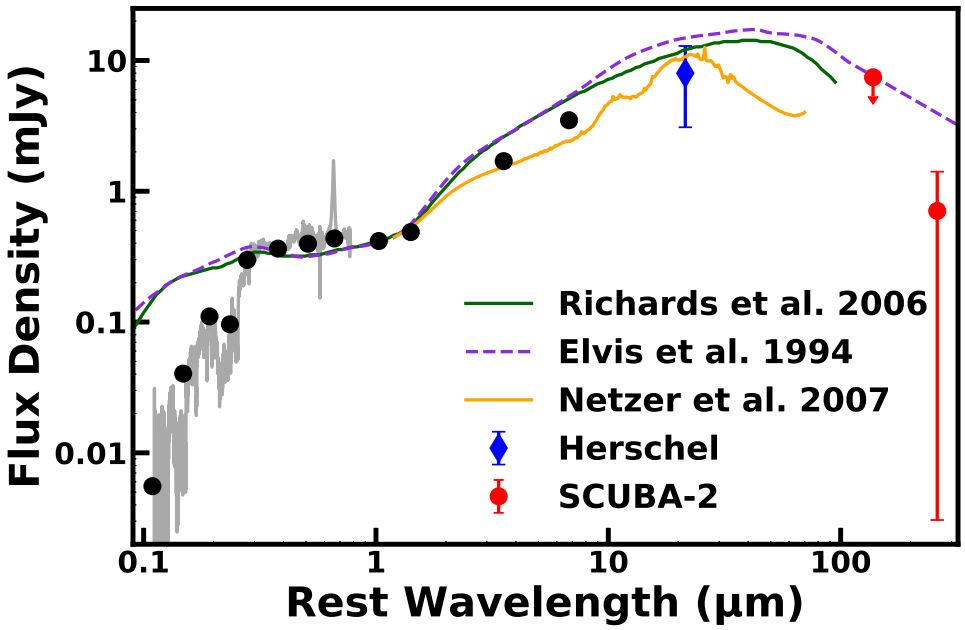

Figure 4.15: The broadband photometry data for SDSS J1352+4239 is plotted with mean quasar SEDs from Richards et al. (2006b) and Elvis et al. (1994). Both of these SEDs do not account for star formation, so the quasar intrinsic SED from Netzer et al. (2007) is plotted in orange as well. Black dots are the photometry data from SDSS, 2MASS and WISE as described in § 4.3 and shown in Figure 4.3. The blue dot is the photometry data from Herschel at 70 microns, observed frame. The red dots are the SCUBA-2 data from Violino et al. (2016) at 850 microns and 450 microns, observed frame. The WISE photometry points and Herschel observation of SDSS J1352+4239 are consistent with the intrinsic quasar SED. The starburst component would dominate the SED at around 100 microns if there were enhanced star formation in this quasar (e.g., Farrah et al., 2012). We do not see such a far-infrared excess and therefore conclude that there is no strong starburst contribution in SDSS J1352+4239.

the given black hole mass is 1.08 $\times 10^{48}$ [erg s^{-1}] (§ 4.2.5). SDSS J1352+4239 is radiating near the Eddington limit with $\log\ L_{Bol} = 48.0$ [erg s^{-1}] with the mass accretion rate of 176 $M_\odot$ per year (§ 4.3.1).

3. In § 4.4, we discussed the kinematics and the physical conditions associated with the outflow in SDSS J1352+4239. Our model finds the maximum wind velocity of $\sim -38000\,\mathrm{km\,s^{-1}}$ making it the fastest FeLoBAL outflow ever found. We estimate the total covering-fraction-weighted column density of $\log N_H = 23.22 \pm 0.05\,[\mathrm{cm^{-2}}]$.

4. In § 4.5, we measured the mass outflow rate of 3210^{+270}_{-290} ($M_\odot$ yr^{-1}) with the global covering fraction $\Omega = 0.2$. The mass outflow rate is about 18 times higher than the mass accretion rate. We found that this outflow has the largest kinetic luminosity ever found with $\log\ L_{KE} = 48.1 \pm 0.04$ [erg s^{-1}]. For an estimated log L_{Bol} of 48 [erg s^{-1}], we calculate the ratio $L_{KE}/L_{Bol} \sim 1$, much greater than the 0.5–5% thought to be sufficient to contribute to galaxy feedback.

5. We report the first definitive case where the data require a model component generated from a filtered SED, providing a strong support for the radiation shielding in action (§ 4.4.3). We conclude that this additional absorber is being irradiated with the AGN SED, but with significant amount of ionizing photons taken out by the fast outflow that is located closer to the central engine.

6. In § 4.6.1, we found that the outflow is located near the torus. However, the ratio between the outflow momentum flux and the quasar photon flux is far greater than unity ($\sim$ 20), expected for nuclear/torus scale outflows, suggesting that the extra source of momentum boost is required to explain the dynamics of the outflow we see in SDSS J1352+4239. The dust in the environment near torus could potentially serve as the acceleration mechanism (§ 4.6.2).

CHAPTER 5

The Physical Properties of Low-Redshift FeLoBAL Quasars[1]

5.1. Introduction

Iron low-ionization broad absorption-line quasars (FeLoBALQs) are arguably the most enigmatic of extragalactic objects. Their spectra present a tremendous range of phenomenology that has occasionally baffled experts[2]. Although rare and sometimes hard to find, their analysis may prove key to addressing several important questions involving galaxy evolution and quasar structure and demographics.

Depending on the physical conditions, the Fe^{+} ion can contribute thousands of absorption lines to the near-UV spectrum. The wide range of critical densities and oscillator strengths probed by Fe II makes these features richly diagnostic of the physical state of the absorbing gas (e.g., Lucy et al., 2014). Specifically, the relative strength of the suite of lines shows a strong dependence on density, ionization parameter, and column density within the outflow. What this means is that the physical conditions of the outflows in iron low-ionization broad absorption-line (FeLoBAL) quasars can be measured with a precision that is arguably unequaled among outflow phenomena in quasars.

However, a detailed understanding of FeLoBAL quasars and their origin has been hampered by the complexity of the spectra. The combination of the thousands of absorption lines and velocity dispersion in the outflows (i.e., the lines are broad) results in significant blending. Traditional methods of analysis that involve identification and measurement of individual lines are difficult to use on these complicated spectra. As a result, detailed analysis has been performed on only a handful of objects. Wampler et al. (1995) presented an qualitative analysis of a high-resolution spectrum of the FeLoBAL quasar Q0059−2735

[1]This chapter is reproduced from Choi et al. (2022a) with permission.
[2]https://www.nytimes.com/1999/08/17/us/rarely-bested-astronomers-are-stumped-by-a-tiny-light.html

which was discovered as part of the Large Bright Quasar Survey (LBQS; Morris et al., 1991). The first FeLoBAL quasars subjected to detailed photoionization analyses were QSO 2359−1241 (Arav et al., 2001, 2008; Korista et al., 2008; Bautista et al., 2010) and three objects discovered in the Far-Infrared and Submillimetre Telescope (FIRST) survey (White et al., 2000): FIRST J104459.6+365605 (de Kool et al., 2001; Everett et al., 2002), FBQS 0840+3633 (de Kool et al., 2002a), FIRST J121442.3+280329 (de Kool et al., 2002b). These masterful and difficult analyses yielded the first well-constrained distances to the outflows (from 1–700 pc). The Sloan Digital Sky Survey (SDSS; Blanton et al., 2017) yielded many more FeLoBALQs (e.g., Hall et al., 2002), including some very unusual and interesting objects. Hall et al. (2003) discussed formation scenarios for the narrow Ca II observed in the overlapping-trough object SDSS J030000.56+004828.0. Other FeLoBAL quasars that have been analyzed in varying degree of detail include SDSS J0838+2955 (Moe et al., 2009), SDSS J0318−0600 (Dunn et al., 2010; Bautista et al., 2010), AKARI J1757+5907 (Aoki et al., 2011), SDSS J112526.12+002901.3 (Shi et al., 2016), and PG 1411+442 (Hamann et al., 2019b).

The analysis of complex spectra of broad absorption-line quasars has become possible with the introduction of the novel spectral-synthesis modeling software *SimBAL* (Leighly et al., 2018). Because *SimBAL* uses forward modeling, line blending can be accounted for. In addition, because *SimBAL* models the whole spectrum, it uses the information conveyed by the lines that are *not* present in the observed spectrum. The analysis of the $z = 2.26$ quasar SDSS J135246.37+423923.5 and the discovery of a remarkably powerful outflow in that object (Choi et al., 2020) demonstrated an effective application of the *SimBAL* methodology on an overlapping trough FeLoBAL quasar.

The work described in this chapter contains the results described in the first paper, Choi et al. (2022a), in a series of four papers analyzing the properties of a sample of low-redshift FeLoBAL quasars. In Paper II, Leighly et al. (2022), we discuss the rest-optical spectral properties of a subsample of $z < 1$ FeLoBAL quasars. Paper III, Choi et al. (2022b), combines the FeLoBAL properties discussed in this paper and the emission-line

analysis results from Paper II (Leighly et al., 2022). Finally, in Paper IV (Leighly et al., in preparation), we discuss broad-band optical/IR properties of FeLoBAL quasars and the potential implication for the evolution scenarios for low redshift FeLoBAL quasars. A brief introduction to Papers II and IV can be found in Chapter 7 (§ 7.2).

In this chapter we present analysis of the outflows in 50 low-redshift ($0.66 < z < 1.63$) FeLoBAL quasars. This work increases the number of FeLoBAL quasars with detailed analyses by a factor of five. In addition, the uniform analysis means that the properties of the objects can be easily compared. These objects were drawn from two samples (§ 5.2). The first sample includes low-redshift FeLoBAL quasars that were observed by Spitzer in order to constrain their far-infrared spectral energy distributions (Farrah et al., 2012). The second sample includes 30 objects with sufficiently low redshift and high quality spectra that the Hβ / [O III] region of the spectrum could be analyzed; the results are reported in the companion paper, Leighly et al. (2022). § 5.3 gives a brief recap of the *SimBAL* software, and a description of our method for modeling the spectra using the software. § 5.4 details how we quantified the various physical and kinematic properties of the outflows using the results from the *SimBAL* model-fitting. § 5.5 presents the *SimBAL* model-fitting results and discusses the distributions of the parameters measured directly by the model fitting including the ionization parameter, density, column density, velocity, and parameters extracted from the models including the location of the outflow and its kinetic luminosity. § 5.6 describes the relationships among parameters, properties of the opacity profiles, and several special groups of objects. § 5.7 discusses the implications of this large study for our understanding of the origins, formation, and acceleration of broad absorption line outflows. § 5.8 summarizes the results.

5.2. Sample Selection and Data

Our sample of 53 $0.66 < z < 1.63$ FeLoBAL quasars was chosen from two sources. The data and other parameters are listed in Table 5.1. We report the SDSS names of the objects in Column 1 and throughout this chapter we use the shortened four by four naming

scheme (e.g., SDSS JHHMM+DDMM). Part of the sample was drawn from the 31 objects presented in Farrah et al. (2012) and we analyzed data from 28 of these. For this work we rejected objects that did not have sufficient signal-to-noise ratio (SNR) spectra, clear detection of Fe II absorption features, and no evidence of strong resonance scattering emission from the broad absorption-line (BAL) wind. Specifically, we excluded 3 objects from the sample analyzed in Farrah et al. (2012). SDSS J0911+4446 was excluded due to a low signal-to-noise spectrum which shows unusually strong Fe II emission features potentially coming from resonance scattering from the BAL outflows (e.g., Wang et al., 2016). The spectrum for SDSS J2215−0045 showed BAL features only from Fe III instead of Fe II. Finally, SDSS J2336−0107 was shown to be a double quasar by Foreman et al. (2009), and we could not obtain an adequate spectrum from the SDSS archive for the *SimBAL* analysis.

Additionally we included 25 FeLoBAL quasars from Leighly et al. (2022). All of these objects have $z < 1$ and sufficiently good SNRs that the Hβ / [O III] region of the spectrum could be analyzed. The *SimBAL* analysis of the FeLoBALs in the objects included in Leighly et al. (2022) are discussed in this work; however, we refer to that publication for analysis of the Hβ / [O III] region and Choi et al. (2022b) for the discussion of the relationships between the FeLoBAL properties and the quasar optical emission-line properties. Column 2 of Table 5.1 gives the sample origin of the objects.

In some cases, the object was observed by SDSS and then by Baryon Oscillation Spectroscopic Survey (BOSS; Dawson et al., 2013, 2016). The highest SNR spectrum available from the SDSS (Blanton et al., 2017) archive was chosen for analysis. Multiple spectra are listed when they were averaged for rest-frame optical band analysis when no spectral variability was observed (Leighly et al., 2022). The i-band SDSS magnitudes are listed in Table 5.1 (column 4).

As an accurate redshift is essential to analyzing the outflow properties, we remeasured the SDSS catalogue redshifts where possible. In order of preference and as available, redshifts were measured using (1) the low-ionization narrow emission-lines of [O II] or

narrow Hβ, (2) the narrow high-ionization [Ne V] line, or (3) the Fe II pseudo-continuum template. Failing those methods, the Hewett & Wild (2010) catalogue redshifts were used. Best-fitting redshifts and the emission line used for their measurements are listed in Table 5.1 (columns 6 and 7).

Table 5.1. The Sample

SDSS Object Name	Sample[a]	Spectra[b]	m_i[c]	SDSS DR14Q Redshift	Redshift Used	Redshift Origin[d]
011117.36+142653.6	F	5131-55835-0054	17.73	1.154	1.1551 ± 0.0002	[O II]
015813.56-004635.5	O	7837-56987-0485	20.44	0.896	0.8959± 0.0002	narrow Hβ
024254.66-072205.6	F	0456-51910-0378	18.71	1.2166	1.2175 ± 0.0002	[O II]
025858.17-002827.0	O	4242-55476-0028	19.00	0.875	$0.8758^{+0.0009}_{-0.0005}$	[O II]
		9372-58074-0974				
030000.57+004828.0	F	0410-51877-0623	16.61	0.900	0.8907 ± 0.0002	[O II]
033810.84+005617.6*	F	0714-52201-0326	18.35	1.6295	1.6316 ± 0.0006	Hewett & Wild (2010)
080248.18+551328.8	O	7281-57007-0616	17.90	0.663	$0.6636^{+0.0001}_{-0.00008}$	[O II]
080957.39+181804.4	O	4493-55585-0632	17.44	0.970	0.970	SDSS DR14Q
081312.61+432640.1	F	0547-51959-0242	18.80	1.0865	1.0894 ± 0.0008	[O II]
		0546-52205-0449				
		0547-52207-0274				
083522.77+424258.3	F, O	8280-57061-0366	17.42	0.806	0.8066± 0.0002	[O II]
084044.41+363327.8	F	8858-57450-0056	16.25	1.235	1.2372 ± 0.0001	FeII
091658.43+453441.1	O	7517-56772-0266	19.81	0.915	0.9141± 0.0002	narrow Hβ

Table 5.1 (cont'd)

SDSS Object Name	Sample[a]	Spectra[b]	m_i[c]	SDSS DR14Q Redshift	Redshift Used	Redshift Origin[d]
091854.48+583339.6	F	0484-51907-0598	19.19	1.315	1.3110 ± 0.0004	[NeV]
094404.25+500050.3	O	7292-56709-0400	19.31	0.965	0.9656± 0.0003	[O II]
100605.66+051349.0	F	0996-52641-0243	18.67	0.9704	0.9683 ± 0.0002	[O II]
101927.37+022521.4	F	0503-51999-0464	18.61	1.3643	1.3648 ± 0.0002	[O II]
102036.10+602339.0	F	7087-56637-0979	18.28	1.015	1.0145 ± 0.0004	[O II]
102226.70+354234.8	O	4564-55570-0360	19.46	0.818	0.8207± 0.0003	[O II]
102358.97+015255.8	F	0504-52316-0268	19.12	1.0761	1.07537 ± 0.00009	[O II]
103036.92+312028.8	O	6451-56358-0440	17.65	0.864	0.8605± 0.0002	[O II]
		10465-58144-0458				
		11383-58485-0722				
103903.03+395445.8	O	4633-55620-0278	19.66	0.864	0.8637± 0.0002	[O II]
104459.60+365605.1	O	8851-57460-0737	16.65	0.703	0.703	SDSS DR14Q
105748.63+610910.8*	F	0774-52286-0278	19.49	1.2757	1.2743 ± 0.0006	Hewett & Wild (2010)
112526.12+002901.3	F, O	3839-55575-0812	17.90	0.864	$0.8636^{+0.0003}_{-0.0002}$	[O II]
112828.31+011337.9	F, O	4730-55630-0172	18.38	0.893	0.8930± 0.0002	narrow Hβ

Table 5.1 (cont'd)

SDSS Object Name	Sample[a]	Spectra[b]	m_i[c]	SDSS DR14Q Redshift	Redshift Used	Redshift Origin[d]
112901.71+050617.0	F	0837-52642-0400	19.42	1.2775	1.2814 ± 0.0008	Hewett & Wild (2010)
114556.25+110018.4	F	1226-52734-0375	18.81	0.9330	0.9350± 0.0006	[NeV]
115436.60+030006.3	F	4765-55674-0082	17.70		1.46968 ± 0.00007	FeII
115852.86-004301.9	F	0285-51930-0189	19.38	0.9833	0.9835 ± 0.0002	[O II]
120049.54+632211.8	F, O	7106-56663-0915	18.86	0.887	0.8862± 0.0001	narrow Hβ
120627.62+002335.4	F	0286-51999-0499	18.68	1.114	1.1369 ± 0.0008	Hewett & Wild (2010)
120815.03+624046.4	O	6974-56442-0404	19.72	0.799	$0.7982^{+0.00004}_{-0.00003}$	narrow Hβ
121231.47+251429.1	O	5975-56334-0556	19.32	0.842	0.8427± 0.0004	[O II]
121441.42-000137.8	F	0287-52023-0514	18.81	1.046	$1.04571^{+0.0002}_{-0.0001}$	[O II]
121442.30+280329.1	O	6476-56358-0374	17.16	0.695	0.6945± 0.0002	[O II]
		2229-53823-0557				
123549.95+013252.6	F	0520-52288-0001	19.16	1.2918	1.2902 ± 0.0002	[O II]
124014.04+444353.4	O	6617-56365-0631	20.10	0.964	$0.9634^{+0.0001}_{-0.0002}$	narrow Hβ
132117.24+561724.5	O	6828-56430-0710	19.53	0.794	0.7941± 0.0001	[O II]
132401.53+032020.5	F, O	4761-55633-0136	18.97	0.927	0.9254± 0.0001	[O II]

Table 5.1 (cont'd)

SDSS Object Name	Sample[a]	Spectra[b]	m_i[c]	SDSS DR14Q Redshift	Redshift Used	Redshift Origin[d]
133632.45+083059.9	O	1801-54156-0530	18.23	0.805	0.7988± 0.0003	Fe II, broad Hβ
135525.24+575312.7	O	8199-57428-0180	20.59	0.855	0.8552± 0.0001	[O II]
135640.34+452727.2	O	6629-56365-0728	19.52	0.802	0.8025± 0.00009	[O II]
142703.62+270940.4	F	6018-56067-0412	18.13	1.165	1.1669 ± 0.0001	[O II]
144800.15+404311.7	O	5172-56071-0836	16.80	0.805	0.805	SDSS DR14Q
		8498-57105-0724				
151708.94+232857.5	O	3961-55654-0256	20.30	0.810	0.8093± 0.0001	[O II]
152737.17+591210.1	O	6799-56478-0458	18.33	0.930	0.930	SDSS DR14Q
153145.01+485257.2	O	6728-56426-0078	19.60	0.945	0.9445± 0.0002	[O II]
155633.77+351757.3	F	4965-55721-0548	18.04		1.501	Schulze et al. (2017)
164419.75+530750.4	O	8057-57190-0707	17.90	0.781	0.7813± 0.0002	[O II]
173753.97+553604.9*	F	0358-51818-0056	19.86	1.1017	1.1109 ± 0.0007	[NeV]
210712.77+005439.4	F	0985-52431-0522	20.42	0.9244	0.9266 ± 0.0002	[O II]
213537.44-032054.8	O	4385-55752-0286	18.59	0.815	$0.8127^{+0.0002}_{-0.0001}$	[O II]
230730.69+111908.5	O	6154-56237-0120	19.51	0.878	0.8770± 0.00009	narrow [O II]

[a]F: objects drawn from Farrah et al. (2012); O: objects included in Leighly et al. (2022)

[b]Multiple spectra are listed when combined to increase SNR in the optical band. The first spectrum listed set the wavelength sampling and flux level, and subsequent spectra were resampled and scaled to match.

[c]The magnitudes are taken from the point-source function magnitudes in the AB system from the SDSS DR16, uncorrected for Galactic extinction

[d]The origin of the redshift in column 5. An emission line signals measurement directly from the spectrum.

5.3. Spectral Modeling with *SimBAL*

5.3.1. The Spectral Synthesis Software *SimBAL*

The traditional method for analyzing BAL quasar spectra involves line identification of individual BALs and measurement of the ionic column densities for each identified line in order to constrain the physical properties of the absorbing gas (e.g., Bautista et al., 2010; Dunn et al., 2010; Arav et al., 2013; Lucy et al., 2014). This process becomes extremely challenging and ambiguous when the lines are broad and severe line blending causes the BALs to overlap and create wide troughs in the spectrum. Some FeLoBAL quasars show thousands of line transitions from Fe II. The spectral synthesis code *SimBAL* was introduced by Leighly et al. (2018) and further developed by Leighly et al. (2019b) and Choi et al. (2020). We describe the basic properties here but refer to those publications and Chapter 3 (§ 3.2) for details. *SimBAL* uses a forward-modeling technique that allows the analysis of heavily absorbed and blended BAL quasar spectra. Six physical parameters are required to create an individual synthetic BAL. The parameters are: the dimensionless ionization parameter $\log U$, the gas density $\log n$ $[\mathrm{cm}^{-3}]$, a column density parameter $\log N_H - \log U$ $[\mathrm{cm}^{-2}]$ which represents the thickness of the gas column with respect to the hydrogen ionization front, the velocity offset v_{off} $(\mathrm{km\ s}^{-1})$, width of the absorption lines v_{width} $(\mathrm{km\ s}^{-1})$, and a dimensionless covering fraction parameter $\log a$ where larger $\log a$ represents lower partial covering of the emission source.

Leighly et al. (2018) demonstrated the use of the "tophat accordion model" to model the opacity profile of broad absorption-lines. Gaussian opacity profiles often fail to accurately model heavily saturated BAL troughs or fit small scale structures found within the wide troughs. The tophat accordion model uses a group of velocity-adjacent rectangular bins to divide the opacity profile into smaller velocity segments. Each tophat bin may be allowed to have independent physical properties or they may be constrained to have a common value. Therefore, not only do we obtain a better fit to the complex velocity structures of the BAL outflows, but we can also measure the physical properties of the outflowing gas

as a function of velocity. Leighly et al. (2019b) introduced a two-covering factor model where the absorption lines can have different partial covering parameter $\log a$ values for the continuum and the emission lines.

As discussed in Chapter 3 (§ 3.2.1) and Choi et al. (2020), *SimBAL* has been updated to include an expanded atomic data information and the grid of column densities created using *Cloudy* version c17.01 (Ferland et al., 2017). The main focus of the update was to incorporate more excited-state transitions and more iron-peak elements. However the line transitions from those excited state ions or rare metal ions do not contribute to the spectrum for low-ionization and low-density BAL outflows. To save computation time, some of the objects were modeled using the column density grid from the older version of *SimBAL* which used the c13.03 version of *Cloudy* (Ferland et al., 2013).

5.3.2. *SimBAL* Analysis of FeLoBAL Quasar Spectra

SimBAL can model FeLoBAL quasar spectra with various spectral morphologies using the updates made to *SimBAL* (Chapter 3; § 3.2.1) and the software allows the use of user-defined models that are based on various physical models of BAL outflows. For example, in some objects (13 out of 53) we found evidence for more than one BAL outflow absorber in the spectrum and we included more than one outflow component in their *SimBAL* models (§ 5.6.2). Each component was modeled using a set of accordion tophat bins or a Gaussian profile, each with their own independent set of physical parameters. The multiple outflow components in a given object were found to have overlapping velocity structures or they were observed to be completely separated by velocity (Figure 5.10; 5.11). These multiple BALs were treated as independent outflows so that separate outflows were analysed independently and all figures include the points for these outflows. These outflows are identified with a letter of the alphabet following the name of the object (Appendix 5.A). For some objects, strong narrow emission lines such as [O II]$\lambda\lambda 3726, 3729$ were removed from the spectrum before model fitting.

When using the tophat accordion model for the absorption features, a fixed number of

bins need to be specified before the fitting process and a user can decide if they want to allow each bin to have their own independent physical parameters or a single set can be given to the entire ensemble of bins. We started by fitting the spectra with one ionization parameter ($\log U$) and density ($\log n$) for all bins. After we retrieved the preliminary model fits, we then tried to fit the objects with more flexible models where we would let the ionization parameter and/or density to vary between bins. The number of bins for the tophat accordion models was determined based on the total width of the trough as well as whether the trough shows fine velocity structures. The tophat accordion models for some of the objects with narrow BALs used 3 bins and the objects with the widest troughs used 12 bins. Considering the spectral resolution of the data (~ 70 km s^{-1}) the minimum bin width was ~ 200 km s^{-1}. The choice of the total number of bins does not affect the *SimBAL* analysis, unless too few or too many bins are used (Leighly et al., 2018).

The default partial-covering model in *SimBAL*, power-law partial covering parameterized using $\log a$ (Leighly et al., 2018, 2019b), provided robust model fits to the majority of our FeLoBAL quasars. Moreover, a *SimBAL* model can have two sets of partial-covering parameters each applied to the continuum emission and the emission lines separately to reproduce the difference between the partial covering observed in continuum emission and in emission lines. However, six objects required a modified partial-covering scheme to obtain robust model fits (§ 5.5.1.1). The spectra of these six objects were initially fit with a pair of $\log a$ parameters in order to separately model the partial-covering of the line emission and the continuum emission. If the results of that fit argued that the line emission is not absorbed by the BAL components, we then proceeded with the modified partial-covering model where the BAL components are not allowed to absorb the line emission. We performed statistical tests (e.g., χ^2, F-test) to confirm our model selection.

Notes on the *SimBAL* model fits and specifications (e.g., number of tophat bins) for individual objects are given in Appendix 5.B.

5.3.3. Objects and BALs Excluded from the Analysis

Based on preliminary analysis with *SimBAL*, we excluded three more objects from the initial sample of 53 objects:

1. the absorption features observed in the spectra showed properties more consistent with them being an intervening absorber than a quasar-driven outflow

2. no clear FeLoBAL feature, with observable Fe II absorption lines, was detected in the spectra

Following the same reasoning we also excluded several outflow components that were identified with using multi-component outflow models.

Some of the objects had very narrow features and only ground state transitions that were more consistent with metal lines from intervening absorbers. They could be distinguished from intervening absorbers by partial covering and kinematic properties (e.g., Hamann et al., 2011); see discussion in Appendix 5.C. Additionally, the physical properties of a couple of BAL components could not be constrained reliably because only Mg II (and Al III in some cases) absorption lines were present in the spectra. For these reasons, we rejected two objects: SDSS J1057+6109 and in SDSS J0338+0056. The absorption lines we found in SDSS J1057+6109 has an extreme offset velocity and the very narrow width of the absorption lines that suggested an intervening absorber. The best-fitting model for SDSS J0338+0056 identified an extreme low-ionization broad absorption-line (LoBAL) in this object with Mg II trough located at ~ 2500 Å and spanning from $-43,300\ \mathrm{km\ s^{-1}}$ to $-26,400\ \mathrm{km\ s^{-1}}$, but no absorption from Fe II. Also, the assumed Mg II trough sits on top of the Fe II emission lines which makes this BAL identification uncertain. No other absorption lines besides the Mg II trough was observed and we could not constrain the physical properties of the BAL gas with any certainty. Therefore we excluded these two object from the analysis.

We excluded one of the two BALs found in SDSS J1214−0001 from further analysis. We identified two BAL systems in SDSS J1214−0001 (Pitchford et al., 2019); they were

modeled with a Gaussian profile component for a narrow absorption component and a set of tophat bins for the broad trough feature. However, we could not get a reliable continuum emission model due to the broad tophat component with $v_{width} \sim 10800$ km s^{-1} and $v_{off} \sim -12600$ km s^{-1} covering the entire Fe II emission line region (∼2200–2750 Å) with low apparent opacity. Furthermore, we found the constrained physical properties for this broad BAL component from the model fit to be unreliable. We kept the narrow BAL component from this object in the BAL sample because it was not affected by the uncertainty in the continuum emission placement. In addition, we did not find any absorption features in SDSS J1737+5536. This object was included in the Farrah et al. (2012) sample but the best-fitting model did not yield any absorption lines. These three objects were excluded from further discussion, leaving 50 objects in our final sample.

In SDSS J1324+0320 and SDSS J1531+4852, we were able to clearly identify absorption features from metal lines from an intervening absorber. They were found at extreme offset velocities from the quasar rest-frame ($v_{off} \lesssim -20,000$ km s^{-1}) and had narrow absorption line width ($v_{width} \lesssim 50$ km s^{-1}) which strongly suggested that these absorption lines did not originate in a quasar-driven wind. These absorption features were nonetheless modeled with *SimBAL* and included in the best-fitting model plots but are not included in the discussion.

The best-fitting model for SDSS J1644+5307 has two absorption components. The main Fe II trough and the most of the BAL features were fit using a 6-bin tophat component but an additional Gaussian component at lower velocity was needed to fit the deep Mg II trough. However, the lower-velocity component only appeared in Mg II and therefore we could not reliably constrain its physical properties. Therefore this component was excluded from further discussion. Similarly, the best-fitting models for SDSS J0916+4534 and SDSS J1531+4852 have extra Gaussian components included to fit low opacity absorption features ($I/I_0 > 0.9$) from the Mg II transitions located near the main BAL component. These components are essentially LoBAL absorbers. They improved the overall model fit but we did not include them in the discussion because the opacity they contributed was

insignificant and their physical properties could not be constrained well.

5.4. Calculation of Critical Parameters

5.4.1. Bolometric Luminosity Estimates and Spectral Index α_{ui}

The bolometric luminosities (L_{Bol}) of the quasars used throughout this work were calculated using the bolometric correction factor at 3 μm (BC=8.59) from Gallagher et al. (2007). The flux at rest-frame 3 μm was estimated from fitting the quasar composite spectral energy distribution (SED) by Richards et al. (2006b) to the *WISE* photometry data and interpolating the flux at 3 μm from the composite SED. The bolometric luminosity estimates are listed in Table 5.A.2 (column 8)

We defined α_{ui} to be the point to point spectral slope between rest-frame 2000 Å and 3 μm flux densities:

$$\alpha_{ui} = \frac{\log f_{3\mu\mathrm{m}} - \log f_{2000\mathring{\mathrm{A}}}}{\log \lambda_{3\mu\mathrm{m}} - \log \lambda_{2000\mathring{\mathrm{A}}}}$$

We used the continuum emission model extracted from the best-fitting *SimBAL* model to estimate the observed flux density at rest-frame 2000 Å. The value of α_{ui} can depend on three quasar properties: reddening, the intrinsic shape of quasar SED, and the strength of the torus emission. For instance, a quasar that either has a flat SED, is reddened, or has strong hot dust emission will have a flatter, i.e., a larger value of $\alpha_{ui} \sim 0$. For reference, the Richards et al. (2006b) composite quasar SED has $\alpha_{ui} \sim -1.23$. The values of α_{ui} for the sample are listed in Table 5.A.2 (column 9).

5.4.2. Derived Physical Properties and Kinematic Properties of the Outflows

Using the Markov Chain Monte Carlo (MCMC) chains from the best-fitting *SimBAL* models, we computed the physical and kinematic properties of the outflows and the associated uncertainties. Throughout this chapter we report and plot median values and 2σ (95.45%) confidence intervals calculated from the posterior distributions as our uncertainty measurements. Some of the physical properties can be directly extracted from the *SimBAL* physical parameters: dimensionless ionization parameter ($\log U$, definition

below), gas density ($\log n$ in $[\mathrm{cm}^{-3}]$), column density (parameterized as $\log N_H - \log U$ in $[\mathrm{cm}^{-2}]$), and dimensionless covering fraction parameter $\log a$ for the inhomogenous partial covering ($\tau = \tau_{max} x^a$, $x \in (0, 1)$; Arav et al., 2005; Sabra & Hamann, 2005). We calculated the offset velocities and widths of the BALs, the distance of the BAL gas from the central supermassive black hole (SMBH) $\log R$, the mass outflow rate $\dot{M}$, and the kinetic luminosity L_{KE}. The covering-fraction-corrected column density of the outflow was calculated by summing $\log U$ and $\log N_H - \log U$ and then correcting the values according to the $\log a$ to account for the power-law partial covering ($\log N_H = (\log N_H - \log U) + \log U - \log(1 + 10^{\log a})$; Arav et al., 2005; Leighly et al., 2018, 2019b; Choi et al., 2020).

The radius of the outflow (or the distance of the outflow from the central engine) can be calculated from $\log U$ and $\log n$ from the *SimBAL* results using the definition of the ionization parameter

$$U = \frac{\phi}{nc} = \frac{Q}{4\pi R^2 nc},$$

where ϕ is the photoionizing flux in the units of $\mathrm{photons\,s^{-1}\,cm^{-2}}$, and Q is the number of photoionizing photons per second emitted from the central engine. We estimated Q from the SED fits of the photometry data for each object.

The mass outflow rate was calculated using

$$\dot{M} = 8\pi\mu m_p \Omega R N_H v,$$

where the mean molecular weight (μ) is assumed to be 1.4, the global covering fraction is given by Ω, and R, N_H, and v are calculated from the best-fitting parameters from *SimBAL*. This equation can be derived from taking the time derivative of $M = 4\pi\mu m_p \Omega R^2 N_H$, then substituting $dR/dt = v$ (assuming $dN_H/dt = 0$; Dunn et al., 2010). The value of global covering fraction for FeLoBAL outflows is uncertain. The commonly used value $\Omega = 0.2$ (e.g., Hewett & Foltz, 2003) was derived from a fraction of high-ionization broad absorption-line (HiBAL) quasars observed in the optically selected sample of quasars; the

fraction can be as large as ~ 0.4 for the luminous infrared-selected quasars (Dai et al., 2008). FeLoBAL quasars are a rarer kind of BAL quasars; the observed fraction can be as small as $\sim 1\%$ in a given quasar sample (e.g., Trump et al., 2006; Dai et al., 2012), but it is not clear whether their rarity reflects a small covering fraction, a short lifetime, or a selection bias that makes them difficult to detect. Detailed discussion on how to best explore the different values of global covering fraction of FeLoBAL outflows can be found in Choi et al. (2020) where we also performed a multiple global fraction scenario with the idea that a BAL outflowing gas can be seen as different types of BALs depending on the viewing angle. In this work, we adopt a single global covering fraction $\Omega = 0.2$ which yields the mass outflow rate estimates for FeLoBALs that are slightly larger (~ 0.5 dex) than the multiple global fraction scenario calculations (Choi et al., 2020). The strength of the outflow can be quantified by calculating the kinetic luminosity (L_{KE}) of the outflows with the equation $\dot{E}_k = \dot{M}v^2/2$. The outflow column density, mass outflow rate, and kinetic luminosity for BALs modeled using tophat accordion models were calculated from the sum of the values calculated for each tophat bin.

In order to generate summary statistics for the widths (v_{width}) and the offset velocities (v_{off}) of the BAL outflows in a consistent manner we adopted a method similar to calculating the balnicity index (BI; Weymann et al., 1991). Continuum emission normalized spectra (I/I_0) for a single line transition were generated from the best-fitting *SimBAL* models and absorption features were defined as regions where the normalized flux I fell below 0.9. We used the Mg IIλ2796 line transition which has a higher transition probability ($f_{ik} = 0.609$) in the Mg II$\lambda\lambda 2796, 2803$ doublet to generate the I/I_0 for all identified BAL outflows. We estimated the width of the outflow by identifying the start (v_{max}) and the end (v_{min}) of the absorption features. The summary offset velocity for each BAL component was estimated by calculating the opacity (column density) weighted velocities. We used

$$v_{off} = \frac{\int v \times N_H(v) dv}{\int N_H(v) dv}$$

where N_H represents the covering-fraction-corrected hydrogen column density. The tophat accordion model produces physical parameters of the outflow as a function of velocity with which we calculated the summary offset velocity for an ensemble of tophat bins for a given BAL component. For Gaussian profiles, this calculation simply yields the velocity at the center of the profile. By calculating the velocity offsets this way, we avoid overestimating or underestimating the velocities compared to other metrics (e.g., v_{max}), especially when the trough has extended low opacity features in one or both velocity directions. In this work we retain the signs for the offset velocities as calculated from the quasar rest frame: the outflows have negative offset velocities and the inflows have positive velocities. For the objects that were modeled with more than a single BAL component, the outflow width and the velocity offset were measured for each component.

5.4.3. Opacity Profiles and BAL strengths of Select Transitions

We extracted the opacity profiles of several absorption line transitions seen in FeLoBALs from the best-fitting *SimBAL* models in addition to the Mg IIλ2796 used to calculate the kinematic properties (§ 5.4.2). The transitions we used are the ground-state Fe IIλ2383 with $f_{ik} = 0.343$ and the excited-state (0.99 eV above ground) Fe II*λ2757 with $f_{ik} = 0.307$. These are among the stronger transitions from Fe II multiplets in the near-UV band. We generated I/I_0 models for all BAL components with *SimBAL* from the MCMC chains of the best-fitting spectral models. The wavelength dispersion at each pixel was also taken into account in generating the profiles (Chapter 3; § 3.2.1). From the models, we visually inspected the shapes of the profiles and measured the kinematic information for each line transition. The widths for each transition were measured using the same method described in § 5.4.2: we used the normalized flux at 0.9 as the boundary of absorption. In addition, we measured the velocity at the location of the minimum normalized flux for each transition. We emphasize that v_{off}, opacity weighted velocity (§ 5.4.2), is used throughout this chapter as the representative outflow velocity; the velocities at the minima are just used to compare the kinematic properties of the 3 transitions (§ 5.6.3).

We extracted Ca II K, He I*λ3889, and Hα information from the *SimBAL* models for each BAL component. We used the absorption strength (A) defined by Capellupo et al. (2011) to measure the BAL strengths. The absorption strength is defined as the fraction of the normalized flux removed by absorption. This empirical parameter may not accurately reflect the physical properties of the outflowing gas, but it can be used as a summary statistic for the apparent BAL strength. For each BAL component, a single absorption strength value was reported from the averaged model flux within the absorption interval where $I/I_0 < 0.9$. To represent the strengths of Ca II doublet and Balmer series, we chose the transitions with the greatest transition probability which are Ca II K and Hα, respectively. Depending on the redshift of the FeLoBAL quasars the three line transitions of interest for some of the objects are located outside the bandpass of the SDSS/BOSS spectra used in this work. Moreover, we only modeled the spectra to ~ 4700 Å which means that the strongest Balmer transition observed in the given wavelength range was Hγ.

5.5. Results

5.5.1. Best-Fitting *SimBAL* Models

We present *SimBAL* model fits of the FeLoBAL quasars. Figure 5.1 shows the best-fitting models of all 50 objects from the sample. From these results we derived the physical properties and calculated the outflow properties, with associated uncertainties (Appendix 5.A). We identified 60 BAL features and 55 of them were classified as outflows with negative offset velocities. Eleven objects in the sample were modeled with more than one outflow component where either multiple sets of tophats bins or a combination of tophat bins and Gaussian profiles were used.

Analysis of SDSS J1352+4239 (Choi et al., 2020) showed that the outflow consisted of three components that were distinguished by their distinct physical properties as well as the kinematic properties. The majority of the multiple-outflow objects we discovered in this sample were found using similar rigorous *SimBAL* modeling. We found that majority

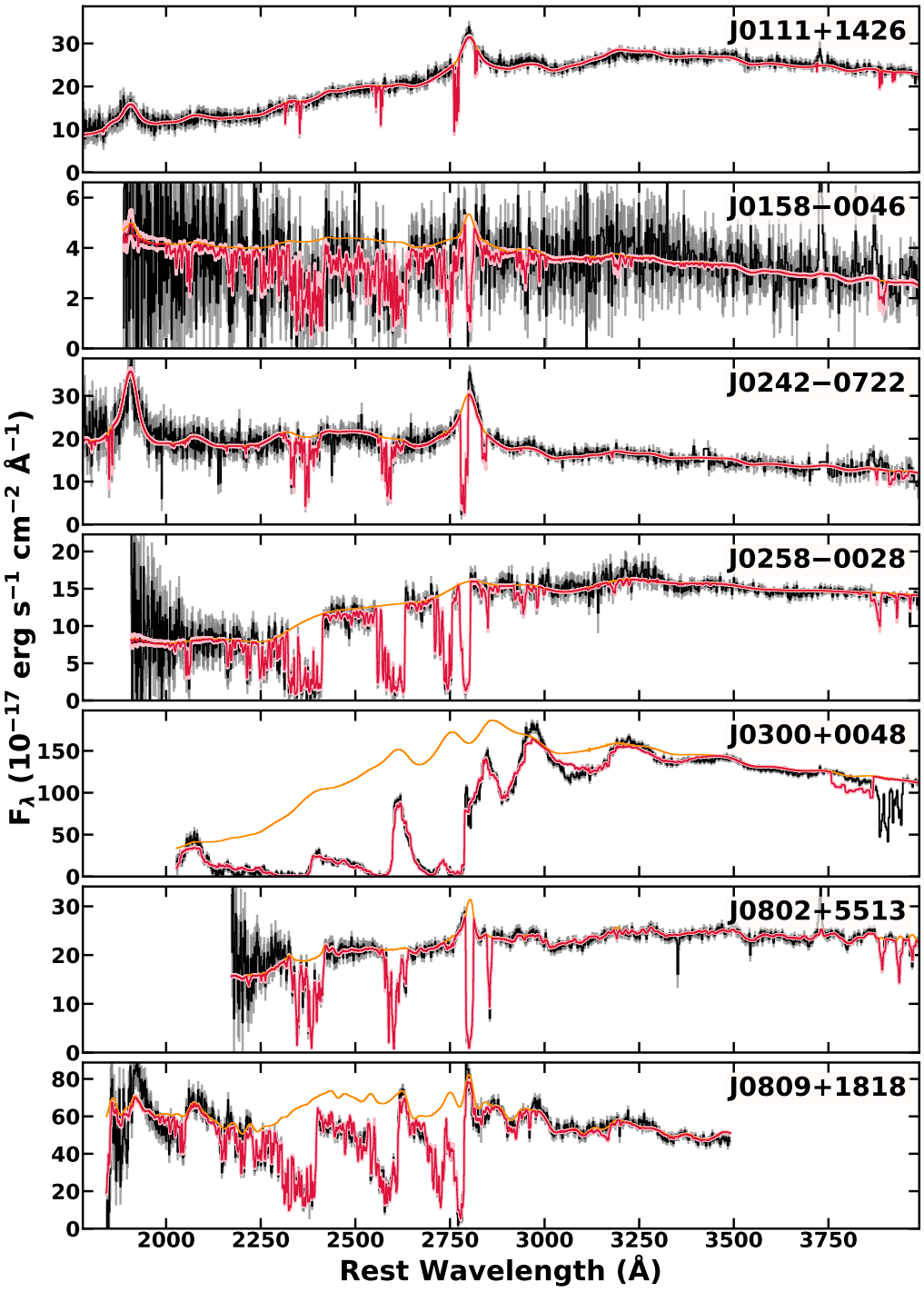

Figure 5.1: The best-fitting *SimBAL* models are plotted in red, along with the 2σ (95.45%) confidence models and unabsorbed continuum models in pink and orange, respectively. The binned data and the associated uncertainties are plotted in black and grey, respectively.

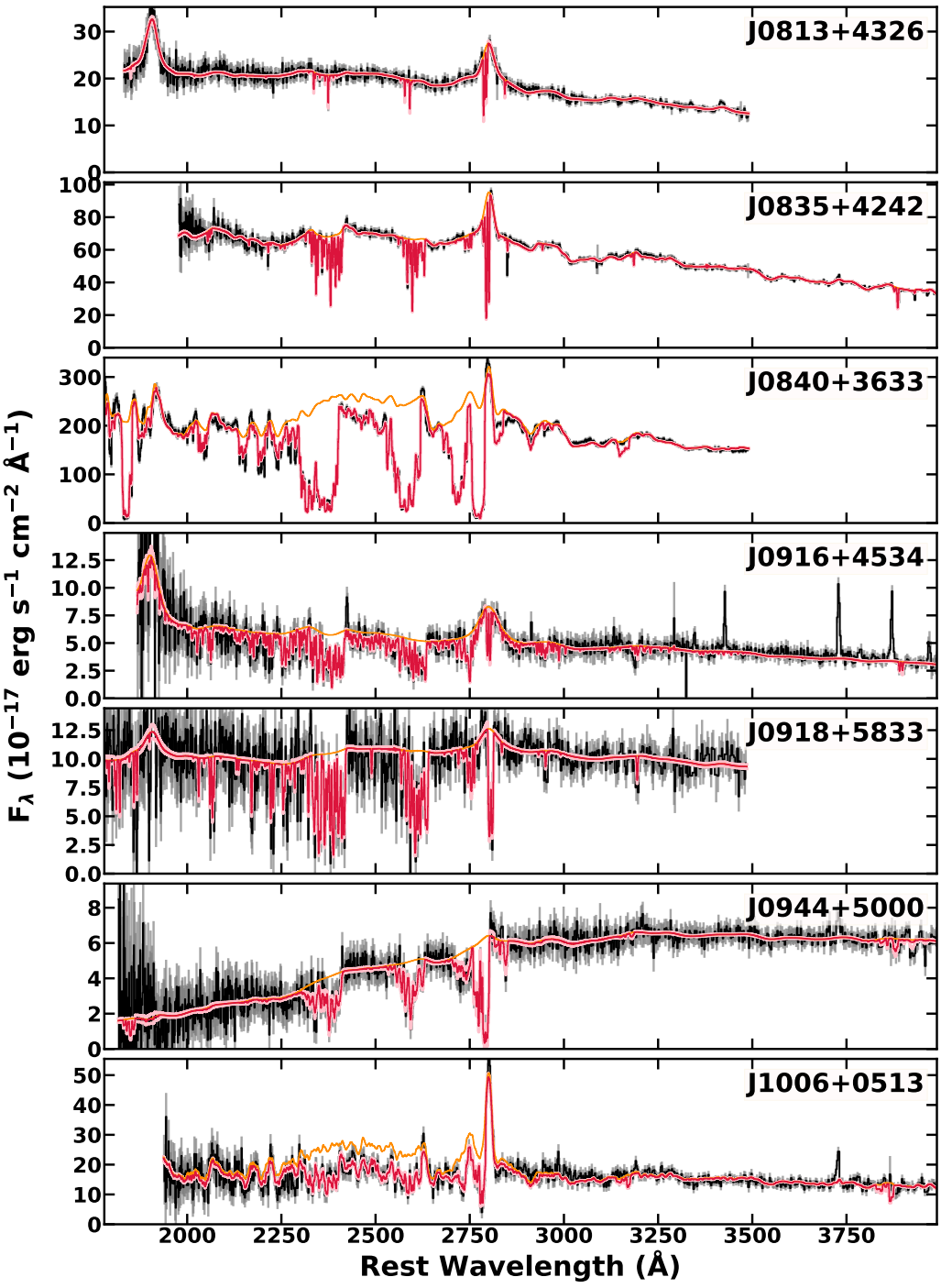

Figure 5.1: (Continued).

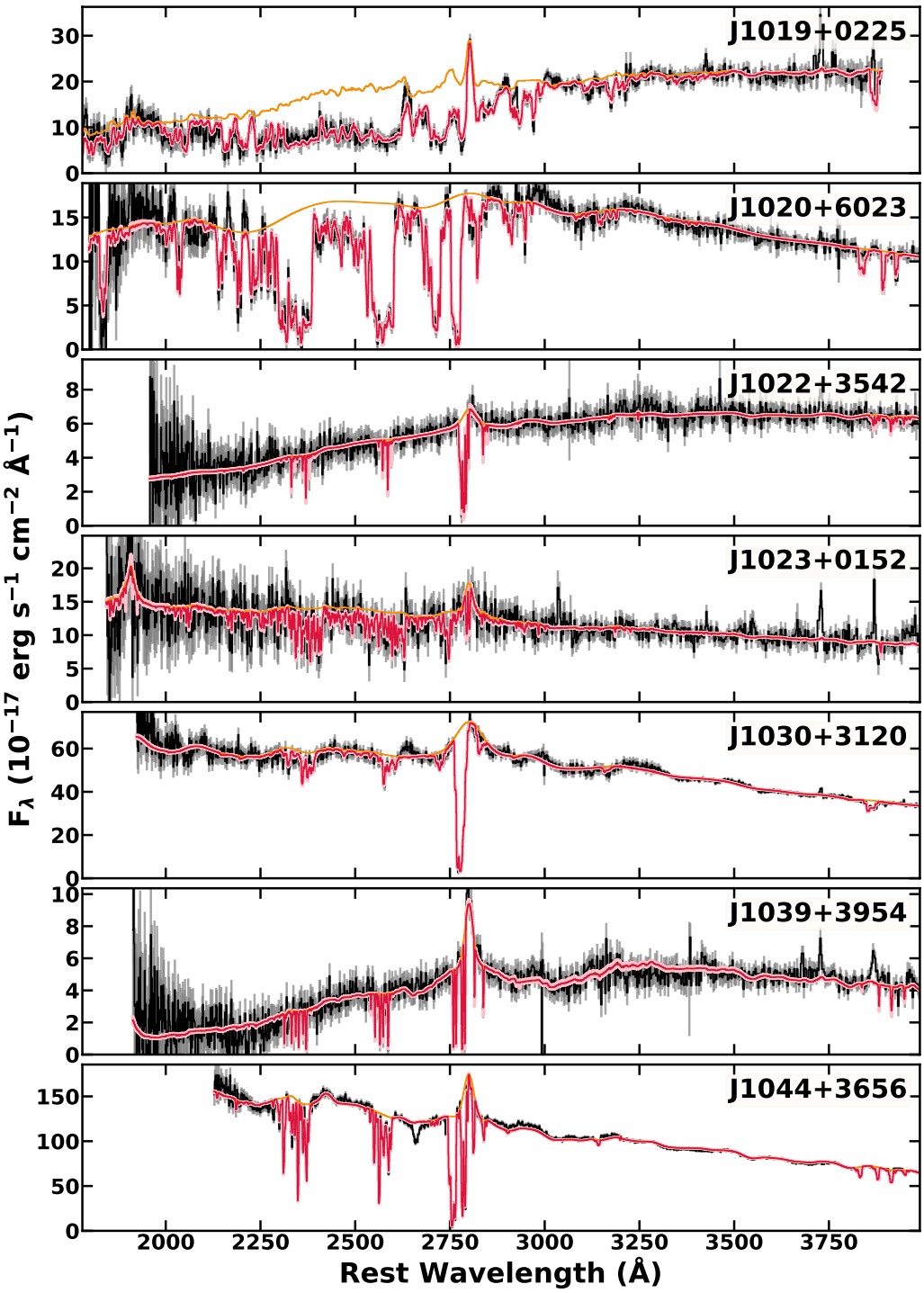

Figure 5.1: (Continued).

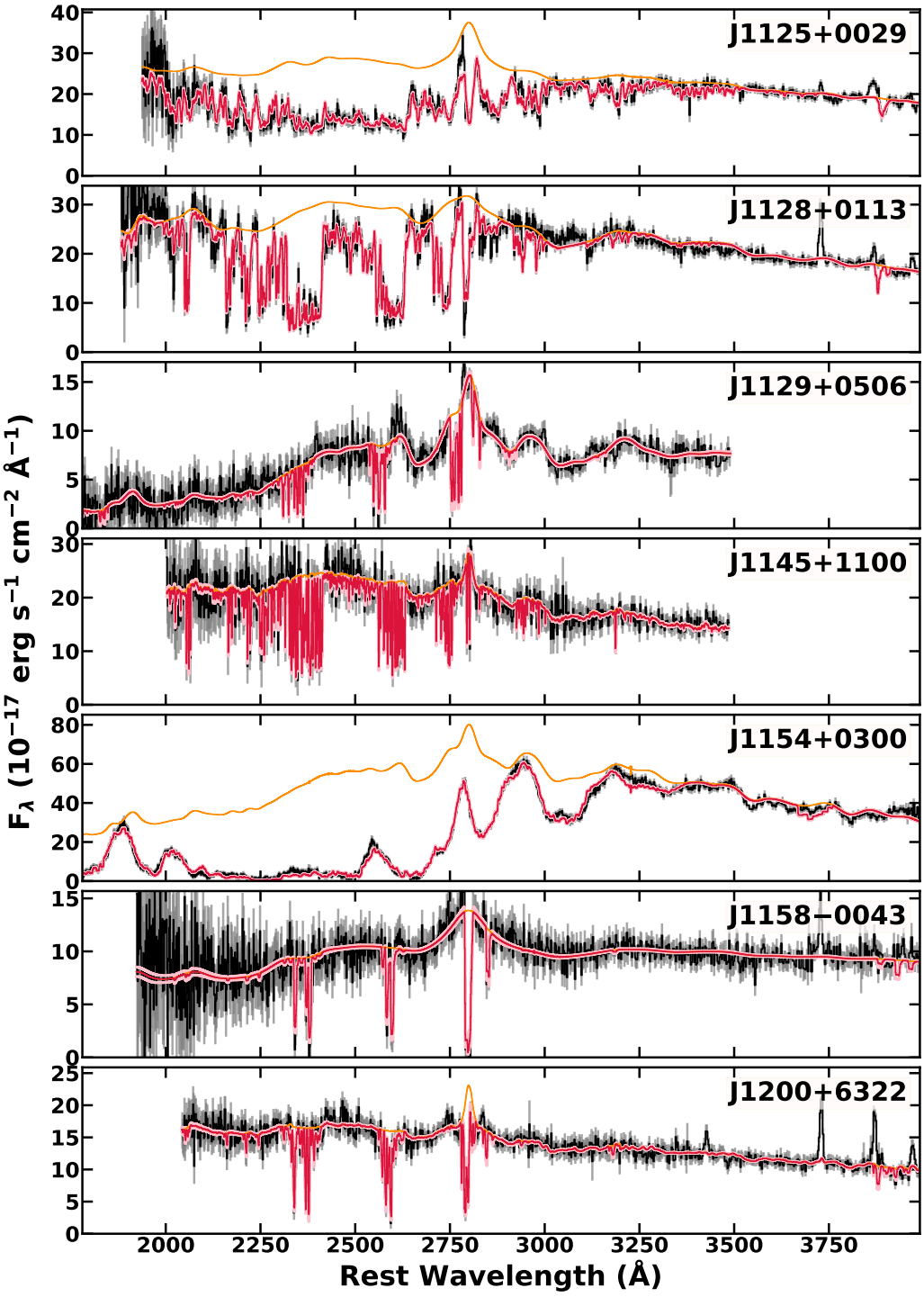

Figure 5.1: (Continued).

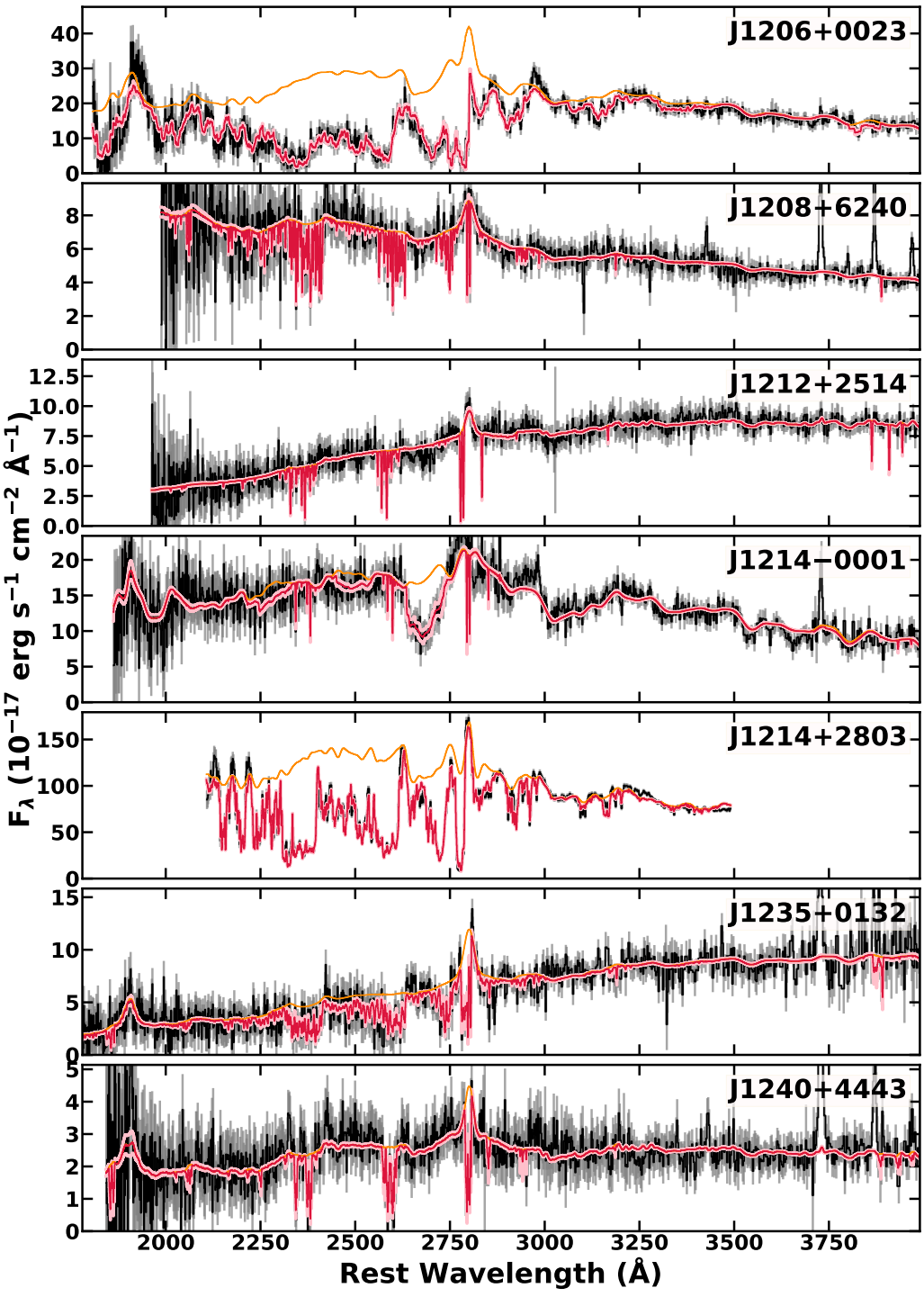

Figure 5.1: (Continued).

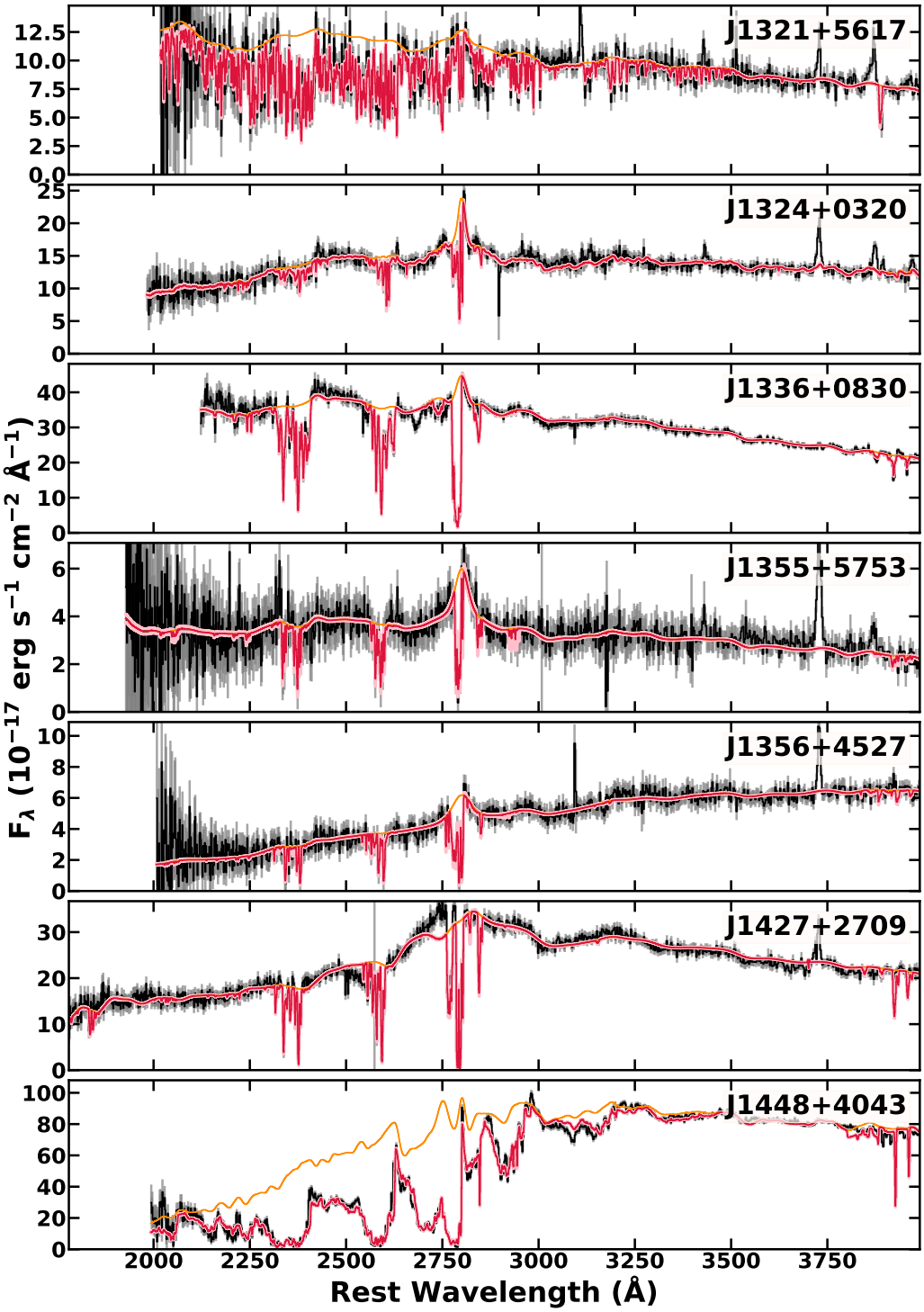

Figure 5.1: (Continued).

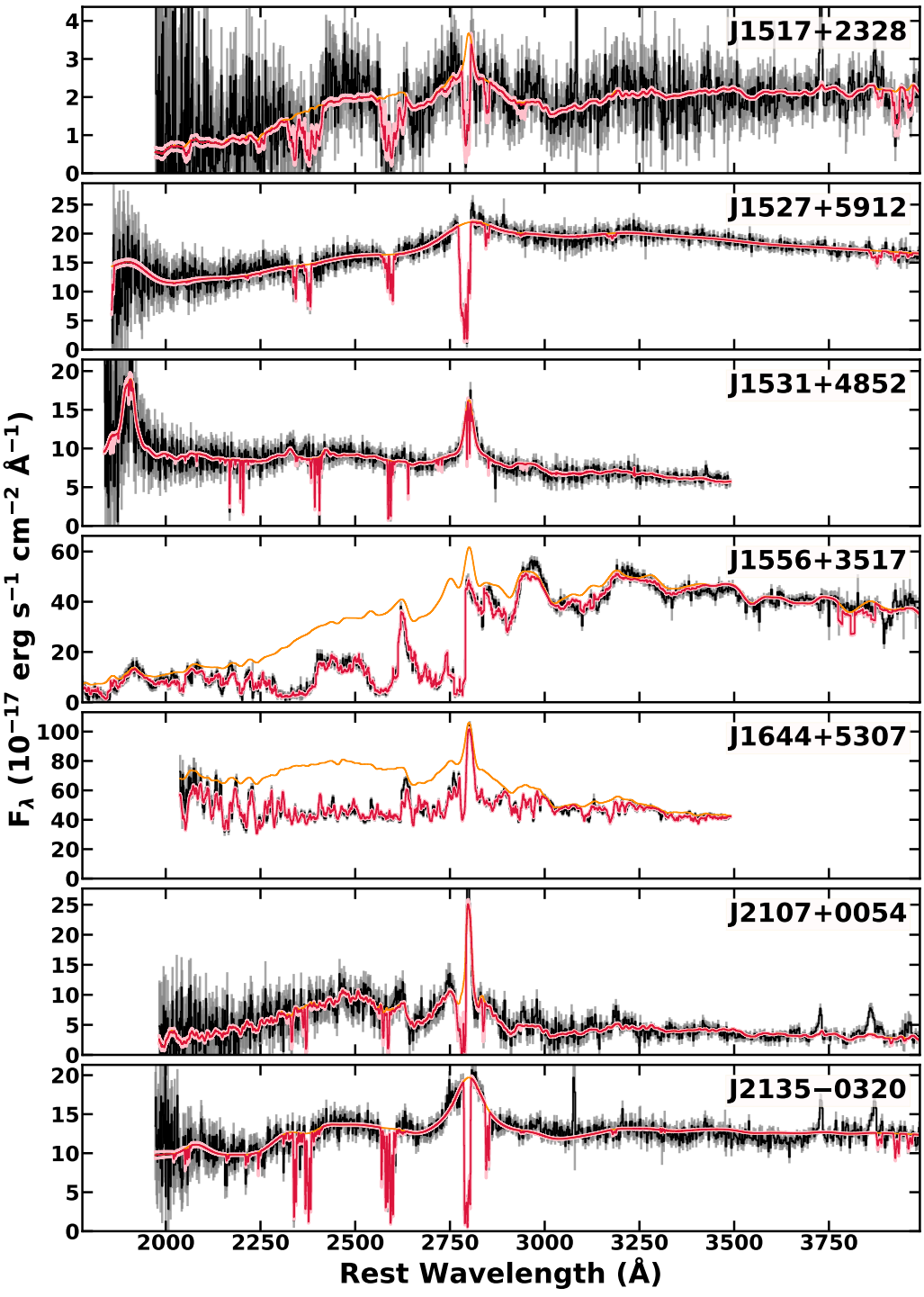

Figure 5.1: (Continued).

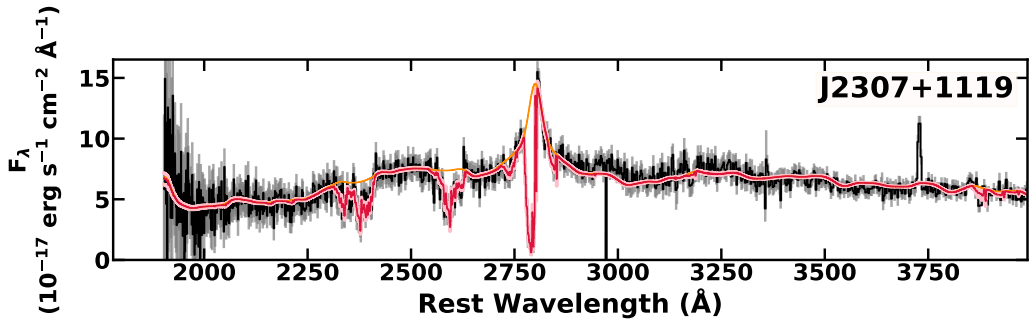

Figure 5.1: (Continued).

of the objects with the accordion tophat models were well fit with a single set of tophat bins with a single ionization parameter and density. Nonetheless, *SimBAL* model fits of some objects revealed a subset of bins that showed significantly different physical properties (e.g., ionization parameter and density). For those objects, we divided the tophat bins into two or three groups with a single ionization parameter and density for all bins in each group. In some objects a Gaussian profile was used for the lower-velocity components: SDSS J0258−0028, SDSS J1125+0029, and SDSS J1448+4043 (Figure 5.11).

5.5.1.1. *SimBAL* Models with Modified Partial Covering

Six objects in the sample required *SimBAL* models with the modified partial covering scheme. The best-fitting models for SDSS J1128+0113, SDSS J1145+1100, and SDSS J1321+5617 included unabsorbed emission line components and SDSS J1019+0225, SDSS J1125+0029, and SDSS J1644+5307 required a fraction of continuum emission to be unabsorbed by BALs (Figure 5.2). Five out of 6 objects are further classified as "loitering outflow objects" (§ 5.5.1.3; 5.6.5).

In the extreme cases of non-zero flux at the bottoms of the troughs in the spectra of SDSS J1019+0225, SDSS J1125+0029, and SDSS J1644+5307, an unabsorbed line-emission component alone was not sufficient to model the spectral features, and unabsorbed flux from the continuum emission was necessary to obtain the best-fitting spectral models. We modified the spectral model for these objects in two ways to account for the large

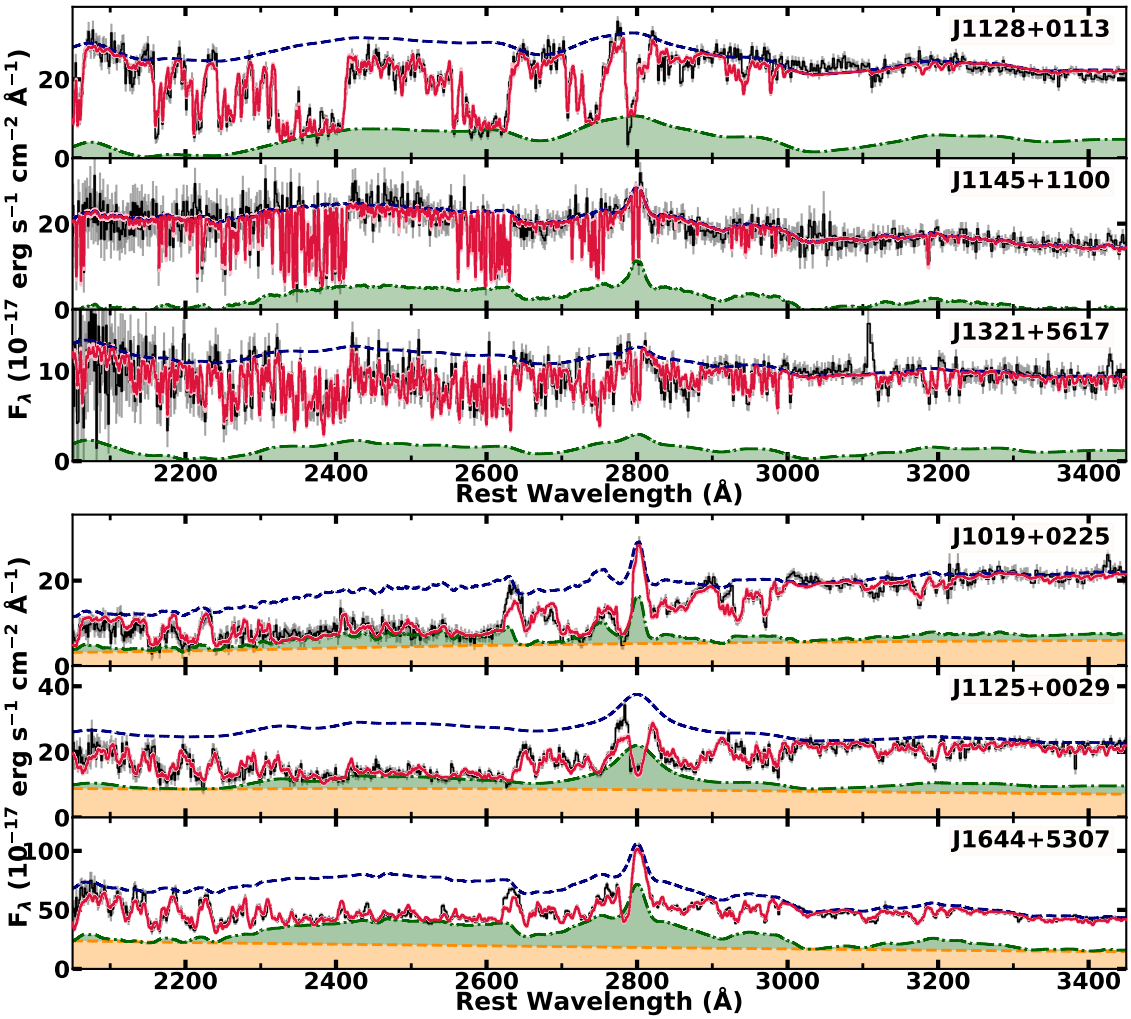

Figure 5.2: The best-fitting *SimBAL* models for six objects modeled using the modified partial covering scheme. The best-fitting models and the unabsorbed continuum emission models are shown in red solid lines and blue dashed lines, respectively. *Top*: The FeLoBAL gas does not absorb the emission lines (green shaded-region). *Bottom*: The FeLoBAL gas does not absorb both emission lines and a fraction of the continuum emission (green and orange shaded-regions). The power-law partial covering ($\log a$) used in *SimBAL* alone could not model the heavy non-black saturation seen in these spectra.

amount of flux seen underneath the troughs. First, the line emission is not absorbed by the BAL, and second, only a fraction of power-law continuum emission is absorbed by BAL similar to the homogeneous step-function partial covering (e.g., $I = C_f e^{-\tau} + (1 - C_f)$, C_f =covering fraction; Arav et al., 2005). The absorbed part still requires the power-law opacity ($\log a$) to model the significant contribution of weak absorption lines. In other words, the BAL winds in these objects have both inhomogenous partial covering presumably originating from the complex cloud structures within the BAL gas (e.g., de Kool et al., 2002c; Leighly et al., 2019b) and the homogeneous partial covering that originates from the BAL gas absorbing only a fraction of continuum and none of the line emission from the central engine. With this model setup, we were able to create the overlapping trough features with blended saturated absorption lines and still have a significant amount of flux underneath the troughs. From the three objects we obtained $C_f \sim 0.65 - 0.71$.

We note that the lower-velocity components in the spectral models for SDSS J1125+0029 and SDSS J1644+5307 were allowed to freely absorb both the continuum and line emission in a standard fashion unlike the higher-velocity components as described above. That is because the lower-velocity components in these objects are presumed physically separate from the main higher-velocity component and are located at larger distances from the accretion disk and the broad line region (BLR). This allowed the lower-velocity components to fit deep Mg II absorption features seen in the spectra.

5.5.1.2. Absorption Lines in FeLoBAL Quasars

FeLoBAL quasars are known to show absorption lines from Fe II as well as various iron-peak elements, such as Cr II, Ni II, in the near-UV wavelengths from their high column density gas (e.g., de Kool et al., 2002b; Choi et al., 2020). Often these transitions are blended and thus isolation of individual line transitions is not possible in many cases, making it extremely challenging to analyze the FeLoBAL quasar spectra and to constrain the physical properties of the FeLoBAL absorbing gas. The forward modeling technique

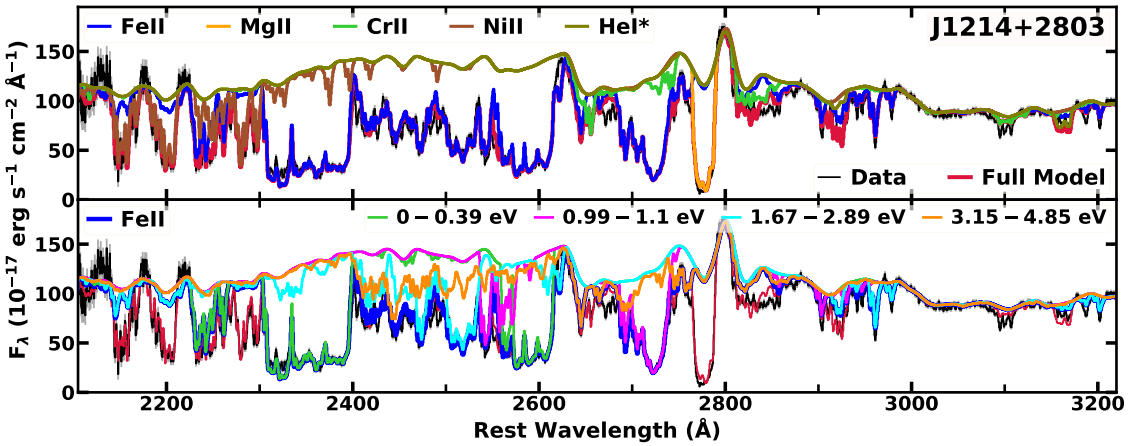

Figure 5.3: Anatomy of the near-UV spectrum of an FeLoBAL quasar. *SimBAL* models for SDSS J1214+2803 showing some of the principal line transitions observed in FeLoBAL troughs is plotted. *Top*: The best-fit model has been divided by the ionic species that are the major contributors of the opacity in the near-UV bandpass for FeLoBALs. *Bottom*: The Fe II model has been further broken up into 4 different models depending on the lower-level excitation energy.

used in *SimBAL* allows us not only to analyze heavily absorbed spectra with line blending features, but also to study the individual line transitions observed in the spectra using spectral synthesis.

Figure 5.3 highlights some of the major absorption lines observed in FeLoBALs with special *SimBAL* models generated using the best-fitting model parameters and user-defined line transition lists. We used SDSS J1214+2803 as an example because this object has a high-opacity BAL absorbing gas ($\log N_H - \log U \sim 23.4$ [cm^{-2}]). The FeLoBAL in this object showed most of the prominent absorption lines found in FeLoBAL quasars. The strength and/or the presence of (or the lack of) absorption lines from certain ionic species provide specific information about the physical conditions of the outflowing gas. The iron-peak elements are rare (e.g., [Ni/Fe]~ -1.2 for $Z = Z_\odot$) and therefore their absorption lines only appear when the column density is sufficiently high and these lines are often not saturated unlike Fe II or Mg II absorption lines. For example, the absorption feature near $\lambda \sim 2200$ Å from Ni II can be used as an excellent indicator of outflow column density. They suffer less line blending with Fe II absorption lines and produce

stronger absorption lines compared to other rare iron-peak elements, such as Cr II. This particular feature is not observed in FeLoBAL quasars with low column density BALs (e.g., SDSS J2307+1119, $\log N_H - \log U \sim 23.0$ [cm^{-2}] in Figure 5.1). In addition, absorption line from He I*λ3188, also noted in Figure 5.3, has been previously known as a column density and ionization diagnostic (Leighly et al., 2011). For FeLoBALs, the ionization parameter is directly related to the column density of the gas (§ 5.5.3; Figure 5.7), which means the overall amount of opacity observed in the troughs scales with ionization and this parameter is constrained by not just a subset of line transitions, but by an ensemble of absorption lines.

The bottom panel in Figure 5.3 shows the models of Fe II absorption lines that have been grouped by the lower-level excitation energy. Fe II has a large number of excited state levels and the plethora of absorption lines they produce can be used to constrain the density of the outflowing gas (e.g., Lucy et al., 2014; Choi et al., 2020). Most FeLoBAL quasars show excited state Fe II* absorption lines with lower-level excitation of $E_{lower-level} \sim 1$ eV in their spectra (e.g., SDSS J0840+3633). Most excited state Fe II transitions have critical densities $\log n \sim 4.5$ [cm^{-3}] or greater (e.g., Korista et al., 2008). If the density exceeds this value, then the BAL will show strong absorption lines from Fe II across various excited energy levels, including high-excitation levels ($E_{lower-level} \sim 5$ eV) especially when the density is high. For instance, SDSS J1214+2803 shown in the figure has a high density outflowing gas ($\log n \sim 7.8$ [cm^{-3}]) and we observe significant opacity from the Fe II* absorption lines form multiple excited levels. If an absorbing gas has low enough density and no Fe II in the excited states, then the FeLoBAL will mostly only show absorption features from the ground state Fe II (e.g., SDSS J0802+5513, $\log n \sim 4.4$ [cm^{-3}]). In some BALs with no excited state Fe II* absorption lines, we were only able to constrain density upper limits ($\log n \ll 2.8$ [cm^{-3}], column density grid limit). And thus, these BALs will have lower limits on their distance estimates from the central engines (see § 5.4.2). Also, high ionization can populate Fe II to excited states because the temperature is higher.

5.5.1.3. Classifications of FeLoBALs

In the figures throughout this chapter, we mark three special types of FeLoBALs identified in the sample: (1) Overlapping troughs, (2) Loitering BALs, and (3) Inflows. The overlapping trough identification was done based on the spectral morphology. If an object showed heavily blended Fe II absorption feature in the spectrum shortward of $\lambda \sim 2800$ Å, we then classified it as having overlapping trough features (e.g., SDSS J0300+0048 and SDSS J1154+0300). Second, based on the outflow properties obtained from *SimBAL* modeling, we classified "loitering BALs" by selecting BALs that have $\log R < 1$ [pc] and $|v_{off,\ \mathrm{FeII\ excited}}| < 2000$ km s^{-1} (offset velocities calculated from the excited-state Fe II*λ2757; § 5.4.3). Lastly, the inflows ($v_{off} > 0$ km s^{-1}) were classified based on the opacity weighted velocities (§ 5.4.2). We note that unlike loitering BAL or inflow classifications, the overlapping trough classification is solely based on empirical visual classification and not based on the physical and kinematic properties. Also, FeLoBALs can have multiple classifications. For instance, the majority of loitering BALs are also classified as overlapping troughs and inflows. Following the classification scheme we identify: 8 overlapping troughs, 11 loitering BALs, and 5 inflows. 41 out of 60 FeLoBALs do not belong in any of the three special classes and they can be considered typical outflowing FeLoBALs with moderate opacity. Detailed discussion on overlapping troughs and loitering BALs can be found in § 5.6.4 and § 5.6.5, respectively.

Following the theoretical predictions (e.g., Scannapieco & Oh, 2004; Di Matteo et al., 2005; Hopkins & Elvis, 2010), we identified energetic BALs as those that have outflow energy (L_{KE}) greater than 0.5% of the bolometric luminosity (L_{Bol}) of the quasar. Because some of the BAL outflows were constrained with lower limits on the distances of the BAL absorbers from the central engines, not all BALs in our sample have robust constraints on the outflow energy calculations. Therefore, among the energetic BALs that meet $L_{KE} > 0.005 L_{Bol}$ condition we only selected the ones with well constrained physical properties (e.g., $\log U$, $\log n$) as powerful BALs. They are represented in the figures with cyan (or pink) square outlines.

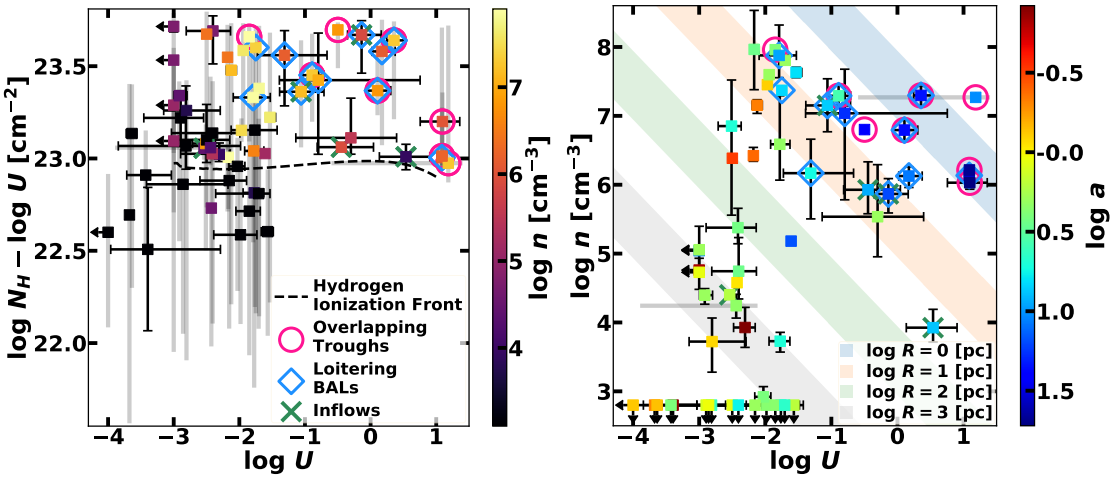

Figure 5.4: The FeLoBAL outflows in our sample show a wide range of physical properties including ionization parameter ($\log U$) and density ($\log n$). The grey shaded bars represent the range of values among the tophat model bins for each BAL. For Gaussian opacity profile models or when the tophat bins for a given BAL had a single ionization and/or density parameter, the 2σ (95.45%) uncertainties from the MCMC posterior distributions are plotted as error bars. Some of the special BALs are marked as follows: red circles for overlapping trough BALs (§ 5.6.4), blue diamonds for loitering BALs (§ 5.6.5), and green crosses for inflows. *Left panel*: The dashed line shows the location of the hydrogen ionization front as a function of ionization parameter. *Right panel*: The locations of the BAL gas from the central SMBH ($\log R$) are marked as shaded areas for reference. They were calculated assuming the typical ranges of photoionizing photon flux used in our sample of FeLoBAL quasars ($\log Q \sim 55.5 - 56.5$ [photons s^{-1}]).

5.5.2. Best-Fitting Parameters

5.5.2.1. Physical Gas Properties of the BALs

Figure 5.4 shows the distribution of $\log U$, $\log N_H - \log U$, and $\log n$ of the FeLoBALs in our sample. The FeLoBALs have a wide range of ionization parameter ($\log U \sim -4$ to 1.2) and density ($\log n \sim 2.8 - 8.0$ [cm^{-3}]); these values span our computational grid. Most of the BALs have column density parameter ($\log N_H - \log U$) high enough to encompass the hydrogen ionization front ($\log N_H - \log U \sim 23$ [cm^{-2}]). This high column density is expected for FeLoBALs because a column density thick enough to include the hydrogen ionization front is necessary to produce the observed Fe II absorption (e.g., Lucy et al., 2014). As shown in the left panel of Figure 5.4, we found no FeLoBALs with

$\log U > -1.5$ and $\log N_H - \log U < 22.9$ [cm^{-2}], because insignificant Fe II is produced in that region of parameter space.

Starting at lower $\log U$ FeLoBALs ($\log U \lesssim -2$), the outflows have lower density ($\log n \lesssim 5$ [cm^{-3}]) and some of them have column densities insufficient to breach the hydrogen ionization front ($\log N_H - \log U \lesssim 23$ [cm^{-2}]). The physical condition of the gas at low ionization parameter and density does not dramatically change across the hydrogen ionization front in the lower $\log U$ gas and thus the ionic column density of Fe II gradually increases across the ionization front. Therefore, BAL gas with lower $\log U$ can populate Fe II ions even at the slightly lower $\log N_H - \log U$ before the gas column density encompasses the hydrogen ionization front. Their spectra are least absorbed with no significant line blending or saturation and often the individual absorption lines can be easily identified. The opacity mainly comes from the ground state Fe II and Mg II with weak or no observable opacity from the excited state Fe II or other rare metal ions (e.g., SDSS J0835+4242, SDSS J1240+4443 in Figure 5.1). Although we were able to constrain the densities of most FeLoBALs, we assigned density upper limits for some of the low-$\log U$ FeLoBALs that showed no absorption lines from the excited-state Fe II.

Most of our FeLoBALs have a moderate ionization parameter of $\log U \sim -2$. These medium-$\log U$ FeLoBALs have the widest range of densities, spanning the entire range we found in our sample ($2.8 \lesssim \log n \lesssim 8.0$ [cm^{-3}]). These FeLoBALs have the spectral morphology of "typical" FeLoBALs with strong absorption lines from Mg II and ground state Fe II as well as excited state Fe II and other iron-peak elements depending on the gas density and column density (e.g., SDSS J0840+3633, SDSS J1214+2803 in Figure 5.1). Moreover, standard BAL spectral features (e.g., non-black saturation, line blending) can be easily found in their spectra. Most of the previously well-studied FeLoBALs belong to moderate-$\log U$ FeLoBALs (e.g., QSO2359−1241, Arav et al. 2001; FIRST J104459.6+365605, de Kool et al. 2001; FBQS 0840+3633, de Kool et al. 2002a; FIRST J121442.3+280329, de Kool et al. 2002b).

We discovered a number of FeLoBALs with high ionization parameter ($\log U \gtrsim -1$;

e.g., SDSS J0158−0046, SDSS J1154+0300 in Figure 5.1), which were responsible for the large range of ionization parameter we found in our FeLoBAL sample. High ionization FeLoBALs have higher column density gas that includes a significantly larger number of excited state ions compared with the low $\log U$ FeLoBALs. Most of the FeLoBALs with high ionization parameter also have special classifications, due to their spectral morphology and physical properties (e.g., overlapping troughs, loitering BALs; § 5.5.1.3). These high opacity FeLoBALs (e.g., overlapping trough BALs) have not been previously analyzed in detail due to the difficulty in analyzing FeLoBAL quasars with the extreme absorption features that are often seen in these objects.

The FeLoBALs with higher $\log U$ also have higher $\log n$ and larger $\log a$ (less covering; Figure 5.4). The absence of FeLoBALs with high ionization and low density can be explained by the geometrical constraints expected from the outflows. The physical thickness of outflowing gas ($\Delta R \sim U/n$, for a fixed $\log N_H - \log U$) cannot be greater than the distance of the gas from the central engine ($\log R$). The overlapping trough BALs and loitering BALs (marked with red circles and blue diamonds, respectively) have both higher $\log U$ and $\log n$ compared to the rest of the BALs. The trend between $\log U$ and $\log a$ might be as a selection effect. In high-$\log U$ outflows, the large amount of opacity from larger number of excited state ions and rare metal ions would heavily absorb the quasar spectrum. Therefore, unless the covering fraction is low (high $\log a$), FeLoBALs with high $\log U$ can not be detected easily.

5.5.2.2. Kinematic properties of the BALs

Figure 5.5 shows how the kinematics of the outflow (e.g., outflow velocity and width) compare with the physical properties of the gas (i.e., $\log U$, $\log n$, and $\log N_H - \log U$). Of the 60 BALs in our sample, we found 5 BALs with positive offset velocities (SDSS J0158−0046, SDSS J0802+5513, SDSS J0916+4534, SDSS J0918+5833, and the second BAL component in SDSS J1125+0029). We have robust redshift measurements for theses objects from the narrow emission lines of [O II], narrow Hβ component, or

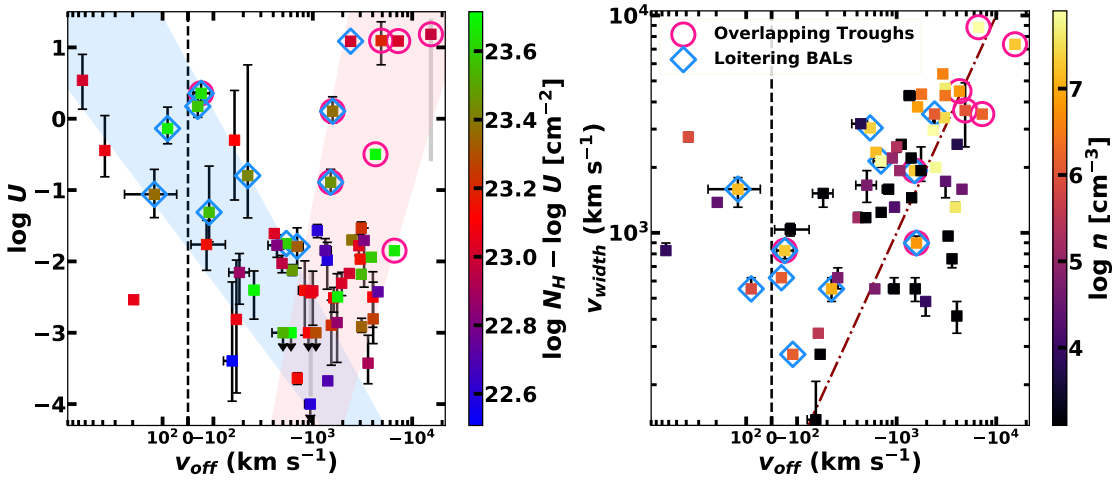

Figure 5.5: *Left panel*: We found no strong correlations between the offset velocities and the physical properties of the BAL gas ($\log U$ and $\log N_H - \log U$) for the whole FeLoBAL sample. Instead, there is a 'v' shape with high $\log U$ BALs present at the lowest and highest velocities (red and blue shades). *Right panel*: The widths of the BALs scale with the velocity offsets. The distribution roughly follows a one-to-one ratio (brown dotted-dashed line) which indicates that the most of FeLoBAL outflows are not detached from the emission line at rest. A linear scale was used in the region $|v_{off}| < 100$ km s^{-1} and log scale was used elsewhere in the x-axis. Markers and error bars as in Figure 5.4.

high-ionization [Ne V] line. The offset velocity of the FeLoBALs does not seem to be correlated with either $\log U$ or $\log N_H - \log U$, and for a given outflow velocity we found a wide range of physical properties. However, we found that the FeLoBALs with the highest velocities have higher ionization parameters, but the converse is not true. The subtle v-shaped distribution seen between v_{off} and $\log U$ potentially suggests that there may be more than a single population within FeLoBAL quasars; this topic as well as the analysis of the relationship between quasar properties (e.g., Eddington ratio) and outflow (kinematic) properties are explored further using the Hβ / [O III] properties in Choi et al. (2022b). We discuss the potential acceleration mechanisms for the FeLoBAL outflows in § 5.7.3.

The distribution of the widths and the velocities of the outflows shows a nearly one-to-one relationship (the right panel in Figure 5.5). This suggests that most of the outflows in our sample have widths similar to the offset velocities; the outflows are not detached but rather they start from near rest (~ 0 km s^{-1}). Our result is consistent with what has been seen in composite spectra of BAL quasars that showed troughs beginning from near the peaks of the emission lines (Hamann et al., 2019a; Rankine et al., 2020). The outflows with the higher velocities have proportionately larger widths and tend to have higher density compared to other outflows in our sample, although there are also FeLoBALs with low velocity and high density. Most of the overlapping trough BALs (red circles in Figure 5.5) have the highest outflow velocities with large widths as well as high density.

5.5.3. Derived Physical Properties of the Outflows

The large range in ionization parameter and density observed means that the outflows are located throughout the quasar, ranging from near the torus at $\log R \sim 0$ [pc] to the host galaxy $\log R \sim 3$ [pc]. We recovered an inverse relationship between $\log R$ and the two gas parameters $\log U$ and $\log n$ that can be explained with the definition of $\log U$ ($U \propto 1/nR^2$). Given the range of the total number of photoionizing photons per second (Q) from the active galactic nucleus (AGN) for the objects in our sample and the range of densities

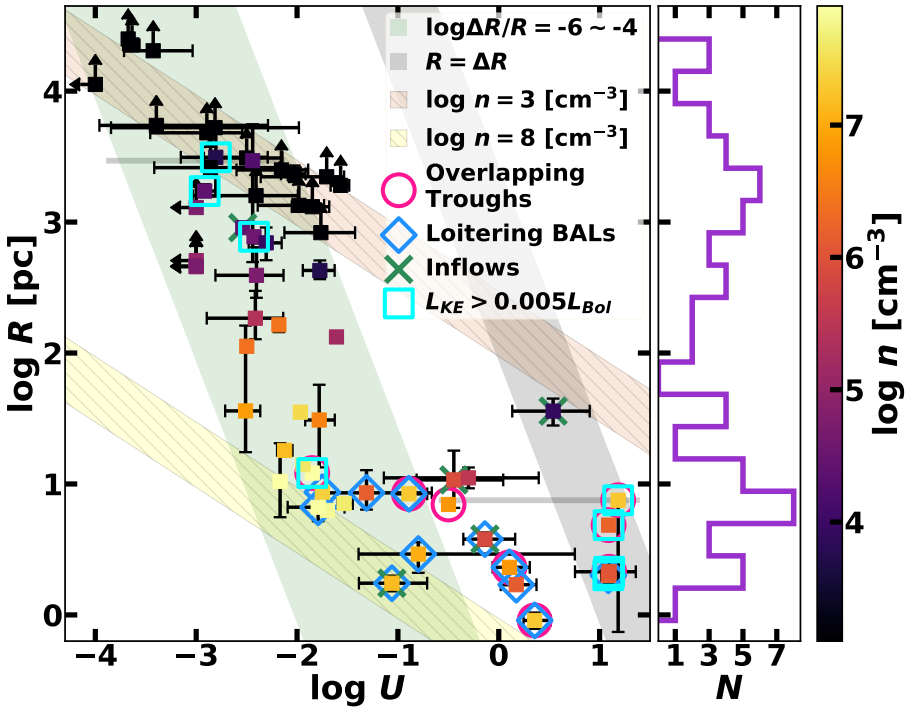

Figure 5.6: The BALs have a wide range of distances from the central engine, ranging from a torus-scale (∼pc) to a host galaxy scale (∼kpc). The cyan squares mark the powerful outflows that have well-constrained physical parameters ($\log U$ and $\log n$) and kinetic luminosity (L_{KE}) greater than 0.5% of the bolometric luminosity of the quasar (L_{Bol}). The powerful outflows are located in a various distances from the central black hole and they have a variety of physical properties. The histogram on the y-axis shows the distribution of $\log R$ in our sample. There is a lack of FeLoBALs near $\log R \sim 2$ [pc] (§ 5.7.1). A range of BAL cloud volume filling factors (or normalized radial widths, $\log \Delta R/R$) and two $\log n$ values are marked as shaded areas for reference. Markers and error bars as in Figure 5.4.

we have for the BAL clouds, we can identify a region in the $\log R - \log U$ parameter space where we expect the BALs to be located. If the values of $\log U$ and $\log n$ were distributed evenly for our sample of FeLoBALs, we would find them evenly distributed in the area between the two dashed-shaded strips for $\log n = 3$ and 8 [cm^{-3}] in the Figure 5.6 (calculated assuming $\log N_H - \log U = 23 \sim 23.5$ [cm^{-2}] and $\log Q \sim 55.5 - 56.5$ [photons s^{-1}]); it is clear they are not. Instead of a uniform distribution we find that high $\log U$ outflows have higher $\log n$ and the outflows with lower $\log n$ tend to have lower $\log U$ as well. This behavior is found because most of our FeLoBALs have a small range of volume filling factors (or normalized radial widths, $\log \Delta R/R \sim -5$; $\log \Delta R = \{\log U + (\log N_H - \log U)\} - \log n$) except for the compact BALs that are located $\log R \lesssim 1$ [pc] which have large volume filling factors ($\log \Delta R/R \gtrsim -3$). We discuss this point and other geometrical constraints in § 5.7.2 and Paper III (Choi et al., 2022b).

We found mass outflow rates of $\dot{M}_{out} = 0.049 \sim 520\ \mathrm{M}_\odot\ \mathrm{yr}^{-1}$. The mass outflow rates span more than four orders of magnitude which reflects the wide range of v_{off} we found in our FeLoBAL outflows. We also report mass inflow rates of $\dot{M}_{in} = 0.016 \sim 55\ \mathrm{M}_\odot\ \mathrm{yr}^{-1}$ from the 5 BALs with $v_{off} > 0\ \mathrm{km\ s}^{-1}$. For a couple of BAL components with $v_{off} \sim 0\ \mathrm{km\ s}^{-1}$ that were modeled using tophats, we calculated both the mass outflow and inflow rates depending on the velocities of the bins. Except for SDSS J1125+0029 in which there is an additional outflowing BAL, SDSS J0158−0046, SDSS J0802+5513, SDSS J0916+4534, and SDSS J0918+5833 only showed inflow BALs and did not have other outflowing BALs in the spectra. These inflow BALs are mostly located within $\log R < 2$ [pc] (one at $\log R \sim 3$ [pc]) and have low offset velocities ($v_{off} \lesssim 600\ \mathrm{km\ s}^{-1}$). We note that there is a caveat that mass outflow rates are dependent on the assumed global covering fraction (Ω) of (FeLo)BALs. We used $\Omega = 0.2$ in this work (§ 5.4.2), and detailed discussion on global covering fraction for FeLoBALs can be found in Choi et al. (2020) and Chapter 4 (§ 4.5).

Figure 5.7 shows that the higher $\log U$ outflows have higher partial-covering-corrected

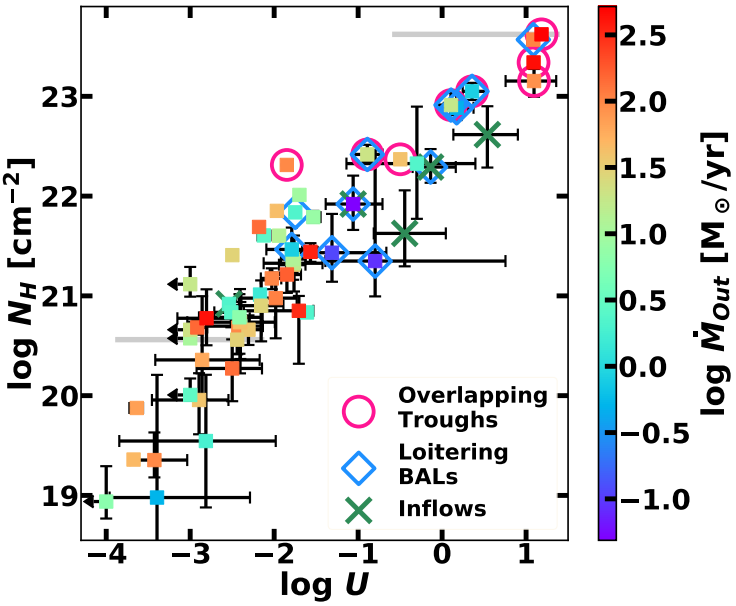

Figure 5.7: The BALs with high $\log U$ have larger covering-fraction-corrected hydrogen column densities. The strong correlation between the two parameters is expected for FeLoBALs that require the gas column densities to be high enough to reach the hydrogen ionization front ($\log N_H - \log U \sim 23$ [cm^{-2}]). Markers and error bars as in Figure 5.4.

column density. The correlation may be an artifact of sample selection because the column density of the outflowing gas needs to be high enough to reach the hydrogen ionization front for the FeLoBALs ($\log N_H - \log U \gtrsim 23.0$ [cm^{-2}], left panel in Figure 5.4; § 5.5.2.1). Moreover, we see a relatively small dynamic range of about 1 dex across $\log N_H - \log U$ whereas $\log U$ ranges from ~ -4 to ~ 1.5. From the distributions of the parameters alone we can expect $\log N_H$ is highly dependent on $\log U$ so that the gas with higher $\log U$ also has higher $\log N_H$.

The mass outflow rate ($\dot{M}$) does not seem to be strongly correlated with either ionization parameter or partial-covering-corrected column density. Outflows with high mass outflow rates ($\dot{M}_{out} \sim 100$ M$_\odot$yr^{-1}) were found across the entire $\log N_H$ and $\log U$ range. This is because the magnitude of the mass outflow rate is mainly determined by the outflow velocity rather than the location or the physical properties of the gas (§ 5.6.1).

We found a strong correlation between the outflow strength and the outflow velocity

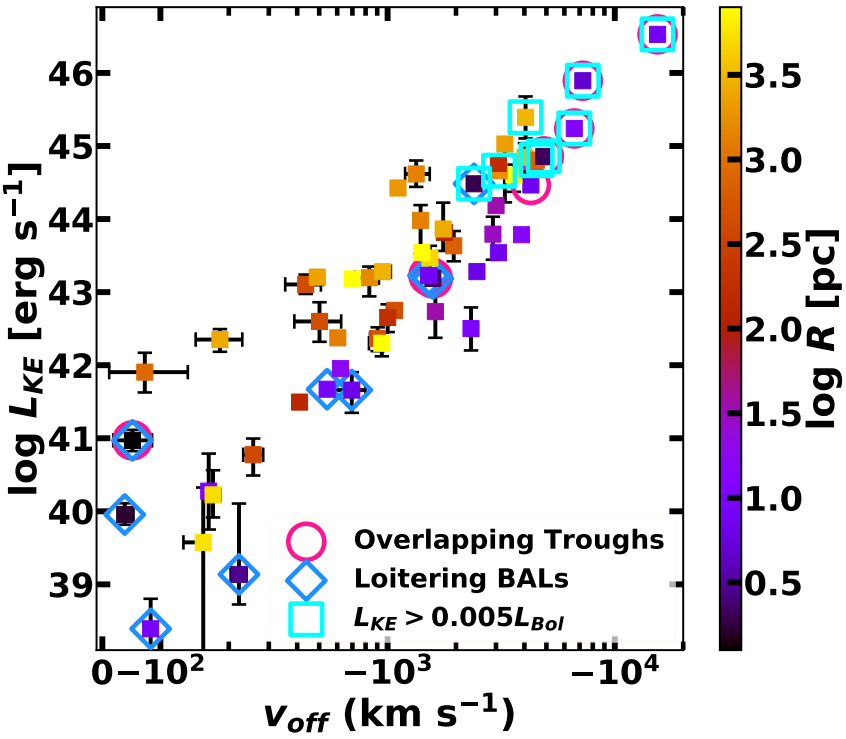

Figure 5.8: The kinetic luminosities (L_{KE}) of the FeLoBAL outflows scale with the outflow velocities with the slope of ~ 3. This relationship is expected from the definition of L_{KE}. The scatter in the L_{KE} direction can be mainly ascribed to the range of mass outflow rate ($\dot{M}$) of the outflows as well as gas physical conditions such as covering-fraction-corrected hydrogen column densities. The colors of the markers represent the locations of the outflows ($\log R$). For an FeLoBAL outflow at a given outflow velocity, a larger $\log R$ will yield larger $\dot{M}$ and greater L_{KE}. We did not find any particular trend with $\log R$ and the properties plotted in the figure; however, the outflows with the highest velocities in our sample were all found to be within the vicinity of torus $\log R \lesssim 1$ [pc]. The 5 BALs with inflows are not plotted.

(Figure 5.8). Considering that $\dot{M} \propto v$, L_{KE} of an outflow is proportional to v^3 , which explains the tight correlation between L_{KE} and v_{off} observed in our sample of FeLoBALs. All the outflows with the highest outflow velocities (8 out of 55 FeLoBALs with $v_{off} \lesssim -2,400$ km s^{-1}) in our sample have enough energy to produce quasar feedback (§ 5.7.5). While many of these powerful outflows with high velocities are located near the vicinity of torus $\log R \leq 1$ [pc], we did not find robust evidence suggesting a connection between $\log R$ and L_{KE} (§ 5.6.1). This lack of correlations suggests that the outflow strength or the outflow's role in quasar feedback is mainly determined by the outflow velocity and the physical properties of the gas. In other words, where the outflows are located at present does not have significant influence on the inferred energetics of the outflow.

5.6. Analysis of the Full Sample

5.6.1. Correlations

In order to systematically study the relationship between the physical and kinematic properties of FeLoBALs and the derived wind properties, we calculated the Kendall rank correlation coefficients for all pairs of the measured quantities and examined the ones that showed significant correlations ($p < 0.01$). Because we have BALs with upper or lower limits of $\log n$ or $\log U$, we used `pymccorrelation` by Privon et al. (2020)[3] which provides a python implementation of Kendall's tau rank correlation coefficient calculator for censored data (Isobe et al., 1986). Only the values from the BALs from the outflowing gas ($v_{off} < 0$ km s^{-1}) were used for correlation analysis with outflow properties ($\dot{M}_{out}$, L_{KE}). The results are shown in Figure 5.9.

5.6.1.1. Outflow Physical Properties

Among the fit parameters that were directly constrained from the models, we found correlations between $\log n$ and $\log U$ and $\log N_H - \log U$ for gas physical properties, and between v_{off} and v_{width} for gas dynamical parameters. The correlations with $\log n$ suggest that for the FeLoBALs in our sample, the gas with higher density also tends to be more

[3]https://github.com/privong/pymccorrelation/

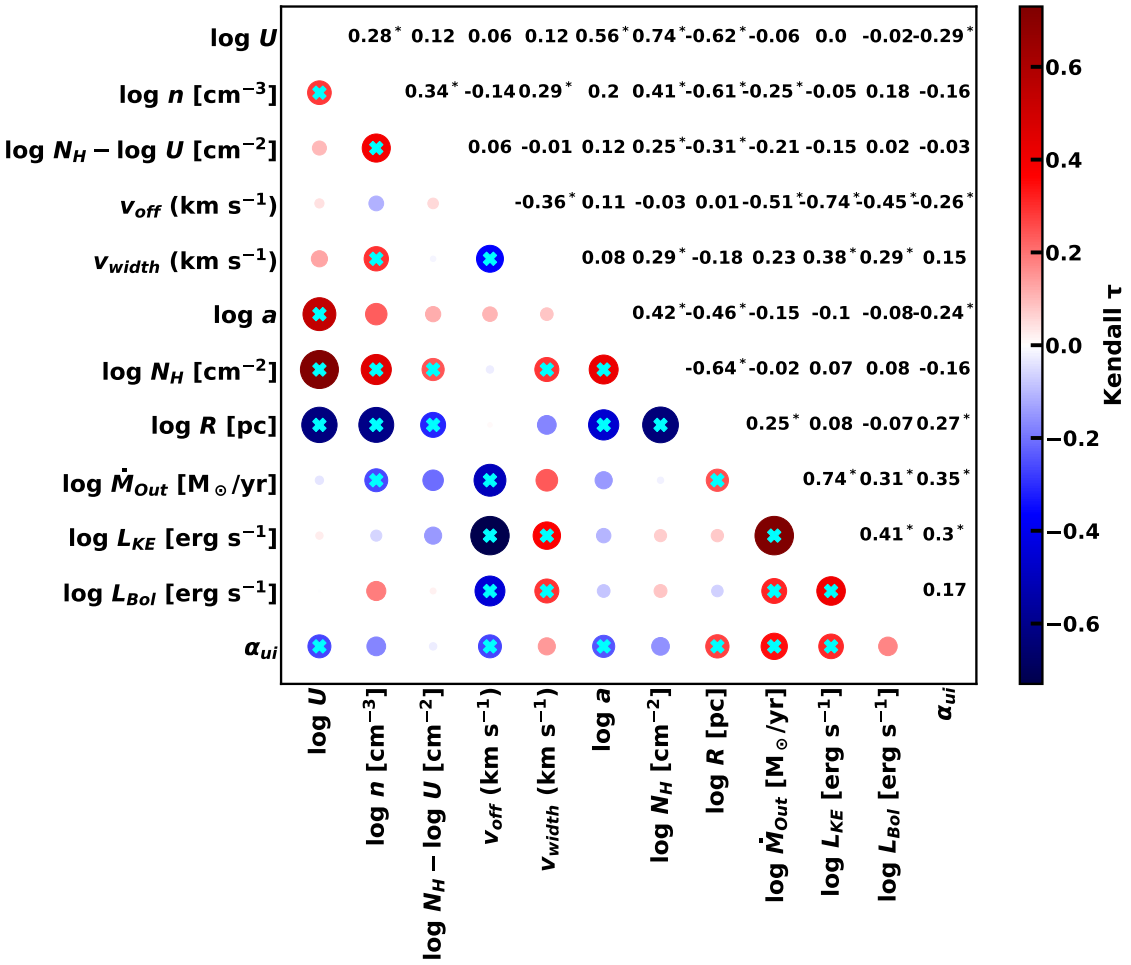

Figure 5.9: The correlation coefficients calculated for all measured BAL property pairs. The size and the color of the markers reflect the values of Kendall's rank correlation coefficient. The values with asterisks and cyan crosses represent the pairs that showed statistically significant correlations ($p < 0.01$). The first six parameters ($\log U$, $\log n$, $\log N_H - \log U$, v_{off}, v_{width}, and $\log a$) are the best-fitting model parameters from *SimBAL* and the rest are the derived properties calculated from the model parameters.

highly ionized and thicker with a higher column density. The covering fraction parameter $\log a$ was also highly correlated with $\log U$. The correlations between $\log U$, $\log n$, and $\log a$ were seen on the right panel of Figure 5.4 where the BALs with higher $\log U$ were found to be denser with lower partial covering (higher $\log n$ and $\log a$). As we discussed in § 5.5.2, the correlation between the partial covering parameter $\log a$ and the ionization parameter maybe due to a selection effect: FeLoBALs with high $\log U$ and low $\log a$ (large covering) are unlikely to be detected due to heavy absorption. We only observe high $\log U$ outflows that have high $\log a$ (i.e., not completely covered).

While we also found that $\log U$ shows correlations with both $\log R$ and $\log N_H$, we interpret these correlations mainly arising from a selection effect (§ 5.5.3). $\log R$ is calculated using the definition of $\log U$: $R \propto (Q/nU)^{1/2}$ (§ 5.4.2). The range of number of photoionizing photons per second emitted from the AGN, Q, in this sample only spans about a dex for the FeLoBAL quasars, and therefore we can expect $\log R$ to be negatively correlated with both $\log U$ and $\log n$, as found. Similarly, the correlation we observe between $\log U$ and $\log N_H$ (partial-covering-corrected column density) is expected for a FeLoBAL sample because FeLoBALs require the outflow gas to be thick enough to reach the hydrogen ionization front $\log N_H - \log U \sim 23.0$ [cm^{-2}] (§ 5.5.3).

A negative correlation between velocity offset and velocity width is seen in the right panel of Figure 5.5 (as well as with the correlation coefficient). The FeLoBAL outflows in our sample show a near one-to-one correlation between the two velocity parameters, which indicates that FeLoBAL features are seldom seen as detached troughs; the absorption starts from rest. We can also see from the p-value and the correlation coefficient that there is a weak positive correlation between $\log n$ and v_{width} but not with v_{off}. Although the statistical test suggests that there exists a correlation between these parameters in our sample of low redshift FeLoBAL quasars, we cannot confidently conclude whether they represent a true global trend in the parameter space. We will need to analyze a larger homogeneous sample of FeLoBAL quasars in order to substantiate this result.

The parameters that measure the strength of the outflow ($\dot{M}_{out}$, L_{KE}) showed strong

correlations with BAL velocity offset. As discussed in § 5.5.2, it is expected that $\dot{M}_{out}$ and L_{KE} should be strongly dependent on v_{off}. The correlation analysis from our FeLoBALs further supports the relationship between the two properties and also suggests that the dependence of $\dot{M}_{out}$ and L_{KE} on the dynamics of the gas (v_{off}) is so strong that physical properties of the gas (e.g., $\log U$, $\log N_H - \log U$) do not significantly influence the energetics of the BAL outflow or the outflow's potential impact on the host galaxy. We did not observe any significant correlations between L_{KE} and other parameters used to calculate this value ($\log R$ or $\log N_H$), again emphasizing its strong dependence on velocity above all other parameters (Figure 5.8).

5.6.1.2. Quasar Properties

In addition to the BAL properties, we also investigated potential connections between the outflows and the properties of the quasars. The quasar properties (e.g., L_{Bol}) were measured using the observation data and *SimBAL* modeling (§ 5.4.1)

We found a strong positive correlation between the velocity offset and the bolometric luminosity of the quasar (L_{Bol}). Our result is consistent with previous studies that found that quasars with higher L_{Bol} have outflows with higher velocities (e.g., Laor & Brandt, 2002; Ganguly et al., 2007; Fiore et al., 2017). The outflow velocity is expected to depend on the bolometric luminosity normalized by the Eddington value (L_{Bol}/L_{Edd}) for radiatively driven quasar winds. We explore this correlation in Paper III (Choi et al., 2022b) using the objects that have black hole mass measurements from the rest-optical emission-lines (Leighly et al., 2022). Because the velocity offset determines the strength of the outflow, we found a positive correlation between L_{Bol} and L_{KE}; more luminous quasars tend to have faster and more energetic outflows.

We found that α_{ui} is strongly correlated with $\log R$ and $v_{outflow}$ (v_{off}). Quasars with flatter SEDs ($\alpha_{ui} \gtrsim -0.5$) have redder colors and have faster and thus more powerful outflows. The quasars with steeper or bluer SEDs ($\alpha_{ui} \lesssim -0.5$) have FeLoBALs that are located closer to the central engine (smaller $\log R$) that are more ionized (higher $\log U$)

and they tend to have smaller outflow velocities. Most of these compact, low-velocity FeLoBALs are the loitering BALs (§ 5.6.5) that do not show properties expected for typical quasar-driven winds. We further discuss the properties of these FeLoBALs in § 5.6.5.

Our result seems somewhat similar with what have been found in extremely red quasars (ERQs). These objects show a higher incidence of outflow signatures in [O III]$\lambda\lambda 4959, 5007$ emission lines than typical blue quasars and a correlation between the outflow speeds and the redness of the SED has been found (Hamann et al., 2017; Perrotta et al., 2019). We note, however, that the FeLoBAL quasars in our sample are not ERQs and the quasar winds seen in emission lines can exhibit different properties than the BAL winds. We discuss the implications of the SED color on the acceleration mechanism of the BAL outflows in § 5.7.3.

In summary, the only physically significant correlations that we found from the FeLoBAL and quasar properties were between L_{Bol} and v_{off}, which propagates because of the functional dependence to $\dot{M}_{out}$ and L_{KE}. We also found correlations with α_{ui} where FeLoBALs found in objects with flatter (redder) spectral slope have larger $\log R$ and L_{KE}.

5.6.2. Objects with multiple FeLoBAL outflows

We identified more than one outflow component in 9 objects (excluding the broad Mg II component in SDSS J1214−0001 and the extra component in SDSS J1644−5307 only seen in Mg II; see § 5.5.1 and Appendix 5.B). While three of the nine objects showed several troughs distinctly separated by velocity, the others required a rigorous modelling with *SimBAL* to identify multiple outflows in blended troughs.

Figure 5.10 and Figure 5.11 show the two groups of objects with more than one BAL component. The three objects in the first group have more than one narrow Mg II trough that are separated by velocity (e.g., SDSS J1044+3656 in Figure 5.10). In these objects the differences in gas physical parameters were not extreme and the estimated distances for the BALs only differ by a moderate amount (Figure 5.12). In the second group (Figure 5.11), the features are blended. *SimBAL* analysis identified multiple components

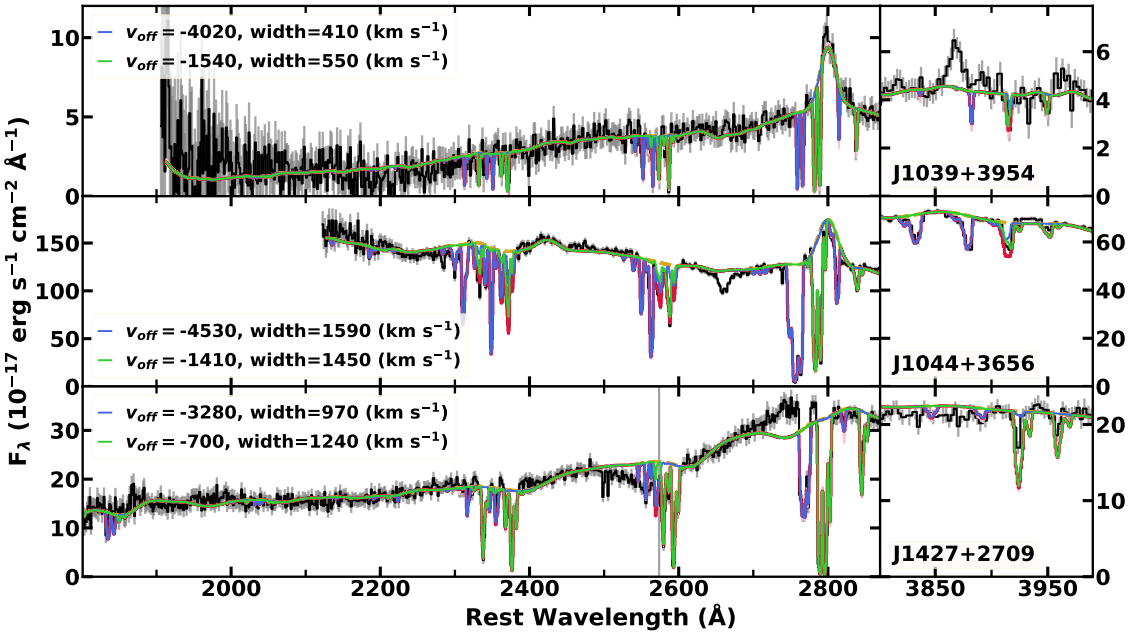

Figure 5.10: Objects that show multiple outflows where each BAL component (indicated with blue and green model curves) is clearly separated (Mg II$\lambda\lambda 2796, 2803$ troughs are not blended, left column). The data (error) is plotted in black (grey) and the best-fitting model is shown in red with the BAL components are over-plotted in green and blue. The column on the right shows the wavelength region where He I*$\lambda 3188$, Ca II H$\lambda 3968$ and K$\lambda 3393$ absorption lines are found. Note the BALs in these objects have low ionization and no He I* absorption-lines are observed.

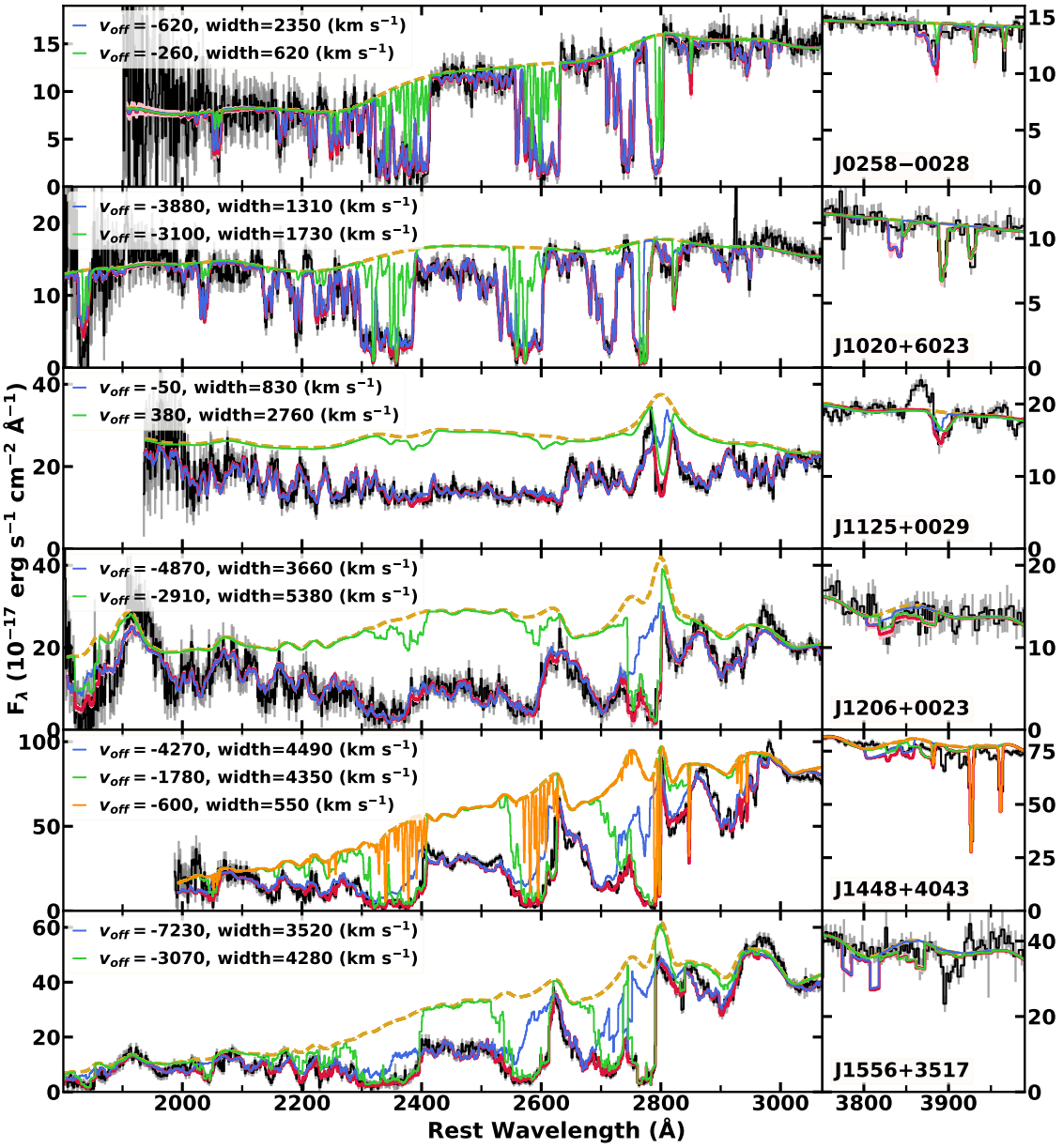

Figure 5.11: Objects that have multiple blended BAL components. The differences in gas physical properties can be observed most clearly with Ca II H and K lines where these absorption lines are only found the lower-velocity components with lower $\log U$ and $\log n$ (right column). For example, we found three BAL components in SDSS J1448+4043 with the lowest-velocity component showing deep Mg I absorption line as well as Ca II H and K absorption lines (plotted in orange). The data (error) is plotted in black (grey) and the best-fitting model is shown in red with the BAL components are over-plotted in green and blue with the continuum plotted in dashed tan lines.

and large differences in the gas properties, especially $\log U$, were found (Figure 5.12). The difference in $\log U$ resulted in large differences in $\log R$. The BAL components with higher $\log U$ include a plethora of absorption line transitions including the rare transitions from the excited state ions, but due to the large $\log a$ (low covering fraction) the depth of these troughs is small. These particular components played a critical role in creating the overlapping trough features because they provided excited state Fe II transitions around ~ 2500Å (i.e., between the ground-state multiplet features near ~ 2400Å and ~ 2600Å) as well as the absorption lines observed longward of ~ 2800Å (§ 5.6.4; see also Lucy et al., 2014).

The higher-velocity components in the multiple-outflow objects have higher $\log U$ and lower covering fraction compared with the lower-velocity component
(e.g., SDSS J1020+6023 in Figure 5.11; Figure 5.12). They produced opacity from both the excited-state and the ground-state Fe II transitions. In contrast, the lower-velocity components produced higher opacity overall from the ground-state Fe II and Mg II only and were responsible for the most of the strong Mg II absorption features observed in the spectra. Choi et al. (2020) and Leighly et al. (2018) both observed a similar trend where they found higher ionization parameter and lower covering fraction for the tophat bins with higher velocities in the best-fitting *SimBAL* models. The distinct gas properties constrain the location to different radii: the higher-velocity component is found much closer to the SMBHs than the lower-velocity component in a given object.

The FeLoBAL quasars with multiple blended components show some of the most extreme spectral features, such as overlapping troughs (e.g., SDSS J1556+3517 in Figure 5.11). However, the BAL component decomposition revealed that the lower-velocity components in these objects actually resemble a typical FeLoBAL. In other words, without the higher-velocity components these FeLoBAL quasars would show spectra that are indistinguishable from those of moderately absorbed FeLoBAL quasars with low to moderate ionization parameter (§ 5.5.2.1). Because of the difference in location we expect the dynamic time scales between the higher-velocity components and the lower-velocity com-

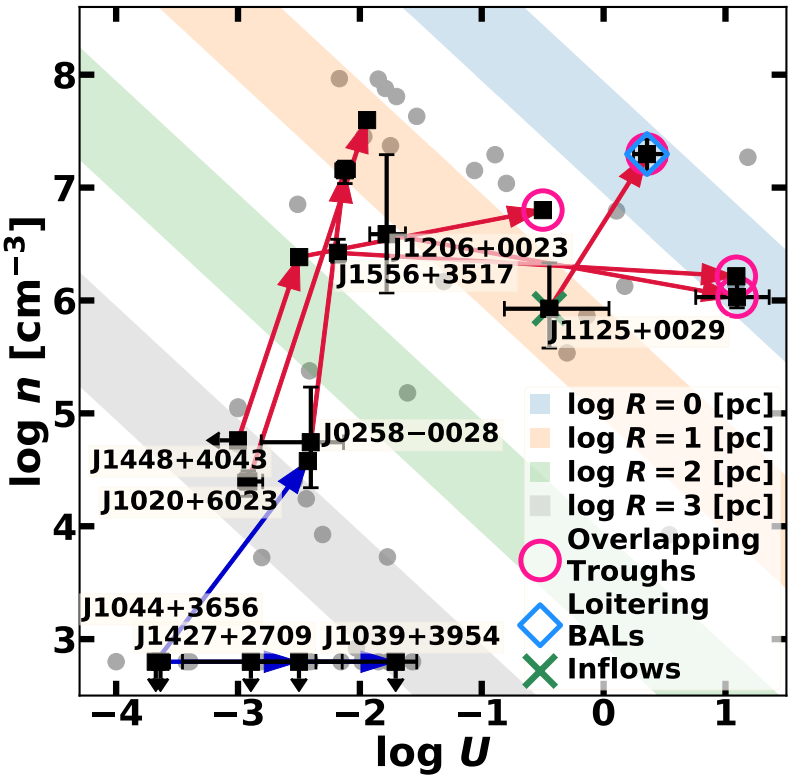

Figure 5.12: The outflows from the objects that have more than one FeLoBAL feature are plotted with squares and the rest of the outflows shown by grey dots. The arrows start from the lower-velocity component and end at the higher-velocity component in the same object. Blue and red arrows (labelled by object) represent objects shown in Figure 5.10 and 5.11, respectively. The shaded diagonal bars for $\log R$ were calculated using the typical range of photoionizing photon flux found in our sample of FeLoBAL quasars ($\log Q \sim 55.5 - 56.5$ [photons s^{-1}]). All of the higher-velocity components have higher ionization parameter and the majority of them have higher density compared to the lower-velocity components in the same object. Thus the higher-velocity components are located closer to the central black hole. Four of the higher-velocity components with significantly higher $\log U$ are overlapping trough BALs. The error bars show 2σ (95.45%) uncertainties.

ponents would be dramatically different, with the higher-velocity components expected to have much shorter time scales. It is plausible that these higher-velocity components at $\log R \lesssim 1$ [pc] may represent a a transient phenomenon. For example, objects that have overlapping trough features originating from higher-velocity components may show BAL variability in which overlapping trough disappears to reveal spectra that look like typical FeLoBAL quasars. Such variability has been seen in a number of FeLoBAL quasars (e.g., Rafiee et al., 2016).

There could be many origins of the lower-velocity components for the multi-component objects. *SimBAL* modeling assumes that these multiple components are not physically related (i.e., independent photoionization modeling for each absorber). Because the BAL components in a given multi-BAL FeLoBAL quasar are separated by a large radial distance, it is unlikely that they are physically related and formed in the same gas. One possibility is that the lower-velocity components might represent the remnants from earlier ejection episodes that are located along the line of sight (e.g., Choi et al., 2020). A variability study of these objects could potentially give us more detailed picture of the geometry of the multi-BAL system. For instance, we may expect systematically different variability pattern between the two absorbers if we assume the two gas clouds are not physically related (e.g., Leighly et al., 2015).

Nevertheless, it is possible that the multiple absorbers in a given object may be related in terms of their photoionization processes. Voit et al. (1993) proposed structures in outflowing gas cloudlets that can produce BALs with stratified ionization conditions based on the observations of high-ionization BALs (C IV$\lambda\lambda 1548, 1550$) and low-ionization BALs (e.g., Mg II$\lambda\lambda 2796, 2803$). In their models, highly ionized gas can be formed in the higher velocity portion of the BAL gas clumps, while the lower ionization environment is found near the lower velocity end, similar to how we found higher-velocity components with higher ionization. If the multiple components found in a given object are physically related and their photoionization processes are interdependent, it would be conceivable that we may be overestimating the distances between the lower-velocity BALs and the

higher-velocity BALs. In such scenario, a single absorbing gas may be able to produce multiple components with different ionization states; however, *SimBAL* neither has grids nor performs dynamical photoionization modeling needed to reproduce such physical conditions. Furthermore, the objects in our current sample have too low redshift to observe the C IV lines that we need to investigate such scenario; therefore we do not have robust observational evidence supporting complex ionization structure in absorbing gas. We will investigate this question using a sample of higher redshift FeLoBAL quasars.

A third possibility is that the lower velocity gas may originate from more distant structures in the quasar system. At the distances calculated from the gas properties (10s–1000s pc), molecular clouds in the host galaxy could be the source for the material illuminated by the quasar (e.g., Faucher-Giguère et al., 2012).

5.6.3. Opacity profiles of the outflows

5.6.3.1. Mg II and Fe II Absorption Lines

Comparing the opacity profiles between line transitions from the ions that have different properties can potentially tell us about the structure of the BAL winds. For instance, Voit et al. (1993) proposed a schematic picture of BAL clouds based on the differences in the opacity profiles between the high-ionization lines (e.g., C IV) and the low-ionization lines (e.g., Mg II). They suggested that the BALs originate from a turbulent absorbing region and absorbing gas clouds may have structures with dense cores with inhomogeneous photoionization conditions.

We found evidence for gas structure in the profiles in our sample. Although most of the FeLoBALs were modeled with a single ionization parameter and a single density (§ 5.5.1), we found dramatic changes in column density and covering fraction across the BAL velocity profile. Two of the I/I_0 models for SDSS J0840+3633 and SDSS J1527+5912 are shown in Figure 5.13. These models show remarkable differences between the profiles of the Fe II and Mg II lines that is caused by a change in both $\log N_H - \log U$ and $\log a$ across the trough. In particular, the excited state Fe II opacity profile for SDSS J0840+3633

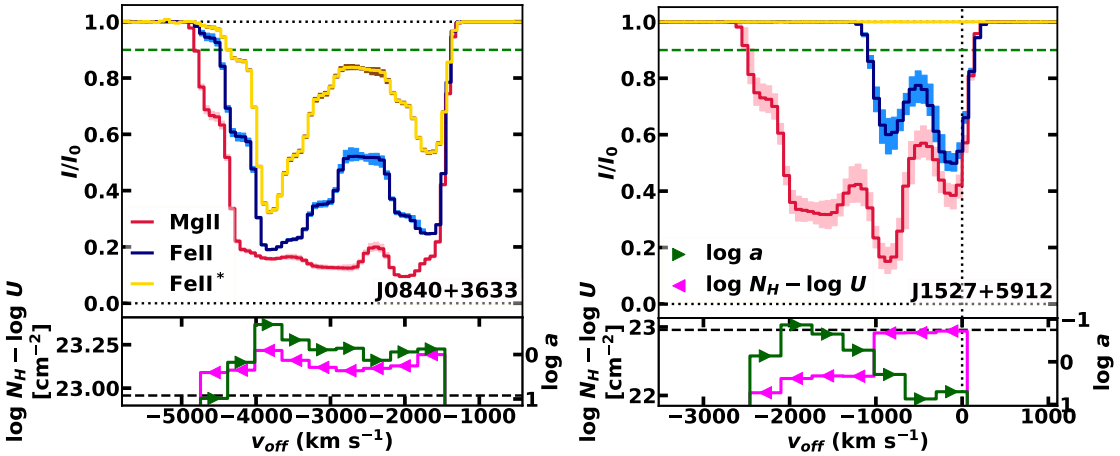

Figure 5.13: The top panels show normalized spectrum (I/I_0) models for three line transitions (Mg IIλ2796, Fe IIλ2383, and Fe II$^*\lambda$2757) from SDSS J0840+3633 and SDSS J1527+5912. The lighter shaded regions around each model represent 2σ (95.45%) uncertainties. In the bottom panels, the column density parameter ($\log N_H - \log U$) and the covering fraction parameter ($\log a$) as a function of velocity are plotted in pink and green, respectively. The complete figure with I/I_0 models from all 60 BALs is available in Appendix 5.D).

has a prominent double-peak structure with lower apparent opacity in the center that is not obvious in the opacity profile of the Mg II. The I/I_0 model for SDSS J1527+5912 shows the presence of a high-column density core at the lower velocity end of the profile; therefore, we observe a narrower width for Fe II. This BAL has low density ($\log n \sim 4.7$ [cm^{-3}]) and the excited state Fe II transition is not observed.

Figure 5.14 shows that the BAL widths measured from Fe II transitions are generally smaller or similar to those measured from Mg II. The widths of the excited state Fe II transitions were significantly smaller than the widths of the ground state Fe II and Mg II. Since a higher column density is required to accumulate significant opacity in excited state Fe II*, this means that the trough column density is not constant with velocity. In other words, the differences in widths can be ascribed to the intrinsic inhomogeneous physical structure of BAL gas, such as change in $\log N_H - \log U$ across the BAL troughs. For example, the model for SDSS J1527+5912 show a significantly wider profile in Mg II than in the ground state Fe II because the bins at higher velocities show a drop in $\log N_H - \log U$

(below the hydrogen ionization front at $\log N_H - \log U \sim 23$ [cm^{-2}]) and thus they do not produce opacity from Fe II. BALs identified with substantially larger Mg II widths than the Fe II widths showed extended low $\log N_H - \log U$ structure where the bins at the lowest and highest ends in velocity only produced Mg II opacity. Similarly the opacity from the excited state Fe II only appeared in the bins with high $\log N_H - \log U$ and oftentimes these high opacity concentrations or "cores" were only found in a small subset of bins for a given BAL component.

In addition to the change in column density, the covering fraction also varies with velocity and the combination of the two can change the relative widths of these lines. For saturated lines, the line depths and shapes are mostly controlled by the partial covering. *SimBAL* takes both of the effects into consideration when using tophat accordion models to fit the spectra. For example, in Figure 5.13, both $\log N_H - \log U$ and $\log a$ change significantly across the trough and as a result we observe a sawtooth-shaped line profile in excited state Fe II in the I/I_0 model for SDSS J0840+3633.

We measured the offset velocities for all three transitions separately (§ 5.4.3) using the I/I_0 models and they showed no systematic difference from the summary outflow velocities we calculated from the distributions of intrinsic opacity for each BAL (§ 5.4.2). This result shows that our definition of summary outflow velocities is not biased against any particular transition and that in general where the intrinsic opacity is high, the maximum of the apparent opacity is also high despite partial covering heavily influencing the apparent line and opacity profiles.

Voit et al. (1993) found that the low-ionization lines such as Mg II and Al III are typically only located at the low-velocity ends of the BAL troughs with narrow line profiles whereas high-ionization lines C IV appear in a wider velocity range extending to much higher velocity showing much broader line profiles. They concluded that nonmonotonic acceleration or deceleration of outflow gas scenarios can explain such velocity structure. Although we found physical properties change across the BAL troughs and thus the opacity profiles for different transitions may show completely different shapes for a given BAL

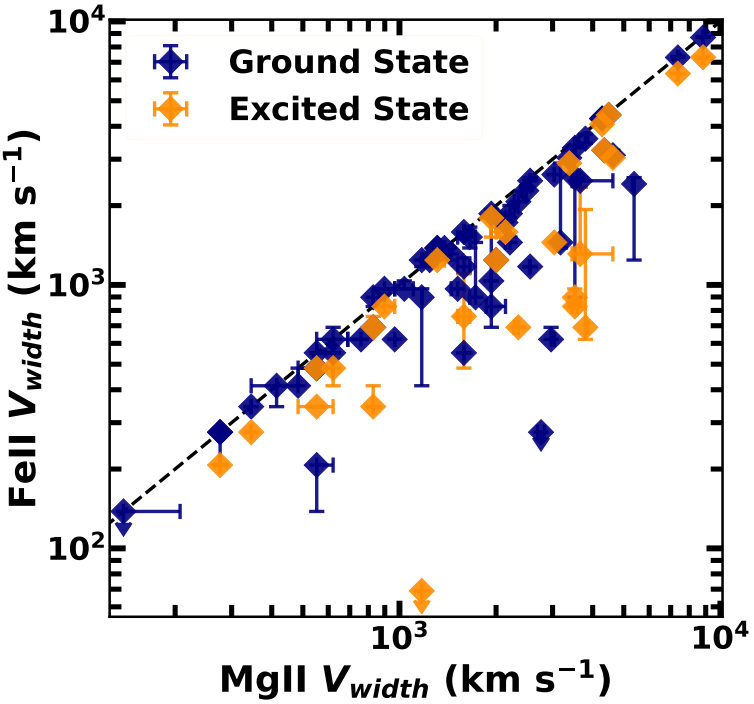

Figure 5.14: The width measurements from different line transitions are plotted with 2σ (95.45%) error bars. The widths measured with the excited state Fe II are noticeably smaller than the widths measured from the Mg II or the ground state Fe II transitions. Objects with the excited state Fe II transition are plotted with orange diamonds.

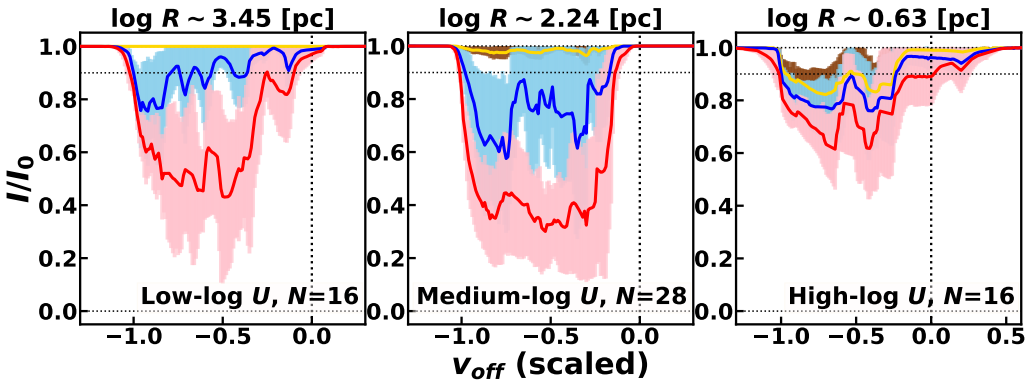

Figure 5.15: The three composite I/I_0 model spectra are plotted. The left panel shows the median composite I/I_0 model spectrum for the low-$\log U$ BALs and the middle and the right panel shows the same model for the medium-$\log U$ BALs and high-$\log U$ BALs, respectively. The median $\log R$ for each group is noted above each panel. The numbers of BAL components used to generate each composite are also noted. The Mg IIλ2796, Fe IIλ2383, and Fe II*λ2757 transition models are plotted in red, blue, and yellow, respectively. The pink, light blue, and brown shaded areas represent the median absolute deviation for the Mg IIλ2796, Fe IIλ2383, and Fe II*λ2757 transitions, respectively. The normalized v_{off} was used on the x-axis where 0 represents $v_{off} = 0$ km s^{-1} and -1 (or 1 for $v_{off} > 0$) represents the maximum BAL velocity measured for each I/I_0 model.

component, we did not find robust systematic trends between the profiles of Mg II, Fe II, and Fe II*. Future work with a sample of high redshift FeLoBAL quasars will allow us to study the absorption line profiles of C IV using SDSS spectra and we will be able to examine how their line profiles differ from the low-ionization lines and to investigate the potential ionization structure in BAL absorbing clouds.

Trends in the absorption-line structure hold promise for illuminating the nature of the acceleration mechanisms or gas cloud structure as a function of radial position in the quasar. To explore this possibility, we created composite I/I_0 profiles for subsamples with similar ionization and radial location for the outflowing gas. Specifically, we grouped the BALs into three groups using $\log U$ values: 16 low-opacity BALs with low $\log U$ that have lower limits on $\log R$ estimates (due to upper limits on $\log n$ constraints); 28 intermediate-opacity BALs with $\log U < -1.5$ that have well-constrained $\log R$ (and $\log n$); 16 high-opacity BALs with $\log U > -1.5$. The median $\log U$ for the three groups

are -2.66, -2.24, and -0.02. Because there is a strong correlation between $\log R$ and $\log U$ (§ 5.5.3, § 5.6.1), these groups also showed clear differences in $\log R$ properties: the median $\log R$ for the low-$\log U$, intermediate-$\log U$, and high-$\log U$ BAL group are 3.45, 2.24 and 0.63 [pc], respectively. The three groups represent (1) distant, low ionization BALs with kiloparsec-scale winds, (2) intermediate-scale medium ionization BALs, and (3) compact high ionization BALs that are located within ~ 10 pc from the central engine with size scales comparable to the torus scale. The I/I_0 models for each BAL component were normalized with respect to their maximum offset velocity where in the new normalized v_{off} axis -1 (or 1 for $v_{off} > 0$) represents the maximum velocity measured from the I/I_0 models (a similar parameterization can be found in Borguet & Hutsemékers, 2010). We then median combined the I/I_0 models and calculated the median absolute deviation. Figure 5.15 shows the composite I/I_0 model spectra from the three BAL groups.

The composite I/I_0 models showed large differences in the line depths of Mg IIλ2796 and the excited-state Fe II$^*\lambda$2757. Noting that $\log U$ is correlated with $\log n$ and $\log a$, we expect the BALs in the low $\log R$ BAL group with high $\log U$ to also have higher $\log n$ and $\log a$ (less covering) as observed. The high $\log a$ (less covering) makes all the line transitions appear shallow, which is why the line depth of Mg II is the smallest in the composite for the small-$\log R$ group. On the other hand, the higher value of $\log n$ can populate the excited state Fe II ions in the gas and create strong excited-state Fe II absorption lines, so we see the deepest excited state Fe II line profile compared to the other composites. The composite for the low $\log U$ group with distant winds shows no opacity from the excited state Fe II. While the differences in the line depths seen in the composites for different $\log R$ can be unambiguously explained by the differences in the physical properties, we did not find robust evidence for a systematic difference in gas structures or opacity profiles between the composite I/I_0 models. We may expect to find a more definitive answer with composite I/I_0 models from a larger sample; however, the large dispersion (median absolute deviation) seen in Figure 5.15 suggests that the line profiles depend more strongly on the individual physical conditions of each FeLoBALs

than any global trend. We also expect larger differences between the low-ionization lines considered here, and high-ionization lines such as C IV$\lambda\lambda 1549, 1551$.

5.6.3.2. Ca II, He I*, and Balmer Absorption Lines

Ca II H and K, He I*$\lambda 3889$, and Balmer absorption lines found in the rest-optical wavelengths can provide crucial information about the physical properties of the outflowing gas. Leighly et al. (2014) analyzed Ca II, Na I, and He I* absorption lines observed in the optical spectrum of the nearby Seyfert 1 object Mrk 231 to discover evidence for an interaction between a quasar outflow and surrounding the ISM. Leighly et al. (2011) discussed the advantages of using He I*$\lambda 3889$ absorption line to study BAL winds that have high column densities. The density of the BAL gas needs to be high ($\log n \gtrsim 7$) in order to produce an observable amount of opacity from Balmer transitions (e.g., Leighly et al., 2011). Therefore, Balmer absorption lines can be used as diagnostics to detect compact BAL winds (small $\log R$) with high densities.

We found that many of our FeLoBAL quasars show Ca II, He I*, and Balmer absorption lines in the spectra. The best-fit models provided excellent fit both for the main Fe II and Mg II troughs and for the rest-optical absorption lines as well (Figure 5.1; 5.10; 5.11). In contrast, previous BAL studies only found a small number (FeLo)BAL quasars with Ca II BAL features (e.g., Boksenberg et al., 1977; Arav et al., 2001; Hall et al., 2003). Moreover, Balmer absorption lines have been observed in only a small number of FeLoBAL quasars (e.g., Hall, 2007; Shi et al., 2016; Schulze et al., 2018). That is maybe because there has been no systematic study of FeLoBAL quasars prior to this work. We investigated how these rest-optical absorption lines are related to the FeLoBAL winds and what information about outflows we can gain from analyzing these transitions.

Out of 60 BAL components analyzed, we found 26, 40, and 18 BAL components are predicted to show opacity from Ca II H, K, He I*$\lambda 3889$, and Balmer transitions, respectively. Because our sample contains a wide range of redshifts ($0.66 < z < 1.63$), not all SDSS/BOSS spectra we analyzed included these transitions in the bandpass. Therefore, we

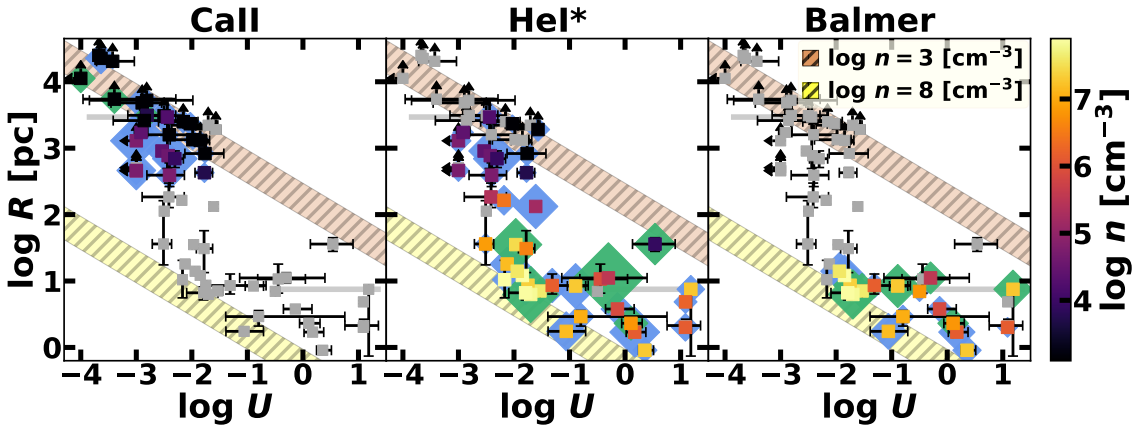

Figure 5.16: Figure 5.6 modified to show the distributions of absorption strengths (§ 5.4.3) of select line transitions predicted using the I/I_0 models. Our results point towards the presence of specific absorption lines as being key diagnostics for the location of the outflow (R). The blue diamonds represent the absorption strengths calculated from best-fitting models. The absorption strengths represented with green diamonds were calculated from the extrapolated *SimBAL* models (see text). The grey squares represent the BAL components that are not predicted show any opacity from the line transition featured in each panel. The size of the diamonds is proportional to values of the absorption strength parameter (i.e., larger markers represent stronger absorption). The Ca II absorption lines are only found in distant BALs ($\log R \gtrsim 3$ [pc]) and Balmer absorption lines are found in BALs with $\log R \lesssim 1$ [pc]. He I* absorption lines are predicted and found in nearly all FeLoBALs. The error bars show 2σ (95.45%) uncertainties and the grey shaded bars represent the range of the values among the tophat model bins for each BAL.

had to extrapolate the best-fitting models to longer wavelengths to calculate the absorption strengths for some of the BALs. Figure 5.16 shows the distributions of absorption strength predicted by the models (§ 5.4.3) along the $\log U$ and $\log R$ axes.

The opacity from Balmer transitions is only found in BALs with $\log R \lesssim 1$ [pc]. In other words, we suggest that the presence of Balmer absorption lines can be used as an indicator for compact BAL winds. In contrast, only the kiloparsec-scale BAL winds showed opacity from Ca II. This is expected given the distant BALs have low $\log U$ and low $\log n$ (Figure 5.4), the physical conditions required to create Ca^{+} ions. However, in a few cases Ca II BALs were observed with other high-$\log U$ or high-$\log n$ absorption lines at similar velocities (e.g., He I*, excited state Fe II), and therefore these Ca II outflows likely lie at small radii ($\log R \ll$kpc) and have unusual physical conditions. For instance, Leighly et al. (2014) inferred a density increase at the hydrogen ionization front to explain Na ID absorption in Mrk 231. Hall et al. (2002) suggested a significant gas temperature change to explain the Ca II absorption lines observed in SDSS J0300+0048. The opacity from He I* was found in the majority of FeLoBALs over a wide range of $\log R$. This result is consistent with what has been reported by Liu et al. (2015) where they also found a large fraction of Mg II selected LoBAL quasars with He I* absorption lines observed in the spectra. The presence of He I* absorption lines in (Fe)LoBAL quasars is a direct consequence of absorbing gas having high enough column density to produce observable low-ionization absorption lines such as Mg II (Fe II).

In summary, the absorption lines from Ca II, He I*, and Balmer transitions observed and predicted in rest-optical spectra of FeLoBAL quasars provide us with critical information about the physical properties. In particular, the presence of Ca II or Balmer absorption lines can be used to estimate the size scales of the BAL outflows and the He I* absorption line can be used to identify (Fe)LoBALs. This shows that even without a detailed photoionization modeling of rest-UV (FeLo)BAL quasar spectrum, one could potentially predict the approximate outflow spectral properties from the rest-optical spectrum.

5.6.4. Overlapping Trough FeLoBALs

Overlapping troughs show magnificent absorption features in the rest-UV spectra where the continuum emission is often nearly completely absorbed between $\lambda \sim 2000$ Å and $\lambda \sim 2800$ Å by a multitude of Fe II absorption lines. Hall et al. (2002) introduced several objects with overlapping troughs and discussed their spectral features; however, in-depth analysis of overlapping trough BALs has not been possible with conventional methods (e.g., measuring ionic column densities from the individual line profiles) due to extreme line blending. *SimBAL* can be used to analyze spectra with overlapping troughs, as demonstrated in SDSS J1352+4239, a heavily-absorbed overlapping-trough object (Choi et al., 2020).

The term "overlapping trough" has been used differently by different authors (e.g., Hall et al., 2002; Meusinger et al., 2016). In the literature, overlapping-trough objects generally refer to the FeLoBAL quasars with very broad absorption features reaching near-zero flux at the bottom, following the more stringent criteria introduced by Hall et al. (2002). We used a modified criterion to identify overlapping troughs that is based only on BAL morphology: such BALs were identified based on whether the continuum emission at $\lambda \sim 2500$ Å (outflow reference frame) where the absorption lines from the excited state Fe II are expected to appear in the spectrum is heavily absorbed or not. This method allowed us to focus only on the morphology of the troughs and identify all extremely wide troughs regardless of the amount of partial covering or the continuum shape.

Figure 5.17 shows the eight objects with overlapping troughs we found in our sample as well as SDSS J1352+4239 (Choi et al., 2020). We observe a great diversity in spectral morphology and gas kinematics as well as outflow gas properties. Their broad troughs have been fit with tophat models and five objects (SDSS J0300+0048, SDSS J1154+0300, SDSS J1556+3517, SDSS J1206+0023, SDSS J1448+4043) required the use of general reddening (Choi et al., 2020) to model the anomalous reddening. Three out of the eight objects (SDSS J1019+0225, SDSS J1125+0029, SDSS J1644+5307) also required an

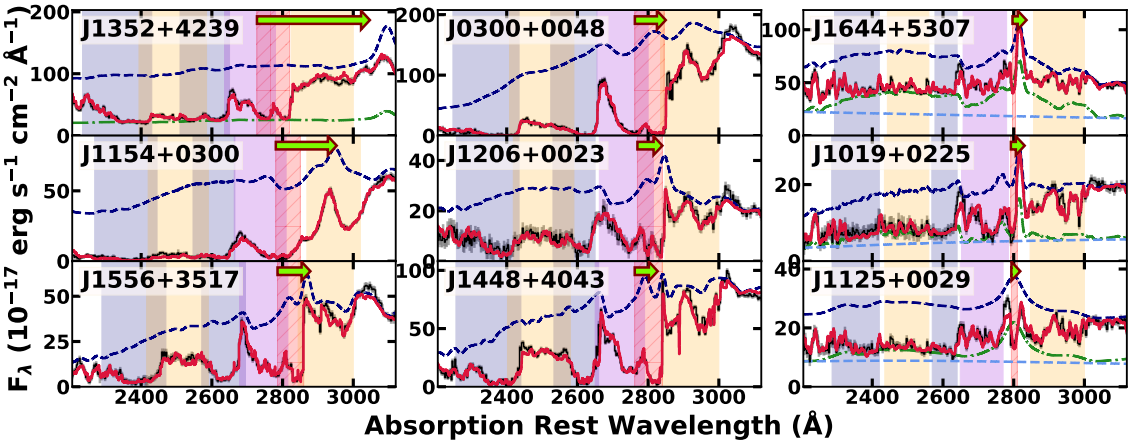

Figure 5.17: The eight objects with overlapping troughs are plotted with SDSS J1352+4239 (Choi et al., 2020). All the spectra have been shifted to the reference frame of the main BAL trough. The arrows extend from the estimated center of the Mg II trough to the center of emission line to illustrate the BAL offset velocity. The full spectral models and the continuum models are plotted in red and dashed blue lines, respectively. The green dot-dashed lines show the unabsorbed line emission and continuum emission if present. The additional blue dashed lines in the three objects on the right column represent the unabsorbed power-law continuum emission. The shaded regions represent various absorption lines and absorption-line classes: red, Mg II; blue, low-excitation Fe II; pink, high-opacity moderate-excitation Fe II; yellow, low-opacity moderate-excitation Fe II. Also see Figure 5.3.

additional unabsorbed components underneath the troughs (§ 5.5.1.1). A similar plot can be found in Figure 12 of Lucy et al. (2014) where they show different spectral morphologies of FeLoBALs with narrower lines.

Although the significant absorption seen in overlapping troughs indicates high-opacity and high-column density gas, this feature does not mean necessarily mean the overlapping trough BALs have high kinetic luminosities (L_{KE}). The wide range of outflow velocities seen in the overlapping trough BALs (marked by the lengths of the arrows in Figure 5.17) shows that some of them have no significant outflow velocity and thus are not carrying any significant mass or energy in the wind. As shown in § 5.6.1, the most important factor in determining the kinetic luminosity of an outflow is the outflow velocity. Thus, we found that five objects have overlapping trough BALs that are powerful outflows with $|v_{off}| > 4000$ km s^{-1} and $L_{KE}/L_{Bol} > 0.5\%$. These five objects also show blended troughs reaching near-zero flux at the bottom and can be called overlapping-trough objects based on the classification criteria by Hall et al. (2002). They are further distinguished by the presence of anomalous reddening (e.g., Choi et al., 2020). The other three objects, represented in the third column in Figure 5.17, have outflows with low velocities ($|v_{off}| < 1600$ km s^{-1}) thus do not have the high L_{KE} required for the quasar feedback.

In contrast to the wide range of outflow velocities found in the overlapping trough BALs, all of these outflows were found at similar distances from the central engine ($\log R \lesssim 1$ [pc]). Figure 5.6 shows where the overlapping trough BALs are found in the distributions of $\log R$ and $\log U$ as well as $\log n$. The BAL gas that creates overlapping troughs has higher densities ($\log n \gtrsim 6$ [cm^{-3}]), higher ionization parameters ($\log U \gtrsim -1.85$), and higher hydrogen column densities (Figure 5.7) compared to the BALs in the overall sample. These conditions are required to produce the high-excitation transitions that yield the necessary opacity at $\lambda \sim 2500$ Å. While the overlapping trough BALs have a range of $\log U$ that spans about two dex, they are all found to be located in the vicinity of the dusty torus ($\log R \lesssim 1$ [pc]). Based on the results from our sample, we conclude that the overlapping trough features in the FeLoBAL quasar spectra can be used to identify

compact BAL winds. Overlapping trough BALs could give us information about the inner regions of quasars where we expect most of the acceleration to occur for radiatively driven outflows (e.g., Arav & Li, 1994).

We identified three main ways FeLoBAL outflows create overlapping troughs. The most straightforward method is with large velocity widths. Although the kinematic properties of the BALs showed a wide range among the overlapping troughs in our sample, the high velocity overlapping troughs plotted in the left two panels in Figure 5.17 represent the FeLoBALs with the highest outflow velocities and widths in our sample (Figure 5.5). For instance, SDSS J1154+0300 has the largest BAL width with ~ 7400 km s^{-1} and the offset velocity of $\sim -15,400$ km s^{-1}. Naturally, with larger widths the line blending is significant and the high opacity gas in these winds will be able to create a wide overlapping trough FeLoBAL features.

Secondly, overlapping troughs can be produced from moderate to narrow width BALs with large amount of opacity from rare transitions. The width of the trough in SDSS J1644+5307 is only ~ 900 km s^{-1}, a value that is comparable or slightly smaller to the average value from other non-overlapping FeLoBAL troughs. The overlapping trough feature in that object is caused by the large number of excited state Fe II transitions and absorption lines from multiple iron-peak elements between ∼2000 Å and ∼3000 Å. If an outflowing gas has a high enough density, ionization parameter, and column density to have a significant population of highly excited state Fe II ($E_{lower-level} \gtrsim 3$ eV), then the gas will be able to create thousands of absorption lines (see Figure 5.3). Because these absorption lines are densely packed, they can easily form a wide trough by line blending even with a narrow absorption line velocity width.

Finally, objects that have an ordinary FeLoBAL component at lower velocity with an additional high-opacity component at higher velocity may show overlapping troughs in the spectra. As discussed in § 5.6.2, some of the objects in the sample required more than one BAL component, and overlapping trough features were created by the higher velocity, higher $\log U$ components. For example, in Figure 5.12 we see that most of the

higher-velocity components in objects with blended multi-BALs features (red arrows) are also identified as overlapping trough BALs (pink circles). Figure 5.11 shows how these higher-velocity components produce the majority of the opacity needed to complete the overlapping trough features near $\lambda \sim 2500$ Å. The lower-velocity components (Figure 5.11, plotted in green) resemble typical FeLoBALs, mainly showing BALs from the ground state Fe II and Mg II transitions with little to no highly excited state Fe II transitions (see Figure 5.3; § 5.5.1.2). Without the higher-velocity components, these objects would appear nearly indistinguishable from the non-overlapping trough FeLoBAL quasars.

Some compact HiBAL outflows show BAL variability possibly due to the transverse motion of the outflow clouds or change in photoionization state of the outflow gas (e.g., Capellupo et al., 2013). For instance, the disappearance of overlapping troughs has been observed in FBQS J140806.2+305448 (Hall et al., 2011) and in SDSS J123103.70+392903.6 (Rafiee et al., 2016; McGraw et al., 2015). It is plausible that in some cases the variability might be coming from the disappearance of the higher-velocity component. For example, while the overlapping trough features from Fe II disappeared in these two objects, the strength of the deep absorption feature from Mg II at the lower velocity end remained consistent. The sample of radio-selected quasars analyzed by Zhang et al. (2015b) showed an enhanced spectral variability rate for the overlapping-trough objects. However, multiple observations from three objects (SDSS J0300+0048, SDSS J1125+0029, SDSS J1154+0300) have been analyzed by McGraw et al. (2015) but no evidence for BAL variability was found. Shi et al. (2016) found evidence for spectral variability in SDSS J1125+0029, the variability they found was attributed to changes in the unabsorbed line emission flux underneath the Fe II trough and they did not find any significant change in the BAL troughs.

Some of the multi-component objects with overlapping troughs (SDSS J1125+0029 and SDSS J1206+0023) showed a lower-velocity and lower-$\log U$ component that only produces significant opacity from Mg II with little Fe II opacity (§ 5.6.2). The velocity of these components extends across ~ 0 km s^{-1} and they are located at about an order of

magnitude larger distances than the higher-velocity components (Figure 5.12). The origins of these BAL components are uncertain. Discussions related to redshifted BALs that have similar kinematic characteristics have suggested rotationally dominated outflows or infalls as potential origins (Hall et al., 2013).

Three objects (SDSS J1019+0225, SDSS J1125+0029, SDSS J1644+5307) were modeled with a modified partial covering scheme (§ 5.5.1.1), because the usual power-law partial covering that is used in *SimBAL* was not sufficient to model the observed non-black saturation. Although these three objects show overlapping trough BALs in the spectra with no continuum emission recovery shortward of $\lambda \sim 2800$ Å, they do not meet the usual criteria for overlapping-trough object classification due to significant flux beneath the troughs. Choi et al. (2020) discussed the unabsorbed component under the overlapping troughs in SDSS J1352+4239 as scattered flux where $\sim 29\%$ of the light from the accretion disk and the BLR is scattered directly into the line of sight. In these three objects, the inferred scattered fraction would have to be greater than 50%; this is unphysical. All three of these objects have compact outflows with $\log R \lesssim 1$ [pc], and their close proximity to the BLR and the accretion disk suggests that the BAL gas is physically only covering part of the continuum and line emission. Thus the non-zero flux at the bottom of the troughs are due to a strong partial covering effect. In Paper III (Choi et al., 2022b), we discuss the angular size scales of the accretion disk and broad line region seen from the locations of the BAL winds using the black hole masses and Eddington ratio estimates obtained in Paper II (Leighly et al., 2022). We conclude that the large angular size scales of the accretion disk seen from the BAL gas at these small $\log R$ values can plausibly produce this partial covering scenario.

5.6.5. "Loitering" Outflows

We identified a group of eleven compact FeLoBAL winds with small offset velocities and distinct properties, and classified them "loitering" outflows (we use the term "outflow" in the nomenclature, but note that some loitering outflows have $v_{off} > 0$ km s^{-1}).

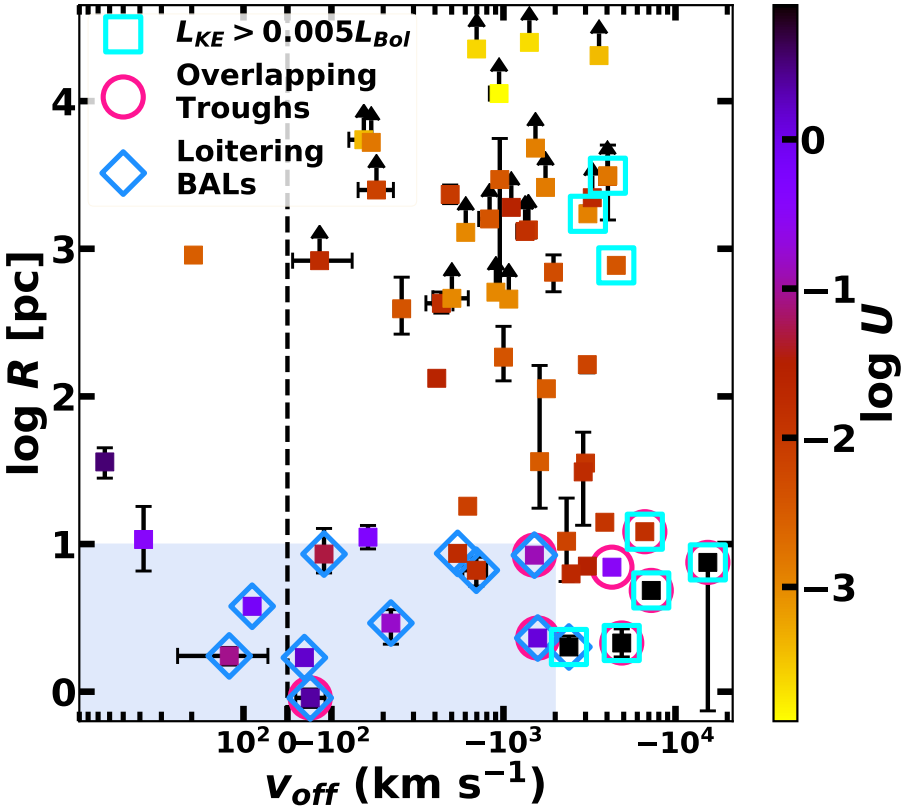

Figure 5.18: The distributions of the offset velocities (v_{off}) and the distances of the BALs from the central SMBHs ($\log R$). The blue shaded region represents the defining criteria for the loitering outflows ($\log R < 1$, $|v_{off,\ \mathrm{FeII\ excited}}| < 2000$ km s^{-1}, and $v_{width,\ \mathrm{FeII\ excited}} < 2000$ km s^{-1}). Excluding the loitering outflows and the inflows ($v_{off} > 0$), we found robust statistical evidence ($p < 0.05$) for a correlation between $\log R$ and v_{off} where the high velocity flows are found closer to the central engine. The error bars show 2σ (95.45%) uncertainties.

The loitering outflows are defined by the following properties: a) $\log R < 1$ [pc]; b) $|v_{off,\ \mathrm{FeII\ excited}}| < 2000$ km s^{-1} and $v_{width,\ \mathrm{FeII\ excited}} < 2000$ km s^{-1}. In other words, the loitering outflows are relatively static gas clouds that are located close to the central SMBHs within the vicinity of the torus and thus they are appeared to be neither outflowing or inflowing. Figure 5.18 shows how the distribution of the physical properties of loitering outflows differs from the other more typical BAL winds and our defining criteria.

Instead of using v_{off} and v_{width} estimated from the Mg II transition, we used the values measured from the excited-state Fe II$^{*}\lambda2757$ extracted from the I/I_0 models discussed in § 5.4.3. This was done to avoid excluding any BALs with narrow Fe II absorption features that may have larger v_{off} or v_{width} due to extended Mg II opacity profiles. Moreover, the opacity profile of the excited state Fe II traces the high-density cores within the BAL gas structure that produce the majority of opacity and carry most of the mass and energy in the wind. However as can be see in Figure 5.18, our classifications would not have been significantly affected if we had used the standard v_{off} and v_{width} from Mg II. Only one BAL, in SDSS J1006+0513, showed modest differences between the values ($v_{off} \sim -2400$ km s^{-1}, $v_{width} \sim 3500$ km s^{-1}; $v_{off,\ \mathrm{FeII\ excited}} \sim -1420$ km s^{-1}, $v_{width,\ \mathrm{FeII\ excited}} \sim 830$ km s^{-1}). We note that the selection criteria were chosen based on the visual inspection of the distribution of parameters obtained from our low redshift sample. Future work with larger samples and high redshift objects may modify our selection criteria.

The loitering outflows have high $\log U$ with lower partial covering (high $\log a$) and five out of eleven BALs required a modified partial-covering model. Conversely, five out of 6 objects modeled with modified partial-covering were found to have loitering outflows. These BALs show an extremely large number of absorption line transitions in the spectra because the high-$\log U$ FeLoBALs also have high column density and such a thick gas slab can produce a plethora of rare line transitions from various excited states Fe II as well as rarer iron-peak elements such as Co and Zn (Figure 5.3). Three of the eleven (SDSS J1019+0225, SDSS J1125+0029, and SDSS J1644+5307) loitering

outflows are also classified as overlapping trough BALs. These three were notable because they required step-function partial covering for the power-law continuum emission and unabsorbed line emission in the model. In addition to these objects, SDSS J1128+0113 and SDSS J1321+5617 were modeled with modified partial-covering where the line emission was unabsorbed (Figure 5.2). The remaining six were modeled using the standard power-law partial covering. These objects were characterized by lower signal-to-noise ratios (median SNR$\sim 3-6$), and it is possible that modified partial-covering would be required in higher signal-to-noise ratio spectra where the bottoms of the troughs would be better defined.

The locations of the loitering outflows in the quasar suggests the torus as a potential origin for the absorbing gas. The dust sublimation radius for quasars with $\log L_{bol} \sim 46.0-47.0$ [erg s^{-1}] is $R_{sub} \sim 0.2-0.6$ pc (Laor & Draine, 1993). The outer radius of the torus was estimated to be $R_o \sim 40-120$ [pc] using the equation $R_o < 12L_{45}^{1/2}$ pc ($L_{45} = L_{bol}/10^{45}$ erg s^{-1}; Nenkova et al., 2008). The loitering outflows are located at $R \sim 1-10$ pc which is within the region where we expect the dusty torus to be. A wind origin of the torus has been proposed by Elitzur & Shlosman (2006), and recent studies using magnetohydrodynamic models of a dusty wind have been successful in finding potential connections between the outflowing winds and the windy torus structure (e.g., Keating et al., 2012; Gallagher et al., 2015). Paper II (Leighly et al., 2022) investigates the accretion properties of the FeLoBAL quasars that have loitering outflows (or so-called "loitering outflow objects"). We found that the loitering outflows all had lower-than-average accretion rates. Elitzur & Shlosman (2006) predict that at low accretion rates, the wind forming the torus fails. In Paper IV (Leighly et al., in preparation), we conjecture that in the loitering outflow objects, the torus wind is on the verge of failing, so that it is not optically thick enough to reprocess continuum into the infrared band, but is still optically thick enough to produce the observed Fe II absorption.

As expected from the similar size scales of the outflows ($\log R \lesssim 1.0$ [pc]), the spectral morphology of the loitering outflows resembles that of FeLoBAL quasars with Balmer

absorption lines (§ 5.6.3.2). Using this spectral property, we can use the presence of the narrow Balmer absorption lines (as well as He I* to differentiate BALs from galaxy contamination) in the optical spectra to search for quasars with loitering outflows.

We found a significant correlation between the v_{off} of the BAL outflows and $\log R$ ($p = 0.02$, Kendall τ; Figure 5.18) when the loitering outflows and the inflows are removed ($N = 46$). The remaining compact BAL winds that are located at $\log R \lesssim 1.0$ [pc] have the highest outflow velocities and most of them were also identified as overlapping trough BALs with powerful outflows ($L_{KE}/L_{bol} > 0.5\%$; § 5.6.4). Assuming the BAL clouds have not traveled significantly such that their current locations in the quasars represent where they were initially launched, simulations and statistical calculations predict that such a correlation should exist. For the line-driven outflows the terminal velocities of the winds roughly correlate with the Keplerian circular velocity or the escape velocity at the launch radius (e.g., Proga & Kallman, 2004; Giustini & Proga, 2019). A simple equation of motion derivation using the radiative acceleration also predicts v_{off} or $v_{\infty} \propto R_{in}^{-1/2}$ where R_{in} is the inner wind radius or the launch radius (e.g., Hamann, 1998; Leighly et al., 2009; Choi et al., 2020). Because the correlation was not apparent when the loitering outflows were included in the analysis, we postulate that the loitering outflows may represent a different BAL phenomenon with potentially different acceleration mechanisms involved (see also Paper III, Choi et al. 2022b).

5.7. Discussion

5.7.1. Location and Origin of FeLoBAL Winds

Our results show that the FeLoBAL winds span a large range of radii or distances from the central SMBH. However, the number density of objects may not be constant with R. There is an apparent gap near $\log R \sim 2$ [pc]; see Figure 5.6. While a larger sample may fill this gap, we can use the assumed break around $\log R \sim 2$ [pc] to divide the FeLoBALs into two groups: compact outflows with special spectral morphologies, and the distant galactic-scale outflows that could have potentially formed in-situ (Faucher-Giguère et al.,

2012). In other words, these two groups that are largely separated in physical size may represent two intrinsically different types of BAL outflows that have different origins and physical processes including their acceleration.

The winds observed in these objects are not continuous but are clumpy (e.g., Hamann et al., 2011). Without an external confinement mechanism, the clumps should dissipate in order of sound crossing time $t_{sc} = l/c_s$ where l is the characteristic cloud size and c_s is the sound speed (Hamann et al., 2001; Schaye, 2001; Finn et al., 2014). For $l \sim \Delta R \sim 0.01$ pc (median from the sample) and T$\sim 10^4$ K BAL gas, the cloud will survive for ~ 670 yr; however, it is more likely that the BAL wind is comprised of many smaller clouds with $l \sim \Delta R/N$ where N is the number of clouds (Hamann et al., 2013). In comparison, a characteristic flow time $t_f \sim R/v_{outflow}$ for a BAL wind with $v_{outflow} \sim 1,000$ km s^{-1} and $R \sim 1$ pc is $t_f \sim 1,000$ yr. Based on these calculations and considering that the dissipation time-scale cannot exceed the flow time-scale, we can assume the FeLoBAL winds have not traveled far from their origin.

Theoretical disk wind models (e.g., Foltz et al., 1987; Arav & Li, 1994) suggest the location of disk winds at $R \sim 0.01$ pc for luminous quasars (e.g., Proga et al., 2000; Proga & Kallman, 2004). However, none of the FeLoBAL outflows in our sample was found at such a compact scale. Rather, the compact outflows in our sample ($R \sim 1 - 10$ pc) suggest a torus wind model where the winds originate from the dusty torus (e.g., Gallagher et al., 2015; Chan & Krolik, 2016, 2017; Vollmer et al., 2018). It is possible that the polar dust discovered in spatially resolved mid-infrared observation (e.g., Hönig et al., 2013) has the same origin as these winds. Similar to the dusty torus winds, polar dust models also predict dust at comparable size-scales $R \sim 1 - 100$ pc with large dust masses, $M_{dust} \sim 100$s M$_\odot$ (Hönig & Kishimoto, 2017; Stalevski et al., 2019).

The torus wind models may also provide intriguing explanations for some of the inflows we observed in the sample (§ 5.5.1.3; § 5.5.3). Most of the inflowing FeLoBAL gas is found at $R < 100$ pc (one at $R \sim 1000$ pc; Figure 5.18). It is plausible that these compact inflows may represent some kind of disruption in the vicinity of the torus where

the resulting material falls towards the central engine. The distant inflow might be cause by some compaction of gas flows in the host galaxy.

Between $\sim$ 100 pc and $\sim$ 1000 pc from the center, photoionized gas can be observed in emission lines from the narrow line region (NLR). Observational evidence for quasar driven winds at this size-scale is often observed in blueshifted [O III] lines (e.g., Zakamska et al., 2016; Vayner et al., 2021). These outflows have mass outflow rates comparable to the FeLoBAL outflows ($1 \lesssim \log \dot{M}_{out} \lesssim 3$ [$M_\odot$ yr^{-1}]). Although a direct connection between the [O III] outflows and BAL outflows is yet inconclusive (Paper III, Choi et al. 2022b), it is possible that outflowing gas in the NLR can manifest as either BAL winds or emission line outflows or both depending on the physical conditions of the gas and/or sightlines.

Lastly, the potential origin of the kiloparsec scale BAL winds can be explained by a model introduced by Faucher-Giguère et al. (2012), where a low radial filling factor results from in situ formation of outflows from the interaction between a dense interstellar medium and a quasar blast wave. They concluded that the FeLoBAL outflowing gas may have properties comparable to massive molecular outflows that are generally found at similar distances from the central SMBHs (e.g., high momentum flux ratio; § 5.7.4).

5.7.2. Geometry Properties of FeLoBAL Winds[4]

The volume filling factor ($\Delta R/R,\ \Delta R = N_H/n_H$) gives us information about the physical size scales of the outflowing gas. It is most directly interpreted as the fractional volume of space occupied by the outflow. Typically, using the values for column density, density, and radius derived using excited state absorption lines, small log volume filling factors, mostly ranging between -6 to -4 are found (e.g., Korista et al., 2008; Moe et al., 2009; Dunn et al., 2010). The volume occupied by the absorbing clouds ranges from 0.01% to 1%. The volume filling factor tells us how thin or extended in the radial direction the BAL cloud structure is and provides us with information about the BAL

[4]This subsection is reproduced from the § 4.3.1 in Choi et al. (2022b) with permission.

physical conditions. A small volume filling factor ($\log \Delta R/R \sim -5$) for BALs may imply a pancake- or shell-like geometry that is very thin in the radial direction (e.g., Gabel et al., 2006; Hamann et al., 2011, 2013). These BAL absorbers with $\log \Delta R/R \lesssim -3$ may be composed of smaller gas clouds (e.g., Waters & Proga, 2019) that are potentially supported by magnetic confinement in order to avoid dissipation (e.g., de Kool & Begelman, 1995). In contrast, Murray & Chiang (1997) proposed that a continuous flow from the accretion disk is the origin of broad emission lines and BAL features; such a flow would have a volume filling factor of 1. We emphasize that our results are not consistent with a direct observation of a disk wind because the size scales that we measure are too large. The minimum distance of the outflow from the central engine found in our sample is $R \sim 1$ pc in SDSS J1125+0029, whereas reasonable size scales for disk wind outflows should be comparable to the size of the accretion disk ($R \ll 0.01$ pc). That does not imply that disk winds do not exist but rather that we do not find them to have rest-UV BAL outflow signatures. This result is consistent with the literature; among the FeLoBAL quasars previously subjected to detailed analysis, typical outflow distances lie between 0.4 and 700 parsecs (e.g., de Kool et al., 2001, 2002a,b; Moe et al., 2009; Dunn et al., 2010; Aoki et al., 2011; Lucy et al., 2014; Shi et al., 2016; Hamann et al., 2019b; Choi et al., 2020), i.e., no closer than the BLR.

We calculated the volume filling factors for the full sample and examined the dependence on BAL properties (Figure 5.19). The strong correlation seen between $\log \Delta R/R$ and $\log U$ can be explained by the mathematical relationship between the parameters as follows. First, the BAL physical thickness (ΔR) is proportional to the hydrogen column density (N_H) which is also proportional to the ionization parameter U since $\log N_H - \log U$ is nearly constant in the FeLoBAL quasar sample, and the distance of the outflow from the central SMBH (R) is inversely proportional to $U^{1/2}$, both for a fixed density. Dividing the BAL thickness by its distance from the center, we obtain the volume filling factor $\Delta R/R \propto U^{1.5}$, and we find a slope of ~ 1.5 in the left panel of Figure 5.19. We observe a scatter around that line because of the range of $\log N_H - \log U$ and $\log n$ for the FeLoBALs

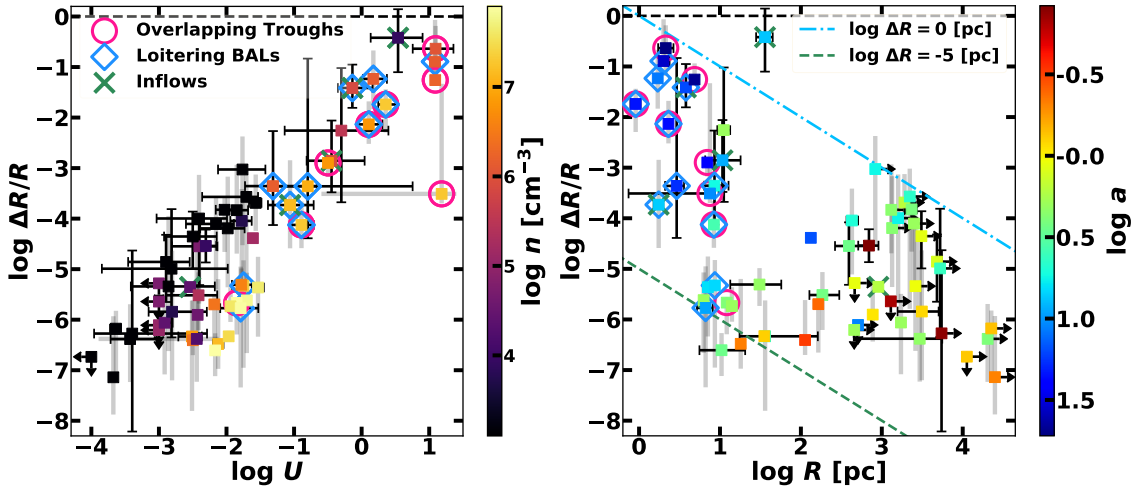

Figure 5.19: The volume filling factor ($\log \Delta R/R$) as a function of the ionization parameter ($\log U$) and the location of the outflow ($\log R$). We found a wide range of $\log \Delta R/R$, with the overlapping trough and loitering BALs having higher values of $\log \Delta R/R$. *Left panel*: $\log \Delta R/R$ increases with $\log U$ following the slope of ~ 1.5. This tight correlation is expected given the relationship between $\log U$ and $\log N_H$ for FeLoBALs (§ 5.5.3). One of the main sources of the scatter along the $\log \Delta R/R$ can be ascribed to the range of $\log n$ observed in the sample. *Right panel*: We found a wider range of $\log \Delta R/R$ distribution for the FeLoBALs that are located close to the central black holes. The green (dashed) and blue (dotted-dashed) diagonal lines represent the locations of the constant physical thickness of the BAL winds at $\log \Delta R = -5$ and 0 [pc], respectively. Markers and error bars as in Figure 5.4.

in our sample (Figure 5.4). There is also a range in photoionizing flux Q which we assume to be proportional to $L_{\rm Bol}$. This parameter enters through $U = Q/4\pi R^2 nc$. Therefore, larger values of $\log N_H - \log U$ (thicker outflows), smaller density, or smaller $\log L_{bol}$ correspond to a larger value of $\log \Delta R/R$.

The distribution of $\log \Delta R/R$ is not uniform across $\log R$. At large radii, corresponding to $\log U \lesssim -1$, the volume filling factors mostly range between -6 to -4. These values are similar to those reported in the literature for samples of high-ionization BAL quasars (e.g., Gabel et al., 2006; Hamann et al., 2011, 2013). In contrast, the outflows that are found at $\log R \lesssim 1$ have a very wide range of $\log \Delta R/R$, ranging from -6 to nearly almost zero. These are mostly the special types of BALs such as the overlapping trough (§ 5.6.4) and loitering BALs (§ 5.6.5).

The analysis shows significant differences in $\log \Delta R/R$ as a function of radius. This result suggests that BAL winds may favor different models at different radii (Leighly et al. in preparation; § 5.7.1). The compact winds at $\log R \lesssim 1$ [pc] showed a wide range of $\log \Delta R/R$ that agrees with the predictions of the various BAL physical models that explain either thin shell-like outflows (small volume filling factor) or stream-like outflows (large volume filling factor). On the other hand, the properties of distant BAL winds only favor the physical model with thin pancake-like BAL geometry. Specifically, Faucher-Giguère et al. (2012) proposed that FeLoBALs with large $\log R \gtrsim 3$ [pc] and small $\log \Delta R/R \sim -5$ are formed by "cloud crushing" where the ambient ISM is shocked by the supersonic energy-conserving quasar outflow and the FeLoBALs are formed in-situ at kiloparsec scales rather than formed near the accretion disk. In addition, in order for distant BALs to have large filling factors, the BAL clouds would need to have large physical radial thicknesses proportional to their distances from the central engine ($\Delta R \gtrsim 10$ pc). Maintaining such large structure is physically challenging due to cloud destruction processes (e.g., Proga & Waters, 2015).

5.7.3. Acceleration Mechanisms and SED Properties

We used *Cloudy* to calculate the force multiplier (FM) for a radiatively driven outflow using the physical parameters obtained from the best-fitting models to investigate the relationship between the photoionization properties of the gas and the wind acceleration (i.e., outflow velocity). The force multiplier is defined as the ratio of the total cross section (line and continuum processes) to the Thompson cross section. It represents how much radiative force the cloud can harness from the photons to power the outflow acceleration.

Figure 5.20 shows the distribution of FM as a function of $\log U$ and v_{off}. FM decreases with $\log U$ which is consistent with analytical calculations that used the equation derived from the definition of FM (e.g., Castor et al., 1975; Arav & Li, 1994; Arav et al., 1994). High $\log U$ gas is not only highly ionized but also has larger hydrogen column density ($\log N_H$) and more material since $\log N_H - \log U$ is nearly constant in our FeLoBAL

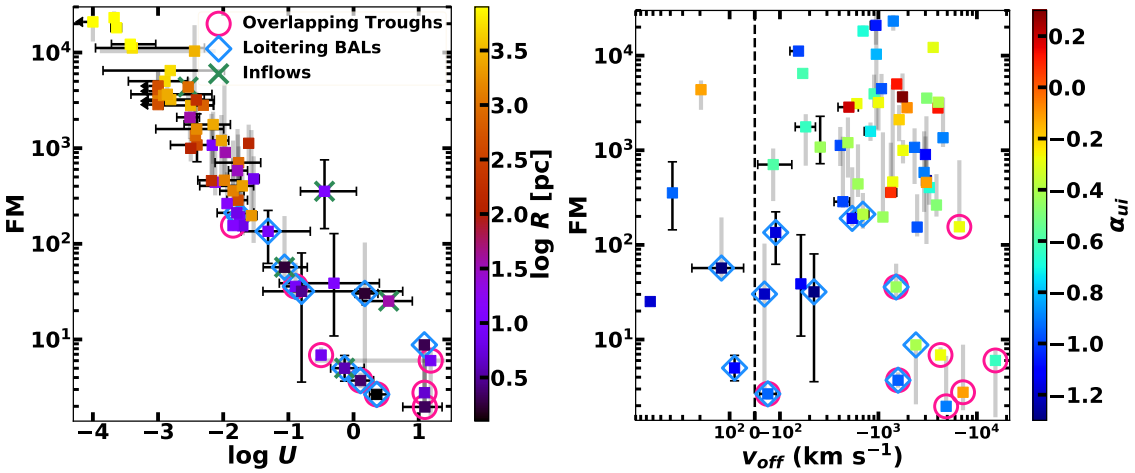

Figure 5.20: The FM calculated using *Cloudy* with physical parameters from the best-fitting *SimBAL* models. *Left panel*: The force multiplier is strongly correlated with ionization parameter. *Right panel*: We did not find robust correlation between the force multiplier and the outflow velocity. The outflows with the highest outflow velocities have relatively smaller FM. An extra source of opacity to capture the photon momentum, such as dust, or another acceleration mechanisms may be needed to explain the high velocity FeLoBALs. The high values of α_{ui}, flat or red SEDs, found in these objects could potentially indicate dusty outflows. Markers and error bars as in Figure 5.4.

sample (§ 5.5.2.1). We found no correlation between FM and outflow velocity from our sample. In fact, the outflows with the highest velocities have among the lowest values of FM.

The low FM values in BALs with extreme outflow velocities ($v_{off} \sim -10,000\ \mathrm{km\ s^{-1}}$) suggest that another acceleration mechanism is also playing a significant role. For instance, radiation pressure on dust may play a significant role in accelerating the gas (e.g., Thompson et al., 2015; Murray et al., 2005; Ishibashi et al., 2017). Some of these high outflow velocity BALs are overlapping trough BALs with anomalous reddening (§ 5.6.4) and they have flatter SED slopes (α_{ui}) than the rest (represented by the colors of the marker in the right panel of Figure 5.20). The flat SED slopes may indicate reddening in the quasar which may suggest the BALs in these objects are dusty. That is not to say that the BALs themselves have high dust content; dust reddening tends to suppress photoionization.

Figure 5.21 reveals that the outflow velocity is correlated with α_{ui} ($p = 0.003$, Kendall τ). The top axis shows the inferred values of $E(B-V)$ calculated using the composite quasar SED from Richards et al. (2006b) ($\alpha_{ui} = -1.23$) and SMC reddening (Prevot et al., 1984). This strong correlation between the SED slope and outflow velocities in the FeLoBAL outflows is consistent with what has been found for ERQs. Hamann et al. (2017) analyzed a unique sample of ERQs at $2.0 < z < 3.4$ and discovered a high BAL fraction ($\sim 30 - 68$ %) and frequently the presence of outflow features. Perrotta et al. (2019) analyzed the [O III] emission lines in a subsample of ERQs from Hamann et al. (2017). They found a correlation between $\mathrm{i} - \mathrm{W3}$ color and outflow velocity where faster and more powerful outflows were found in redder quasars. It is plausible that this trend can be explained by FeLoBAL quasars being at a similar evolutionary stage as dusty, red quasars in a transitional phase in quasar evolution where obscured quasars are expelling gas and dust via outflows to become normal quasars (e.g., Hopkins et al., 2005; Urrutia et al., 2008; Glikman, 2017; Glikman et al., 2018). However, FeLoBAL quasars in our sample are not ERQs and the link between the red quasars and FeLoBAL quasars is still uncertain; LoBAL quasars are found among red quasars but no enhanced merger rates

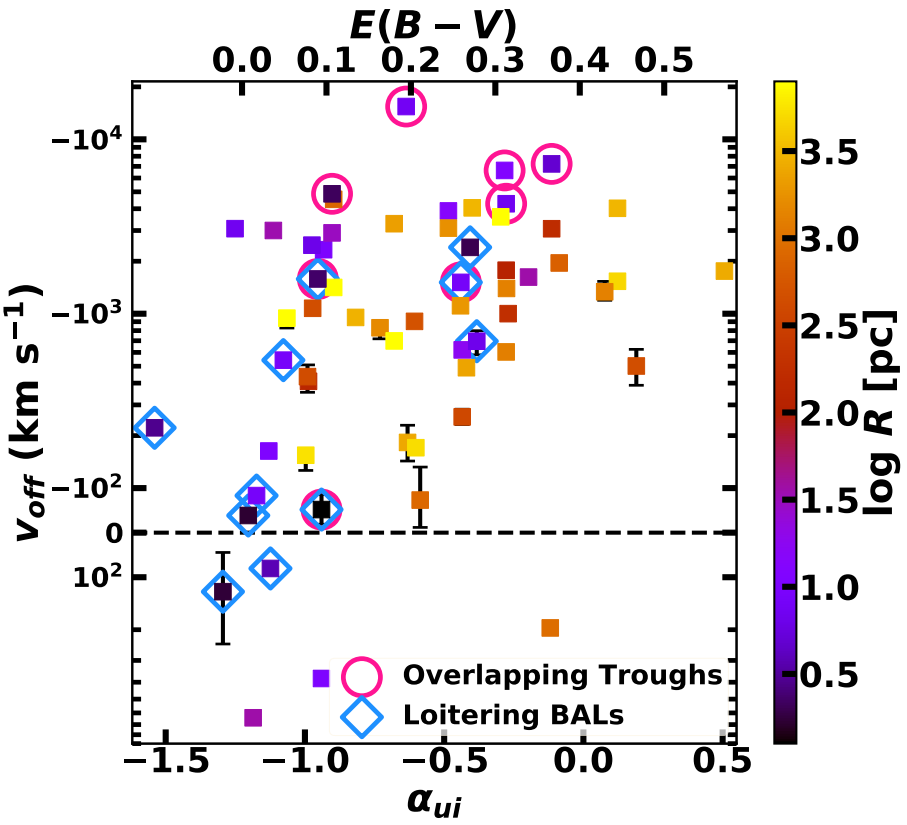

Figure 5.21: The outflow velocity (v_{off}) is plotted against the SED slope parameter (α_{ui}). FeLoBALs with higher outflow velocities are found in objects with flatter or redder SEDs, where FeLoBAL quasars with steeper or bluer SEDs have compact outflows ($\log R \lesssim 1$ [pc]). Most of the compact outflows with steep SEDs are loitering outflows, and α_{ui} in these objects might be potentially affected by other SED properties than reddening such as the strength of IR emission from the torus (Leighly et al., in preparation). The top axis shows the values of $E(B-V)$ that correspond to the range of α_{ui} plotted on the bottom axis (assuming a composite quasar SED (Richards et al., 2006b) and SMC reddening (Prevot et al., 1984)). The vertical error bars show 2σ (95.45%) uncertainties.

or star formation rate has been found for FeLoBAL quasars (e.g., Violino et al., 2016; Villforth et al., 2019).

A simpler explanation for the correlation between the two properties is that the outflow itself as the source of reddening. First of all, a quasar outflow from the dusty torus can form a dusty wind (e.g., Gallagher et al., 2015). The dust is then sublimated, and we see BAL. Further downstream, the dust precipitates out of the gas (Elvis et al., 2002) producing the reddening. For instance, Dunn et al. (2015) suggested that the reddening in FeLoBAL quasars occurs at larger radial distances than the outflows. A multiwavelength SED analysis of red quasars supports the idea that dust in the winds are responsible for the reddening in these objects (Calistro Rivera et al., 2021). Thus for our FeLoBALs, flatter or redder SEDs can be the result of high-velocity outflows that carry more mass and energy causing more dust reddening. Similarly, the FeLoBAL quasars with the steepest, or the bluest, SEDs have the compact, low mass outflows with the lowest outflow velocities that are characteristics of loitering outflows (§ 5.6.5).

In summary, FM analysis using *Cloudy* suggested that radiative line driving is insufficient for outflows with the highest outflow velocities located close to the central engine. We found a compelling evidence that FeLoBAL quasars with redder SEDs have faster outflows. Based on these results, we speculate that the additional acceleration mechanism is acceleration by dust for these FeLoBALs. We note that the SED slope (α_{ui}) calculated from specific fluxes at rest-frame 2000 Å and 3 μm used in this work can be affected not only by reddening but by other properties of the quasar such as the strength of torus. This point is investigated further in Paper IV (Leighly et al., in preparation).

5.7.4. Comparison with other forms of outflows

Observational evidence for quasar outflows can be found both in blueshifted absorption lines and blueshifted or broad emission lines (e.g., Fabian, 2012; King & Pounds, 2015). All together, AGN-driven winds are found at a wide range of distance scales, from the ultra fast outflows (UFOs) seen in X-ray band that are located in subparsec scales (e.g.,

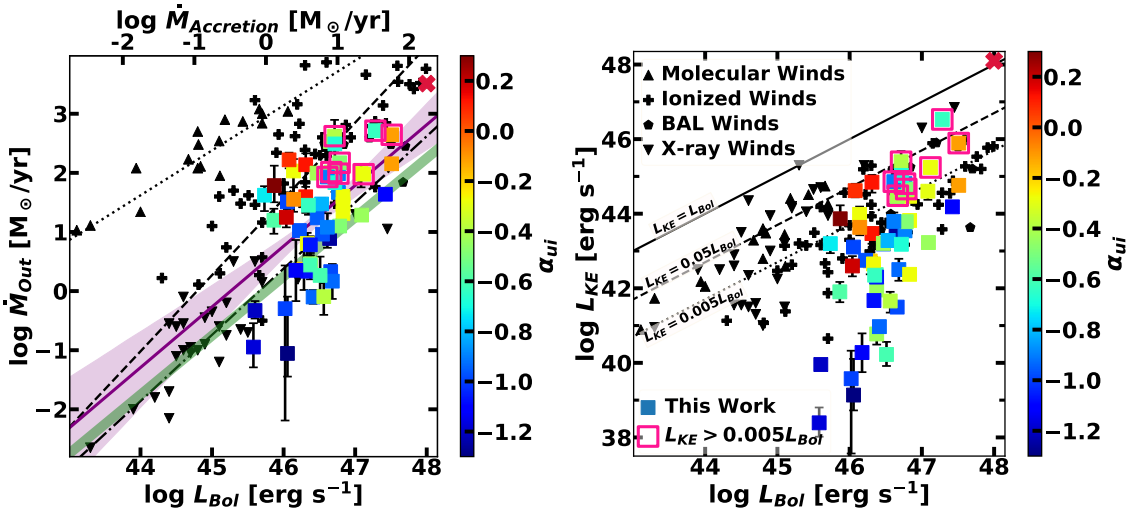

Figure 5.22: Our sample of FeLoBAL outflows and the compilation of outflows from Fiore et al. (2017). *Left panel*: the regression slopes shown as the dotted, dashed, and dotted-dashed lines for the molecular outflows, ionized winds, and X-ray outflows, respectively, taken from Fiore et al. (2017). The green line has a slope of one that represents $\dot{M}_{Out} = \dot{M}_{Accretion}$ (assuming the energy conversion efficiency, $\eta = 0.1$). The purple line (shade) showing the regression for our sample of FeLoBALs has the slope of 1.02 ± 0.25 which is consistent with both ionized winds (1.29 ± 0.38; dashed line) and X-ray outflows (1.12 ± 0.16; dotted-dashed line). This result is also consistent with $\dot{M}_{Out}/\dot{M}_{Accretion} \sim 3$, although we observe a wide range of this ratio from ∼0.04 to ∼80 among the objects in our sample. *Right panel*: the solid, dashed, and dotted lines show $L_{KE} = 1.0,\ 0.05,\ 0.005\ L_{Bol}$, respectively. Pink square outlines denote the powerful outflows ($L_{KE}/L_{Bol} > 0.005$) in our sample that have well-constrained physical parameters and outflow properties. The red cross represents the outflow in SDSS J1352+4239 (Choi et al., 2020). The vertical error bars show 2σ (95.45%) uncertainties.

Tombesi et al., 2010) to molecular winds at kiloparsec scales (e.g., Cicone et al., 2014). BAL outflows (e.g., Arav et al., 2018; Leighly et al., 2018; Choi et al., 2020) and the outflows seen as blueshifted [O III]$\lambda\lambda 4959, 5007$ emission lines (e.g., Harrison et al., 2014; Zakamska et al., 2016) are often found at parsec to kiloparsec scales, i.e., between the size scales of the X-ray and molecular outflows. It is conceivable that the different forms of outflows we observe are related and originate in the same AGN-driven outflow phenomenon.

Fiore et al. (2017) compiled an extensive list of quasar outflows and their properties with more than one hundred wind measurements from the literature, limited to those that have robust estimates of the physical sizes of the outflows. Only 7 BAL outflows were included in their sample, possibly because BAL outflows were not the main focus of their investigation. Figure 5.22 shows our FeLoBAL outflows ($v_{off} < 0\ \mathrm{km\ s^{-1}}$) combined with the Fiore et al. (2017) sample, as well as the FeLoBAL outflow in SDSS J135246.37+423923.5 (Choi et al., 2020). The color bar illustrates our observation of a strong relationship between the outflow properties and the observed shape of the SED. Outflows found in objects with flatter SED slope tend to be more massive and powerful, which is expected given there is a strong relationship between the outflow velocity and the slope of the SED (§ 5.6.1; § 5.7.3).

Similar to the other forms of quasar outflows, $\dot{M}$ and L_{KE} both increase with L_{Bol} in our FeLoBAL sample. We performed a Bayesian linear regression using `linmix`[5], a python implementation of Kelly (2007), to determine how the correlation we found among the FeLoBALs in our sample compares with the other outflow channels. We took into account the uncertainties associated with $\dot{M}_{Out}$ for the regression analysis. The log linear slope for our FeLoBALs is 1.02 ± 0.25 which is similar to the values Fiore et al. (2017) found for other types of quasar outflows, except for the molecular outflows which were found to have a flatter slope of 0.76 ± 0.06 and higher mass outflow rates. Our slope is steeper than the values expected from the theoretical models (e.g., King & Pounds, 2015, $\dot{M}_{out} \propto L_{Bol}^{1/3}$); however, as Fiore et al. (2017) pointed out in their discussion, the discrepancy might be explained by the presence of multiphase winds (i.e., underestimated $\dot{M}_{out}$). Our regression slope for FeLoBALs corresponds to the ratio between the mass outflow rate and the mass accretion rate of 3. However, there is a large range in this ratio among the objects in our sample, from ∼0.04 to ∼80, more than 2 orders of magnitude. This result strongly suggests that a simple prescription of a fixed ratio between the mass outflow rate and mass accretion (or inflow) rate used in the subgrid

[5]https://github.com/jmeyers314/linmix/

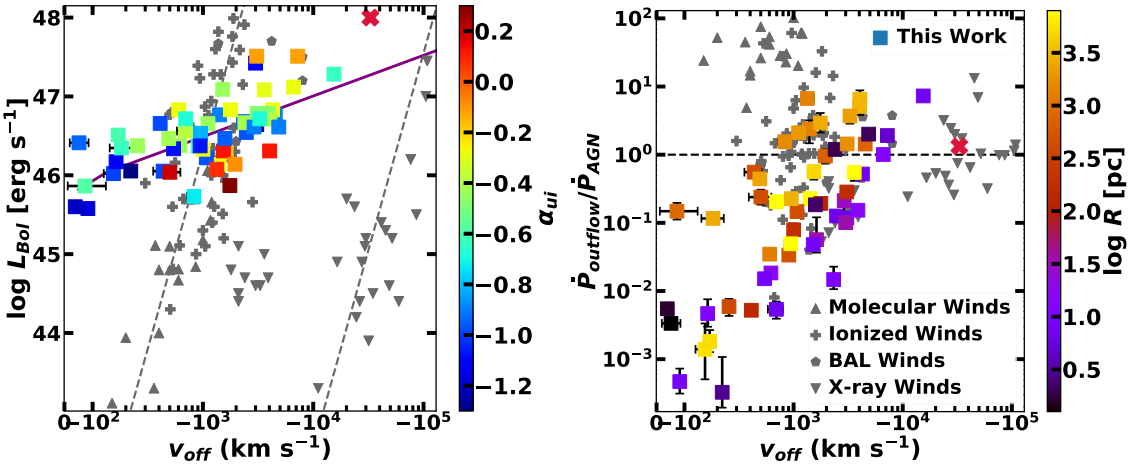

Figure 5.23: *Left panel*: the bolometric luminosity as a function of outflow velocity. The grey points represent the compilation of outflows from Fiore et al. (2017) and the red cross shows the FeLoBAL outflow in SDSS J1352+4239 (Choi et al., 2020). The purple line represents the regression slope, $L_{Bol} \propto v_{off}^{0.5}$, for our sample of FeLoBAL outflows which differs dramatically from the $L_{Bol} \propto v_{off}^{5}$ scaling (dashed grey lines) described in Fiore et al. (2017). *Right panel*: the momentum flux ratio ($\dot{P}_{outflow}/\dot{P}_{AGN}$) as a function of outflow velocity. The dashed horizontal line marks the expected ratio for a momentum conserving outflow. The error bars show 95% uncertainties.

physics in cosmological simulations (e.g., Choi et al., 2012) may not be adequate to reproduce realistic quasar outflows and mechanical quasar feedback from BAL winds. The sample of FeLoBAL quasars we analyzed contains a number of BALs with low outflow velocities ($|v_{off}| < 1000\mathrm{km\ s^{-1}}$, Figure 5.5), which are seen in the right panel of Figure 5.22 in the comparatively lower values of L_{KE}. Objects with weak or less massive outflows possibly have not been included in the Fiore et al. (2017) compilation or have not been analyzed in detail due to publication bias. The objects in our sample, on the other hand, were chosen to either have low redshift (Leighly et al., 2022) or from the objects analyzed by Farrah et al. (2012), and are included in the sample regardless of the strength of the outflow.

We found a positive correlation between L_{Bol} and v_{off} in our sample of FeLoBAL outflows (left panel in Figure 5.23) that is consistent with trends observed in quasar outflows in general (e.g., Laor & Brandt, 2002; Ganguly et al., 2007; Spoon et al., 2013;

Veilleux et al., 2013b; Fiore et al., 2017). Also, BALs with higher outflow velocities are found in objects with flatter or redder SED for a given bolometric luminosity (§ 5.7.3). This further propagates to the mass outflow rates and kinetic luminosity of the outflows (Figure 5.22) where for a given bolometric luminosity, objects that are redder have more massive and powerful outflows.

In a simple model for radiatively accelerated outflows where the wind is driven by the scattering of photons, and that process provides the momentum to accelerate the gas (i.e., a momentum-driven/conserving outflow), the maximum value for the momentum flux ratio ($\dot{P}_{outflow}/\dot{P}_{AGN}$; $\dot{P}_{outflow} = \dot{M}_{out}v_{outflow},\ \dot{P}_{AGN} = L_{Bol}/c$) is about 1 (e.g., King, 2003; King & Pounds, 2003). The right panel in Figure 5.23 shows that the FeLoBALs from our sample mostly show $\dot{P}_{outflow}/\dot{P}_{AGN} \lesssim 1$ and only a small fraction of outflows with high velocities have $1 \lesssim \dot{P}_{outflow}/\dot{P}_{AGN} \lesssim 10$. The distribution in momentum flux ratios can be ascribed to the relationship that outflows at larger distances from the center ($\log R$) have larger momentum flux ratios due to the winds being more massive ($\dot{M} \propto RN_Hv$). However, it is also possible that the bolometric luminosity may have changed since the winds were launched thus potentially creating a large range of the momentum flux ratios depending on how the luminosities evolved in these objects (e.g., Ishibashi & Fabian, 2018; Zubovas, 2018). For instance, King et al. (2011) showed that an outflow may persist for an order of magnitude longer than the duration of the AGN event that powered it.

The outflows that have $\dot{P}_{outflow}/\dot{P}_{AGN} \gg 1$ may require different acceleration mechanisms to explain the large momentum load. Dust in the outflows can increase the opacity of the gas and harness the momentum of the photons more effectively and this mechanism could potentially produce a momentum flux ratio above unity (e.g., Fabian et al., 2008, 2018). For the compact outflows with the highest outflow velocities, it seems likely the dust opacity has contributed to the momentum flux (§ 5.7.3). Molecular winds located at large distances ($\log R \gtrsim 2$ [pc]) also have high momentum flux ratios ($\dot{P}_{outflow}/\dot{P}_{AGN} > 10$); these outflows are thought to be accelerated by an energy conserving outflow mechanism (e.g., King & Pounds, 2015). A large fraction of the FeLoBAL outflows in our sample

with high $\dot{P}_{outflow}/\dot{P}_{AGN}$ are found at large distances ($\log R \sim 3$ [pc]) which supports the energy conserving outflow scenario. Conversely, not all distant FeLoBAL outflows have high momentum flux ratios and the in-situ wind formation model postulated by Faucher-Giguère et al. (2012) may explain the properties of these outflows more suitably.

5.7.5. Implications for AGN feedback

In order for cosmological models and theoretical calculations to successfully explain the co-evolution of the galaxies and the central black holes and to reproduce AGN feedback, the energy input from the AGNs to the host galaxies needs to be at least $0.5 \sim 5\%$ of the bolometric luminosity of the quasar (e.g., Scannapieco & Oh, 2004; Di Matteo et al., 2005; Hopkins & Elvis, 2010). From the 55 FeLoBAL outflows ($v_{off} < 0$ km s^{-1}), we found that 8 BALs that have kinetic luminosities greater than the 0.5% of the quasar bolometric luminosity. Out of 50 FeLoBAL quasars from the sample, 9 objects with BAL signatures were identified with powerful BAL outflows (note, two high-velocity outflows in SDSS J1448+4043 combined have $L_{KE} > 0.005 L_{Bol}$). Five objects out of the 9 with energetic outflows showed overlapping trough features in the spectra (§ 5.6.4).

We identify a couple of reasons why this number may be underestimating the feedback potential of FeLoBAL outflows. First, we may not be finding many energetic outflows because our sample is dominated by objects with relatively low bolometric luminosities (median $\log L_{bol} \sim 46.4$ [erg s^{-1}]). Energetic outflows are found in luminous quasars and the outflow strength is correlated with the bolometric luminosity (Figure 5.22 right panel). This is further highlighted by the fact that the 9 objects with energetic outflows are among the most luminous quasars in our sample ($\log L_{bol} > 46.6$ [erg s^{-1}]). For example, if we limit our sample to include only high luminosity objects, then we find that 50% of our FeLoBAL quasars have energetic outflows sufficient to power quasar feedback ($46.6 < \log L_{Bol} < 47.6$ [erg s^{-1}]; 18 objects). This result is similar to what Miller et al. (2020) found in their sample of BAL quasars that have similar bolometric luminosity range as this high luminosity subset. The flux-limited nature of survey such as the SDSS means

<table>
<tr><td></td><td>R < 1 pc</td><td>1 < R < 10 pc</td><td>10 < R < 100 pc</td><td>100 < R < 1000 pc</td><td>R > 1000 pc</td></tr>
<tr><td>Quasar Property</td><td>Accretion disk, broad line region</td><td>Torus</td><td>Torus, polar dust, narrow line region (NLR)</td><td>NLR, extended NLR (ENLR)</td><td>ENLR, galaxy</td></tr>
<tr><td>Outflow Channels</td><td>Ultra fast outflows (UFOs)</td><td>BALs</td><td>BALs, ionized outflows (e.g., [OIII])</td><td colspan="2">BALs, ionized outflows, molecular outflows (e.g., CO)</td></tr>
<tr><td>Spectral Morphology</td><td rowspan="5">No FeLoBALs observed</td><td>Overlapping Trough, Loitering BAL
(excited state FeII up to ~ 5 eV; iron peak elements, e.g., CrII, MnII)</td><td colspan="2">Spectral archetype of FeLoBALs
(mainly ground state FeII and MgII; excited state FeII up to ~ 1 eV)</td><td>Resemble intervening absorption systems
(weak or no excited state FeII)</td></tr>
<tr><td>FeLoBAL Gas Properties (Ionization parameter, log U; density log n)</td><td>log U > -1
log n > 6 [cm^{-3}]</td><td>log U ~ -2
log n > 6 [cm^{-3}]</td><td>log U ~ -2
log n < 6 [cm^{-3}]</td><td>log U < -2
log n < 3 [cm^{-3}]</td></tr>
<tr><td>Observed Kinematic Properties</td><td>$-15{,}400 \lesssim v_{off} \lesssim 120$ km s^{-1}
$280 \lesssim v_{width} \lesssim 7{,}400$ km s^{-1}</td><td colspan="2">$-6{,}600 \lesssim v_{off} \lesssim 640$ km s^{-1}
$350 \lesssim v_{width} \lesssim 8{,}800$ km s^{-1}</td><td>$-4{,}000 \lesssim v_{off} \lesssim -150$ km s^{-1}
$140 \lesssim v_{width} \lesssim 4{,}300$ km s^{-1}</td></tr>
<tr><td>Gas Confinement and Structure</td><td>$-3 \lesssim \log \Delta R/R \lesssim 0$</td><td colspan="3">$-6 \lesssim \log \Delta R/R \lesssim -4$</td></tr>
<tr><td>Plausible Acceleration Mechanisms</td><td colspan="2">Radiative line driving, dust acceleration</td><td>Radiative line driving,
in-situ formation by “cloud-crushing”</td><td>In-situ formation by “cloud-crushing”</td></tr>
</table>

Figure 5.24: The summary of FeLoBAL properties found in our sample.

that more luminous objects are found at higher redshifts, and we expect such objects to have more powerful outflows.

Another reason that the outflow energy may be underestimated for FeLoBALs analyzed in this work is that they were calculated from the BAL physical properties estimated from the low-ionization lines, mainly using Fe II and Mg II absorption lines. (Fe)LoBALs also show absorption lines from the high-ionization species (e.g., C IV, Si IV) in the spectra and they often show larger widths with higher outflow velocities (e.g., Voit et al., 1993; Hamann et al., 2019a). Thus we are not including the L_{KE} contributed by the higher velocity portion of the high-ionization lines. In other words, the kinetic luminosity estimates based only on low-ionization lines may be taken as lower limits. Once taking these two effects into consideration, the distributions of FeLoBAL outflows in our sample described in § 5.7.4 may shift to higher velocities and may not appear relatively weaker or less massive compared to other forms of outflows included in the Fiore et al. (2017) compilation.

5.8. Summary

In this work, we presented the results and analysis from the first systematic study of a large sample of low redshift FeLoBAL quasars. This work increases the number of well studied FeLoBAL quasars by a factor of five. We were able to constrain the physical properties of the FeLoBAL outflows from the best-fitting *SimBAL* models and quantify the outflow properties. The summary of FeLoBAL properties is shown in Figure 5.24. Our principal results are the following:

- We performed the first systematic study of a sample of 50 low redshift ($0.66 < z < 1.63$) FeLoBAL quasars using *SimBAL*. From the best-fitting *SimBAL* models, we were able to identify 60 FeLoBAL components and constrain their physical properties as well as calculate their outflow properties (Figure 5.1; § 5.5.2).

- We found a wide range of ionization parameters ($\log U \sim -4$ to 1.2) and densities ($\log n \sim 2.8 - 8.0$ [cm^{-3}]) from our FeLoBALs, each spanning more than five orders of magnitude (Figure 5.4). The forward modeling technique used in *SimBAL* enabled us to analyze high-$\log U$ FeLoBALs from heavily absorbed FeLoBAL quasar spectra.

- The outflow properties calculated using the physical properties extracted from best-fitting *SimBAL* models revealed a wide range of outflow locations ($\log R \sim 0.0 - 4.4$ [pc]; Figure 5.6). We found a significant correlation between outflow strength (L_{KE}) and outflow velocity ($v_{outflow}$) from our sample (Figure 5.8) and confirmed that outflow velocity is the principal factor in determining the outflow strength.

- From the best-fitting *SimBAL* models, we identified multiple outflow components in $\sim 18\%$ of the FeLoBAL quasars in our sample. The higher-velocity components had higher $\log U$ and some of them played a role in creating the overlapping trough BALs (§ 5.6.2; 5.6.4). The line profiles extracted from the *SimBAL* models showed discrete outflow gas structures and demonstrated how the BALs from the rare line transitions

(e.g., He I*, Balmer series) that are found in the rest-optical band alone can be used to estimate the distances and physical properties of the FeLoBAL outflows (Figure 5.16).

- Eight FeLoBAL quasars in our sample showed overlapping trough features in the spectra (Figure 5.17). All of the overlapping trough BALs were found close to the central engine $\log R \lesssim 1$ [pc]. Their kinematic properties showed a wide range ($v_{off} \sim -15,400$ to -50 km s^{-1}, $v_{width} \sim 900-7,400$ km s^{-1}), a fact that suggests that a large width is not required to create an overlapping trough BAL. The five objects ($\sim 63\%$) that showed typical overlapping trough features (e.g., high-velocity troughs reaching near-zero flux at the bottom) and anomalous reddening in the spectra have powerful outflows with L_{KE} exceeding 0.5% of L_{Bol}.

- We identified a new class of FeLoBALs dubbed loitering outflows (§ 5.6.5). They are characterized by compact outflows ($\log R < 1$ [pc]) and low outflow velocities ($|v_{off}| \lesssim 2,000$ km s^{-1}). Loitering outflows have high $\log U$ and high $\log n$ gas with large opacity; however, $\sim 50\%$ of them showed no absorption in the emission lines and $\sim 27\%$ of loitering outflow objects required an additional step-function partial covering in the model because only a fraction of the underlying continuum emission was absorbed by the BAL (§ 5.5.1.1). The FeLoBAL quasars with loitering outflows can be identified by predicted Balmer absorption lines and some of them show overlapping troughs as well. Their outflow property distributions (Figure 5.18) suggest that these objects may represent a distinct sub-population within FeLoBAL quasars.

- We found that the compact outflows are located in the vicinity of a dusty torus where a dusty wind scenario can be used to explain the origin and the acceleration mechanism of these FeLoBALs (§ 5.7.3). A force multiplier analysis showed that radiative line driving alone may not be sufficient to accelerate the compact outflows at $R \lesssim 100$ pc to extreme velocities ($v_{off} \sim -10,000$ km s^{-1}). An additional mode

of acceleration (e.g., dust opacity; Figure 5.20) may be needed to explain these high velocity outflows. In-situ formation of FeLoBALs from the ISM (Faucher-Giguère et al., 2012) is a plausible model to describe the outflow properties of the kiloparsec-scale winds.

- We found a significant correlation between SED slope (α_{ui}) and outflow velocity (Figure 5.21). The objects that have flatter SED slopes have faster and more powerful FeLoBAL outflows. A flatter SED slope may indicate strong dust reddening, noting that the SED slope also depends on intrinsic AGN properties such as slope of the rest-optical/UV power-law and the strength of torus emission.

- We found that more luminous quasars have more powerful outflows (Figure 5.9; 5.22), consistent with trends observed in other forms of quasar outflows. The FeLoBAL outflows in our sample showed a wide range of the ratio between the mass outflow rate and the mass accretion rate, from $\sim$0.04 to $\sim$80, more than 2 orders of magnitude. This wide distribution suggests that a simple fixed ratio prescription used in some cosmological simulations may be insufficient for accurate depiction of feedback by BAL outflows

- Only nine objects out of 50 FeLoBAL quasars have sufficiently powerful outflows to produce quasar feedback. We suspect that a low fraction of powerful outflows is a consequence of the low redshift and therefore lower luminosity of our sample (median $\log L_{bol} \sim 46.4$ [erg s^{-1}]). In addition, our analysis relied exclusively on the information extracted from the low-ionization lines, and it is known that the high-ionization lines from the same outflow tend to show extended structures to higher velocities. Therefore, our kinetic luminosity estimates may be considered to be lower limits.

We have expanded the number of FeLoBAL quasars that are analyzed in detail by a factor of five. More importantly, the detailed analysis made possible by *SimBAL* has

fleshed out our picture of quasar outflows, allowing us to study trends as a function of location and velocity.

Appendix

5.A. FeLoBAL Outflow Properties

The best-fit parameters from the *SimBAL* models and the derived outflow properties are presented in Table 5.A.1 and 5.A.2, respectively. 95% uncertainties estimated from the posterior probability distributions are reported. For the BAL components that were fit using tophat accordion models, the range of values among the bins are reported. We report the opacity (column density) weighted velocity as the representative BAL velocity (v_{off}) and the widths of BALs have been measured from the continuum emission normalized spectra (I/I_0) using the Mg IIλ2796 line transition (§ 5.4.2). The covering-fraction-corrected hydrogen column density ($\log N_H$; § 5.5.3) for each individual BAL is reported in Table 5.A.2.

Table 5.A.1. *SimBAL Fit Results*

Name	$\log U$	$\log n$ [cm^{-3}]	$\log N_H - \log U$ [cm^{-2}]	v_{off} (km s^{-1})	v_{width} (km s^{-1})	$\log a$	Type[a]
J0111+1426	$-3.43^{+0.39}_{-0.29}$	< 2.80	$22.53 - 23.15$	-3600 ± 30	760^{+0}_{-30}	-0.53 to 0.48	
J0158−0046	$-1.06^{+0.35}_{-0.33}$	$7.15^{+0.39}_{-0.38}$	$23.06 - 23.64$	120^{+120}_{-80}	1600^{+210}_{-80}	$0.70 - 1.13$	LB, IF
J0242−0722	-3.89 to -2.12	$4.24^{+0.17}_{-0.18}$	$22.96 - 23.44$	-950^{+60}_{-80}	1300^{+70}_{-80}	$0.13 - 0.51$	
J0258−0028a	$-2.12^{+0.08}_{-0.07}$	$7.15^{+0.08}_{-0.12}$	$22.21 - 23.73$	-620 ± 20	2300^{+0}_{-20}	-0.99 to 0.89	
J0258−0028b	$-2.40^{+0.27}_{-0.41}$	$4.74^{+0.49}_{-0.40}$	$23.69^{+0.08}_{-0.18}$	-260^{+20}_{-30}	620^{+70}_{-30}	$0.44^{+0.13}_{-0.23}$	
J0300+0048	-1.85 ± 0.001	$7.96^{+0.01}_{-0.02}$	$23.09 - 23.72$	-6600 ± 30	8800^{+0}_{-30}	$0.08 - 0.60$	OT
J0802+5513	$-2.54^{+0.04}_{-0.05}$	4.40 ± 0.04	$22.99 - 23.10$	200^{+9}_{-10}	1400^{+0}_{-10}	-1.45 to 0.36	IF
J0809+1818	$-1.53^{+0.09}_{-0.07}$	$7.63^{+0.07}_{-0.08}$	$22.22 - 23.68$	-3100^{+50}_{-60}	4600^{+0}_{-60}	-1.19 to 1.41	
J0813+4326	< -4.00	< 2.80	$22.08 - 22.92$	-940^{+120}_{-60}	550^{+70}_{-60}	-0.54 to 0.11	
J0835+4242	-1.61 ± 0.06	5.18 ± 0.05	$23.00 - 23.03$	-410 ± 10	1200^{+70}_{-10}	$0.58 - 1.26$	
J0840+3633	-1.97 ± 0.03	$7.45^{+0.03}_{-0.01}$	$23.09 - 23.22$	-3000 ± 8	3400^{+0}_{-8}	-0.68 to 0.99	
J0916+4534	$-0.14^{+0.30}_{-0.21}$	$5.87^{+0.22}_{-0.28}$	$23.67^{+0.08}_{-0.21}$	80 ± 10	550^{+70}_{-10}	1.20 ± 0.05	LB, IF

Table 5.A.1 (cont'd)

Name	$\log U$	$\log n$ [cm^{-3}]	$\log N_H - \log U$ [cm^{-2}]	v_{off} (km s^{-1})	v_{width} (km s^{-1})	$\log a$	Type[a]
J0918+5833	$0.54^{+0.36}_{-0.41}$	$3.92^{+0.27}_{-0.21}$	23.01 ± 0.07	640 ± 10	830^{+70}_{-10}	$0.88^{+0.06}_{-0.07}$	IF
J0944+5000	$-2.51^{+0.15}_{-0.20}$	$6.85^{+0.67}_{-1.29}$	$22.50 - 23.18$	-1600 ± 90	3800^{+140}_{-90}	$0.15 - 1.78$	
J1006+0513	$1.09^{+0.01}_{-0.07}$	$6.13^{+0.06}_{-0.10}$	$22.95 - 23.71$	-2400 ± 110	3500^{+140}_{-110}	$0.86 - 2.43$	LB
J1019+0225	$-0.89^{+0.18}_{-0.15}$	$7.29^{+0.15}_{-0.18}$	$23.20 - 23.68$	-1500 ± 20	1900^{+0}_{-20}	$0.39 - 1.42$	OT, LB
J1020+6023a	$-1.94^{+0.05}_{-0.01}$	$7.60^{+0.03}_{-0.05}$	$23.16 - 23.73$	-3900^{+10}_{-20}	1300^{+70}_{-20}	$0.16 - 0.38$	
J1020+6023b	$-2.92^{+0.12}_{-0.08}$	$4.40^{+0.10}_{-0.13}$	$22.55 - 23.42$	-3100^{+20}_{-30}	1700^{+70}_{-30}	-1.18 to 0.80	
J1022+3542	$-1.98^{+0.25}_{-0.41}$	< 2.80	$22.10 - 22.93$	-1400^{+50}_{-60}	2200^{+0}_{-60}	-0.25 to 2.08	
J1023+0152	$-0.80^{+1.55}_{-0.59}$	$7.04^{+0.64}_{-1.26}$	$23.42^{+0.26}_{-0.40}$	-220 ± 20	550^{+70}_{-20}	1.27 ± 0.10	LB
J1030+3120	-2.17 ± 0.04	$7.97^{+0.57}_{-0.59}$	$22.73 - 23.10$	-2300 ± 20	3000^{+410}_{-20}	-0.21 to 1.55	
J1039+3954a	$-2.50^{+0.35}_{-0.42}$	< 2.80	$23.10^{+0.19}_{-0.12}$	-4000 ± 10	410^{+70}_{-10}	$0.07^{+0.20}_{-0.24}$	
J1039+3954b	$-2.89^{+0.35}_{-0.56}$	< 2.80	23.22 ± 0.15	-1500 ± 10	550^{+70}_{-10}	$0.10^{+0.18}_{-0.32}$	
J1044+3656a	-2.43 ± 0.01	$4.58^{+0.04}_{-0.05}$	$21.98 - 23.02$	-4500^{+6}_{-8}	1600^{+0}_{-8}	-1.04 to 0.32	

Table 5.A.1 (cont'd)

Name	$\log U$	$\log n$ [cm^{-3}]	$\log N_H - \log U$ [cm^{-2}]	v_{off} (km s^{-1})	v_{width} (km s^{-1})	$\log a$	Type[a]
J1044+3656b	$-3.67^{+0.04}_{-0.05}$	< 2.80	$21.57 - 23.40$	-1400^{+10}_{-9}	1400^{+0}_{-9}	-0.96 to 2.29	
J1125+0029a	$0.36^{+0.16}_{-0.11}$	$7.30^{+0.13}_{-0.15}$	$23.21 - 23.74$	-50 ± 30	830^{+0}_{-30}	$1.24 - 2.04$	OT, LB
J1125+0029b	$-0.45^{+0.49}_{-0.37}$	$5.93^{+0.41}_{-0.35}$	23.06 ± 0.02	380 ± 30	2800^{+140}_{-30}	0.94 ± 0.07	IF
J1128+0113	$-1.75^{+0.007}_{-0.001}$	$7.37^{+0.02}_{-0.01}$	$22.16 - 23.71$	-540^{+10}_{-20}	3000^{+0}_{-20}	-1.00 to 2.08	LB
J1129+0506	$-2.81^{+0.51}_{-0.35}$	$3.72^{+0.34}_{-0.44}$	$21.91 - 23.42$	-4000^{+280}_{-270}	2600^{+0}_{-270}	-0.41 to 0.57	
J1145+1100	$-0.30^{+0.70}_{-0.84}$	$5.54^{+0.76}_{-0.58}$	$23.11^{+0.22}_{-0.09}$	-160 ± 4	350^{+0}_{-4}	$0.31^{+0.13}_{-0.21}$	
J1154+0300	-0.60 to 1.40	7.27 ± 0.04	$22.87 - 23.72$	-15400 ± 50	7400^{+0}_{-50}	$0.83 - 1.43$	OT
J1158−0043	$-2.15^{+0.27}_{-0.45}$	< 2.80	$22.08 - 23.03$	-180^{+40}_{-50}	1500^{+0}_{-50}	-0.36 to 0.37	
J1200+6322	$-1.77^{+0.15}_{-0.17}$	$3.73^{+0.13}_{-0.16}$	$21.76 - 23.05$	-440^{+80}_{-70}	3200 ± 70	-0.35 to 1.51	
J1206+0023a	$1.09^{+0.26}_{-0.34}$	$6.03^{+0.16}_{-0.09}$	$22.94 - 23.36$	-4900^{+160}_{-130}	3700^{+1200}_{-130}	$1.42 - 2.08$	OT
J1206+0023b	$-1.78^{+0.15}_{-0.14}$	$6.59^{+0.70}_{-0.52}$	$23.01 - 23.07$	-2900^{+160}_{-150}	5400^{+70}_{-150}	$0.12 - 0.59$	
J1208+6240	$-1.31^{+0.65}_{-0.41}$	$6.17^{+0.49}_{-0.66}$	$23.56^{+0.13}_{-0.27}$	-80^{+6}_{-4}	280^{+0}_{-4}	$0.74^{+0.14}_{-0.13}$	LB

Table 5.A.1 (cont'd)

Name	$\log U$	$\log n$ [cm^{-3}]	$\log N_H - \log U$ [cm^{-2}]	v_{off} (km s^{-1})	v_{width} (km s^{-1})	$\log a$	Type[a]
J1212+2514	$-2.31^{+0.15}_{-0.17}$	3.93 ± 0.29	$23.02^{+0.06}_{-0.04}$	-2000^{+9}_{-10}	480^{+0}_{-10}	$-0.92^{+0.50}_{-0.55}$	
J1214−0001	$-2.81^{+0.83}_{-1.03}$	< 2.80	$23.07^{+0.33}_{-0.13}$	-170 ± 10	280^{+0}_{-10}	$0.62^{+0.19}_{-0.31}$	
J1214+2803	$-1.70^{+0.004}_{-0.001}$	7.81 ± 0.01	$22.15 - 23.72$	-2500^{+6}_{-5}	2000^{+0}_{-5}	-1.22 to 0.53	
J1235+0132	$-1.79^{+0.26}_{-0.30}$	$7.88^{+0.44}_{-0.32}$	$22.55 - 23.69$	-700^{+110}_{-100}	2100^{+70}_{-100}	$0.25 - 1.37$	LB
J1240+4443	$-1.76^{+0.34}_{-0.36}$	< 2.80	$22.20 - 23.38$	-70 ± 60	1000^{+70}_{-60}	$0.33 - 1.26$	
J1321+5617	$0.17^{+0.20}_{-0.15}$	$6.13^{+0.13}_{-0.17}$	$23.07 - 23.75$	-40^{+10}_{-20}	620^{+0}_{-20}	$0.91 - 1.14$	LB
J1324+0320	< -3.00	$5.04^{+0.35}_{-0.25}$	$22.71 - 23.53$	-900^{+70}_{-60}	2200^{+70}_{-60}	$0.30 - 2.19$	
J1336+0830	< -3.00	$5.06^{+0.03}_{-0.04}$	$21.95 - 23.79$	-1100^{+20}_{-7}	1900^{+0}_{-7}	-1.07 to 0.70	
J1355+5753	$-2.41^{+0.41}_{-0.63}$	< 2.80	$22.11 - 23.42$	-830^{+110}_{-90}	1600^{+0}_{-90}	-0.22 to 1.86	
J1356+4527	$-1.85^{+0.17}_{-0.20}$	< 2.80	$21.93 - 23.14$	-1300^{+140}_{-200}	4300^{+70}_{-200}	-0.16 to 1.07	
J1427+2709a	$-1.71^{+0.17}_{-0.65}$	< 2.80	$22.08 - 23.22$	-3300^{+30}_{-60}	970^{+0}_{-60}	-0.54 to 1.09	
J1427+2709b	$-3.64^{+0.07}_{-0.09}$	< 2.80	$22.30 - 23.40$	-700 ± 10	1200^{+0}_{-10}	-1.05 to 1.31	

Table 5.A.1 (cont'd)

Name	$\log U$	$\log n$ [cm^{-3}]	$\log N_H - \log U$ [cm^{-2}]	v_{off} (km s^{-1})	v_{width} (km s^{-1})	$\log a$	Type[a]
J1448+4043a	$-0.50^{+0.008}_{-0.002}$	6.80 ± 0.01	$23.49 - 23.74$	-4300 ± 30	4500^{+0}_{-30}	$1.24 - 1.67$	OT
J1448+4043b	$-2.50^{+0.01}_{-0.02}$	$6.38^{+0.01}_{-0.02}$	$22.73 - 23.80$	-1800 ± 20	4300^{+0}_{-20}	-1.48 to 0.74	
J1448+4043c	< -3.00	$4.76^{+0.05}_{-0.06}$	23.72 ± 0.03	-600 ± 2	550^{+0}_{-2}	$-0.82^{+0.11}_{-0.13}$	
J1517+2328	< -3.00	$4.73^{+0.20}_{-0.25}$	$23.03 - 23.60$	-500^{+110}_{-120}	1700^{+280}_{-120}	-0.23 to 0.62	
J1527+5912	$-1.57^{+0.08}_{-0.10}$	< 2.80	$22.04 - 22.94$	-1100 ± 30	2600^{+0}_{-30}	-0.86 to 0.87	
J1531+4852	$-3.40^{+1.11}_{-0.56}$	< 2.80	$22.51^{+0.34}_{-0.44}$	-150^{+30}_{-7}	140^{+70}_{-7}	$-0.89^{+0.84}_{-0.59}$	
J1556+3517a	$1.09^{+0.005}_{-0.013}$	$6.21^{+0.06}_{-0.03}$	$22.95 - 23.28$	-7200^{+50}_{-60}	3500^{+0}_{-60}	$1.03 - 2.06$	OT
J1556+3517b	$-2.18^{+0.06}_{-0.04}$	$6.42^{+0.12}_{-0.08}$	$22.71 - 23.72$	-3100^{+40}_{-50}	4300^{+0}_{-50}	-1.33 to 0.67	
J1644+5307	$0.11^{+0.20}_{-0.17}$	$6.79^{+0.14}_{-0.16}$	$23.23 - 23.61$	-1600 ± 30	900^{+70}_{-30}	$0.93 - 2.10$	OT, LB
J2107+0054	$-2.86^{+0.69}_{-0.56}$	< 2.80	$22.05 - 23.13$	-1800^{+90}_{-110}	1900^{+550}_{-110}	-0.37 to 1.14	
J2135−0320	$-2.03^{+0.11}_{-0.13}$	$2.92^{+0.15}_{-0.11}$	$22.28 - 23.11$	-490 ± 20	1200^{+0}_{-20}	-0.93 to 0.71	
J2307+1119	$-2.41^{+0.28}_{-0.48}$	$5.38^{+0.28}_{-0.23}$	$22.98 - 23.05$	-1000^{+60}_{-50}	2500^{+70}_{-50}	$0.30 - 1.01$	

[a]OT, overlapping-trough BAL; LB, loitering BAL; IF, inflow.

Table 5.A.2. Derived Outflow Properties

Name	$\log N_H$ [cm^{-2}]	$\log R$ [pc]	$\log \dot{M}_{out}$ [M$_\odot$ yr^{-1}]	$\log \dot{M}_{in}$ [M$_\odot$ yr^{-1}]	$\log \dot{P}$ [dyne]	$\log L_{KE}$ [erg s^{-1}]	$\log L_{Bol}$ [erg s^{-1}]	α_{ui}
J0111+1426	$19.35^{+0.28}_{-0.17}$	> 4.31	$1.99^{+0.15}_{-0.23}$	$\cdots$	$36.35^{+0.14}_{-0.23}$	$44.60^{+0.14}_{-0.23}$	47.08	-0.30
J0158−0046	$21.92^{+0.28}_{-0.26}$	0.24 ± 0.06	$-1.31^{+0.42}_{-0.51}$	$-0.82^{+0.42}_{-0.35}$	$32.06^{+0.43}_{-0.56}$	$39.33^{+0.44}_{-0.63}$	45.42	-1.29
J0242−0722	$20.56^{+0.16}_{-0.15}$	$3.47^{+0.28}_{-0.77}$	$1.47^{+0.10}_{-0.09}$	$\cdots$	35.41 ± 0.09	43.28 ± 0.09	46.53	-0.82
J0258−0028a	21.61 ± 0.04	1.26 ± 0.04	$0.41^{+0.07}_{-0.05}$	$\cdots$	$34.16^{+0.08}_{-0.05}$	$41.95^{+0.09}_{-0.06}$	46.37	-0.44
J0258−0028b	$20.70^{+0.24}_{-0.33}$	$2.59^{+0.21}_{-0.17}$	$0.46^{+0.18}_{-0.26}$	$\cdots$	$33.67^{+0.20}_{-0.27}$	$40.77^{+0.22}_{-0.28}$	46.37	-0.44
J0300+0048	22.31 ± 0.01	1.08 ± 0.01	1.98 ± 0.01	$\cdots$	36.64 ± 0.01	45.24 ± 0.01	47.12	-0.28
J0802+5513	$20.92^{+0.03}_{-0.04}$	$2.96^{+0.03}_{-0.02}$	0.33 ± 0.05	1.03 ± 0.03	33.55 ± 0.06	40.73 ± 0.06	46.62	-0.12
J0809+1818	$21.79^{+0.06}_{-0.05}$	$0.85^{+0.02}_{-0.01}$	0.89 ± 0.06	$\cdots$	35.24 ± 0.06	43.54 ± 0.07	46.64	-1.25
J0813+4326	$18.94^{+0.35}_{-0.17}$	> 4.05	$0.78^{+0.14}_{-0.18}$	$\cdots$	$34.59^{+0.14}_{-0.18}$	$42.30^{+0.15}_{-0.18}$	46.37	-1.06
J0835+4242	20.83 ± 0.05	2.12 ± 0.03	0.33 ± 0.04	$\cdots$	33.90 ± 0.05	41.50 ± 0.06	46.66	-0.99
J0840+3633	21.85 ± 0.02	$1.55^{+0.005}_{-0.008}$	$1.64^{+0.01}_{-0.02}$	$\cdots$	$35.95^{+0.01}_{-0.02}$	$44.18^{+0.01}_{-0.02}$	47.42	-1.11
J0916+4534a	$22.29^{+0.18}_{-0.16}$	0.58 ± 0.05	$\cdots$	$-0.47^{+0.19}_{-0.18}$	$\cdots$	$\cdots$	45.73	-1.12

Table 5.A.2 (cont'd)

Name	$\log N_H$ [cm^{-2}]	$\log R$ [pc]	$\log \dot{M}_{out}$ [M$_\odot$ yr^{-1}]	$\log \dot{M}_{in}$ [M$_\odot$ yr^{-1}]	$\log \dot{P}$ [dyne]	$\log L_{KE}$ [erg s^{-1}]	$\log L_{Bol}$ [erg s^{-1}]	α_{ui}
J0918+5833	$22.62^{+0.28}_{-0.33}$	$1.56^{+0.10}_{-0.11}$	···	$1.74^{+0.20}_{-0.26}$	···	···	46.41	-1.19
J0944+5000	$20.83^{+0.13}_{-0.15}$	$1.56^{+0.65}_{-0.32}$	$0.37^{+0.59}_{-0.35}$	···	$34.56^{+0.58}_{-0.36}$	$42.73^{+0.58}_{-0.36}$	46.28	-0.20
J1006+0513	$23.57^{+0.04}_{-0.08}$	$0.30^{+0.07}_{-0.03}$	$2.01^{+0.06}_{-0.05}$	···	$36.27^{+0.07}_{-0.06}$	44.48 ± 0.08	46.67	-0.41
J1019+0225	$22.42^{+0.10}_{-0.07}$	0.92 ± 0.03	$1.29^{+0.10}_{-0.08}$	···	$35.29^{+0.10}_{-0.09}$	$43.23^{+0.10}_{-0.09}$	47.09	-0.44
J1020+6023a	$21.60^{+0.03}_{-0.02}$	$1.15^{+0.01}_{-0.02}$	1.10 ± 0.03	···	35.49 ± 0.03	43.79 ± 0.03	46.78	-0.48
J1020+6023b	20.68 ± 0.07	3.24 ± 0.05	$2.17^{+0.07}_{-0.06}$	···	$36.46^{+0.07}_{-0.06}$	$44.66^{+0.07}_{-0.06}$	46.78	-0.48
J1022+3542	$20.98^{+0.26}_{-0.40}$	> 3.13	$2.03^{+0.20}_{-0.45}$	···	$36.04^{+0.20}_{-0.45}$	$43.98^{+0.21}_{-0.45}$	46.14	-0.28
J1023+0152	$21.35^{+1.11}_{-0.35}$	$0.46^{+0.09}_{-0.14}$	$-1.05^{+0.96}_{-0.39}$	···	$32.09^{+0.97}_{-0.40}$	$39.14^{+0.97}_{-0.41}$	46.05	-1.54
J1030+3120	$21.01^{+0.04}_{-0.05}$	$1.02^{+0.29}_{-0.27}$	$0.17^{+0.29}_{-0.30}$	···	$34.37^{+0.29}_{-0.30}$	$42.50^{+0.29}_{-0.30}$	46.68	-0.93
J1039+3954a	$20.27^{+0.29}_{-0.33}$	> 3.49	$2.14^{+0.19}_{-0.28}$	···	$36.54^{+0.19}_{-0.28}$	$44.85^{+0.19}_{-0.28}$	46.31	0.12
J1039+3954b	$19.96^{+0.27}_{-0.34}$	> 3.68	$1.60^{+0.17}_{-0.27}$	···	$35.58^{+0.17}_{-0.27}$	$43.47^{+0.17}_{-0.27}$	46.31	0.12
J1044+3656a	20.68 ± 0.01	2.89 ± 0.02	$1.99^{+0.03}_{-0.02}$	···	$36.45^{+0.03}_{-0.02}$	$44.81^{+0.03}_{-0.02}$	46.77	-0.90

Table 5.A.2 (cont'd)

Name	$\log N_H$ [cm^{-2}]	$\log R$ [pc]	$\log \dot{M}_{out}$ [M$_\odot$ yr^{-1}]	$\log \dot{M}_{in}$ [M$_\odot$ yr^{-1}]	$\log \dot{P}$ [dyne]	$\log L_{KE}$ [erg s^{-1}]	$\log L_{Bol}$ [erg s^{-1}]	α_{ui}
J1044+3656b	19.36 ± 0.03	> 4.40	1.67 ± 0.01	$\cdots$	$35.65^{+0.01}_{-0.02}$	43.54 ± 0.02	46.77	-0.90
J1125+0029a	23.05 ± 0.09	-0.04 ± 0.06	$-0.10^{+0.12}_{-0.11}$	$-0.31^{+0.14}_{-0.12}$	33.46 ± 0.13	$40.97^{+0.14}_{-0.15}$	46.41	-0.94
J1125+0029b	$21.63^{+0.43}_{-0.33}$	$1.03^{+0.22}_{-0.21}$	$\cdots$	$0.01^{+0.28}_{-0.27}$	$\cdots$	$\cdots$	46.41	-0.94
J1128+0113	21.84 ± 0.01	0.94 ± 0.01	0.34 ± 0.01	-0.50 ± 0.04	34.04 ± 0.01	$41.67^{+0.01}_{-0.02}$	46.34	-1.08
J1129+0506	$20.78^{+0.29}_{-0.27}$	$3.49^{+0.21}_{-0.30}$	$2.62^{+0.28}_{-0.27}$	$\cdots$	37.05 ± 0.28	$45.39^{+0.28}_{-0.29}$	46.71	-0.40
J1145+1100	$22.33^{+0.57}_{-0.55}$	1.05 ± 0.08	$0.35^{+0.51}_{-0.52}$	$\cdots$	$33.36^{+0.51}_{-0.52}$	$40.28^{+0.51}_{-0.53}$	46.17	-1.13
J1154+0300	23.62 ± 0.02	$0.88^{+0.03}_{-1.01}$	$2.71^{+0.03}_{-0.02}$	$\cdots$	$37.67^{+0.03}_{-0.02}$	$46.53^{+0.03}_{-0.02}$	47.28	-0.64
J1158$-$0043	$20.90^{+0.25}_{-0.36}$	> 3.40	$1.45^{+0.13}_{-0.16}$	$0.87^{+0.22}_{-0.30}$	$34.93^{+0.14}_{-0.16}$	$42.35^{+0.14}_{-0.17}$	46.35	-0.63
J1200+6322	$21.31^{+0.14}_{-0.15}$	$2.63^{+0.08}_{-0.07}$	1.51 ± 0.12	1.01 ± 0.17	35.32 ± 0.13	$43.11^{+0.14}_{-0.13}$	46.05	-0.99
J1206+0023a	$23.15^{+0.12}_{-0.16}$	$0.33^{+0.10}_{-0.09}$	$1.93^{+0.07}_{-0.09}$	$\cdots$	$36.44^{+0.07}_{-0.09}$	$44.86^{+0.08}_{-0.10}$	46.61	-0.90
J1206+0023b	$21.37^{+0.14}_{-0.13}$	$1.49^{+0.27}_{-0.36}$	$1.08^{+0.24}_{-0.35}$	$\cdots$	$35.46^{+0.24}_{-0.35}$	$43.79^{+0.24}_{-0.35}$	46.61	-0.90
J1208+6240	$21.43^{+0.39}_{-0.29}$	$0.93^{+0.17}_{-0.13}$	$-0.95^{+0.40}_{-0.34}$	$\cdots$	$31.77^{+0.41}_{-0.36}$	$38.39^{+0.41}_{-0.37}$	45.58	-1.17

Table 5.A.2 (cont'd)

Name	$\log N_H$ [cm^{-2}]	$\log R$ [pc]	$\log \dot{M}_{out}$ [M$_\odot$ yr^{-1}]	$\log \dot{M}_{in}$ [M$_\odot$ yr^{-1}]	$\log \dot{P}$ [dyne]	$\log L_{KE}$ [erg s^{-1}]	$\log L_{Bol}$ [erg s^{-1}]	α_{ui}
J1212+2514	$20.66^{+0.14}_{-0.15}$	$2.84^{+0.12}_{-0.13}$	$1.55^{+0.20}_{-0.21}$	$\cdots$	$35.64^{+0.20}_{-0.21}$	$43.63^{+0.20}_{-0.21}$	46.14	-0.09
J1214−0001b	$19.55^{+0.66}_{-0.67}$	> 3.72	$0.27^{+0.32}_{-0.30}$	$\cdots$	$33.29^{+0.33}_{-0.30}$	$40.23^{+0.34}_{-0.31}$	46.51	-0.60
J1214+2803	22.01 ± 0.01	$0.80^{+0.007}_{-0.005}$	0.96 ± 0.01	$\cdots$	35.17 ± 0.01	43.28 ± 0.01	46.54	-0.97
J1235+0132	$21.47^{+0.22}_{-0.25}$	$0.82^{+0.09}_{-0.11}$	$-0.09^{+0.23}_{-0.31}$	$-1.45^{+0.29}_{-0.37}$	$33.82^{+0.23}_{-0.31}$	$41.66^{+0.25}_{-0.31}$	46.56	-0.38
J1240+4443	21.33 ± 0.28	> 2.92	$1.20^{+0.19}_{-0.23}$	$0.92^{+0.22}_{-0.25}$	$34.56^{+0.23}_{-0.25}$	$41.91^{+0.26}_{-0.28}$	45.86	-0.59
J1321+5617	$22.89^{+0.13}_{-0.12}$	$0.23^{+0.03}_{-0.04}$	$-0.33^{+0.16}_{-0.14}$	$-0.74^{+0.11}_{-0.15}$	$32.86^{+0.16}_{-0.14}$	$39.96^{+0.15}_{-0.14}$	45.60	-1.20
J1324+0320a	$20.01^{+0.16}_{-0.06}$	> 2.71	$0.44^{+0.15}_{-0.18}$	$\cdots$	$34.42^{+0.16}_{-0.18}$	$42.37^{+0.15}_{-0.17}$	46.37	-0.61
J1336+0830	20.57 ± 0.02	> 2.66	1.02 ± 0.02	$\cdots$	34.91 ± 0.02	$42.75^{+0.02}_{-0.03}$	46.22	-0.97
J1355+5753	$20.74^{+0.33}_{-0.51}$	> 3.20	$1.62^{+0.15}_{-0.27}$	$\cdots$	$35.45^{+0.15}_{-0.26}$	$43.20^{+0.15}_{-0.26}$	45.73	-0.73
J1356+4527	$21.21^{+0.16}_{-0.18}$	> 3.12	$2.22^{+0.12}_{-0.14}$	$\cdots$	36.42 ± 0.16	44.62 ± 0.18	46.08	0.08
J1427+2709a	$20.85^{+0.15}_{-0.53}$	> 3.35	$2.49^{+0.08}_{-0.81}$	$\cdots$	$36.81^{+0.08}_{-0.81}$	$45.03^{+0.08}_{-0.80}$	46.72	-0.68
J1427+2709b	19.88 ± 0.04	> 4.35	1.83 ± 0.02	$\cdots$	35.55 ± 0.02	$43.18^{+0.02}_{-0.03}$	46.72	-0.68

Table 5.A.2 (cont'd)

Name	$\log N_H$ [cm^{-2}]	$\log R$ [pc]	$\log \dot{M}_{out}$ [M$_\odot$ yr^{-1}]	$\log \dot{M}_{in}$ [M$_\odot$ yr^{-1}]	$\log \dot{P}$ [dyne]	$\log L_{KE}$ [erg s^{-1}]	$\log L_{Bol}$ [erg s^{-1}]	α_{ui}
J1448+4043a	22.37 ± 0.01	$0.84^{+0.005}_{-0.006}$	$1.60^{+0.01}_{-0.02}$	$\cdots$	$36.07^{+0.01}_{-0.02}$	$44.47^{+0.01}_{-0.02}$	46.83	-0.28
J1448+4043b	21.41 ± 0.01	2.05 ± 0.01	1.47 ± 0.01	$\cdots$	35.64 ± 0.02	43.82 ± 0.02	46.83	-0.28
J1448+4043c	20.66 ± 0.02	> 3.11	1.31 ± 0.02	$\cdots$	34.89 ± 0.02	42.37 ± 0.02	46.83	-0.28
J1517+2328	$21.12^{+0.17}_{-0.12}$	> 2.66	$1.25^{+0.18}_{-0.17}$	$< -1.80^{+1.49}$	34.94 ± 0.22	$42.60^{+0.26}_{-0.28}$	46.04	0.19
J1527+5912	$21.44^{+0.09}_{-0.10}$	> 3.28	$2.53^{+0.06}_{-0.07}$	$\cdots$	$36.50^{+0.06}_{-0.08}$	$44.43^{+0.07}_{-0.08}$	46.65	-0.44
J1531+4852b	$18.98^{+1.23}_{-0.64}$	> 3.74	$-0.30^{+0.73}_{-1.89}$	$\cdots$	$32.69^{+0.74}_{-1.95}$	$39.57^{+0.75}_{-2.01}$	46.02	-1.00
J1556+3517a	23.34 ± 0.02	$0.69^{+0.02}_{-0.03}$	2.64 ± 0.03	$\cdots$	37.31 ± 0.03	45.89 ± 0.03	47.51	-0.11
J1556+3517b	21.69 ± 0.03	$2.22^{+0.04}_{-0.06}$	$2.15^{+0.06}_{-0.08}$	$\cdots$	$36.49^{+0.06}_{-0.08}$	$44.76^{+0.06}_{-0.08}$	47.51	-0.11
J1644+5307a	$22.91^{+0.12}_{-0.10}$	0.36 ± 0.03	$1.24^{+0.10}_{-0.09}$	$\cdots$	$35.26^{+0.10}_{-0.09}$	$43.19^{+0.10}_{-0.09}$	46.47	-0.95
J2107+0054	$20.36^{+0.64}_{-0.40}$	> 3.42	$1.79^{+0.34}_{-0.28}$	$\cdots$	$35.86^{+0.35}_{-0.29}$	$43.86^{+0.36}_{-0.30}$	45.87	0.51
J2135$-$0320	$21.17^{+0.10}_{-0.11}$	3.37 ± 0.06	$2.00^{+0.09}_{-0.10}$	$\cdots$	$35.63^{+0.09}_{-0.10}$	$43.20^{+0.09}_{-0.11}$	46.47	-0.42
J2307+1119	$20.78^{+0.23}_{-0.36}$	$2.27^{+0.21}_{-0.16}$	$0.80^{+0.18}_{-0.20}$	$\cdots$	$34.75^{+0.18}_{-0.20}$	$42.65^{+0.18}_{-0.20}$	46.33	-0.27

5.B. Notes on Individual Objects

We report the notes on the *SimBAL* spectral model fits and specifications for individual objects. For the objects that have been previously analyzed or have additional observations, we included an additional description [6].

011117.36+142653.6 This object is included in the Farrah et al. (2012) sample, and has been observed twice by SDSS. It was originally classified as an FeLoBAL quasar by Trump et al. (2006). It was reported have been detected by ROSAT (Anderson et al., 2007), and was detected in the near-UV by Galaxy Evolution Explorer (GALEX; Trammell et al., 2007). It was observed using *SCUBA-2* but was not detected (Violino et al., 2016). Two Gaussian absorption profiles were used to model the absorption features. They were constrained to have the same ionization parameter and density while other parameters were allowed to vary. However, we combined the two Gaussians together for the analysis as a single BAL outflow component for determining the outflow mass rates and the hydrogen column densities. The break in the continuum near 3000 Å required the use of a general reddening curve (Choi et al., 2020)

015813.56-004635.5 This object was observed once by SDSS and is included in the DR14 SDSS quasar catalog (Pâris et al., 2018). A four-bin tophat model (single ionization parameter and single density) was used.

024254.66-072205.6 This object is included in the Farrah et al. (2012) sample, and has been observed once by SDSS. It was originally classified as an FeLoBAL quasar by Trump et al. (2006). It was observed using *SCUBA-2* but was not detected (Violino et al., 2016). A six-bin tophat with two-covering model was used. All bins were constrained to have a single-density parameter while other parameters, including the ionization parameter, were allowed to vary. The Small Magellanic Cloud (SMC) reddening for this object was fixed to a value of $E(B-V) = 0.075$ obtained from a fit to the photometry.

[6] Co-authors in Choi et al. (2022a) have made a significant contribution to preparing this material.

025858.17-002827.0 This object has been observed three times using SDSS, and is included in the DR14 SDSS quasar catalog (Pâris et al., 2018). It was identified as a BAL quasar in the DR10 SDSS quasar catalog (Pâris et al., 2014). A combination of an eight-bin tophat (single ionization parameter and single density) and a Gaussian opacity profile was used to model the two BAL components found in the spectrum. The general reddening law was used in the continuum model.

030000.57+004828.0 This bright overlapping-trough BAL quasar has been observed three times using SDSS, and is included in the Farrah et al. (2012) sample. It was first classified as an FeLoBAL quasar by Hall et al. (2002), and Hall et al. (2003) presented an analysis of the spectacular narrow Ca II absorption lines. Despite the heavy absorption, near-UV emission was detected by GALEX (Trammell et al., 2007). DiPompeo et al. (2011) reported spectropolarimetry observations; the continuum is modestly polarized (2%), but the emission and absorption lines do not show any different polarization. Vivek et al. (2012) obtained two additional spectra; they found no variability in the optically thickest portions of the outflow, but reported variability that may be associated with the optically thinner portion or the underlying continuum or line emission. McGraw et al. (2015) also investigated the variability in this object; they concluded that there is no variability in the BALs but tentative variability in the associated absorption lines. It was observed using *SCUBA-2* but was not detected (Violino et al., 2016). Villforth et al. (2019) presented near-IR imaging observations obtained using Hubble Space Telescope (HST); the image was dominated by the PSF. Lawther et al. (2018) used HST to image the object in the UV, within the BAL troughs, and in the near-IR. They found that that the host galaxy properties are consistent with those of non-BAL quasars. Rogerson et al. (2011) observed this object with Chandra to study the X-ray absorption and constrained the lower limit for the column density of the X-ray absorbing gas to be $\log N_H \geq 24.3$ $[\mathrm{cm}^{-2}]$ with density $\log n \sim 6$ $[\mathrm{cm}^{-3}]$. A twelve-bin tophat (single ionization parameter and single density) model with two covering factors was used. We only fit the main Fe II trough and ignored

the much narrower Ca II absorption lines that were observed at the lower velocity end of the main overlapping trough. The physical constraints on the main Fe II trough from the best-fitting model are unaffected by this exclusion. Hall et al. (2003) concluded that the Ca II must have formed in a different region within the same BAL outflow gas with a significant temperature difference.

033810.84+005617.6 This object is included in the Farrah et al. (2012) sample, and has been observed five times by SDSS. It was first classified as an FeLoBAL quasar by Hall et al. (2002). It was detected in the near-UV by GALEX (Trammell et al., 2007). Spectropolarimetry observations (DiPompeo et al., 2011) revealed that it is unpolarized. A model with the nine-bin tophat bins (single ionization parameter and single density) and the general reddening law was used. The best-fitting *SimBAL* model found a Mg II trough spanning from $-43,300$ km s^{-1} to $-26,400$ km s^{-1}, exceeding that discovered in GQ 1309+2904, the previously discovered fastest LoBAL (Fynbo et al., 2020). We excluded this object from the analysis because we could not constrain the physical properties of the outflow gas since no other absorption line was found in the spectrum (also makes this object a LoBAL quasar instead of FeLoBAL quasar), and the BAL identification was uncertain due to the location of the trough in the region where strong Fe II emission is generally found.

080248.18+551328.8 This object was observed twice by SDSS, and was first classified as a BAL quasar by Gibson et al. (2009). Liu et al. (2015) reported He I* absorption in the SDSS spectrum. Yi et al. (2019) reported variability in the Mg II absorption line equivalent width with 3.4σ confidence. A five-bin tophat model (single ionization parameter and single density) was used.

080957.39+181804.4 This object was observed twice by SDSS, and is included in the DR14 SDSS quasar catalog (Pâris et al., 2018). Liu et al. (2015) reported He I* absorption in the SDSS spectrum. Villforth et al. (2019) presented near-IR imaging

observations obtained using HST; the image is dominated by the PSF. A nine-bin tophat (single ionization parameter and single density) with two-covering model was used.

081312.61+432640.1 This object is included in the Farrah et al. (2012) sample, and has been observed three times by SDSS. It was first classified as an FeLoBAL quasar by Trump et al. (2006). Two Gaussian profiles were used to model the absorption feature, mainly following the shapes of the Mg II$\lambda\lambda 2796, 2803$ doublet lines. They were combined and analyzed as a single BAL outflow.

083522.77+424258.3 This object was discovered in the First Bright Quasar Survey (FBQS J083522.7+424258; White et al., 2000), and is included in the Farrah et al. (2012) sample. It has been observed three times by SDSS. The He I* absorption lines were noted by Liu et al. (2015). Vivek et al. (2012) reported no BAL variability over 5 years in the object's rest frame. Two Gaussian profiles were used based on the shape of the Mg II doublet lines. Only the lower-velocity Gaussian component of the two was used in the analysis because the other Gaussian component presented no Fe II lines. The Fe II and Mg II absorption lines as well as the He I$^*\lambda 3188$ and He I$^*\lambda 3889$ transitions in this object were well modeled with *SimBAL*. However, the model underpredicts the opacity for Ca II$\lambda\lambda 3934, 3969$ doublet lines as well as the Mg I$\lambda 2853$ line.

084044.41+363327.8 This object was identified as a radio-loud BAL quasar in the FIRST Survey (FBQS J0840+3633; Becker et al., 1997), and is included in the Farrah et al. (2012) sample. It was observed by SDSS three times. It is a highly polarized, with complex polarization structure across the troughs (Brotherton et al., 1997). It was detected by Chandra, with inferred $\alpha_{ox} = 2.11$ (Green et al., 2001). de Kool et al. (2002a) performed a heroic, in-depth analysis of a Keck echelle spectrum. They found evidence for two absorption systems, with the higher-excitation one located ~ 230 pc from the nucleus. Lewis et al. (2003) reported no detection in the sub-millimeter band from a *SCUBA* observation. Both Vivek et al. (2014) and McGraw et al. (2015) found that the

broad absorption lines were not variable. A nine-bin tophat (single ionization parameter and single density) model with two covering factors was used. Even though the absorber velocity profile from our model encompasses both of the BAL components analyzed in de Kool et al. (2002a), we do not find compelling evidence for the two separate outflows from our low-resolution data.

091658.43+453441.1 This object was observed once using SDSS, and is included in the DR14 SDSS quasar catalog (Pâris et al., 2018). Two Gaussian profiles were used based on the shape of the Mg II doublet lines. One of the Gaussian profile components was added to model the weak absorption feature seen only in Mg II lines; thus this component was not included in the analysis.

091854.48+583339.6 This object is included in the Farrah et al. (2012) sample, and has been observed once by SDSS. It was first classified as an FeLoBAL quasar by Trump et al. (2006). It was detected in the near-UV by GALEX (Trammell et al., 2007). A single Gaussian model was used.

094404.25+500050.3 This object was observed once using SDSS, and is included in the DR14 SDSS quasar catalog (Pâris et al., 2018). It was identified as an FeLoBAL quasar using the convolutional neural network FeLoNET (Dabbieri et al., in preparation). The model included an eleven-bin tophat, the general reddening law, and a template spectrum for the long-wavelength region (~ 4700 Å).

100605.66+051349.0 This object is included in the Farrah et al. (2012) sample, and has been observed once by SDSS. It was first classified as an FeLoBAL quasar by Trump et al. (2006). It was detected in the FIRST survey and has an unresolved core morphology (Kimball et al., 2011). An eight-bin tophat model (single ionization parameter and single density) was used.

101927.37+022521.4 This object is included in the Farrah et al. (2012) sample, and has been observed once by SDSS. It was first classified as an FeLoBAL quasar by Trump et al. (2006). It was detected in the FIRST survey and has a resolved core morphology (Kimball et al., 2011). Schulze et al. (2017) presented near-infrared observations of this object, determining that the rest-frame optical-band-based redshift is 1.364. The spectrum also shows substantial Balmer absorption from the BAL outflow (Schulze et al., 2018). A four-bin tophat model (single ionization parameter and single density) with a modified partial covering was used. This object showed significant nonzero offset flux at the bottoms of the troughs, and we used a modified partial covering model in which the emission lines and a fraction of continuum emission were not absorbed by the outflow. The width of absorption lines is not significantly larger than other objects (~ 3000 km s^{-1}); nonetheless J1019+0225 may be classified as an overlapping trough FeLoBAL quasar as we see no continuum recovery around $\lambda \sim 2500$ Å due to the large opacity from the rare excited-state Fe II produced in the high-ionization and high-density gas. The kinematic properties (narrow width and small v_{off}) combined with the compactness of the outflow ($\log R < 1$ [pc]) classify the BAL found in this object as a loitering outflow.

102036.10+602339.0 This object is included in the Farrah et al. (2012) sample, and has been observed twice by SDSS. It was first classified as an FeLoBAL quasar by Trump et al. (2006). Despite the heavy absorption, near-UV emission was detected by GALEX (Trammell et al., 2007). Liu et al. (2015) reported He I* absorption in the SDSS spectrum. Yi et al. (2019) found that the Mg II absorption line equivalent width did not vary between the two observations. Villforth et al. (2019) found that the host galaxy showed signs of disturbance in an *HST* near-IR image. A two-covering model with two sets of tophat bins with each group having a single ionization parameter and density was used. The higher-velocity group ($v_{off} \sim -3900$ km s^{-1}) with 3 tophat bins produced most of the Fe II opacity needed to create the iron troughs found in the spectrum with $\log U \sim -1.9$ and $\log n \sim 7.6$ [cm^{-3}]. A lower-velocity group ($v_{off} \sim -3100$ km s^{-1}) with 5 bins was

needed to model the wide Mg II trough and deep Ca H+K and Mg I lines that were not sufficiently modeled with the higher-velocity group. Also, some of the deeper dips in the troughs (∼2300–2600 Å) required the opacity from the bins from the lower-velocity group. The lower-velocity group shows substantially lower ionization parameter and density compared to the higher-velocity group ($\log U \sim -2.9$ and $\log n \sim 4.4$ [cm^{-3}]). From the above values, one can come to a conclusion that the two outflow components are separated by more than 2 dex in distance ($R \propto (1/nU)^{1/2}$). The FWHM of the emission model was fixed to a value determined from the long-wavelength part of the spectrum where the absorption is not severe ($\lambda \gtrsim 3000$ Å, FWHM ~ 11000 km s^{-1}).

102226.70+354234.8 This object was observed twice by SDSS and is included in the DR14 SDSS quasar catalog (Pâris et al., 2018). A nine-bin tophat model (single ionization parameter and single density) was used.

102358.97+015255.8 This object is included in the Farrah et al. (2012) sample, and has been observed once by SDSS. It was first classified as an FeLoBAL quasar by Trump et al. (2006). A single Gaussian model was used.

103036.92+312028.8 This object was observed four times by SDSS and is included in the DR14 SDSS quasar catalog (Pâris et al., 2018). A model with a six-bin tophat (single ionization parameter and single density) and the general reddening law was used. We used a long-wavelength template spectrum to model this object to ~ 4000 Å.

103903.03+395445.8 This object was observed once by SDSS and is included in the DR14 SDSS quasar catalog (Pâris et al., 2018). It was identified as an FeLoBAL quasar using the convolutional neural network FeLoNET (Dabbieri et al., in preparation). The model included two Gaussian opacity profiles, the general reddening law and a template spectrum for the long-wavelength region (~ 4700 Å). Each Gaussian profile modeled one of the two BAL components that had a large velocity separation.

104459.60+365605.1 This object was discovered in the First Bright Quasar Survey (FBQS J104459.5+365605; Becker et al., 2000; White et al., 2000); Kimball et al. (2011) reported that the radio emission is unresolved. It has been observed three times by SDSS. A Keck High Resolution Echelle Spectrometer (HIRES) spectrum was analyzed in detail by de Kool et al. (2001); they found that the absorber is located $\sim 700\,\mathrm{pc}$ from the continuum source. DiPompeo et al. (2010) reported the detection of significant polarization that increases toward shorter wavelengths. Runnoe et al. (2013) observed the rest-frame optical spectrum; they report that for a Hβ FWHM of 3615 $\mathrm{km\,s^{-1}}$ and a log bolometric luminosity of 46.57 [$\mathrm{erg\,s^{-1}}$], the log black hole mass is 8.87 [$\mathrm{M_\odot}$], and the Eddington ratio is 0.33. While the Hβ FWHM and bolometric luminosity are similar, the other values are different than those obtained by Leighly et al. (2022) from the BOSS spectrum ($\log M_{BH} = 7.82$ [$\mathrm{M_\odot}$] and $\log L_{Bol}/L_{Edd} = 0.8$). McGraw et al. (2015) reported a tentative detection of absorption variability in the high-velocity LoBAL feature, but not in the FeLoBAL troughs modeled in this paper. Yi et al. (2019) also found evidence for variability. A thirteen-bin tophat was divided into two groups with each group having a single ionization parameter and single density. The model also included a long-wavelength template spectrum to model this object to ~ 4000 Å. The higher-velocity group (-5500 to -4000 $\mathrm{km\,s^{-1}}$) was composed of 6 tophat bins, and the lower-velocity group group (-2600 to -640 $\mathrm{km\,s^{-1}}$) used the remaining 7 tophat bins. de Kool et al. (2001) also found two velocity structures in this object; however, they did not treat them as two separate outflow components. Although not included in the best-fitting *SimBAL* model, the shallow absorption feature observed at $\lambda \sim 2650$ Å may be the Mg II absorption lines from a high-velocity LoBAL outflow.

105748.63+610910.8 This object was observed once using SDSS and is included in the Farrah et al. (2012) sample. It was first identified as an FeLoBAL quasar by Trump et al. (2006). This object was modeled with a single Gaussian opacity profile. The narrow absorption lines (FWHM $\sim 150\mathrm{km\,s^{-1}}$) show full covering of the emission source, which is uncommon for quasar outflows, and an unusually high outflow velocity

$v_{Off} \sim -9500\mathrm{km\ s^{-1}}$. The key spectral signatures of BAL outflows include the broad width of the absorption lines and partial coverage (e.g., Ganguly & Brotherton, 2008). The absorption lines in this object, on the other hand, closely resemble the properties of an associated quasar absorber originating from a gas that is potentially located within the quasar host galaxy or its surrounding medium (Appendix 5.C). In addition, this absorption system has been previously classified as an associated absorber in several catalogues (e.g., Quider et al., 2011; Chen et al., 2018); however, it is difficult to strictly differentiate between an outflow signature and an associated absorber; therefore we proceed with caution in analyzing this outflow. Although this object was included in Farrah et al. (2012), we excluded this BAL from the sample due to its ambiguous nature.

112526.12+002901.3 This object was featured in Hall et al. (2002) where they commented on the He I*λ3889 and Ca II H&K absorption lines, as well as the low covering fraction and high-excitation Fe II lines. Hall et al. (2013) discussed the redshifted absorption found in this object and a handful of other BAL outflows. Shi et al. (2016) compared the SDSS and BOSS spectra, and determined that variability between the two arises from a change in broad line emission, which is not absorbed by the compact outflow in this object. Zhang et al. (2017) reported the X-ray detection in a 3.8 ks Chandra observation; the object is 34.1 times X-ray weaker than an unabsorbed quasar. Near-IR observations obtained using HST revealed that the image is dominated by the PSF (Villforth et al., 2019). A four-bin tophat (single ionization parameter and single density) and a Gaussian opacity profile model were used. We also used a modified partial covering model in which the emission lines and a fraction of continuum emission were not absorbed by the outflow. The principal Fe II opacity was modeled by the tophat component and the Gaussian component provided the extra opacity needed to create the deep Mg II absorption trough. This additional Gaussian component was allowed to freely absorb the emission lines and the continuum emission, unlike the main tophat component.

112828.31+011337.9 This object is identified as an FeLoBAL quasar by Hall et al. (2002). Hall et al. (2013) discussed the redshifted absorption also found in this object. Yi et al. (2019) found evidence for variability among the three SDSS observations. Zhang et al. (2017) reported the results of a 5.4 ks Chandra observation; the object was not detected, implying that it is more than 50 times weaker than a comparable unabsorbed object. Near-IR observations obtained using HST revealed a resolved target with a somewhat disturbed morphology (Villforth et al., 2019). An eight-bin tophat (single ionization parameter and single density) model was used. The line emission is unabsorbed by the BAL in this model, and we used a long-wavelength template spectrum to model this object to ~ 4000 Å.

112901.71+050617.0 This object was first classified as an FeLoBAL quasar by Trump et al. (2006). It was detected by the FIRST survey and has an unresolved core morphology (Kimball et al., 2011). No variability was detected between two SDSS observations (Yi et al., 2019). An eight-bin tophat (single ionization parameter and single density) model with two covering factors was used.

114556.25+110018.4 This object is included in the Farrah et al. (2012) sample, and was observed once by SDSS. It was first classified as an FeLoBAL quasar by Trump et al. (2006). A single Gaussian opacity model was used. The line emission is unabsorbed by the BAL and no reddening component was included in the model.

115436.60+030006.3 This spectacular overlapping trough FeLoBAL quasar was first identified by Hall et al. (2002). It has been observed twice by SDSS and was included in the Farrah et al. (2012) sample. McGraw et al. (2015) did not observe variability among three observations, including one taken at MDM observatory. A model with a seven-bin tophat and the general reddening law was used. All bins were constrained to have a single density parameter but the three highest-velocity bins were group together and allowed to have a different ionization parameter than the rest of the four lower-velocity bins. It has one of the highest outflow velocities ($v_{off} \sim -15,400$ km s^{-1}; $v_{max} \sim -17,000$ km s^{-1})

in the sample and also shows anomalous reddening.

115852.86-004301.9 This object was first classified as an FeLoBAL quasar by Trump et al. (2006). It has been observed twice by SDSS. It was detected in the FIRST Survey; Kimball et al. (2011) reported a jet with a recognizable morphology with a 21 cm flux density of 87 mJy. A five-bin tophat (single ionization parameter and single density) model was used.

120049.54+632211.8 This object was first classified as an FeLoBAL quasar by Trump et al. (2006), and it is included in the Farrah et al. (2012) sample. It has been observed four times by SDSS, but no variability among was found (Yi et al., 2019). A twelve-bin tophat (single ionization parameter and single density) model with two covering factors was used.

120627.62+002335.4 This object was first classified as an FeLoBAL quasar by Trump et al. (2006), and is included in the Farrah et al. (2012) sample. It has been observed once by SDSS. Hutsemékers et al. (2017) reported that the object is significantly polarized at $1.7\% \pm 0.36\%$. The model included an eight-bin tophat that is divided into two groups (single ionization parameter and single density per group), the general reddening law and a template spectrum for the long-wavelength region (~ 4400 Å). The principal Fe II opacity was modeled by the higher-velocity group (-6800 to -1900 km s^{-1}) with 4 tophat bins, and the lower-velocity group group (-5600 to -300 km s^{-1}) used the remaining 4 tophat bins.

120815.03+624046.4 This object has been observed once by SDSS, and is included in the DR14 SDSS quasar catalog (Pâris et al., 2018). It was identified as an FeLoBAL quasar using the convolutional neural network FeLoNET (Dabbieri et al., in preparation). A single Gaussian opacity model was used. A long-wavelength template spectrum was included to model this object to ~ 4400 Å.

121231.47+251429.1 This object has been observed once by SDSS, and is included in the DR14 SDSS quasar catalog (Pâris et al., 2018). It was identified as an FeLoBAL quasar using the convolutional neural network FeLoNET (Dabbieri et al., in preparation). A single Gaussian opacity model was used. A long-wavelength template spectrum was included to model this object to ~ 4700 Å.

121441.42−000137.8 A nine-bin tophat (single ionization parameter and single density) and a Gaussian opacity profile model were used. A long-wavelength template spectrum was included to model this object to ~ 4500 Å. The extremely broad tophat component seen in the Mg II trough that extends from -18000 to -6200 km s^{-1} was excluded in the analysis. No substantial Fe II opacity or other absorption lines were observed from this component and we could not extract robust physical constraints from only the Mg II trough. Moreover, the continuum placement near the assumed wavelength region where the troughs from the Fe II are expected was highly uncertain due to the Fe II emission lines. Pitchford et al. (2019) observed this object in the mid-infrared to study the star formation property of the quasar and found that this object has the highest star formation rate among FeLoBALQs (~ 2000 M$_\odot$yr^{-1}).

121442.30+280329.1 This object was discovered in the First Bright Quasar Survey (FBQS J1214+2803; Becker et al., 2000; White et al., 2000). It has been observed twice by SDSS. A Keck HIRES spectrum was analyzed in detail by de Kool et al. (2002b). They found that the absorber is located between 1 and 30 parsecs from the continuum source. Branch et al. (2002) and Casebeer et al. (2008) presented an alternative resonance-scattering interpretation of the spectrum. DiPompeo et al. (2010) found a low continuum polarization (0.4%±0.13%). Zhang et al. (2017) found no evidence for variability between the two SDSS spectra, but McGraw et al. (2015) found significant variability among several MDM observations. An eight-bin tophat (single ionization parameter and single density) model with two covering factors was used. The outflow properties measured by de Kool et al. (2002b) ($-2.0 < \log U < -0.7$, $7.5 < \log n < 9.5$ [cm^{-3}], and $21.4 < \log N_H <$

22.2 $[\mathrm{cm}^{-2}]$) were consistent with the values that we got from our best-fitting *SimBAL* model ($\log U = -1.7^{+0.002}_{-0.001}$, $\log n = 7.8^{+0.005}_{-0.006}$ $[\mathrm{cm}^{-3}]$, $\log N_H = 22.0 \pm 0.003$ $[\mathrm{cm}^{-2}]$).

123549.95+013252.6 This object was first classified as an FeLoBAL quasar by Trump et al. (2006), and is included in the Farrah et al. (2012) sample. It has been observed once by SDSS. It was observed using *SCUBA-2* but was not detected (Violino et al., 2016). An eight-bin tophat (single ionization parameter and single density) model with was used. A long-wavelength template spectrum was included to model this object to ~ 4000 Å.

124014.04+444353.4 This object was originally classified as a type 2 quasar (Yuan et al., 2016). It is actually a Seyfert 1.8, as a faint and broad Hβ line can be seen in the sole SDSS spectrum (Leighly et al., 2022). It was identified as an FeLoBAL quasar using the convolutional neural network FeLoNET (Dabbieri et al., in preparation). A six-bin tophat (single ionization parameter and single density) model with was used. A long-wavelength template spectrum was included to model this object to ~ 4700 Å.

132117.24+561724.5 This object was observed once by SDSS and is included in the DR14 SDSS quasar catalog (Pâris et al., 2018). It was identified as an FeLoBAL quasar using the convolutional neural network FeLoNET (Dabbieri et al., in preparation). A two-bin tophat (single ionization parameter and single density) model was used. The line emission is unabsorbed by the BAL in this model and we used a long-wavelength template spectrum to model this object to ~ 4400 Å.

132401.53+032020.5 This object was first classified as an FeLoBAL quasar by Trump et al. (2006), and is included in the Farrah et al. (2012) sample. Liu et al. (2015) observed He I* absorption in the SDSS spectrum. Young et al. (2009) reported a serendipitous X-ray detection with signal-to-noise ratio of 5.8 that yields an $\alpha_{ox} = -1.85$. Yi et al. (2019) found no variability between the two SDSS observations. An eight-bin tophat (single ionization parameter and single density) and a Gaussian opacity profile model were used.

A long-wavelength template spectrum was included to model this object to ~ 4400 Å. An additional Gaussian component was included to model the narrow intervening absorber at -21000 km s^{-1} relative to quasar rest frame; this component was excluded from the analysis.

133632.45+083059.9 This object was observed twice by SDSS and is included in the DR14 SDSS quasar catalog (Pâris et al., 2018). This object was classified as an unusual BAL quasar by Meusinger et al. (2012b). It was identified as an FeLoBAL quasar using the convolutional neural network FeLoNET (Dabbieri et al., in preparation). A nine-bin tophat (single ionization parameter and single density) model with was used. A long-wavelength template spectrum was included to model this object to ~ 4700 Å. A strong degeneracy between the power-law slope and the reddening was observed in the *SimBAL* model, so we used the composite SED from Richards et al. (2006b) with a normalization parameter in place of the power-law continuum model to eliminate the slope parameter.

135525.24+575312.7 This object was observed once by SDSS and is included in the DR14 SDSS quasar catalog (Pâris et al., 2018). This object was identified as an FeLoBAL quasar by visual examination. An eight-bin tophat (single ionization parameter and single density) model with was used. A long-wavelength template spectrum was included to model this object to ~ 4400 Å.

135640.34+452727.2 This object was observed once by SDSS and is included in the DR14 SDSS quasar catalog (Pâris et al., 2018). A nine-bin tophat and a Gaussian opacity profile model were used. The tophat bins and the Gaussian component were modeling a single BAL component together so they were given a single ionization parameter and single density. A long-wavelength template spectrum was included to model this object to ~ 4700 Å.

142703.62+270940.4 This object was discovered in the First Bright Quasar Survey (FBQS J142703.6+270940; Becker et al., 2000; White et al., 2000). DiPompeo et al. (2010) found significant continuum polarization of about 2% that rises toward short wavelengths. The model included a nine-bin tophat that is divided into two groups (single ionization parameter and single density per group), the general reddening law and a template spectrum for the long-wavelength region (~ 4700 Å). The higher-velocity group (-3700 to -2800 km s^{-1}) was composed of 3 tophat bins and the lower-velocity group group (-1100 to 90 km s^{-1}) used the remaining 6 tophat bins. The FWHM of the emission model was fixed to a value determined from the long-wavelength part of the spectrum where the absorption is not severe ($\lambda \gtrsim 3000$ Å, FWHM ~ 5000 km s^{-1}).

144800.15+404311.7 This spectacular overlapping trough object was first classified as a BAL quasar by Gibson et al. (2009). Villforth et al. (2019) presented near-IR imaging observations obtained using HST; the image was dominated by the PSF. It has been observed three times by SDSS. The model included an eight-bin tophat that is divided into two groups (single ionization parameter and single density per group) and an extra Gaussian component with both using two covering factors, the general reddening law and a template spectrum for the long-wavelength region (~ 4700 Å). The higher-velocity group (-6900 to -2400 km s^{-1}) was composed of 4 tophat bins and the lower-velocity group group (-5000 to -710 km s^{-1}) used the remaining 4 tophat bins. The additional Gaussian component at ~ -600 km s^{-1} was required for the narrow outflow component that was identified by the narrow Mg I and Ca II H and K absorption lines.

151708.94+232857.5 This object was observed once by SDSS and is included in the DR14 SDSS quasar catalog (Pâris et al., 2018). It was identified as an FeLoBAL quasar using the convolutional neural network FeLoNET (Dabbieri et al., in preparation). A seven-bin tophat (single ionization parameter and single density) with two-covering model was used. A long-wavelength template spectrum was included to model this object to ~ 4700 Å.

152737.17+591210.1 This object was observed once by SDSS and is included in the DR14 SDSS quasar catalog (Pâris et al., 2018). The model included a seven-bin tophat, the general reddening law and a template spectrum for the long-wavelength region (~ 4700 Å).

153145.01+485257.2 It was identified as an FeLoBAL quasar using the convolutional neural network FeLoNET (Dabbieri et al., in preparation). Three Gaussian profiles were used in the model. Only one of the Gaussian components was included in the analysis because the other two Gaussian components were included to model a narrow intervening system at ~ -23000 km s^{-1} relative to the quasar rest frame and for a weak Mg II opacity structure near rest velocity.

155633.77+351757.3 This object was identified as a radio-loud BAL quasar in the FIRST Survey (FIRST J155633.8+351758; Becker et al., 1997), and is included in the Farrah et al. (2012) sample. It was observed by SDSS three times. It is highly polarized, up to $\sim 10\%$ at short wavelengths, with lower polarization and complex structure across the deepest troughs (Brotherton et al., 1997). Najita et al. (2000) presented a near-infrared spectrum; they found strong Balmer lines and Fe II emission, and a Balmer-line-based redshift of $z = 1.5008 \pm 0.0007$. Lewis et al. (2003) found that the object was not detected in the sub-millimeter band using *SCUBA*. Brotherton et al. (2005) reported results of a Chandra observation; 40 photons were detected, and they suggest that the X-ray emission was suppressed by a absorption by a factor of 49. A second longer Chandra observation netted 531 photons (Berrington et al., 2013); a heavily absorbed spectrum could be ruled out, and a partial covering model was favored. Jiang & Wang (2003) performed European VLBI Network observations at 1.6 GHz; they found that the object is unresolved at 20 mas, and inferred a flat spectrum. Yi et al. (2019) reported no variability between the first two SDSS observations. The model included a nine-bin tophat that is divided into two groups (single ionization parameter and single density per group) with two-covering, the general reddening law and a template spectrum for the long-wavelength region (~ 4100 Å). The

higher-velocity group (-9000 to -5600 km s^{-1}) was composed of 4 tophat bins and the lower-velocity group group (-5500 to -1400 km s^{-1}) used the remaining 5 tophat bins.

164419.75+530750.4 This object was first categorized as a QSO by Popescu et al. (1996). It was observed once by SDSS and is included in the DR14 SDSS quasar catalog (Pâris et al., 2018). It was identified as an FeLoBAL quasar by visual inspection. A six-bin tophat (single ionization parameter and single density) and a Gaussian opacity profile model were used. We also used a modified partial covering model in which the emission lines and a fraction of continuum emission were not absorbed by the outflow. The Gaussian component was excluded from the sample because it only produced Mg II opacity and thus we could not constrain the physical properties of that outflow component.

173753.97+553604.9 This object was first identified as an FeLoBAL quasar by Trump et al. (2006), and it is included in the Farrah et al. (2012) sample. It was observed once by SDSS. We did not find any absorption features in this object, and therefore we excluded this object from the analysis.

210712.77+005439.4 This object was first identified as an FeLoBAL quasar by Trump et al. (2006), and it is included in the Farrah et al. (2012) sample. It was observed once by SDSS. It was observed using *SCUBA-2* but was not detected (Violino et al., 2016). An eight-bin tophat (single ionization parameter and single density) model with was used. A long-wavelength template spectrum was included to model this object to ~ 4700 Å.

213537.44-032054.8 This object was observed once by SDSS and is included in the DR14 SDSS quasar catalog (Pâris et al., 2018). It was identified as a BAL quasar in the DR10 SDSS quasar catalog (Pâris et al., 2014). A six-bin tophat (single ionization parameter and single density) model with was used. A long-wavelength template spectrum was included to model this object to ~ 4400 Å.

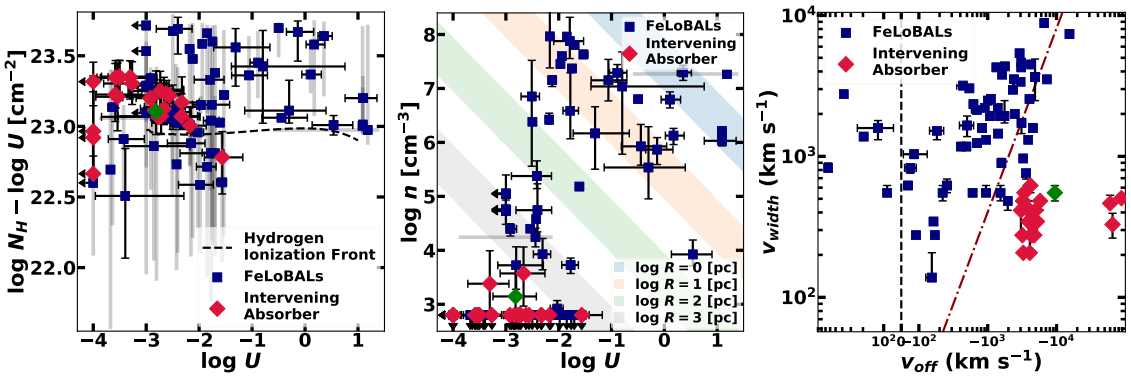

Figure 5.C.1: *Left panel*: the physical parameter distribution of intervening absorbers cannot be easily differentiated from that of an FeLoBAL. *Middle panel*: intervening absorbers have low densities, and we were able to constrain only the density upper limits ($\log n \lesssim 2.8$ [cm^{-3}]) for the majority of them. Based on the ionization parameter and the density, we found the inferred distances from the central engine to the intervening absorber gas to be $\log R \gtrsim 3$ [pc], if we assume the radiation from AGN as the ionizing source for these absorbers. *Right panel*: the kinematic properties show the clearest distinction between the intervening absorbers and FeLoBALs. The intervening absorbers have very narrow width ($v_{width} \lesssim 200$ km s^{-1}) and disproportionately large offset velocities ($v_{off} \ll -3,000$ km s^{-1}), relative to the quasar rest frame, compared to FeLoBALs. The brown dotted-dashed line shows a one-to-one ratio. We rejected SDSS J1057+6109 (green diamonds) from the analysis because the properties of the absorption feature seen in the spectra resembled more the intervening absorbers than the quasar driven outflows (§ 5.3.3). A linear scale was used in the region $|v_{off}| < 100$ km s^{-1}, and log scale was used elsewhere in the x-axis. The error bars show 95% uncertainties and the grey shaded bars represent the range of the values among the tophat model bins for each BAL.

230730.69+111908.5 This object was observed once by SDSS and is included in the DR14 SDSS quasar catalog (Pâris et al., 2018). A five-bin tophat and a Gaussian opacity profile model were used. The tophat bins and the Gaussian component were modeling a single BAL component together so they were given a single ionization parameter and single density. A long-wavelength template spectrum was included to model this object to ~ 4100 Å.

5.C. Intervening Absorbers

The intrinsic quasar absorption lines (e.g., BAL) have five main spectroscopic characteristic that are not seen in intervening absorbers: (1) wider absorption lines, (2) partial

coverage of the emission source (3) time variability of the troughs (4) higher ionization parameter (5) higher metallicity (e.g., Barlow & Sargent, 1997; Ganguly & Brotherton, 2008). Therefore, BALs that show narrow and deep features could easily be confused with intervening absorbers. In order to systematically check whether we could differentiate the intervening absorbers from BALs using *SimBAL*, we fit 20 quasar spectra that were identified to have intervening absorption features. The objects were drawn from the intervening Mg II quasar absorption line catalogue by Quider et al. (2011), and we chose objects that have the similar redshift range ($1 < z < 1.5$). We then selected the ones that have Mg II absorbers located close to the background quasar ($z_{qso} \sim z_{abs}$) because these objects have the spectral features that most closely resemble BAL spectra. The spectra of these objects show Mg II absorption lines near $\lambda_{rest} \sim 2750$ Å that could be confused with quasar-driven BAL or associated absorption-line (AAL; e.g., Hamann et al., 2011).

Figure 5.C.1 shows the distributions of physical and kinematic parameters of the intervening absorption lines and the FeLoBALs, both obtained from *SimBAL* modeling. The distributions of physical parameters (e.g., ionization parameter and density) do not show a clear distinction between the intervening absorbers and FeLoBALs. However, most of the intervening absorbers were constrained to have an extremely low density ($\log n \lesssim 3$ $[\mathrm{cm}^{-3}]$). The kinematic properties of the absorption line systems showed the clearest difference between the intervening Mg II absorbers and FeLoBALs. The intervening absorption lines have narrower widths and higher offset velocities than the majority of FeLoBALs in the sample. We note that accurate modeling of intervening absorbers requires photoionization calculations using the correct photoionzing SED. For this experiment, we used the same ionic column density grid used with FeLoBAL quasars that was generated with quasar SED, which may have a different shape than the photoionizing SEDs required for the intervening absorption line gas. Nevertheless, we conclude that the intervening absorption systems could be identified by examining the kinematic properties of the absorption lines, in particular the width of the lines. This result implies that intervening absorbers will be easily excluded in data from the upcoming missions that will provide

better spectral resolution, such as 4MOST (de Jong et al., 2019).

5.D. I/I_0 Models

We extracted the opacity profiles of several principal absorption line transitions seen in FeLoBALs from the best-fitting *SimBAL* models (Figure 5.D.1). We selected the following line transitions: the Mg II$\lambda 2796$ line transition which has a higher transition probability ($f_{ik} = 0.609$) in the Mg II$\lambda\lambda 2796, 2803$ doublet, the ground-state Fe II$\lambda 2383$ with $f_{ik} = 0.343$, and the excited-state (0.99 eV above ground) Fe II*$\lambda 2757$ with $f_{ik} = 0.307$. Detailed description of the opacity profile models can be found in § 5.4.3.

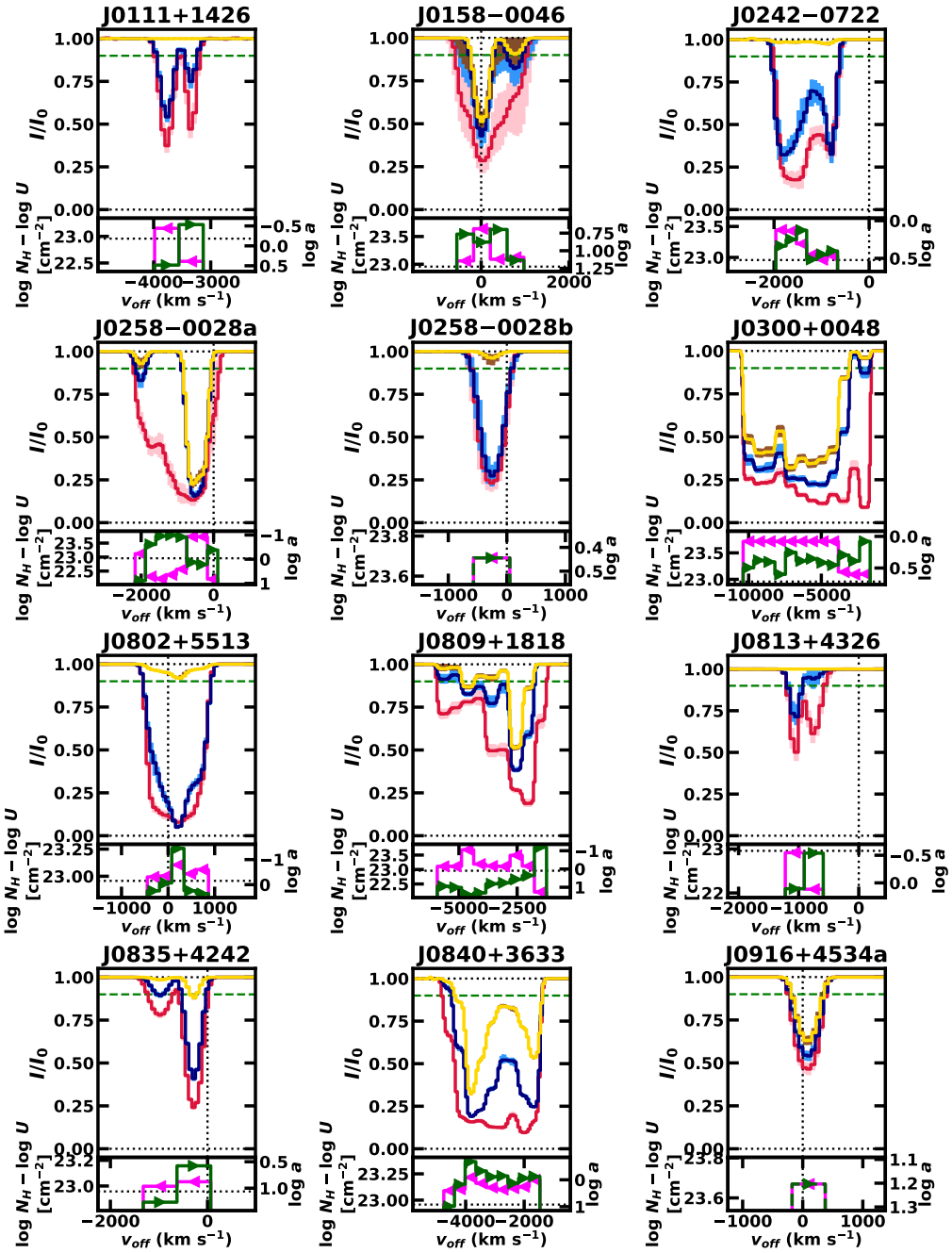

Figure 5.D.1: The top panels in each individual figures show normalized spectrum (I/I_0) models for three line transitions (Mg IIλ2796, Fe IIλ2383, and Fe II$^*\lambda$2757 in red, blue, and yellow, respectively). The lighter shaded regions around each model represent 2σ (95.45%) uncertainties. In the bottom panels, the column density parameter ($\log N_H - \log U$) and the covering fraction parameter ($\log a$) as a function of velocity are plotted in pink and green, respectively.

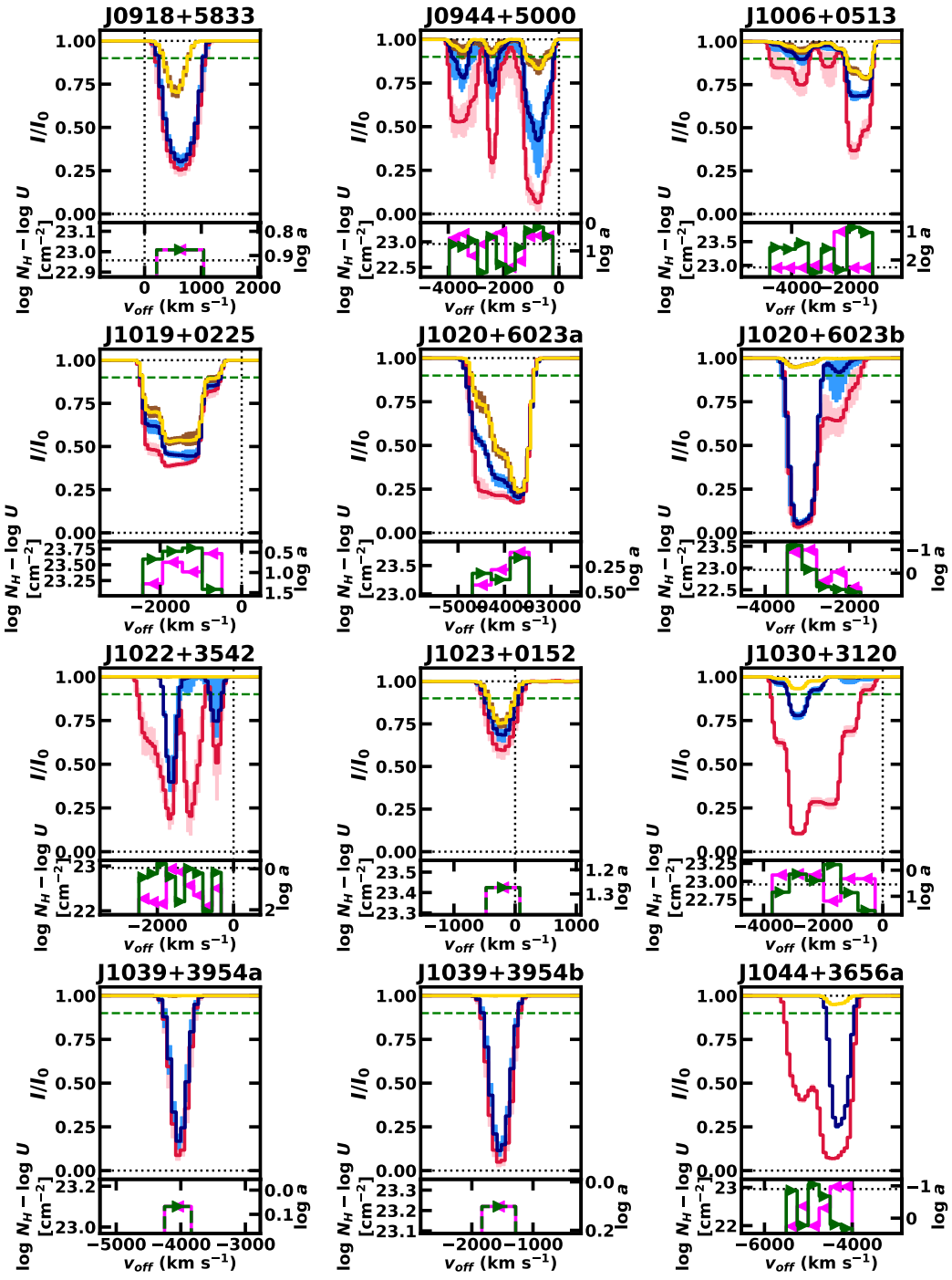

Figure 5.D.1: (Continued).

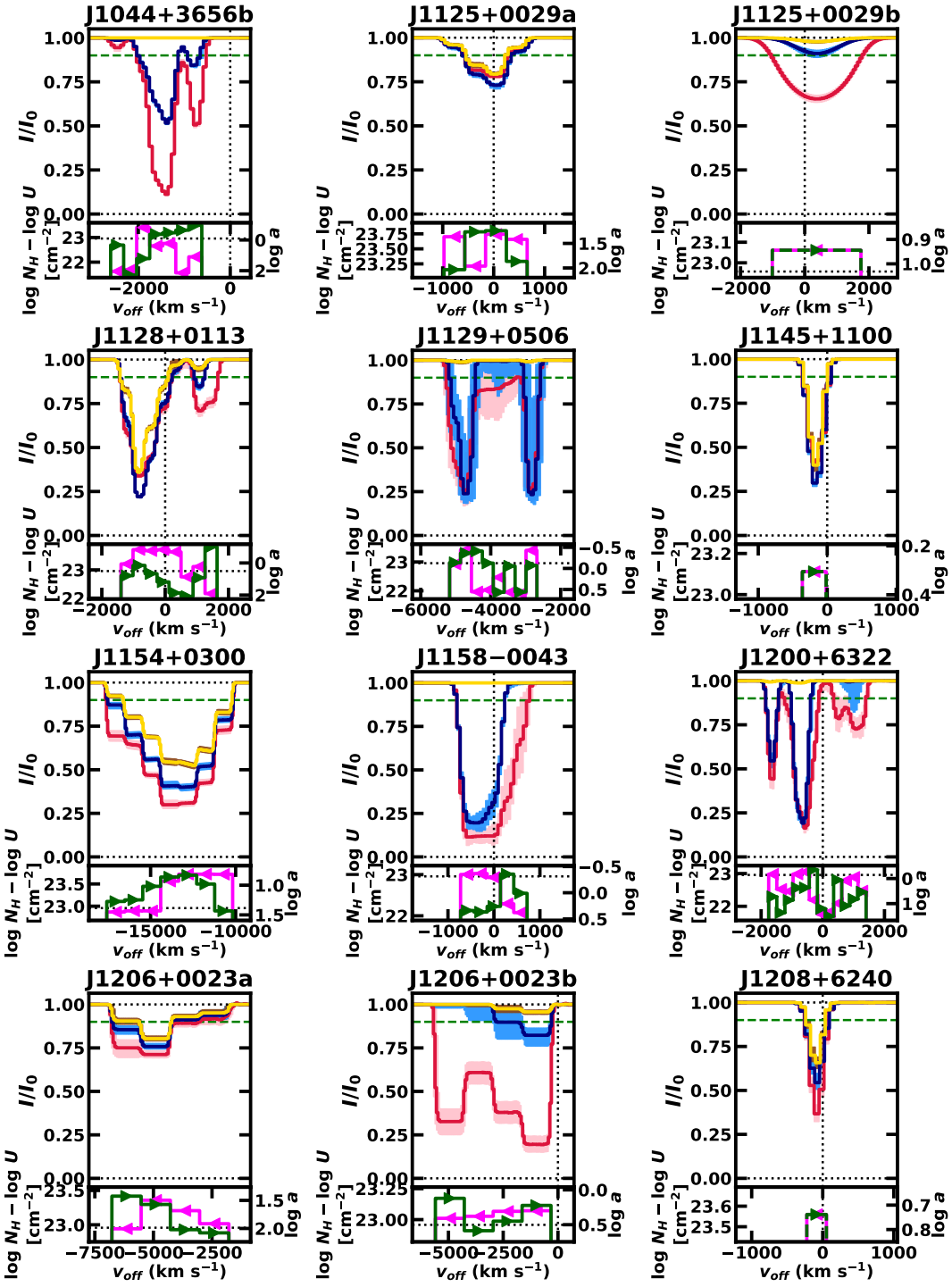

Figure 5.D.1: (Continued).

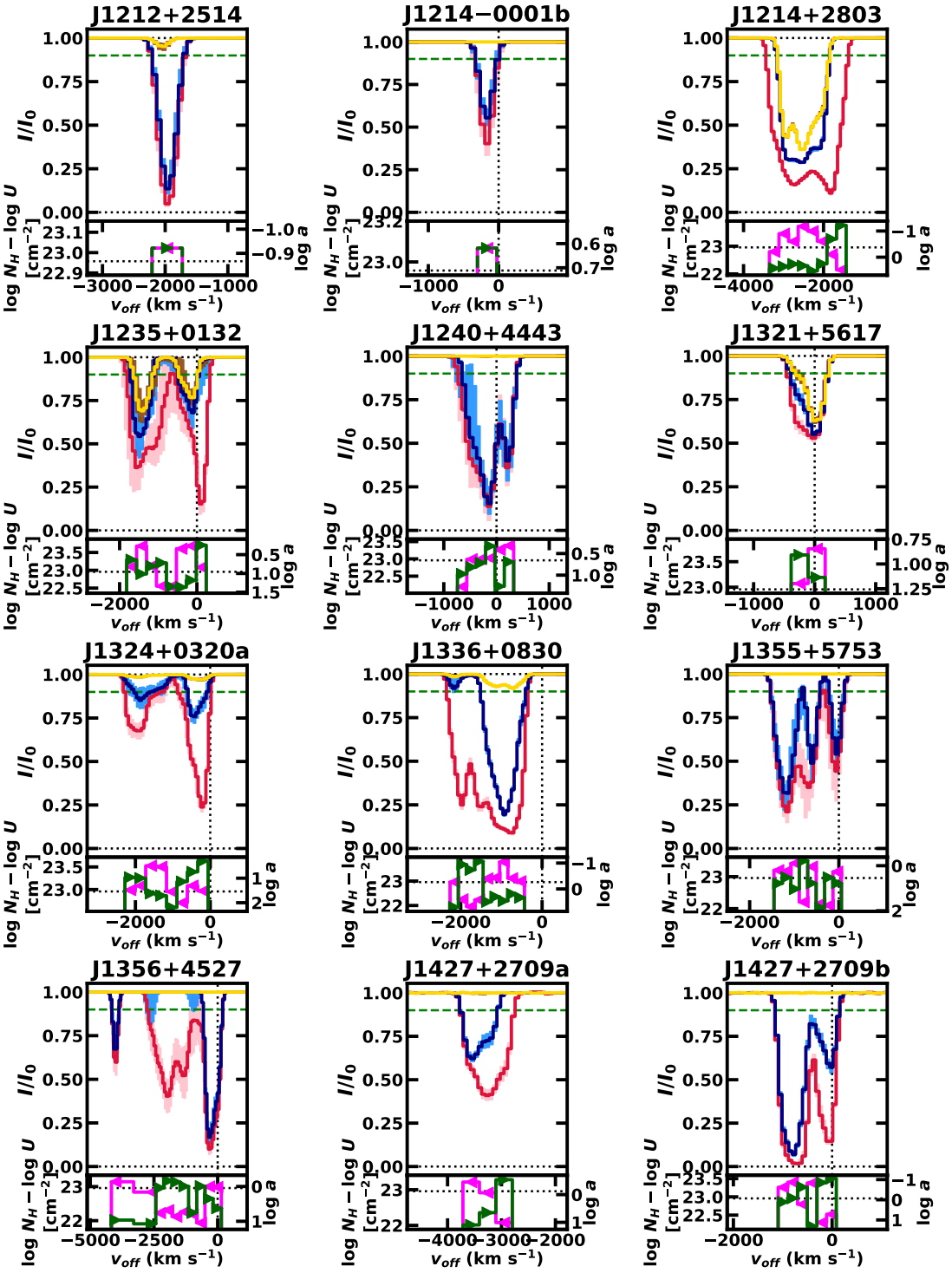

Figure 5.D.1: (Continued).

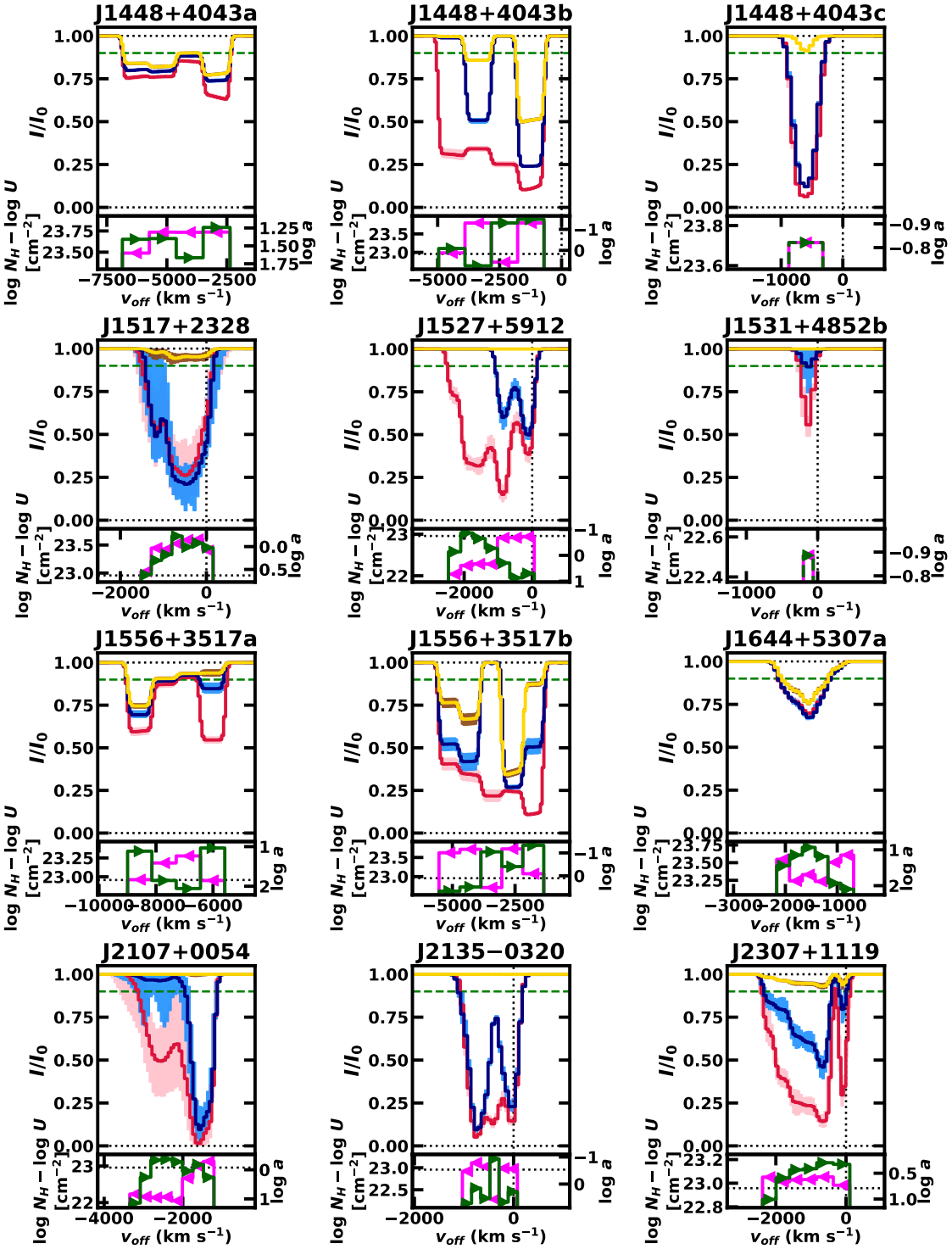

Figure 5.D.1: (Continued).

CHAPTER 6

The Massive Extremely High-Velocity Outflow in the Quasar J164653.72+243942.2[1]

6.1. Introduction

About 20% of quasars are observed with broad absorption-line (BAL) features in their rest-UV spectra showing unambiguous evidence for powerful outflows originating from the central supermassive black holes (SMBHs; e.g., Hewett & Foltz, 2003; Reichard et al., 2003; Trump et al., 2006; Knigge et al., 2008; Gibson et al., 2009). These BAL quasar outflows may significantly impact their host galaxies. Both observations and cosmological simulations demonstrate the need for black hole/galaxy feedback, and BAL outflows are potentially a critical driver of feedback that produces the coevolution of galaxies and SMBHs.

The majority of BAL quasars show resonance absorption lines from highly ionized atoms (C IV, Si IV, N V, O VI) in their spectra with the offset velocities (i.e., outflow velocities) of less than $0.1c$. Baskin et al. (2015) found only 4% of BAL quasars have full width at half maximum (FWHM) greater than 10,000 km s^{-1} in a sample drawn from the Sloan Digital Sky Survey (SDSS) Data Release 7 (DR7) quasar catalogue (Shen et al., 2011). While only a small number of BAL quasar outflows have extremely-high speeds ($v \gtrsim 0.2c$), they might play the most significant role in feedback because the outflow kinetic power is proportional to v_{off}^3. Moreover, these Extremely-High Velocity Outflows (EHVOs) may also provide critical information about the process by which BAL winds are launched and accelerated. A small number of individual quasars with

[1]This chapter contains reproduced materials (with permission) from selected sections in Rodríguez Hidalgo et al. (in preparation) anticipated to be published in the Astrophysical Journal

BAL outflows with extremely-high velocities have been studied (e.g., Jannuzi et al., 1996; Rodríguez Hidalgo et al., 2011) and Rodríguez Hidalgo et al. (2020) presented one of the first studies of a sample of EHVOs. No systemic search for EHVOs has been done prior to Rodríguez Hidalgo et al. (2020) because most large surveys of BAL outflows restricted their search to C IV$\lambda\lambda 1548, 1550$ BALs with an outflow velocity limit of $\sim 0.1c$ to avoid the misidentifying the Si IV$\lambda\lambda 1402, 1393$ absorption lines as C IV BALs.

J164653.72+243942.2, hereafter referred to as J1646+2439, was first discovered in Rodríguez Hidalgo et al. (2020). They performed a systematic search using the Data Release 9 quasar catalog (DR9Q; Pâris et al., 2012) of the SDSS. Among the 40 cases reported in Rodríguez Hidalgo et al. (2020), J1646+2439 shows the broadest C IV absorption trough (Δv ∼12,500 km s^{-1} measured at 90% normalized flux density). J1646+2439 has a redshift of $z = 3.040 \pm 0.002$ (Hewett & Wild, 2010). It has been previously observed and catalogued in the Data Release 5 (DR5) of SDSS (Adelman-McCarthy et al., 2007), where it was classified as a BAL quasar. Gibson et al. (2009) reported the balnicity index (BI; Weymann et al., 1991) of 2285 km s^{-1} that was measured from only the C IV absorption trough at lower velocities. The more recent observation of J1646+2439 from the SDSS DR9 revealed that the lower-velocity absorption component disappeared while the EHVO remains

In this chapter I present the *SimBAL* analysis of the absorption in the multi-epoch spectra of J1646+2439. This work represents my contribution to the collaborative project that is being led by Dr. Rodríguez Hidalgo at the University of Washington Bothell (Rodríguez Hidalgo et al., in preparation). The goals and the analyses of the project include a range of topics; however, only the part I led, which is *SimBAL* analysis of the spectra, is reported in this chapter. This analysis demonstrates that *SimBAL* can be used to systematically analyze spectroscopic time series data and provide us with a clear physical picture of the origin of BAL variability. Here I demonstrate how this analysis can be performed on a pair of spectra obtained from a high-redshift BAL quasar.

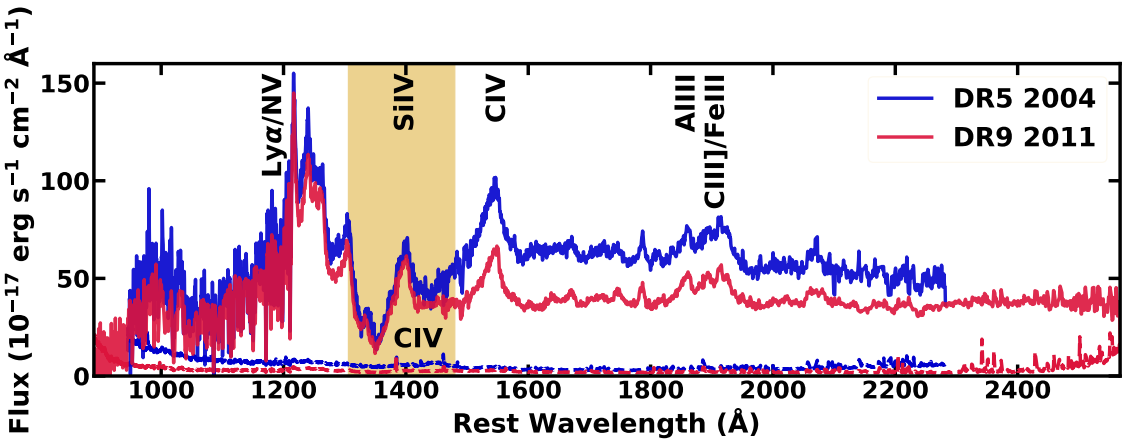

Figure 6.2.1: The spectra of J1646+2439 in SDSS DR5 and Baryon Oscillation Spectroscopic Survey (BOSS) DR9 (plotted in blue and red, respectively). Some of the major quasar emission lines are labeled above the spectra. The C IV trough is highlighted in beige. Although the absorption features show evidence for variability, we do not observe robust evidence for the emission line variability.

6.2. Data

The data used in this work were obtained from the SDSS (Blanton et al., 2017) archive (Figure 6.2.1). J1646+2439 was first observed on June 11, 2004, as part of the SDSS-I project (York et al., 2000). It was reobserved during the BOSS of SDSS-III project (Eisenstein et al., 2011) on May 4, 2011. The two spectra were taken $\sim$ 1.7 years apart in the quasar rest frame.

6.3. Analysis & Results

6.3.1. Continuum Modeling using *SimBAL*

SimBAL, when it was first developed, was used to model the absorption lines alone using a continuum-normalized spectrum (see Leighly et al., 2018). Instead, in this work as in Choi et al. (2020, 2022a), we modeled both the pseudo-continuum (continuum + emission features) and absorption lines simultaneously. Choi et al. (2022a) introduced the use of spectral principal components analysis (SPCA) eigenvectors for the emission line modeling for rest-UV spectra within *SimBAL*. SPCA pseudo-continuum modeling can

reproduce realistic emission line features for a given wavelength range with fewer model parameters than individual line-fitting procedures that require multiple parameters for each of the emission lines in the model.

We used a power-law model for the continuum emission for the BOSS spectrum and a broken power-law model for the SDSS spectrum with an "elbow", to model the observed spectral shape. The slope break point for the broken power-law model was constrained $\lambda \sim 1690$ Å from the *SimBAL* fit. To fit the emission lines, we used three sets of eigenvectors because there is not a suitable single set that spans the whole SDSS/BOSS spectral region. We used one set for emission lines between 1030 and 1290 Å and another for emission lines between 1290 and 1700 Å. The first set was constructed from a sample of 78 $z \sim 3$ quasars discussed in Pâris et al. (2011) and a detailed discussion on this eigenvector set can be found in Chapter 3 (§ 3.3). The second set was made from a sample of ∼100 quasars that show strong blueshift in C IV emission lines (Leighly et al., in preparation); this second one was preferred in the region where the two sets overlap since it models better the C IV emission line. Redward of 1700 Å, we used the eigenvectors described in Appendix A of Choi et al. (2022a), which are built from a set of 2626 objects. Each set of spectral principal component analysis (PCA) eigenvectors has six parameters: four coefficient parameters that yield the shape and the line ratios of the emission lines, and two additional parameters, the width parameter and the amplitude parameter, that control the overall strengths and the widths of the emission lines. The width parameter is not required for the eigenvector reconstruction. It is a convolution parameter used to replicate the range of emission line widths observed in quasars. Nevertheless, we included the parameter in our model to provide it with an additional method to reproduce a broad range of emission line widths observed in quasar spectra.

Figure 6.3.1 shows the pseudo-continuum models extracted from the best-fitting *SimBAL* models for SDSS DR5 and BOSS DR9. We also plotted the scaled emission-line composite with our pseudo-continuum models to examine the emission line strengths and ratios seen in the best-fitting *SimBAL* models. We compared our model with a composite

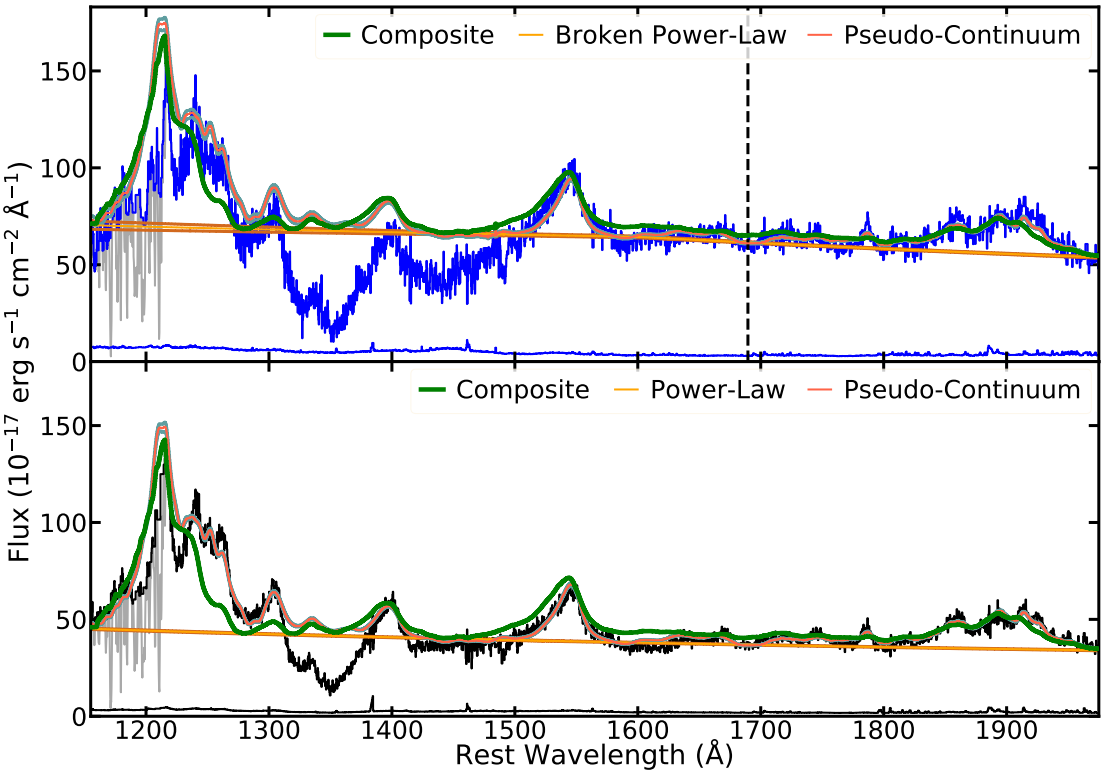

Figure 6.3.1: The pseudo-continuum model components extracted from the best-fitting *SimBAL* models for SDSS DR5 (top) and BOSS DR9 (bottom). Our emission line models generated from the SPCA eigenvectors show realistic rest-UV quasar emission lines with line ratios and strengths comparable to what are found in a composite spectrum. The grey points at $\lambda \lesssim 1216$ Å show the data points affected by the Lyman α forest features identified by our iterative method and they were ignored for *SimBAL* fitting. The emission composite from Temple et al. (2021) is plotted in green. The vertical line in the top panel shows the location of the slope break point ($\lambda \sim 1690$ Å) for the broken power-law model used in SDSS DR5.

template to examine whether our emission line model from spectral PCA eigenvectors has produced a reasonable emission line ratios and shapes that are comparable to those observed in real data. Temple et al. (2021) provides high-EW and high-blueshift emission line templates generated from the SDSS spectra. We took the high blueshift emission-line template because it showed a good match with the data around C IV and C III] emission line regions. We performed an additional continuum emission subtraction between $\sim$ 1440 Å and $\sim$ 2000 Å because the original template showed unusually strong Fe II emission features throughout that bandpass and we suspected that it was a contamination from inaccurate continuum subtraction. The modified emission line template was then scaled to match the strengths of the emission lines that are not affected by BAL, such as C IV and the emission lines around C III], and we added the scaled template to our continuum models. We found that our SPCA reconstructed pseudo-continuum models match very closely with the ones made with the emission-line template. Although our object (and the models) shows sightly stronger low-ionization emission lines (e.g., Si II), major emission lines (e.g., Lyα, Si IV, C IV) show a good match. This verifies that our SPCA reconstruction method indeed produces realistic emission line models and also shows that J1646+2439 has emission line properties typical of quasars with highly blueshift emission lines.

In EHVO quasars, Si IV absorption lines are often located on top of Lyα+N V emission lines, making it difficult to estimate the true strengths of the emission complex and the amount of Si IV opacity from the BALs. Choi et al. (2022a) found that in some BAL quasars, the emission lines were not absorbed by the BAL. We modeled J1646+2439 with and without emission line absorption and found that a spectral model with no emission line absorption produced a more self consistent fit. The models with emission line absorption predicted strong Lyα+N V emission features that are not found in EHVO quasars (see composite described above). This was because the models predicted a moderate amount of Si IV opacity near the Lyα+N V region and, in order to match the flux levels observed in that region, the models produced strong emission lines to compensate for the absorption from Si IV BAL. In contrast, the models with no emission line absorption from the

BAL produced pseudocontinuum models that resemble typical emission features seen in EHVO quasars. While this modification to the models resulted in much weaker Lyα+N V emission lines in the pseudo-continuum models than the initial model we tried, the overall BAL physical properties did not show significant differences. We note again that the continuum and line emission fitting was done simultaneously with the BAL absorption modeling.

We did not find evidence for significant emission line variability between SDSS and BOSS (Figure 6.2.1). Therefore, we simultaneously fit both the SDSS and the BOSS spectrum, constraining the values of eigenvector coefficient parameters and the width parameters of the emission lines to be the same for both SDSS and BOSS spectra models. The continuum model parameters and the emission line amplitude parameters were allowed to vary between the models for SDSS and BOSS, such that the equivalent widths of the emission lines were allowed to be different for the two models while keeping the shapes of the line profiles to be the same.

6.3.1.1. Identifying Lyα Forest Absorption-Lines

We removed intervening Lyα absorption lines using the following method in order to be able to analyze the potential EHVO absorption present in the Lyα forest. We used an iterative sigma-clipping method to identify the pixels affected by the Lyα lines. Each iteration began with a smoothed spectrum made with a Gaussian kernel of a set width, followed by flagging all data points that fell certain sigma (e.g., $0.5\sigma \sim 2.5\sigma$) below the smoothed spectrum. The subsequent iteration produced a new smoothed spectrum with the same Gaussian kernel but with an updated spectrum where the fluxes for the flagged data points from the previous iteration had been replaced by the interpolated values from the unflagged remaining data points. The iteration ended when no new data points were flagged. We experimented with Gaussian kernels of different widths and varying sigma cutoffs (0.7σ to 2σ) and visually inspected the results to determine the best combination for our data.

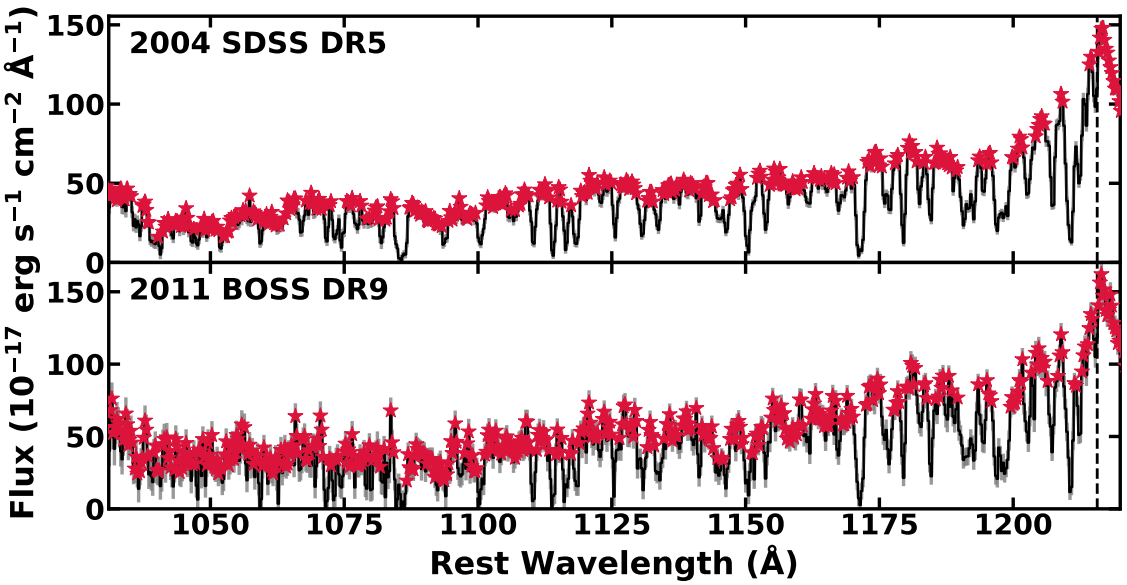

Figure 6.3.2: The top (bottom) panel shows how our iterative method to identify the data points affected by the Lyman α forest features performed with the SDSS DR5 (BOSS DR9) spectrum data. We used the unflagged data (red stars) that is free of non-BAL absorption to fit the *SimBAL* model for our analysis. The location of Lymanα emission line (1216 Å) from which we performed the iterative sigma-clipping is shown as vertical dashed-lines.

The result of our Lyα forest absorption-lines flagging procedure is shown in Figure 6.3.2. We flagged 39% (49%) of the data points between 1030 Å and 1216 Å as affected by non-BAL absorption following our iterative method from BOSS (SDSS) spectrum. We tested different non-BAL absorption flags produced by various sigma cutoff values for the *SimBAL* fitting and found that the solutions from the best-fitting *SimBAL* models show no significant difference.

The use of this method is possible for the BAL quasar spectra because the intrinsic absorption features from the outflows are broad and smooth, unlike the narrow absorption lines from the Lyα forest. Otherwise, the iterative sigma-clipping method would also flag the intrinsic absorption features along with the Lyα lines. We do not analyze the wavelengths shortward of 1030 Å because the sensitivity and signal-to-noise ratio (SNR) are reduced at the edge of the SDSS/BOSS spectrum and an additional opacity from Lyβ absorption lines starts to contaminate the spectra, making it more difficult to estimate the

quasar continuum.

6.3.2. Absorption Modeling using *SimBAL*

We simultaneously fit both the DR5 and DR9 spectra using *SimBAL* and compared the constrained physical properties of the outflow gas seen in both epochs. *SimBAL* uses six parameters to model the absorption features: ionization parameter $\log U$, density $\log n$ (cm^{-3}), thickness of the gas relative to the hydrogen ionization front $\log N_H - \log U$ (cm^{-2}), outflow velocity v $(\mathrm{km\ s}^{-1})$, velocity width σ or Δv (km s^{-1}), and a dimensionless covering fraction parameter $\log a$ (higher value corresponds to a lower covering fraction). The absorption troughs can be modeled by a Gaussian opacity profile or the "tophat accordion" model where a broad opacity profile is divided into multiple velocity-adjacent "tophat" bins with each bin allowed to have independent set of physical parameters (Leighly et al., 2018). We refer to Leighly et al. (2018, 2019b) for detailed discussion on how the model is implemented in the software and the physical interpretations of the power-law partial covering. A comprehensive introduction to the software can be found in Chapter 2 (§ 3.2).

Figure 6.3.3 shows our best-fitting *SimBAL* models. These models for J1646+2439 have the following prescription:

$$f_{model}(\lambda) = f_{continuum}(\lambda) \times I_{BAL}(\lambda) + f_{line\ emission}(\lambda),$$

where the power-law (or broken power-law for SDSS DR5) continuum emission is absorbed by the outflow gas (I_{BAL}) and the emission lines are not absorbed by the outflow gas (§6.3.1). Due to their different widths, we used a 19-bin tophat accordion model to fit the troughs in the DR5 J1646+2439 data and a 11-bin model for DR9 to fit the troughs in DR9. The number of bins used in tophat accordion model does not affect the robustness of the *SimBAL* model fits (Leighly et al., 2018).

For this object, the tophat bins for each accordion model were constrained to have the same $\log U$ and $\log n$ while allowing $\log N_H - \log U$ and $\log a$ for each bin to freely

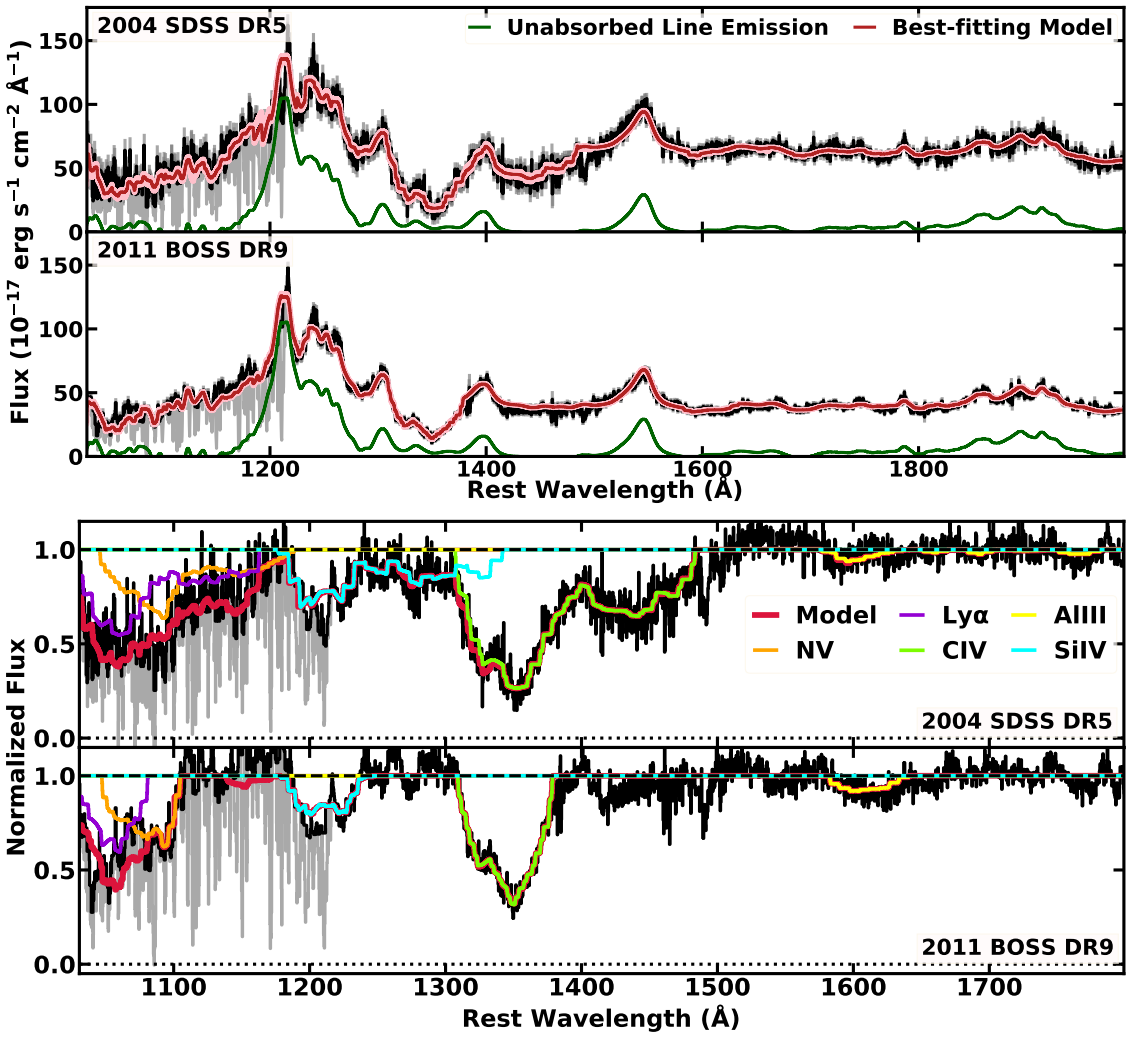

Figure 6.3.3: The top two panels show the best-fitting *SimBAL* models and 95.5% uncertainties (red and pink, respectively) for 2004 SDSS DR5 and 2011 BOSS DR9; the bottom two panels show the normalized models with the line identifications. The grey lines show the spectrum data that includes both the outflow BAL troughs and the Lyman forest absorption lines and the black lines show the data we used for the *SimBAL* model fitting where the non-BAL absorption lines have been flagged and ignored. The data and the models have been normalized using the pseudo-continuum models extracted from the full best-fitting models. The unabsorbed emission line features (green) reveal a large amount of unabsorbed flux in the Lyα+N V emission line region. The BAL trough extends to lower-velocity with a larger width in the 2004 SDSS DR5 data. The model for 2011 BOSS DR9 shows some opacity from low-ionization ions such as Al III indicating a higher column density outflow.

vary. Because we do not have any density sensitive diagnostic absorption lines (e.g., Lucy et al., 2014; Arav et al., 2018) that can be used to constrain the density from the model fitting, we instead fixed the density parameter at three values $\log n = 4,\ 6,\ \text{and}\ 8\ (\text{cm}^{-3})$ to systematically check whether the best-fitting models (and the constrained parameters) show dependence on BAL gas density. In addition to the column density grid with the solar metallicity grid, we also tested a model with the enhanced metallicity ($\text{Z} = 3\text{Z}_{\odot}$) grid and the solar metallicity grid that was generated with a hard spectral energy distribution (SED). We refer to Leighly et al. (2018) for details on the currently available column density grids for *SimBAL* (see also § 3.2.4).

As explained in 6.3.1, we used *SimBAL* to fit both the pseudo-continuum (emission lines + continuum) and the absorption lines together. We also fit both epochs simultaneously. We ran *SimBAL* to obtain the converged MCMC chain, and using this chain, we generated best-fitting models for both epochs simultaneously, and extracted posterior distributions of the parameters with which we obtained the physical properties of the outflows. The principal absorption lines found by the best-fitting *SimBAL* models are C IV, Si IV, N V, and Lyα. Visual inspection did not reveal low-ionization transitions in either spectra (such as Mg II and Al III), but the best-fitting models found evidence for weak Al III. In order to make sure *SimBAL* is not misidentifying the noise as low-ionization transitions, we performed the following test: we fit DR5 and DR9 data only up to ~ 1550 Å. Then, we extrapolated the resulting models to longer wavelengths to see if the models would also predict opacity from Mg II and Al III. The extrapolated models indeed showed similar amounts of opacity from these transitions as the best-fitting models that used the full bandpass, which supported the robustness of our best-fitting models.

The best-fitting model for DR5 shows a very broad absorption feature stretched from ~ 1500 Å to ~ 1180 Å (third panel from the top in Figure 6.3.3). The feature consists of blended C IV and Si IV that overlap between ~ 1300 and ~ 1350 Å. We experimented with a modified *SimBAL* model for DR5 with extra tophat bins at the highest velocity end, in order to test the possibility that the absorption corresponds completely to an ultra-

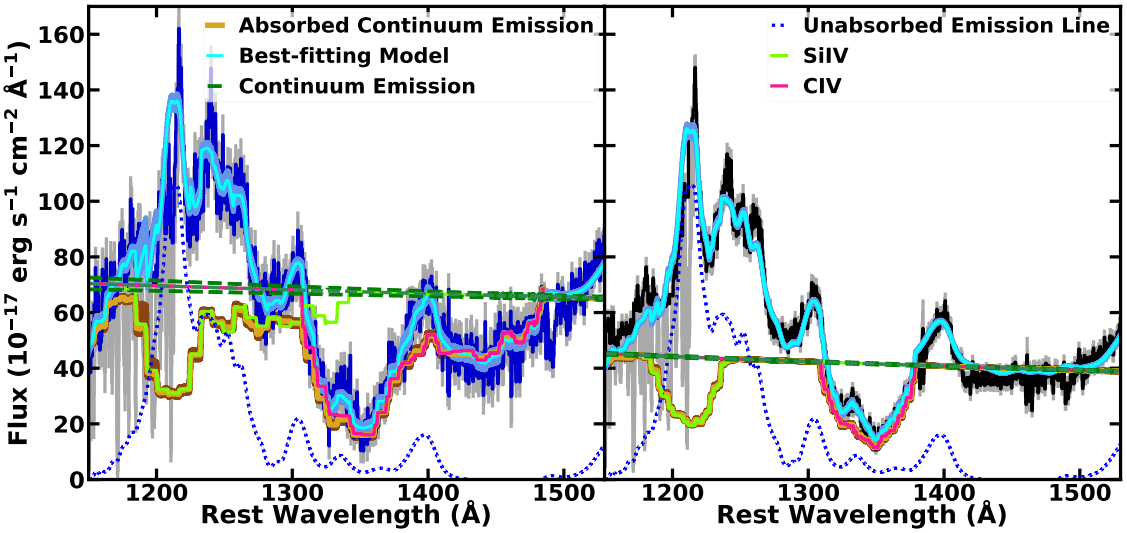

Figure 6.3.4: Si IV absorption identified by best-fitting *SimBAL* models in DR5 (left) and DR9 (right). A considerable amount of absorption from Si IV is seen in the continuum emission models. The opacity profile of Si IV largely resembles that of C IV.

wide trough of C IV. The converged model from this experiment showed no discernible differences from our best-fitting model; in other words, even when inputting a larger velocity of C IV to the test model, the parameters rearranged themselves to create Si IV opacity and only show significant opacity C IV between $\sim$ 1300 Å and $\sim$ 1500 Å, identical to what we found in the best-fitting model. Thus, the possibility that the trough is wider than in the best-fitting model is not supported.

In order to investigate how much Si IV opacity is hidden near the Lyα+N V emission line, we separated the emission lines and continuum emission from the best-fitting models (Figure 6.3.4). The model decomposition clearly shows deep Si IV troughs in the accretion disk continuum emission. In contrast, the best-fitting *SimBAL* models in Figure 6.3.3 only shows a moderate amount of apparent Si IV opacity from the main EHVO. That is because the bottoms of the Si IV troughs have been filled in by the flux from the unabsorbed Lyα+N V emission line, making the apparent depths of Si IV troughs shallower. This type of behavior is also seen in objects with lower velocity outflows, where Lyα+N V BAL is filled in by the emission lines (e.g., Leighly et al., 2019a; Green et al., in preparation).

6.3.3. Absorption Properties from *SimBAL* Models

We extracted the gas physical parameters $\log U$, $\log N_H - \log U$, and the covering fraction parameter $\log a$ as well as the gas kinematics (outflow velocity and width) of the BAL outflows from the best-fitting *SimBAL* models. We report the results extracted from the models generated from two column density grids with different metallicity and gas density fixed at $\log n = 6$ [cm^{-3}]. The outflow properties constrained from the *SimBAL* models are tabulated in Table 6.3.1. Using the Markov Chain Monte Carlo (MCMC) chains produced by *SimBAL*, we calculated the median values and 2σ (95.5%) uncertainties from the posterior distributions of each parameters.

The EHVO BAL trough for BOSS DR9 extends from $-35,200\ \mathrm{km\ s^{-1}}$ to $-49,800\ \mathrm{km\ s^{-1}}$ with the remarkable velocity width of $v_{width} \sim 14,600\ (\mathrm{km\ s^{-1}})$. The SDSS DR5 revealed even more dramatic BAL with the velocity ranging from $-13,400\ \mathrm{km\ s^{-1}}$ to $-50,200\ \mathrm{km\ s^{-1}}$ and $v_{width} \sim 36,900\ (\mathrm{km\ s^{-1}})$. The highest velocities of the BALs in the two spectra are similar, but the BAL in SDSS DR5 extends down to lower velocity by more than $20,000\ \mathrm{km\ s^{-1}}$. From the solar metallicity models, we obtained the ionization parameters of $\log U = -0.92^{+0.09}_{-0.1}$ for SDSS and $\log U = -0.64 \pm 0.07$ for the BOSS spectrum.

From some of the bins, we were only able to obtain upper limits on the column density parameter ($\log N_H - \log U$ [cm^{-2}]) because the lowest value our current column density grids can reach is 21.0 [cm^{-2}] (21.2 for $\mathrm{Z} = 3\mathrm{Z}_{\odot}$ grid). We could not extract reliable posterior distributions for $\log N_H - \log U$ for these bins because the MCMC walkers were approaching the lowest value of the column density available in the ionic column density grid. By design, *SimBAL* can only explore the region of parameter space allowed by the ionic column density grids (Chapter 3;§ 3.2). We took the values of the lower bounds of the grids as the upper limit values for $\log N_H - \log U$ in these bins.

We calculated the total outflow column densities with and without the bins with upper limit values. The total outflow column density is generally calculated by summing the

Table 6.3.1. Absorption Measurements from *SimBAL* Models[a]

Epoch	$\log U$	$\log N_H - \log U$[b] $[\mathrm{cm}^{-2}]$	$\log a$[b]	$\log N_H$ total[c] $[\mathrm{cm}^{-2}]$	v_{min}[d] km s^{-1}	v_{max}[d] km s^{-1}
			$\mathrm{Z} = \mathrm{Z}_\odot$			
DR5	$-0.92^{+0.09}_{-0.1}$	$\lesssim 21.0 - 23.05$	$0.78 - 1.90$	$21.49^{+0.12}_{-0.15}$	-12400	-51200
DR9	-0.64 ± 0.07	$\lesssim 21.0 - 22.92$	$0.97 - 1.30$	21.79 ± 0.08	-34500	-50500
			$\mathrm{Z} = 3\mathrm{Z}_\odot$			
DR5	$-1.24^{+0.07}_{-0.06}$	$\lesssim 21.2 - 22.88$	$0.72 - 1.81$	$20.75 \pm 0.09 - 20.79^{+0.09}_{-0.08}$	-12400	-51200
DR9	$-1.05^{+0.08}_{-0.07}$	$\lesssim 21.2 - 22.42$	$0.96 - 1.49$	$20.93 \pm 0.09 - 20.94 \pm 0.09$	-34500	-50500

[a]We report the values extracted from the best-fitting *SimBAL* models ($\log n = 6\ [\mathrm{cm}^{-3}]$). We used 19-bin and 11-bin accordion tophat models for DR5 and DR7, respectively.

[b]The range of values estimated from the multiple bins is reported.

[c]The total outflow column density is the sum of the covering fraction weighted column densities calculated for each bin. For the $\mathrm{Z} = 3\mathrm{Z}_\odot$ models, the range of values represent whether the bins with upper limits are included in the calculation (see text).

[d]The values were calculated from the edge of the tophat bin at the highest and lowest velocities.

covering fraction weighted column densities calculated from all bins. For our models, including the bins with upper limits may provide us with an upper limits for the total outflow column densities and excluding them may give us lower limits. The total covering fraction weighted outflow column densities are $\log N_H = 21.49^{+0.12}_{-0.15}$ [cm^{-2}] and $\log N_H = 21.79 \pm 0.08$ [cm^{-2}] for SDSS and BOSS, respectively, when calculated including the bins with upper limits. We obtained the same values when we excluded those bins. This is not surprising since out of 19 and 11 bins for SDSS and BOSS accordion tophat models, respectively, only one tophat bin from each model has upper limits and their contributions to the total outflow column density calculations were insignificant ($\log N_H \lesssim 19$ [cm^{-2}]). Therefore, although the models included a small number of bins without well constrained posteriors, we were able to calculate the outflow column densities and the associated uncertainties for the solar metallicity models.

We also performed *SimBAL* analysis using two other available column density grids to explore systemic uncertainties associated with metal abundances and with the choice of SED: an enhanced metallicity ($\mathrm{Z} = 3\mathrm{Z}_{\odot}$) grid and a solar metallicity with a hard SED grid (Leighly et al., 2018). The best-fitting *SimBAL* models using enhanced metallicity grid also produced excellent spectral fits to the data that were indistinguishable from the solar metallicity models; however the outflow physical properties from these models showed physically significant differences. From the enhanced metallicity ($\mathrm{Z} = 3\mathrm{Z}_{\odot}$) models, we obtained slightly lower $\log U$ and all the bins showed $\log N_H - \log U$ that were systemically lower compared to the solar metallicity models. This expected because more metal ions, e.g., Si and C, are available at the higher metallicity. We found $\log U = -1.24^{+0.07}_{-0.06}$ for SDSS and $\log U = -1.05^{+0.08}_{-0.07}$ for the BOSS spectrum from the models with the enhanced metallicity grid. We calculated the total covering fraction weighted outflow column densities of $\log N_H = 20.79^{+0.09}_{-0.08}$ [cm^{-2}] and $\log N_H = 20.94 \pm 0.09$ [cm^{-2}] for SDSS and BOSS, respectively, when the bins with upper limits on $\log N_H - \log U$ are included. When calculated without these bins, we obtained $\log N_H = 20.75 \pm 0.09$ [cm^{-2}] and $\log N_H = 20.93 \pm 0.09$ [cm^{-2}] for SDSS and BOSS, respectively.

The best-fitting models with the hard SED grid performed significantly poorly compared to the models obtained with the other two grids. As reported in Leighly et al. (2018), we also noticed the model over-predicted Lyα opacity. Such result is not surprising because the hard SED used to generate the grid is more appropriate for Seyfert galaxies (Korista et al., 1997) with low bolometric luminosity ($\lesssim 10^{45}\mathrm{erg\ s^{-1}}$). Therefore we rejected the models generated from the hard SED grid and we do not include the results derived from it.

Figure 6.3.5 shows the physical properties of the outflow gas observed in DR5 and DR9 as a function of velocity determined from the best-fitting *SimBAL* models. We found consistently larger values of $\log N_H - \log U$ for all bins in the model for the BOSS spectrum. The figure reports a single ionization parameter value for SDSS DR5 and BOSS DR9 spectra because the tophat bins for each model were constrained to have the same $\log U$. We experimented with a set of models where we allowed $\log U$ to vary; however, they did not produce sufficiently statistically better model fits to justify increasing the number of degrees of freedom and fit parameters of the models.

In addition to the models with $\log n = 6$ [$\mathrm{cm^{-3}}$], we ran *SimBAL* models with outflow gas density fixed at two different values ($\log n = 4$ and 8 [$\mathrm{cm^{-3}}$]) to examine how the best-fitting parameter solutions may change with density. Because there are no absorption lines in the bandpass that are sensitive to density in high-ionization outflows, the best-fitting spectral models with different densities were indistinguishable and the constrained physical parameters (e.g., $\log U$) were consistent within the 1σ uncertainties, as expected. In other words, the physical properties of the outflow constrained by *SimBAL* do not depend on our choice of density. Although there is neither information in the spectra with which we can estimate the density of the outflow gas nor other EHVO outflows with constrained gas densities, $\log n = 6$ [cm^{-3}] is a reasonable assumption for BAL outflow gas and previous *SimBAL* analysis of a BAL quasar SDSS J0850+4451 (Leighly et al. 2018) found similar density constraints. However, we again note that we have no density constraints for the outflows observed in J1646+2439.

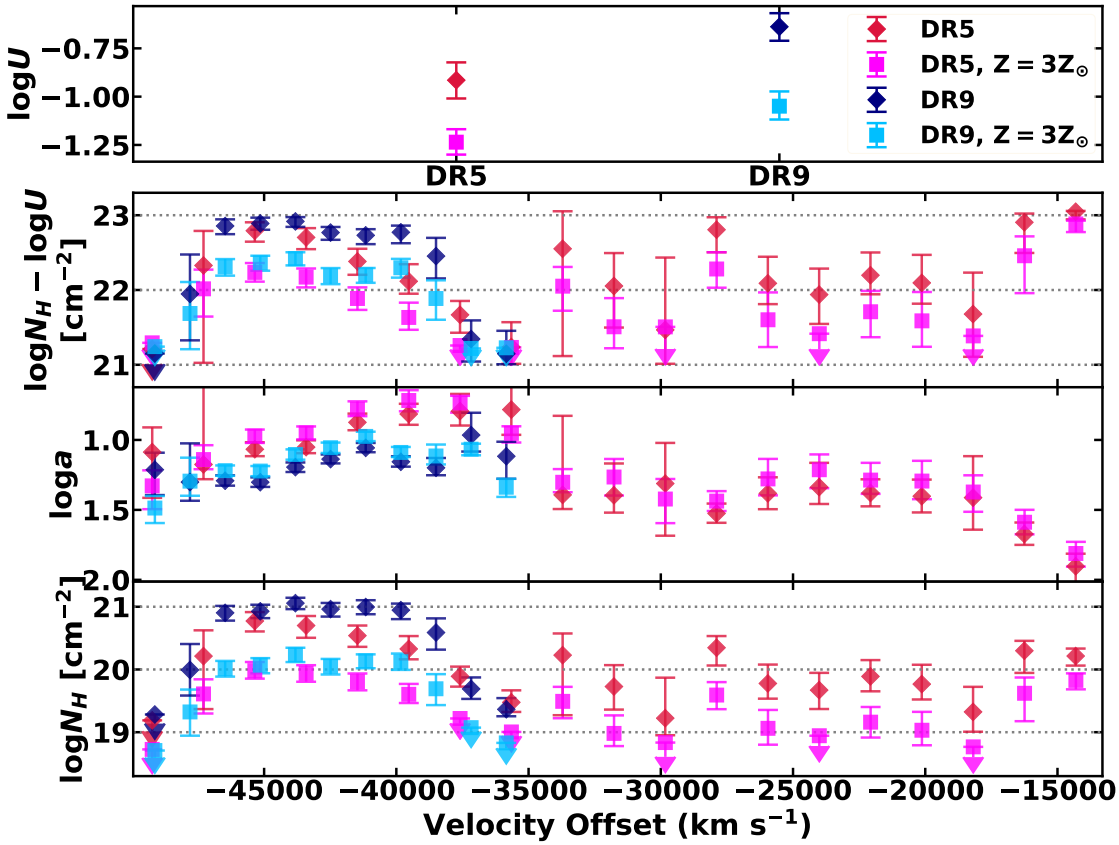

Figure 6.3.5: The outflow physical properties as a function of velocity from the tophat models for SDSS DR5 and BOSS DR9 spectra. The outflow found in BOSS lacks the lower-velocity part of the outflow seen in SDSS spectrum. The enhanced metallicity ($Z = 3Z_{\odot}$) models show lower ionization parameters ($\log U$) and column density parameters ($\log N_H - \log U$ [cm^{-2}]) for both spectra. This result in smaller estimated outflow column densities. The best-fitting models plotted here used a fixed value of $\log n = 6$ [cm^{-3}]. The downward arrows represent the upper-limit estimates because of the finite sizes of the column density grids currently available in *SimBAL*.

6.4. Discussion & Summary

The *SimBAL* analysis provided us with excellent constraints on the ionization parameters and column densities of the outflowing gas observed in the spectra of J1646+2439. However, due to the lack of density-sensitive diagnostic absorption-lines in the spectra, it is not possible to constrain the density of BAL gas directly from spectral analysis. This means we need to infer the location of the outflowing gas using our prior knowledge about BAL cloud geometry and the properties of spectral variability seen in this object to estimate the mass outflow rate and the amount of energy the outflow is carrying.

6.4.1. Estimated Outflow Properties

BAL spectral variability can be caused by several mechanisms. Two major hypotheses includes a change in ionization state of BAL outflowing gas and the transverse motion of the BAL absorbing gas (e.g., Hamann et al., 2011; Capellupo et al., 2012). Based on these ideas we can constrain the probable range of densities and the locations of the outflowing gas. If the BAL variability is assumed to be caused by a change in ionization state of the outflowing gas, we can estimate density of the gas using the equation, $\Delta t \gtrsim 1/n_e\alpha_r$, where Δt is BAL variability timescale, n_e is the electron density of the gas (n in *SimBAL*), and α_r is the recombination-rate coefficient (e.g., Hamann et al., 1995; Capellupo et al., 2013). We obtain $n_e \gtrsim 10^3$ [cm^{-3}] with $\alpha_r = 1.5 \times 10^{-11}$ (T= 20000K, McGraw et al., 2017) and $\Delta t \sim 1.7$ years (§ 6.2). This would put the outflowing gas in this object at $r \lesssim 1500$ pc from the central SMBH. If we consider outflowing gas moving transversely then we can estimate the distance of the outflows with the equation, $r = \frac{GM_{BH}}{v_{trans}^2}$ where r is the distance of the outflowing gas from the central SMBH, M_{BH} is the mass of the SMBH, G is the gravitational constant, and v_{trans} is the transverse velocity of the clouds that can be approximated as Keplerian speed (Moravec et al., 2017). However, we cannot reliably measure the mass of the SMBH for J1646+2439 without the rest-optical spectrum where we can measure the widths of the Balmer lines needed for the calculation of the blackhole mass.

Using the physical constraints provided by the *SimBAL* analysis, we calculated the volume filling factor (or normalized radial widths, $\Delta R/R$) for a range of densities (left panel in Figure 6.4.1). The volume filling factor measures how thin or extended in the radial direction the BAL cloud structure is. For iron low-ionization broad absorption-lines (FeLoBALs), most of the time the outflowing gas has volume filling factor between $\sim 10^{-6}$ and $\sim 10^{-4}$ (Chapter 5 in § 5.7.2; e.g., Korista et al., 2008; Moe et al., 2009; Dunn et al., 2010; Choi et al., 2022b). High-ionization broad absorption-lines (HiBALs) outflows, more similar to EHVO outflows, also have a similar range of values of volume filling factors (e.g., Gabel et al., 2006; Hamann et al., 2011, 2013). Unless the EHVO gas clouds are expected to have dramatically different geometrical properties as typical BAL outflows, we can assume that they may also have comparable volume filling factors. We obtain the density range of $4 \lesssim \log n \lesssim 8$ [cm^{-3}] for the outflowing gas in J1646+2439 to have proportional volume filling factors as typical (FeLo)BALs. Higher (lower) density will make the gas disproportionately too thin (thick), which are not observed in BAL quasars. This range also coincide with the range of density values we experimented with *SimBAL* models (§ 6.3.3).

Based on the range of densities expected for the BAL outflow in J1646+2439, we can calculate the potential distance estimates using the following relationship, $U = Q/(4\pi R^2 nc)$ where Q is the number of photoionizing photons per second emitted from the central engine. The value of Q was estimated by scaling the *Cloudy* input SED to the available photometry data for J1646+2439. We estimated $\log Q \sim 57.2$ [photons s^{-1}]. The right panel in Figure 6.4.1 shows the range of distances of the outflowing gas from the central engine. The distances that correspond to $4 \lesssim \log n \lesssim 8$ [cm^{-3}] are $5 \lesssim R \lesssim 500$ pc. Although it is difficult to further narrow the range of expected locations of the outflowing gas, we can assume the actual location of the outflowing gas may be closer to the lower bound of the range. This is because our best-fitting *SimBAL* model included the unabsorbed emission line component (§ 6.3.1). Such differential partial covering between line emission and continuum emission is difficult to produce with gas

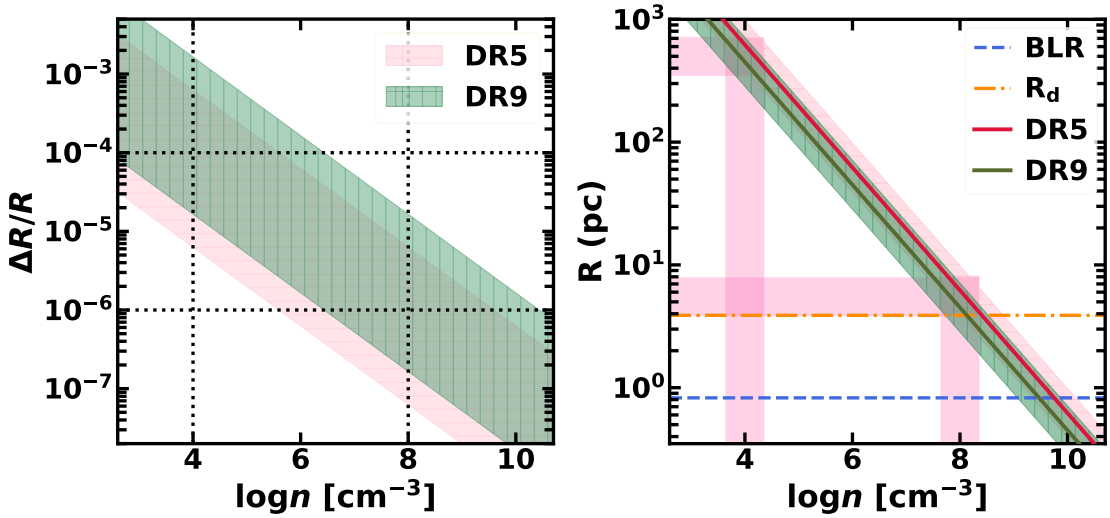

Figure 6.4.1: *Left panel:* The range of possible volume filling factors ($\Delta R/R$, § 5.5.3) are plotted as a function of density. The nominal values observed in BAL outflows, $10^{-6} \lesssim \Delta R/R \lesssim 10^{-4}$, are plotted in horizontal black dotted lines. It is likely that the outflowing gas in J1646+2439 have $4 \lesssim \log n \lesssim 8$ [cm^{-3}], assuming the EHVO gas share comparable cloud geometry as BAL outflows. The shaded areas represent the range of column density values constrained by the bins ($21 \lesssim \log N_H - \log U \lesssim 23$ (cm^{-2}), Figure 6.3.5). *Right panel:* The location of the outflowing gas as a function of probable density range in DR5 and DR9 are plotted in red and green, respectively. The diagonal shaded regions along the solid lines represent potential systematic uncertainties associated with the calculation and the width corresponds to 0.2 dex in each direction. The most likely density of the outflowing gas, $4 \lesssim \log n \lesssim 8$ [cm^{-3}], and the corresponding range of distances are highlighted with pink shades. The radii of the broad line region (BLR) estimated from the monochromatic flux at 5100 Å (Bentz et al., 2013) and the inner edge of torus represented by the dust sublimation radius (R_d, Elitzur & Netzer, 2016) are also plotted for reference.

clouds located at large distance because the angular sizes of the emission sources become extremely small (e.g., Leighly et al., 2019b). Therefore, we expect the BAL outflow in J1646+2439 to be located tens of parsecs from the central SMBH.

We calculated the mass outflow rate and the kinetic energy of the outflow using both the properties constrained by the *SimBAL* analysis and the assumed location of the outflow. The mass outflow rate can be calculated using the equation, $\dot{M}_{out} = 8\pi\mu m_p \Omega R N_H v_{outflow}$ (Dunn et al., 2010) where the mean molecular weight is assumed to be $\mu = 1.4$ and the global covering fraction is given by $\Omega = 0.2$ (e.g., Hewett & Foltz, 2003). We took the column density of the outflow (N_H) and outflow velocity (v_{out}) constrained from the solar metallicity models and assumed the location of the outflows to be $R \sim 50$ pc, which corresponds to $\log n \sim 6$ [cm^{-3}] that falls in the middle of the expected density range. We estimated $\log \dot{M}_{out} \sim 2.5$ [M$_\odot$ yr^{-1}] and $\log \dot{M}_{out} \sim 2.9$ [M$_\odot$ yr^{-1}] for DR5 and DR9, respectively. The kinetic energy of the outflow is given by the equation, $\dot{E}_k = \dot{M}_{out} v_{out}^2/2$. We calculated $\log\ L_{KE} \sim 47.2$ [erg s^{-1}] and $\log\ L_{KE} \sim 47.6$ [erg s^{-1}] for DR5 and DR9, respectively. We note that the kinetic energy and the mass outflow rate of the outflow are both proportional to the assumed location of the outflow. Given that the range of probable outflow location is $5 \lesssim R \lesssim 500$ pc and the estimates reported here are calculated at $R \sim 50$ pc, the probable ranges of the kinetic energy and the mass outflow rate of the outflow span a decade in both directions from the reported estimates.

The enhanced metallicity (Z $= 3$Z$_\odot$) models found lower values of column density ($\log N_H$ [cm^{-2}]) for both DR5 and DR9 (Figure 6.3.5). Therefore the mass outflow rates and kinetic energies of the outflows are substantially smaller than those of the solar metallicity models. We estimated the mass outflow rates $\log \dot{M}_{out} \sim 1.8$ [M$_\odot$ yr^{-1}] and $\log \dot{M}_{out} \sim 2.0$ [M$_\odot$ yr^{-1}] for DR5 and DR9, respectively. The kinetic luminosity estimates are $\log\ L_{KE} \sim 46.5$ [erg s^{-1}] and $\log\ L_{KE} \sim 46.8$ [erg s^{-1}] for DR5 and DR9, respectively.

The momentum flux ratio ($\dot{P}_{outflow}/\dot{P}_{AGN}$; $\dot{P}_{outflow} = \dot{M}_{out} v_{outflow},\ \dot{P}_{AGN} = L_{Bol}/c$) can be used to infer potential outflow acceleration mechanisms of quasar outflows. For

instance, $\dot{P}_{outflow}/\dot{P}_{AGN} \sim 1$ is expected for radiatively driven winds in which the outflowing gas is accelerated by the scattering of photons (momentum conserving, e.g., King, 2003; King & Pounds, 2003). The ratio can exceed unity when dust is present in the gas cloud (Thompson et al., 2015). Quasar outflows with $\dot{P}_{outflow}/\dot{P}_{AGN} \gg 1$ are also observed in ionized winds and molecular outflows (e.g., Fiore et al., 2017). These outflows are believed to be powered by an energy conserving acceleration mechanism and they are mostly found at large distances ($\log R \gtrsim 2$ [pc]) from the central SMBH (e.g., King & Pounds, 2015). For J1646+2439, we estimated $\dot{P}_{outflow}/\dot{P}_{AGN} \sim 4$ and $\dot{P}_{outflow}/\dot{P}_{AGN} \sim 10.4$ from the solar metallicity models for DR5 and DR9, respectively, and $\dot{P}_{outflow}/\dot{P}_{AGN} \sim 0.74$ and $\dot{P}_{outflow}/\dot{P}_{AGN} \sim 1.47$ from the enhanced metallicity models for DR5 and DR9, respectively. These values are consistent with what have been observed in (FeLo)BAL outflows (Chapter 5, Figure 5.23; Fiore et al., 2017; Choi et al., 2022a). We found no compelling observational evidence suggesting that the EHVOs require a special acceleration mechanisms to explain their extremely-high outflow velocities.

The strengths of the outflows are often evaluated relative to the bolometric luminosity of the quasar. For instance, outflows with kinetic energy exceeding 0.5%$\sim$5% of the quasar bolometric luminosity are believed to be able to effectively power active galactic nucleus (AGN) feedback and influence the host galaxy evolution (e.g., Scannapieco & Oh, 2004; Di Matteo et al., 2005; Hopkins & Elvis, 2010). We calculated the bolometric luminosity $\log\ L_{Bol} = 47.8$ [erg s^{-1}] from the monochromatic flux at 5100 Å estimated from the Two Micron All Sky Survey (2MASS) photometry and the bolometric correction from Gallagher et al. (2007). Using the kinetic luminosity estimates from the solar metallicity model, we obtain $L_{KE}/L_{Bol} \sim 25\%$ and $L_{KE}/L_{Bol} \sim 63\%$ for DR5 and DR9, respectively, which indicates the BALs in J1646+2439 may have enough energy to to contribute to feedback. We note again that the kinetic energy of the outflow and the mass outflow rate are both linearly dependent on the location of the outflow. If the true location of the outflowing gas significantly smaller (larger) than the fiducial value used for the estimates ($R \sim 50$ pc), the outflow strengths will also decrease (increase) proportionally.

6.4.2. Summary

We analyzed the multi-epoch spectroscopic data of J1646+2439 using *SimBAL*. Using the two available data sets, SDSS DR5 and BOSS DR9, we performed a simultaneous model fitting where the emissions line shape in the pseudocontinuum model for the two epochs were constrained to be identical. We were able to constrain the ionization parameters and column densities of the outflowing gas from the best-fitting *SimBAL* models (Figure 6.3.5). Although we were not able to constrain the density of the outflow from the *SimBAL* due to the lack of density sensitive diagnostic absorption lines, we estimated a range of density values that is likely allowed for the outflowing cloud in J1646+2439 (Figure 6.4.1). The outflowing gas is expected to be located ~ 10s pc from the central SMBH and we calculated the kinetic luminosity and mass outflow rate assuming the outflow location of $R \sim 50$ pc. Based on this estimate, we calculated $L_{KE}/L_{Bol} \sim 25\%$ and $L_{KE}/L_{Bol} \sim 63\%$ for DR5 and DR9, respectively, which suggested that the outflow in this object is powerful enough to enact feedback.

As the name suggests, EHVOs have extremely-high velocity and thus they are thought to have kinetic power significantly greater than that of typical BAL outflows. While this statement is true, because EHVOs are typically HiBAL outflows and their outflowing gas have low column densities ($\log N_H \lesssim 22$ [cm^{-2}]). In order to produce energetic outflows, the outflowing clouds need to have both high column densities and high velocities. For instance, the current record holder for the most energetic BAL outflow, SDSS J135246.37+423923.5 (Chapter 4, Choi et al., 2020), has a high column density outflow that can produce FeLoBAL features ($\log N_H \gtrsim 23$ [cm^{-2}]) and also extremely high outflow velocities ($v_{off} \sim -38000\,\mathrm{km\,s^{-1}}$). Therefore, EHVOs may be able to produce outflows with significant kinetic power but they are likely not be able to create extreme outflows such as those found in FeLoBAL quasars.

The spectral variability observed in this object is quite unique in that only the lower-velocity part of the outflow showed a strong change in depths between two epochs. This

result is in disagreement with previous work on BAL spectral variability. For example, large scale studies done on multi-year time scales found that higher-velocity BAL components are more likely to vary than lower-velocity part of the outflow (e.g., Capellupo et al., 2011; Filiz Ak et al., 2012). A recent work by Leighly et al. (2015) found more significant changes in higher-velocity BAL features that at lower velocity in Hubble Space Telescope (HST) spectra of a low-redshift narrow-line Seyfert 1 galaxy WPVS 007. The collaborators on this projects, Drs. Patrick B. Hall and Paola Rodríguez Hidalgo, are currently analyzing the results from the *SimBAL* spectral analysis to study the origin of BAL variability in J1646+2439.

CHAPTER 7

Conclusions

7.1. Chapter Summaries

Chapters 2 and 3

In Chapter 2, I briefly described the observational facilities and instruments used to collect the data used in the work presented in this dissertation. The majority of the optical spectra used were observed as part of the Sloan Digital Sky Survey (SDSS) with the Sloan Foundation 2.5-meter telescope, and we obtained the data from the SDSS public archive. We used the Gemini Near-Infrared Spectrograph (GNIRS) instrument at the 8.1-meter Gemini North telescope and TripleSpec instrument at the Apache Point Observatory (APO) 3.5-meter telescope to obtain near-infrared (rest-optical) spectra of SDSS J135246.37+423923.5 (hereafter referred to as SDSS 1352+4239; Chapter 4). In Chapter 3, I introduced the state-of-the-art spectral analysis tool for broad absorption-line (BAL) quasar spectra *SimBAL* our group developed (Leighly et al., 2018). The software uses a spectral synthesis method based on detailed photoionization modeling, an empirical implementation of partial covering, and a number of machine learning techniques to model complex spectral features observed in BAL quasar spectra. *SimBAL* has shown tremendous success in analyzing (FeLo)BAL quasar spectra with a wide range of spectral morphologies and constraining the physical properties of the BAL outflowing gas (Leighly et al., 2018; Choi et al., 2020, 2022a,b). As one of the key developers of the code, I contributed to developing and incorporating updates to *SimBAL* and to guiding new users which involved co-advising undergrad and graduate students and creating tutorial materials. Moreover, I created a new set of spectral principal component analysis (PCA) eigenvectors to model quasar emission lines in the rest-UV bandpass that can be used in *SimBAL* analysis. I plan

to continue in the developer role for the foreseeable future, as well as help prepare the software for the eventual public release.

Chapter 4

We analyzed the rest-UV spectrum of an "overlapping trough" iron low-ionization broad absorption-line (FeLoBAL) quasar SDSS 1352+4239 using the novel spectral synthesis code *SimBAL* (Leighly et al., 2018) and discovered an extraordinarily fast and energetic BAL outflow. The analysis revealed outflow velocities reaching $\sim -38000\,\mathrm{km\,s^{-1}}$ with a velocity width of $\sim\ 10000\,\mathrm{km\,s^{-1}}$ which is the largest FeLoBAL outflow velocity measured to date. The column density of the outflow gas is $\log N_H\ \sim\ 23.2\,[\mathrm{cm^{-1}}]$ with the log kinetic luminosity $\log L_{KE} \sim 48.1$ [erg $\mathrm{s^{-1}}$] which exceeds the bolometric luminosity of the quasar and is energetic enough to effectively drive quasar feedback. The energy estimate for the outflow is far greater than the estimates from any BAL object previously reported. The object also shows "anomalous reddening" and a significant scattered component that we were able to model with *SimBAL*. We found the first definitive case for radiation filtering in an additional zero-velocity absorption component that required an absorbed continuum to produce the particular absorption lines observed (Mg II, Al III and Al II) without also producing high-ionization lines such as C IV.

Chapter 5

In Chapter 5, we presented the first systematic study of 50 low-redshift ($0.66 < z < 1.63$) FeLoBAL quasars using *SimBAL* which represents a more than five-fold increase in the number of FeLoBAL quasars with detailed absorption line spectral analyses. We found the outflows have a wide range of ionization parameters, $-4 \lesssim \log U \lesssim 1.2$ and densities, $2.8 \lesssim \log n \lesssim 8\ [\mathrm{cm^{-3}}]$. The objects in our sample showed FeLoBAL gas located at a wide range of distances $0 \lesssim \log R \lesssim 4.4$ [pc], although we do not find any evidence for disk winds (with $R \ll 0.01$ pc) in our sample. The outflow strength primarily depends on the outflow velocity with faster outflows found in quasars that are luminous or that have flat or redder spectral energy distributions. We found that $\sim 18\%$ of the FeLoBAL quasars in the sample have the significantly powerful outflows needed for quasar feedback.

Eight objects showed *overlapping troughs* in the spectra, and we identified eleven *loitering outflow* objects, a new class of FeLoBAL quasars that are characterized by low outflow velocities and high column density winds located $\log R \lesssim 1$ [pc] from the central engine. The FeLoBALs in loitering outflow objects do show properties that are typically expected for radiatively driven winds, and these objects may represent a distinct population among FeLoBAL quasars. A log volume filling factor between -6 and -4 was found in most outflows, but was as high as -1 for low-velocity compact outflows such as loitering outflow. We discussed how the potential acceleration mechanisms and the origins of the FeLoBAL winds may differ for outflows at different locations in quasars.

Chapter 6

I analyzed multi-epoch spectra of an Extremely-High Velocity Outflow (EHVO) quasar J164653.72+243942.2 (hereafter referred to as J1646+2439) using *SimBAL* (Leighly et al., 2018). Two spectra taken ~ 1.7 years apart in the quasar rest frame showed a disappearance of lower-velocity BAL feature. I performed a simultaneous model fitting and found that BAL troughs observed in the spectra have similar maximum velocity of $\sim -50000\,\mathrm{km\,s^{-1}}$. However, the trough observed in the earlier epoch has a width of $v_{width} \sim 36,900\,\mathrm{km\,s^{-1}}$ whereas the later epoch data showed a much narrower trough with $v_{width} \sim 14,600\,\mathrm{km\,s^{-1}}$. I was able to constrain the ionization parameter and column density of the BAL outflowing wind. Density of the BAL gas could not be constrained due to the lack of density diagnostic absorption-lines in the bandpass. Therefore, the location of the BAL could not be determined with the information extracted from the *SimBAL* analysis. Instead we inferred the range of allowed locations of the outflowing gas based on the BAL gas geometry assuming EHVO clouds have comparable physical and geometrical characteristics as typical BAL clouds. We estimated that the BAL gas is likely to be located $5 \lesssim R \lesssim 500$ pc from the central supermassive black hole (SMBH). Taking the fiducial value of $R \sim 500$ pc, we calculated the outflow strengths of $\log\ L_{KE} \sim 47.2$ [erg s^{-1}] and $\log\ L_{KE} \sim 47.6$ [erg s^{-1}] for DR5 and DR9, respectively. They correspond to $L_{KE}/L_{Bol} \sim 25\%$ and $L_{KE}/L_{Bol} \sim 63\%$ for DR5 and DR9, respectively,

for $\log\ L_{Bol} = 47.8\ [\mathrm{erg\ s^{-1}}]$ calculated for this object and thus we expect the EHVO outflow has enough energy to produce feedback. Although the extreme velocity of the EHVO indicates that the outflow in J1646+2439 is likely to carry more than an order of magnitude greater energy and mass than typical BAL outflows, because the outflowing gas has lower column densities ($\log N_H \lesssim 22\ [\mathrm{cm^{-2}}]$) EHVOs do not have extreme energies compared to FeLoBAL outflows with comparable or lower outflow velocities. The potential cause of the spectral variability in J1646+2439 and its implications are currently being discussed using the results from the *SimBAL* analysis.

7.2. Related Collaborative Work

The low-redshift FeLoBAL quasar project described in Chapter 5 (also, Choi et al., 2022a) is part of the series of four papers. For a subsample of 30 $z < 1$ objects that have Hβ / [O III] region in the SDSS/Baryon Oscillation Spectroscopic Survey (BOSS) spectra, my collaborators analyzed the rest-optical quasar emission-line properties and discovered that FeLoBAL quasars are divided between high accretion rate and low accretion rate objects (Figure 7.2.1; Leighly et al., 2022). The discovery of a low accretion rate FeLoBAL quasar branch was unexpected since previous studies of BAL quasars have indicated high accretion rates (e.g., Boroson, 2002).

We included the BAL outflow properties in the analyses of the newly discovered two populations of FeLoBAL quasars. We were able to identify that the two groups exhibit different BAL outflow phenomena (Figure 7.2.2). The outflow velocity is inversely correlated with the BAL location among the high accretion rate objects, with the highest velocities observed in the parsec-scale outflows, whereas among the low Eddington ratio objects, the parsec-scale outflows had the lowest velocities (Choi et al., 2022b). Combining this information my collaborators and I are discussing a potential scenario wherein the two populations may represent two distinct points in quasar evolution and indicate two different origins of FeLoBAL outflows, with the newly-identified low accretion rate group representing the near-end stage of quasar evolution as the quasar runs out of fuel (Leighly

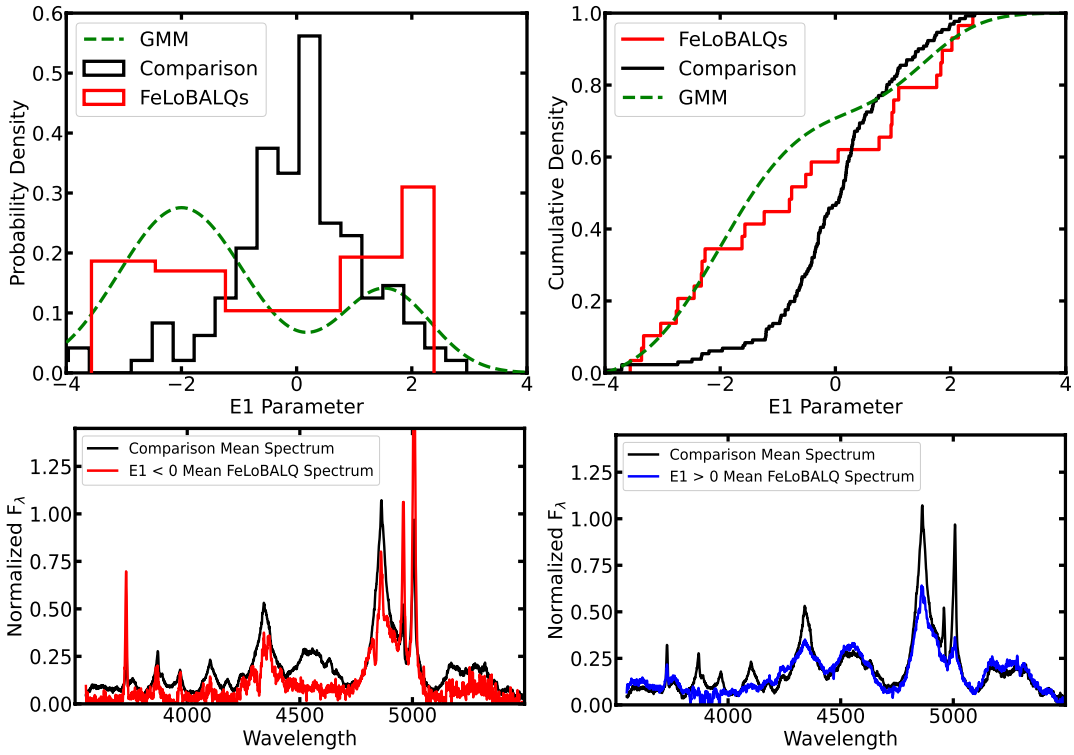

Figure 7.2.1: A subsample of $z < 1$ FeLoBAL quasars revealed a bimodal distribution of the E1 parameter for the FeLoBAL quasars and a strongly peaked distribution for the unabsorbed sample, suggesting two populations of FeLoBAL quasars (taken from Figure 9 in Leighly et al., 2022). The E1 parameter is derived from the properties of rest-optical emission lines, and large values of the E1 parameter corresponds to large Eddington ratios (Eddington-normalized accretion rates). The composite spectra for high accretion rate objects (E1>0) and low accretion objects (E1<0) are plotted in blue and red, respectively

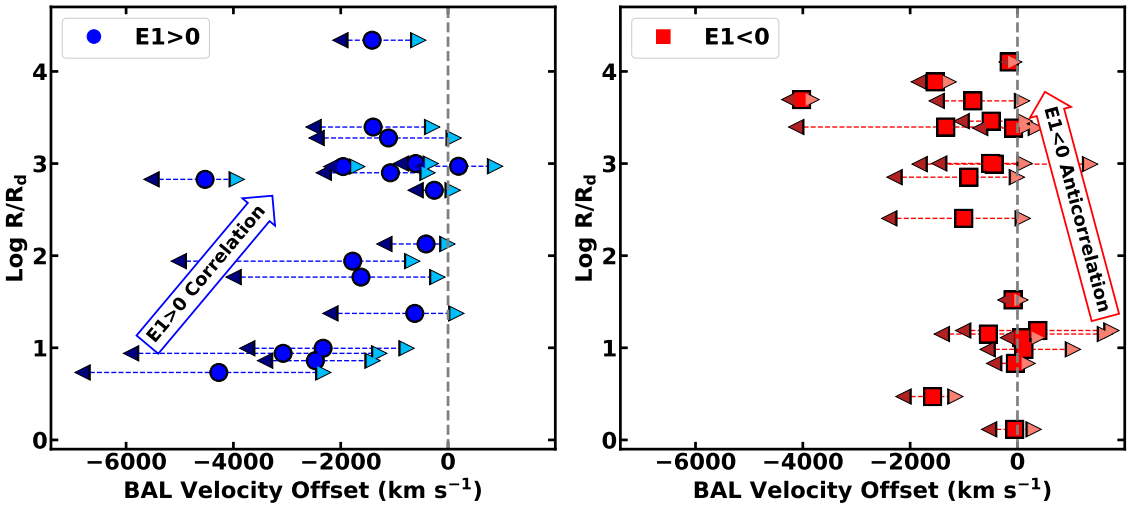

Figure 7.2.2: The location of the outflow normalized by the dust sublimation radius (R_d; inner edge of obscuring dusty torus) as a function of the outflow velocity (taken from Figure 4 in Choi et al., 2022b). We identified correlation between the two properties for high accretion rate objects (E1>0, plotted in blue) and an anticorrelation for low accretion rate objects (E1<0, plotted in red). These different trends potentially suggest a difference in the outflow formation and acceleration mechanisms for the two groups of FeLoBAL quasars.

et al., in preparation). The high accretion rate objects are related to the ultraluminous infrared galaxys (ULIRGs) going through the blowout phase, shedding their cocoon of gas and dust with outflows ("blowout" phase; e.g., Sanders et al., 1988a; Farrah et al., 2012). We are also including the quasar torus properties to further investigate the discovery of the two populations and to study how the idea of torus wind may be linked to the low accretion rate FeLoBAL quasars (Elitzur & Shlosman, 2006).

7.3. Future Work

The series of work presented in this thesis has shown great potential for the unparalleled capabilities of *SimBAL* in spectral analysis of BAL quasar spectra and the importance of (FeLo) BAL quasars as excellent targets to study outflow physics and galaxy evolution and feedback. Among the large number of possible *SimBAL* projects that are closely related to this thesis, we are currently analyzing the spectral variability of high-ionization broad

absorption-line (HiBAL) features seen in the low-luminosity BAL quasar WPVS 007 using the Hubble Space Telescope (HST) data (Green et al., 2021), and a large sample of P V quasars (Hazlett et al., 2019). Here, I describe a few projects I am currently working on.

7.3.1. Analysis of high-redshift FeLoBAL Quasar Sample

I plan to expand my low-redshift FeLoBAL quasar sample project (Chapter 5) to higher redshifts to investigate the following topics: (1) the role of BAL outflows in galaxy feedback and evolution, (2) the evolution of the FeLoBAL outflow phenomenon as a function of quasar properties (e.g., black hole mass and luminosity), and (3) the populations and properties of FeLoBAL quasars at higher redshifts. At higher redshifts, we will explore higher luminosities and black hole masses. This is important because numerous quasar properties are luminosity dependent (e.g., the Baldwin effect; Baldwin, 1977), and a larger black hole mass is predicted to produce a softer spectral energy distribution (SED; e.g., Done et al., 2012) which creates more favorable conditions for BAL outflow acceleration. While it is known that the outflow velocities are correlated with quasar luminosities (left panel in Figure 5.23; e.g., Ganguly et al., 2007), not much is known about how the physical properties of the outflow gas change with the luminosity. This project will allow us to study the evolution of FeLoBAL gas properties as a function of luminosity and to test whether the correlations and trends observed in the low-luminosity sample are replicated in luminous FeLoBAL quasars. In addition, I will investigate the role of BAL outflows in the quasar feedback process with this high redshift sample. These objects are ideal candidates for this goal because their redshift range falls within the cosmic noon during the peak of quasar activity. We will be analyzing the near-infrared (rest-frame optical) spectra taken from Gemini, Large Binocular Telescope (LBT), and APO to measure key quasar properties such as the black hole masses and accretion rates. The outflow properties will be obtained from the SDSS data using *SimBAL*.

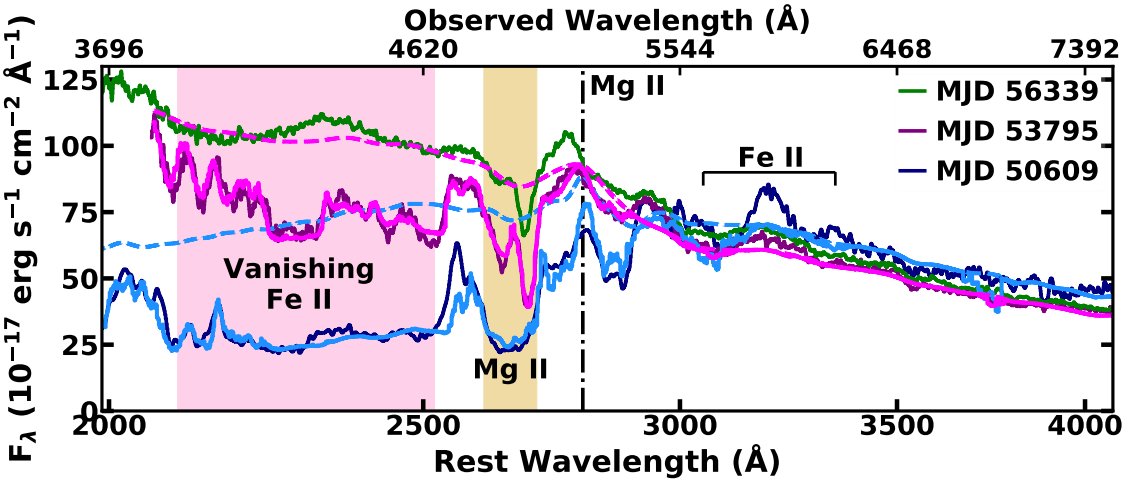

Figure 7.3.1: Spectral variability in J1408+3054. The strong reddening at short wavelengths ($\lambda < 3000$Å) is only observed in the earliest epoch (MJD 50609), and as the Fe II trough disappears the reddening also weakens. The preliminary *SimBAL* models are plotted in light blue and pink for MJDs 50609 and 53795, respectively. The unabsorbed continuum models are also plotted in the same colors with dashed lines. The vertical dotted-dashed lines represent the Mg II emission line at quasar rest-frame and Fe II emission feature is also labeled above the spectra.

7.3.2. Extreme Spectral Variability in SDSS J140806.20+305448.3

Spectral variability in BAL quasars gives us additional information about the outflows such as their gas cloud structure and geometry, dynamic ionization state of the gas, and outflowing gas chemical composition related to dust content (e.g., Capellupo et al., 2013; Mishra et al., 2021). BAL variability is observed more commonly in objects with powerful winds, such as objects with overlapping trough features (§ 5.17; e.g., Zhang et al., 2015b). In some of these objects, the (dis)appearance of the FeLoBAL features occurred simultaneously with the change in reddening. Dust reddening in quasars has been observed to be correlated to quasar outflow activity (e.g., higher frequency of FeLoBAL quasars in red quasars; Urrutia et al., 2009). We also found that faster and more energetic outflows were found in redder objects (Chapter 5, § 5.7.3; Choi et al., 2022a). However, it is unclear how the two phenomena are physically linked.

We identified an FeLoBAL quasar, SDSS J140806.20+305448.3 (hereafter referred

to as J1408+3054), that showed extreme spectral variability where simultaneous disappearance of an overlapping trough BAL and anomalous reddening features (§ 4.3.2) is observed (Figure 7.3.1). This object is a low-redshift ($z = 0.848$) FeLoBAL quasar first discovered in the FIRST Bright Quasar Survey (FBQS, White et al., 2000). Hall et al. (2011) analyzed the spectral variability in this object and discussed the BAL structure with regards to the geometry of the outflowing gas in great detail. However, they failed to identify the presence and gradual weakening of the anomalous reddening in the data from the data. *SimBAL* includes a sophisticated method to model anomalous reddening and can be used to systematically analyze multi-epoch spectra and provide us with a first-ever clear physical picture of the origin of BAL variability and its relationship to dust reddening. This object may provide us with direct observational evidence for coupling between the outflows and dust reddening. Such coupling potentially suggests dust production within outflowing gas clouds in an FeLoBAL quasar by which dense outflowing gas cools and creates a condition in which dust condensation can occur (Elvis et al., 2002). It also suggests that the dust is not located in the host galaxy and thus the host galaxy properties may be decoupled from the quasar properties.

7.3.3. The Origin of Fe III absorption lines

The distinguishing spectral feature of FeLoBAL quasars is the presence of Fe II absorption lines from various excitation states in their rest-frame UV spectra (e.g., Cowie et al., 1994; Menou et al., 2001). In a small fraction of FeLoBAL quasars, absorption lines from doubly-ionized iron atoms (Fe^{+2} or Fe III) with or without any Fe II absorption lines are observed in the near-UV spectra (e.g., Hall et al., 2002). The most prominent Fe III absorption line feature is ultraviolet (UV) multiplet 34 (Moore, 1950) lines that are made up of three transitions at 1895.46, 1914.06, and 1926.30 Å with the excitation energy of the lower-level (E_{low}) of ~ 3.71 eV. Fe III absorption lines are a rare occurrence in FeLoBAL quasar spectra and detailed photoionization analyses of a couple of objects with Fe III BALs has been performed to understand what physical properties are required to

populate Fe III ions. For example, Q0059-2735, one of the first known FeLoBAL quasars, has strong UV34 Fe III absorption lines in its spectra, along with Fe II troughs. Recent work by Xu et al. (2021) suggested an unusually hot gas temperature (i.e., $T_e \sim 20000$ K) for the Fe III BAL gas. de Kool et al. (2002a) and Rogerson et al. (2011) argued that high density (i.e., $\log n \gtrsim 9.5\,[\mathrm{cm}^{-3}]$) can produce Fe III absorption lines in FBQS 0840+3633 and SDSS J221511.94−004549.9 (hereafter SDSS J2215–0045), respectively.

I propose a different mechanism for creating Fe III absorption lines in which BAL gas is irradiated by a continuum that has been absorbed by gas located in between the continuum source and the gas that produces the Fe III absorption lines. The transmitted spectrum can have such an altered shape that the photoionization equilibrium in the gas that produces the Fe III absorption lines is shifted. I used the spectrum of SDSS J2215–0045 to perform the study the Fe III absorption lines. This spectrum has higher excited-state Fe III BAL features from Fe III$\lambda\lambda\lambda 2061, 2068, 2078$ from $E_{low} \sim 5.06$ eV as well as Fe III UV34. This idea of radiation "filtering" has been discussed in Choi et al. (2020) in Chapter 4 (§ 4.4.3). In SDSS 1352+4239, the downstream BAL is illuminated by a continuum that lacks the high-energy photons necessary to create the high-ionization ions, such as C IV and Si IV, and thus no absorption lines from these ions are found in the spectrum. Figure 7.3.2 shows the preliminary results. I have identified a physical condition for the upstream absorbing gas that can create the ideal filtered SED for the downstream gas clouds to produce observable Fe III absorption lines. Future work includes a systematic search in the photoionization parameter space and expanding this work to include the analysis of objects that have significant Fe II BALs as well as strong Fe III absorption lines.

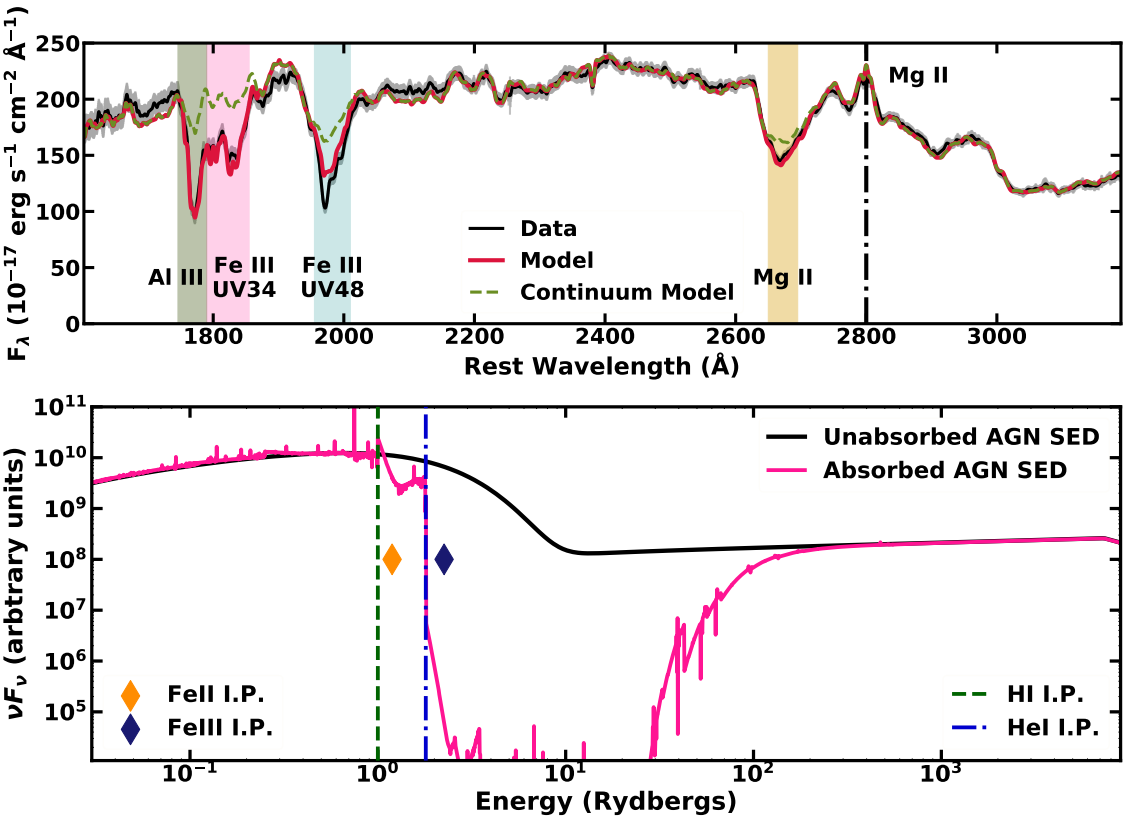

Figure 7.3.2: Upper panel: our best-fitting model generated using a filtered SED. The absorption lines are highlighted in different colors with their identifications noted below the spectrum. The vertical dotted-dashed lines represent the Mg II emission line at the quasar rest-frame. Lower panel: filtered (absorbed) SED used in the analysis. The filtered SED has a particular shape in that the absorption starts at He I ionization potential (I.P.~ 1.8 Ryd). This allows the filtered SED to have enough photons with energies greater than the ionization potential of Fe II (I.P.~ 1.19 Ryd) to populate Fe III but lack photons with energies greater than the ionization potential of Fe III (I.P.~ 2.25 Ryd) that could ionize Fe III to form Fe IV.

References

Abdurro'uf, Accetta, K., Aerts, C., et al. 2022, ApJS, 259, 35, doi: 10.3847/1538-4365/ac4414

Adelman-McCarthy, J. K., Agüeros, M. A., Allam, S. S., et al. 2007, ApJS, 172, 634, doi: 10.1086/518864

Aihara, H., Allende Prieto, C., An, D., et al. 2011, ApJS, 193, 29, doi: 10.1088/0067-0049/193/2/29

Allen, J. T., Hewett, P. C., Maddox, N., Richards, G. T., & Belokurov, V. 2011, Monthly Notices of the Royal Astronomical Society, 410, 860, doi: 10.1111/j.1365-2966.2010.17489.x

Anderson, S. F., Margon, B., Voges, W., et al. 2007, AJ, 133, 313, doi: 10.1086/509765

Aoki, K., Oyabu, S., Dunn, J. P., et al. 2011, PASJ, 63, 457, doi: 10.1093/pasj/63.sp2.S457

Arav, N., Borguet, B., Chamberlain, C., Edmonds, D., & Danforth, C. 2013, MNRAS, 436, 3286, doi: 10.1093/mnras/stt1812

Arav, N., Brotherton, M. S., Becker, R. H., et al. 2001, ApJ, 546, 140, doi: 10.1086/318244

Arav, N., Kaastra, J., Kriss, G. A., et al. 2005, ApJ, 620, 665, doi: 10.1086/425560

Arav, N., & Li, Z.-Y. 1994, ApJ, 427, 700, doi: 10.1086/174177

Arav, N., Li, Z.-Y., & Begelman, M. C. 1994, ApJ, 432, 62, doi: 10.1086/174549

Arav, N., Liu, G., Xu, X., et al. 2018, ApJ, 857, 60, doi: 10.3847/1538-4357/aab494

Arav, N., Moe, M., Costantini, E., et al. 2008, ApJ, 681, 954, doi: 10.1086/588651

Bailey, S. 2012, PASP, 124, 1015, doi: 10.1086/668105

Baldwin, J. A. 1977, ApJ, 214, 679, doi: 10.1086/155294

Barlow, T. A., Junkkarinen, V. T., & Burbidge, E. M. 1989, ApJ, 347, 674, doi: 10.1086/168157

Barlow, T. A., & Sargent, W. L. W. 1997, AJ, 113, 136, doi: 10.1086/118239

Baskin, A., Laor, A., & Hamann, F. 2015, MNRAS, 449, 1593, doi: 10.1093/mnras/stv406

Bautista, M. A., Dunn, J. P., Arav, N., et al. 2010, The Astrophysical Journal, 713, 25, doi: 10.1088/0004-637X/713/1/25

Becker, R. H., Gregg, M. D., Hook, I. M., et al. 1997, ApJL, 479, L93, doi: 10.1086/310594

Becker, R. H., White, R. L., Gregg, M. D., et al. 2000, ApJ, 538, 72, doi: 10.1086/309099

Bentz, M. C., Peterson, B. M., Netzer, H., Pogge, R. W., & Vestergaard, M. 2009, ApJ, 697, 160, doi: 10.1088/0004-637X/697/1/160

Bentz, M. C., Denney, K. D., Grier, C. J., et al. 2013, ApJ, 767, 149, doi: 10.1088/0004-637X/767/2/149

Berrington, R. C., Brotherton, M. S., Gallagher, S. C., et al. 2013, MNRAS, 436, 3321, doi: 10.1093/mnras/stt1808

Bischetti, M., Piconcelli, E., Vietri, G., et al. 2017, A&A, 598, A122, doi: 10.1051/0004-6361/201629301

Blackburne, J. A., Pooley, D., Rappaport, S., & Schechter, P. L. 2011, ApJ, 729, 34, doi: 10.1088/0004-637X/729/1/34

Blanton, M. R., Bershady, M. A., Abolfathi, B., et al. 2017, AJ, 154, 28, doi: 10.3847/1538-3881/aa7567

Boksenberg, A., Carswell, R. F., Allen, D. A., et al. 1977, MNRAS, 178, 451, doi: 10.1093/mnras/178.3.451

Borguet, B., & Hutsemékers, D. 2010, A&A, 515, A22, doi: 10.1051/0004-6361/200913255

Borguet, B. C. J., Arav, N., Edmonds, D., Chamberlain, C., & Benn, C. 2013, ApJ, 762, 49, doi: 10.1088/0004-637X/762/1/49

Boroson, T. A. 2002, ApJ, 565, 78, doi: 10.1086/324486

Branch, D., Leighly, K. M., Thomas, R. C., & Baron, E. 2002, ApJL, 578, L37, doi: 10.1086/344472

Brooks, A., & Christensen, C. 2016, in Astrophysics and Space Science Library, Vol. 418, Galactic Bulges, ed. E. Laurikainen, R. Peletier, & D. Gadotti, 317, doi: 10.1007/978-3-319-19378-6_12

Brotherton, M. S., Laurent-Muehleisen, S. A., Becker, R. H., et al. 2005, AJ, 130, 2006, doi: 10.1086/496948

Brotherton, M. S., Tran, H. D., van Breugel, W., Dey, A., & Antonucci, R. 1997, ApJL, 487, L113, doi: 10.1086/310898

Calistro Rivera, G., Alexander, D. M., Rosario, D. J., et al. 2021, A&A, 649, A102, doi: 10.1051/0004-6361/202040214

Capellupo, D. M., Hamann, F., Shields, J. C., Halpern, J. P., & Barlow, T. A. 2013, MNRAS, 429, 1872, doi: 10.1093/mnras/sts427

Capellupo, D. M., Hamann, F., Shields, J. C., Rodríguez Hidalgo, P., & Barlow, T. A. 2011, MNRAS, 413, 908, doi: 10.1111/j.1365-2966.2010.18185.x

Capellupo, D. M., Hamann, F., Shields, J. C., Rodríguez Hidalgo, P., & Barlow, T. A. 2012, MNRAS, 422, 3249, doi: 10.1111/j.1365-2966.2012.20846.x

Cardelli, J. A., Clayton, G. C., & Mathis, J. S. 1989, ApJ, 345, 245, doi: 10.1086/167900

Casebeer, D., Baron, E., Leighly, K., Jevremovic, D., & Branch, D. 2008, ApJ, 676, 857, doi: 10.1086/528671

Castor, J. I., Abbott, D. C., & Klein, R. I. 1975, ApJ, 195, 157, doi: 10.1086/153315

Chamberlain, C., Arav, N., & Benn, C. 2015, MNRAS, 450, 1085, doi: 10.1093/mnras/stv572

Chan, C.-H., & Krolik, J. H. 2016, ApJ, 825, 67, doi: 10.3847/0004-637X/825/1/67

—. 2017, ApJ, 843, 58, doi: 10.3847/1538-4357/aa76e4

Chartas, G., Saez, C., Brandt, W. N., Giustini, M., & Garmire, G. P. 2009, ApJ, 706, 644, doi: 10.1088/0004-637X/706/1/644

Chen, Z.-F., Huang, W.-R., Pang, T.-T., et al. 2018, ApJS, 235, 11, doi: 10.3847/1538-4365/aaaaec

Choi, E., Ostriker, J. P., Naab, T., & Johansson, P. H. 2012, ApJ, 754, 125, doi: 10.1088/0004-637X/754/2/125

Choi, H., Leighly, K. M., Terndrup, D. M., et al. 2022a, arXiv e-prints, arXiv:2203.11964. https://arxiv.org/abs/2203.11964

Choi, H., Leighly, K. M., Dabbieri, C., et al. 2022b, arXiv e-prints, arXiv:2208.02834. https://arxiv.org/abs/2208.02834

Choi, H., Leighly, K. M., Terndrup, D. M., Gallagher, S. C., & Richards, G. T. 2020, ApJ, 891, 53, doi: 10.3847/1538-4357/ab6f72

Cicone, C., Maiolino, R., Sturm, E., et al. 2014, A&A, 562, A21, doi: 10.1051/0004-6361/201322464

Cohen, M., Wheaton, W. A., & Megeath, S. T. 2003, AJ, 126, 1090, doi: 10.1086/376474

Cohen, M. H., Ogle, P. M., Tran, H. D., et al. 1995, ApJL, 448, L77, doi: 10.1086/309602

Collin, S., Kawaguchi, T., Peterson, B. M., & Vestergaard, M. 2006, A&A, 456, 75, doi: 10.1051/0004-6361:20064878

Collinson, J. S., Ward, M. J., Landt, H., et al. 2017, MNRAS, 465, 358, doi: 10.1093/mnras/stw2666

Costa, T., Sijacki, D., & Haehnelt, M. G. 2014, MNRAS, 444, 2355, doi: 10.1093/mnras/stu1632

Cowie, L. L., Songaila, A., Hu, E. M., et al. 1994, ApJL, 432, L83, doi: 10.1086/187517

Cushing, M. C., Vacca, W. D., & Rayner, J. T. 2004, PASP, 116, 362, doi: 10.1086/382907

Czerny, B., Li, Y.-R., Hryniewicz, K., et al. 2017, ApJ, 846, 154, doi: 10.3847/1538-4357/aa8810

Dabbieri, C., Leighly, K. M., Terndrup, D. M., et al. in preparation, ApJ

Dai, X., Shankar, F., & Sivakoff, G. R. 2008, ApJ, 672, 108, doi: 10.1086/523688

—. 2012, ApJ, 757, 180, doi: 10.1088/0004-637X/757/2/180

Dawson, K. S., Schlegel, D. J., Ahn, C. P., et al. 2013, AJ, 145, 10, doi: 10.1088/0004-6256/145/1/10

Dawson, K. S., Kneib, J.-P., Percival, W. J., et al. 2016, AJ, 151, 44, doi: 10.3847/0004-6256/151/2/44

de Jong, R. S., Agertz, O., Berbel, A. A., et al. 2019, The Messenger, 175, 3, doi: 10.18727/0722-6691/5117

de Kool, M., Arav, N., Becker, R. H., et al. 2001, ApJ, 548, 609, doi: 10.1086/318996

de Kool, M., Becker, R. H., Arav, N., Gregg, M. D., & White, R. L. 2002a, ApJ, 570, 514, doi: 10.1086/339793

de Kool, M., Becker, R. H., Gregg, M. D., White, R. L., & Arav, N. 2002b, ApJ, 567, 58, doi: 10.1086/338490

de Kool, M., & Begelman, M. C. 1995, ApJ, 455, 448, doi: 10.1086/176594

de Kool, M., Korista, K. T., & Arav, N. 2002c, ApJ, 580, 54, doi: 10.1086/343107

Di Matteo, T., Springel, V., & Hernquist, L. 2005, Nature, 433, 604, doi: 10.1038/nature03335

DiPompeo, M. A., Brotherton, M. S., Becker, R. H., et al. 2010, ApJS, 189, 83, doi: 10.1088/0067-0049/189/1/83

DiPompeo, M. A., Brotherton, M. S., & De Breuck, C. 2011, The Astrophysical Journal Supplement Series, 193, 9, doi: 10.1088/0067-0049/193/1/9

Done, C., Davis, S. W., Jin, C., Blaes, O., & Ward, M. 2012, MNRAS, 420, 1848, doi: 10.1111/j.1365-2966.2011.19779.x

Dunn, J. P., Bautista, M., Arav, N., et al. 2010, ApJ, 709, 611, doi: 10.1088/0004-637X/709/2/611

Dunn, J. P., Wasik, B., Holtzclaw, C. L., et al. 2015, ApJ, 808, 94, doi: 10.1088/0004-637X/808/1/94

Eisenstein, D. J., Weinberg, D. H., Agol, E., et al. 2011, AJ, 142, 72, doi: 10.1088/0004-6256/142/3/72

Elias, J. H., Joyce, R. R., Liang, M., et al. 2006a, in Society of Photo-Optical Instrumentation Engineers (SPIE) Conference Series, Vol. 6269, Society of Photo-Optical Instrumentation Engineers (SPIE) Conference Series, ed. I. S. McLean & M. Iye, 62694C, doi: 10.1117/12.671817

Elias, J. H., Rodgers, B., Joyce, R. R., et al. 2006b, in Society of Photo-Optical Instrumentation Engineers (SPIE) Conference Series, Vol. 6269, Society of Photo-Optical Instrumentation Engineers (SPIE) Conference Series, ed. I. S. McLean & M. Iye, 626914, doi: 10.1117/12.671765

Elitzur, M., & Netzer, H. 2016, MNRAS, 459, 585, doi: 10.1093/mnras/stw657

Elitzur, M., & Shlosman, I. 2006, ApJL, 648, L101, doi: 10.1086/508158

Elvis, M., Marengo, M., & Karovska, M. 2002, ApJL, 567, L107, doi: 10.1086/340006

Elvis, M., Wilkes, B. J., McDowell, J. C., et al. 1994, ApJS, 95, 1, doi: 10.1086/192093

Everett, J., Königl, A., & Arav, N. 2002, ApJ, 569, 671, doi: 10.1086/339346

Fabian, A., Ricci, C., & Ishibashi, W. 2018, in 42nd COSPAR Scientific Assembly, Vol. 42, E1.13–29–18

Fabian, A. C. 2012, ARA&A, 50, 455, doi: 10.1146/annurev-astro-081811-125521

Fabian, A. C., Vasudevan, R. V., & Gandhi, P. 2008, MNRAS, 385, L43, doi: 10.1111/j.1745-3933.2008.00430.x

Farrah, D., Lacy, M., Priddey, R., Borys, C., & Afonso, J. 2007, ApJL, 662, L59, doi: 10.1086/519492

Farrah, D., Surace, J. A., Veilleux, S., Sanders, D. B., & Vacca, W. D. 2005, ApJ, 626, 70, doi: 10.1086/428660

Farrah, D., Urrutia, T., Lacy, M., et al. 2012, ApJ, 745, 178, doi: 10.1088/0004-637X/745/2/178

Faucher-Giguère, C.-A., Prochaska, J. X., Lidz, A., Hernquist, L., & Zaldarriaga, M. 2008, ApJ, 681, 831, doi: 10.1086/588648

Faucher-Giguère, C.-A., & Quataert, E. 2012, MNRAS, 425, 605, doi: 10.1111/j.1365-2966.2012.21512.x

Faucher-Giguère, C.-A., Quataert, E., & Murray, N. 2012, MNRAS, 420, 1347, doi: 10.1111/j.1365-2966.2011.20120.x

Ferland, G. J., Porter, R. L., van Hoof, P. A. M., et al. 2013, RMxAA, 49, 137. https://arxiv.org/abs/1302.4485

Ferland, G. J., Chatzikos, M., Guzmán, F., et al. 2017, RMxAA, 53, 385. https://arxiv.org/abs/1705.10877

Ferrarese, L., & Merritt, D. 2000, ApJL, 539, L9, doi: 10.1086/312838

Filiz Ak, N., Brandt, W. N., Hall, P. B., et al. 2012, ApJ, 757, 114, doi: 10.1088/0004-637X/757/2/114

Finn, C. W., Morris, S. L., Crighton, N. H. M., et al. 2014, MNRAS, 440, 3317, doi: 10.1093/mnras/stu518

Fiore, F., Feruglio, C., Shankar, F., et al. 2017, A&A, 601, A143, doi: 10.1051/0004-6361/201629478

Fischer, T. C., Kraemer, S. B., Schmitt, H. R., et al. 2018, ApJ, 856, 102, doi: 10.3847/1538-4357/aab03e

Foltz, C. B., Chaffee, F. H., Hewett, P. C., Weymann, R. J., & Morris, S. L. 1990, in BAAS, Vol. 22, 806

Foltz, C. B., Weymann, R. J., Morris, S. L., & Turnshek, D. A. 1987, ApJ, 317, 450, doi: 10.1086/165290

Foreman, G., Volonteri, M., & Dotti, M. 2009, ApJ, 693, 1554, doi: 10.1088/0004-637X/693/2/1554

Foreman-Mackey, D., Hogg, D. W., Lang, D., & Goodman, J. 2013, PASP, 125, 306, doi: 10.1086/670067

Francis, P. J., Hewett, P. C., Foltz, C. B., et al. 1991, ApJ, 373, 465, doi: 10.1086/170066

Freeman, P., Doe, S., & Siemiginowska, A. 2001, in Society of Photo-Optical Instrumentation Engineers (SPIE) Conference Series, Vol. 4477, Society of Photo-Optical Instrumentation Engineers (SPIE) Conference Series, ed. J.-L. Starck & F. D. Murtagh, 76–87, doi: 10.1117/12.447161

Fynbo, J. P. U., Krogager, J. K., Venemans, B., et al. 2013, ApJS, 204, 6, doi: 10.1088/0067-0049/204/1/6

Fynbo, J. P. U., Møller, P., Heintz, K. E., et al. 2020, A&A, 634, A111, doi: 10.1051/0004-6361/201936957

Gabel, J. R., Arav, N., & Kim, T.-S. 2006, ApJ, 646, 742, doi: 10.1086/505070

Gallagher, S. C., Brandt, W. N., Chartas, G., & Garmire, G. P. 2002, ApJ, 567, 37, doi: 10.1086/338485

Gallagher, S. C., Brandt, W. N., Chartas, G., et al. 2006, ApJ, 644, 709, doi: 10.1086/503762

Gallagher, S. C., Everett, J. E., Abado, M. M., & Keating, S. K. 2015, MNRAS, 451, 2991, doi: 10.1093/mnras/stv1126

Gallagher, S. C., Richards, G. T., Lacy, M., et al. 2007, ApJ, 661, 30, doi: 10.1086/513733

Ganguly, R., & Brotherton, M. S. 2008, ApJ, 672, 102, doi: 10.1086/524106

Ganguly, R., Brotherton, M. S., Cales, S., et al. 2007, ApJ, 665, 990, doi: 10.1086/519759

Gaskell, C. M. 1982, ApJ, 263, 79, doi: 10.1086/160481

Gibson, R. R., Jiang, L., Brandt, W. N., et al. 2009, ApJ, 692, 758, doi: 10.1088/0004-637X/692/1/758

Giustini, M., & Proga, D. 2019, A&A, 630, A94, doi: 10.1051/0004-6361/201833810

Glikman, E. 2017, Research Notes of the American Astronomical Society, 1, 48, doi: 10.3847/2515-5172/aaa0c0

Glikman, E., Lacy, M., LaMassa, S., et al. 2018, ApJ, 861, 37, doi: 10.3847/1538-4357/aac5d8

Goobar, A. 2008, ApJL, 686, L103, doi: 10.1086/593060

Goodman, J., & Weare, J. 2010, Communications in Applied Mathematics and Computational Science, 5, 65, doi: 10.2140/camcos.2010.5.65

Green, K., Gallagher, S., Choi, H., et al. 2021, in American Astronomical Society Meeting Abstracts, Vol. 53, American Astronomical Society Meeting Abstracts, 337.09

Green, K., Gallagher, S., Choi, H., et al. in preparation, ApJ

Green, P. J., Aldcroft, T. L., Mathur, S., Wilkes, B. J., & Elvis, M. 2001, ApJ, 558, 109, doi: 10.1086/322311

Greene, J. E., & Ho, L. C. 2005, ApJ, 630, 122, doi: 10.1086/431897

Griffin, M. J., Abergel, A., Abreu, A., et al. 2010, A&A, 518, L3, doi: 10.1051/0004-6361/201014519

Gunn, J. E., & Peterson, B. A. 1965, ApJ, 142, 1633, doi: 10.1086/148444

Gunn, J. E., Carr, M., Rockosi, C., et al. 1998, AJ, 116, 3040, doi: 10.1086/300645

Gunn, J. E., Siegmund, W. A., Mannery, E. J., et al. 2006, AJ, 131, 2332, doi: 10.1086/500975

Haardt, F., & Madau, P. 1996, ApJ, 461, 20, doi: 10.1086/177035

Hall, P. B. 2007, AJ, 133, 1271, doi: 10.1086/511272

Hall, P. B., Anosov, K., White, R. L., et al. 2011, MNRAS, 411, 2653, doi: 10.1111/j.1365-2966.2010.17870.x

Hall, P. B., Hutsemékers, D., Anderson, S. F., et al. 2003, ApJ, 593, 189, doi: 10.1086/376409

Hall, P. B., Anderson, S. F., Strauss, M. A., et al. 2002, ApJS, 141, 267, doi: 10.1086/340546

Hall, P. B., Brandt, W. N., Petitjean, P., et al. 2013, MNRAS, 434, 222, doi: 10.1093/mnras/stt1012

Hamann, F. 1998, ApJ, 500, 798, doi: 10.1086/305776

Hamann, F., Barlow, T. A., Beaver, E. A., et al. 1995, ApJ, 443, 606, doi: 10.1086/175552

Hamann, F., Chartas, G., McGraw, S., et al. 2013, MNRAS, 435, 133, doi: 10.1093/mnras/stt1231

Hamann, F., Chartas, G., Reeves, J., & Nardini, E. 2018, Monthly Notices of the Royal Astronomical Society, 476, 943, doi: 10.1093/mnras/sty043

Hamann, F., Herbst, H., Paris, I., & Capellupo, D. 2019a, MNRAS, 483, 1808, doi: 10.1093/mnras/sty2900

Hamann, F., Kanekar, N., Prochaska, J. X., et al. 2011, MNRAS, 410, 1957, doi: 10.1111/j.1365-2966.2010.17575.x

Hamann, F., Tripp, T. M., Rupke, D., & Veilleux, S. 2019b, MNRAS, 487, 5041, doi: 10.1093/mnras/stz1408

Hamann, F., Zakamska, N. L., Ross, N., et al. 2017, MNRAS, 464, 3431, doi: 10.1093/mnras/stw2387

Hamann, F. W., Barlow, T. A., Chaffee, F. C., Foltz, C. B., & Weymann, R. J. 2001, ApJ, 550, 142, doi: 10.1086/319733

Harrison, C. M., Alexander, D. M., Mullaney, J. R., & Swinbank, A. M. 2014, MNRAS, 441, 3306, doi: 10.1093/mnras/stu515

Hauschildt, P. H., & Baron, E. 1999, Journal of Computational and Applied Mathematics, 109, 41. https://arxiv.org/abs/astro-ph/9808182

Hazard, C., McMahon, R. G., Webb, J. K., & Morton, D. C. 1987, The Astrophysical Journal, 323, 263, doi: 10.1086/165823

Hazlett, R., Leighly, K., Dabbieri, C., et al. 2019, in American Astronomical Society Meeting Abstracts, Vol. 233, American Astronomical Society Meeting Abstracts #233, 242.41

Hemler, Z. S., Grier, C. J., Brandt, W. N., et al. 2019, ApJ, 872, 21, doi: 10.3847/1538-4357/aaf1bf

Hewett, P. C., & Foltz, C. B. 2003, AJ, 125, 1784, doi: 10.1086/368392

Hewett, P. C., & Wild, V. 2010, MNRAS, 405, 2302, doi: 10.1111/j.1365-2966.2010.16648.x

Hönig, S. F. 2019, ApJ, 884, 171, doi: 10.3847/1538-4357/ab4591

Hönig, S. F., & Kishimoto, M. 2017, ApJL, 838, L20, doi: 10.3847/2041-8213/aa6838

Hönig, S. F., Kishimoto, M., Tristram, K. R. W., et al. 2013, ApJ, 771, 87, doi: 10.1088/0004-637X/771/2/87

Hopkins, P. F., & Elvis, M. 2010, MNRAS, 401, 7, doi: 10.1111/j.1365-2966.2009.15643.x

Hopkins, P. F., Hernquist, L., Cox, T. J., et al. 2005, ApJ, 630, 705, doi: 10.1086/432438

Hutsemékers, D., Hall, P., & Sluse, D. 2017, A&A, 606, A101, doi: 10.1051/0004-6361/201731632

Ishibashi, W., Banerji, M., & Fabian, A. C. 2017, MNRAS, 469, 1496, doi: 10.1093/mnras/stx921

Ishibashi, W., & Fabian, A. C. 2018, MNRAS, 481, 4522, doi: 10.1093/mnras/sty2617

Isobe, T., Feigelson, E. D., & Nelson, P. I. 1986, ApJ, 306, 490, doi: 10.1086/164359

Jannuzi, B. T., Hartig, G. F., Kirhakos, S., et al. 1996, ApJL, 470, L11, doi: 10.1086/310301

Jiang, D. R., & Wang, T. G. 2003, A&A, 397, L13, doi: 10.1051/0004-6361:20021765

Jiang, P., Zhou, H., Ji, T., et al. 2013, AJ, 145, 157, doi: 10.1088/0004-6256/145/6/157

Keating, S. K., Everett, J. E., Gallagher, S. C., & Deo, R. P. 2012, ApJ, 749, 32, doi: 10.1088/0004-637X/749/1/32

Kelly, B. C. 2007, ApJ, 665, 1489, doi: 10.1086/519947

Kimball, A. E., Ivezić, Ž., Wiita, P. J., & Schneider, D. P. 2011, AJ, 141, 182, doi: 10.1088/0004-6256/141/6/182

King, A. 2003, ApJL, 596, L27, doi: 10.1086/379143

King, A., & Pounds, K. 2015, ARA&A, 53, 115, doi: 10.1146/annurev-astro-082214-122316

King, A. R., & Pounds, K. A. 2003, MNRAS, 345, 657, doi: 10.1046/j.1365-8711.2003.06980.x

King, A. R., Zubovas, K., & Power, C. 2011, Monthly Notices of the Royal Astronomical Society, 415, L6, doi: 10.1111/j.1745-3933.2011.01067.x

Kishimoto, M., Hönig, S. F., Beckert, T., & Weigelt, G. 2007, A&A, 476, 713, doi: 10.1051/0004-6361:20077911

Knigge, C., Scaringi, S., Goad, M. R., & Cottis, C. E. 2008, Monthly Notices of the Royal Astronomical Society, 386, 1426, doi: 10.1111/j.1365-2966.2008.13081.x

Kollmeier, J. A., Zasowski, G., Rix, H.-W., et al. 2017, arXiv e-prints, arXiv:1711.03234. https://arxiv.org/abs/1711.03234

Korista, K., Baldwin, J., Ferland, G., & Verner, D. 1997, ApJS, 108, 401, doi: 10.1086/312966

Korista, K. T., Bautista, M. A., Arav, N., et al. 2008, ApJ, 688, 108, doi: 10.1086/592140

Kormendy, J., & Ho, L. C. 2013, ARA&A, 51, 511, doi: 10.1146/annurev-astro-082708-101811

Kramida, A., & Ralchenko, Y. 2021, NIST Atomic Spectra Database, NIST Standard Reference Database 78, National Institute of Standards and Technology, doi: 10.18434/T4W30F

Krawczyk, C. M., Richards, G. T., Gallagher, S. C., et al. 2015, AJ, 149, 203, doi: 10.1088/0004-6256/149/6/203

Krogager, J. K., Geier, S., Fynbo, J. P. U., et al. 2015, ApJS, 217, 5, doi: 10.1088/0067-0049/217/1/5

Kurucz, R. L., & Bell, B. 1995, Atomic line list (Smithsonian Astrophysical Observatory)

Laor, A., & Brandt, W. N. 2002, ApJ, 569, 641, doi: 10.1086/339476

Laor, A., & Draine, B. T. 1993, ApJ, 402, 441, doi: 10.1086/172149

Lawther, D., Vestergaard, M., & Fan, X. 2018, MNRAS, 475, 3213, doi: 10.1093/mnras/stx3203

Lee, J. C., Kriss, G. A., Chakravorty, S., et al. 2013, MNRAS, 430, 2650, doi: 10.1093/mnras/stt050

Lee, K.-G., Suzuki, N., & Spergel, D. N. 2012, AJ, 143, 51, doi: 10.1088/0004-6256/143/2/51

Leighly, K., Terndrup, D., Gallagher, S. C., & Richards, G. 2019a, in American Astronomical Society Meeting Abstracts, Vol. 233, American Astronomical Society Meeting Abstracts #233, 242.39

Leighly, K. M. 2004, ApJ, 611, 125, doi: 10.1086/422089

Leighly, K. M., Choi, H., DeFrancesco, C., et al. 2022, arXiv e-prints, arXiv:2205.12946. https://arxiv.org/abs/2205.12946

Leighly, K. M., Choi, H., Terndrup, D. M., Gallagher, S. C., & Richards, G. T. in preparation, ApJ

Leighly, K. M., Cooper, E., Grupe, D., Terndrup, D. M., & Komossa, S. 2015, ApJL, 809, L13, doi: 10.1088/2041-8205/809/1/L13

Leighly, K. M., Dietrich, M., & Barber, S. 2011, ApJ, 728, 94

Leighly, K. M., Halpern, J. P., Jenkins, E. B., & Casebeer, D. 2007, ApJS, 173, 1, doi: 10.1086/519768

Leighly, K. M., Hamann, F., Casebeer, D. A., & Grupe, D. 2009, ApJ, 701, 176, doi: 10.1088/0004-637X/701/1/176

Leighly, K. M., & Moore, J. R. 2006, ApJ, 644, 748

Leighly, K. M., Terndrup, D. M., Baron, E., et al. 2014, ApJ, 788, 123, doi: 10.1088/0004-637X/788/2/123

Leighly, K. M., Terndrup, D. M., Gallagher, S. C., Richards, G. T., & Dietrich, M. 2018, ApJ, 866, 7, doi: 10.3847/1538-4357/aadee6

Leighly, K. M., Terndrup, D. M., Lucy, A. B., et al. 2019b, ApJ, 879, 27, doi: 10.3847/1538-4357/ab212a

Lewis, G. F., Chapman, S. C., & Kuncic, Z. 2003, ApJL, 596, L35, doi: 10.1086/379053

Lira, P., Kaspi, S., Netzer, H., et al. 2018, ApJ, 865, 56, doi: 10.3847/1538-4357/aada45

Liu, W.-J., Zhou, H., Ji, T., et al. 2015, ApJS, 217, 11, doi: 10.1088/0067-0049/217/1/11

Lucy, A. B., Leighly, K. M., Terndrup, D. M., Dietrich, M., & Gallagher, S. C. 2014, ApJ, 783, 58, doi: 10.1088/0004-637X/783/1/58

Lykins, M. L., Ferland, G. J., Kisielius, R., et al. 2015, ApJ, 807, 118, doi: 10.1088/0004-637X/807/2/118

Lynds, C. R. 1967, ApJ, 147, 396, doi: 10.1086/149021

MacInnis, F. 2018, Master's thesis, The University of Oklahoma, Homer L. Dodge Department of Physics and Astronomy

McGraw, S. M., Shields, J. C., Hamann, F. W., et al. 2015, MNRAS, 453, 1379, doi: 10.1093/mnras/stv1697

McGraw, S. M., Brandt, W. N., Grier, C. J., et al. 2017, MNRAS, 469, 3163, doi: 10.1093/mnras/stx1063

Menou, K., Vanden Berk, D. E., Ivezić, Ž., et al. 2001, ApJ, 561, 645, doi: 10.1086/323218

Meusinger, H., Schalldach, P., Mirhosseini, A., & Pertermann, F. 2016, A&A, 587, A83, doi: 10.1051/0004-6361/201527277

Meusinger, H., Schalldach, P., Scholz, R. D., et al. 2012a, A&A, 541, A77, doi: 10.1051/0004-6361/201118143

—. 2012b, A&A, 541, A77, doi: 10.1051/0004-6361/201118143

Miller, T. R., Arav, N., Xu, X., & Kriss, G. A. 2020, MNRAS, doi: 10.1093/mnras/staa2981

Miller, T. R., Arav, N., Xu, X., et al. 2018, ApJ, 865, 90, doi: 10.3847/1538-4357/aad817

Mishra, S., Vivek, M., Chand, H., & Joshi, R. 2021, MNRAS, 504, 3187, doi: 10.1093/mnras/stab782

Moe, M., Arav, N., Bautista, M. A., & Korista, K. T. 2009, The Astrophysical Journal, 706, 525, doi: 10.1088/0004-637X/706/1/525

Moore, C. E. 1950, An ultraviolet multiplet table - Sect. 1-2 (NBS Circular)

Moravec, E. A., Hamann, F., Capellupo, D. M., et al. 2017, MNRAS, 468, 4539, doi: 10.1093/mnras/stx775

Morris, S. L., Weymann, R. J., Anderson, S. F., et al. 1991, AJ, 102, 1627, doi: 10.1086/115984

Murray, N., & Chiang, J. 1997, ApJ, 474, 91, doi: 10.1086/303443

Murray, N., Quataert, E., & Thompson, T. A. 2005, ApJ, 618, 569, doi: 10.1086/426067

Najita, J., Dey, A., & Brotherton, M. 2000, AJ, 120, 2859, doi: 10.1086/316862

Nenkova, M., Sirocky, M. M., Nikutta, R., Ivezić, Ž., & Elitzur, M. 2008, ApJ, 685, 160, doi: 10.1086/590483

Netzer, H. 2013, The Physics and Evolution of Active Galactic Nuclei (Cambridge University Press)

Netzer, H., Lutz, D., Schweitzer, M., et al. 2007, ApJ, 666, 806, doi: 10.1086/520716

Ogle, P. M., Cohen, M. H., Miller, J. S., et al. 1999, ApJS, 125, 1, doi: 10.1086/313272

Osterbrock, D. E. 1991, Reports on Progress in Physics, 54, 579, doi: 10.1088/0034-4885/54/4/002

Pâris, I., Petitjean, P., Rollinde, E., et al. 2011, A&A, 530, A50, doi: 10.1051/0004-6361/201016233

Pâris, I., Petitjean, P., Aubourg, É., et al. 2012, A&A, 548, A66, doi: 10.1051/0004-6361/201220142

—. 2014, A&A, 563, A54, doi: 10.1051/0004-6361/201322691

—. 2018, A&A, 613, A51, doi: 10.1051/0004-6361/201732445

Parrent, J., Branch, D., & Jeffery, D. 2010, SYNOW: A Highly Parameterized Spectrum Synthesis Code for Direct Analysis of SN Spectra, Astrophysics Source Code Library, record ascl:1010.055. http://ascl.net/1010.055

Perrotta, S., Hamann, F., Zakamska, N. L., et al. 2019, MNRAS, 488, 4126, doi: 10.1093/mnras/stz1993

Peterson, B. M. 1997, An Introduction to Active Galactic Nuclei (Cambridge, New York Cambridge University Press)

Peterson, B. M., & Wandel, A. 1999, ApJL, 521, L95, doi: 10.1086/312190

Pilbratt, G. L., Riedinger, J. R., Passvogel, T., et al. 2010, A&A, 518, L1, doi: 10.1051/0004-6361/201014759

Pitchford, L. K., Farrah, D., Alatalo, K., et al. 2019, MNRAS, 487, 3130, doi: 10.1093/mnras/stz1471

Pogge, R. W., Derwent, M. A., O'Brien, T. P., et al. 2020, in Society of Photo-Optical Instrumentation Engineers (SPIE) Conference Series, Vol. 11447, Society of Photo-Optical Instrumentation Engineers (SPIE) Conference Series, 1144781, doi: 10.1117/12.2561113

Poglitsch, A., Waelkens, C., Geis, N., et al. 2010, A&A, 518, L2, doi: 10.1051/0004-6361/201014535

Popescu, C. C., Hopp, U., Hagen, H. J., & Elsaesser, H. 1996, A&AS, 116, 43. https://arxiv.org/abs/astro-ph/9510127

Prevot, M. L., Lequeux, J., Maurice, E., Prevot, L., & Rocca-Volmerange, B. 1984, A&A, 132, 389

Price-Whelan, A. M., & Foreman-Mackey, D. 2017, The Journal of Open Source Software, 2, doi: 10.21105/joss.00357

Privon, G. C., Ricci, C., Aalto, S., et al. 2020, ApJ, 893, 149, doi: 10.3847/1538-4357/ab8015

Prochaska, J. X., Hennawi, J. F., Westfall, K. B., et al. 2020a, arXiv e-prints, arXiv:2005.06505. https://arxiv.org/abs/2005.06505

Prochaska, J. X., Hennawi, J., Cooke, R., et al. 2020b, pypeit/PypeIt: Release 1.0.0, v1.0.0, Zenodo, doi: 10.5281/zenodo.3743493

Proga, D., & Kallman, T. R. 2004, ApJ, 616, 688, doi: 10.1086/425117

Proga, D., Stone, J. M., & Kallman, T. R. 2000, ApJ, 543, 686, doi: 10.1086/317154

Proga, D., & Waters, T. 2015, ApJ, 804, 137, doi: 10.1088/0004-637X/804/2/137

Quider, A. M., Nestor, D. B., Turnshek, D. A., et al. 2011, AJ, 141, 137, doi: 10.1088/0004-6256/141/4/137

Rafiee, A., Pirkola, P., Hall, P. B., et al. 2016, MNRAS, 459, 2472, doi: 10.1093/mnras/stw634

Rankine, A. L., Hewett, P. C., Banerji, M., & Richards, G. T. 2020, MNRAS, 492, 4553, doi: 10.1093/mnras/staa130

Rauch, M. 1998, ARA&A, 36, 267, doi: 10.1146/annurev.astro.36.1.267

Reichard, T. A., Richards, G. T., Hall, P. B., et al. 2003, AJ, 126, 2594, doi: 10.1086/379293

Richards, G. T., Strauss, M. A., Fan, X., et al. 2006a, AJ, 131, 2766, doi: 10.1086/503559

Richards, G. T., Lacy, M., Storrie-Lombardi, L. J., et al. 2006b, ApJS, 166, 470, doi: 10.1086/506525

Risaliti, G., Elvis, M., & Nicastro, F. 2002, ApJ, 571, 234, doi: 10.1086/324146

Rodríguez Hidalgo, P. 2009, PhD thesis, University of Florida

Rodríguez Hidalgo, P., Choi, H., DeFrancesco, C., Hall, P. B., & Leighly, K. M. in preparation, ApJ

Rodríguez Hidalgo, P., Hamann, F., & Hall, P. 2011, MNRAS, 411, 247, doi: 10.1111/j.1365-2966.2010.17677.x

Rodríguez Hidalgo, P., Khatri, A. M., Hall, P. B., et al. 2020, ApJ, 896, 151, doi: 10.3847/1538-4357/ab9198

Rogerson, J. A., Hall, P. B., Rodríguez Hidalgo, P., et al. 2016, Monthly Notices of the Royal Astronomical Society, 457, 405, doi: 10.1093/mnras/stv3010

Rogerson, J. A., Hall, P. B., Snedden, S. A., Brotherton, M. S., & Anderson, S. F. 2011, NewA, 16, 128, doi: 10.1016/j.newast.2010.07.002

Runnoe, J. C., Ganguly, R., Brotherton, M. S., & DiPompeo, M. A. 2013, MNRAS, 433, 1778, doi: 10.1093/mnras/stt852

Sabra, B. M., & Hamann, F. 2005, ArXiv Astrophysics e-prints

Sanders, D. B., Soifer, B. T., Elias, J. H., et al. 1988a, The Astrophysical Journal, 325, 74, doi: 10.1086/165983

Sanders, D. B., Soifer, B. T., Elias, J. H., Neugebauer, G., & Matthews, K. 1988b, ApJL, 328, L35, doi: 10.1086/185155

Savage, B. D., & Sembach, K. R. 1991, ApJ, 379, 245, doi: 10.1086/170498

Scannapieco, E., & Oh, S. P. 2004, ApJ, 608, 62, doi: 10.1086/386542

Schaye, J. 2001, ApJ, 559, 507, doi: 10.1086/322421

Schmidt, M. 1963, Nature, 197, 1040, doi: 10.1038/1971040a0

Schneider, D. P., Hall, P. B., Richards, G. T., et al. 2005, AJ, 130, 367, doi: 10.1086/431156

Schneider, P. 2015, Extragalactic Astronomy and Cosmology: An Introduction (Springer-Verlag), doi: 10.1007/978-3-642-54083-7

Schulze, A., Misawa, T., Zuo, W., & Wu, X.-B. 2018, ApJ, 853, 167, doi: 10.3847/1538-4357/aaa7f0

Schulze, A., Schramm, M., Zuo, W., et al. 2017, ApJ, 848, 104, doi: 10.3847/1538-4357/aa8e4c

Shen, Y., Richards, G. T., Strauss, M. A., et al. 2011, ApJS, 194, 45, doi: 10.1088/0067-0049/194/2/45

Shi, X.-H., Jiang, P., Wang, H.-Y., et al. 2016, ApJ, 829, 96, doi: 10.3847/0004-637X/829/2/96

Smith, P. S., Schmidt, G. D., Allen, R. G., & Angel, J. R. P. 1995, ApJ, 444, 146, doi: 10.1086/175589

Spoon, H. W. W., Farrah, D., Lebouteiller, V., et al. 2013, ApJ, 775, 127, doi: 10.1088/0004-637X/775/2/127

Sprayberry, D., & Foltz, C. B. 1992, The Astrophysical Journal, 390, 39, doi: 10.1086/171257

Stalevski, M., Tristram, K. R. W., & Asmus, D. 2019, MNRAS, 484, 3334, doi: 10.1093/mnras/stz220

Strömgren, B. 1939, ApJ, 89, 526, doi: 10.1086/144074

Sulentic, J. W., Marziani, P., & Dultzin-Hacyan, D. 2000, ARA&A, 38, 521, doi: 10.1146/annurev.astro.38.1.521

Suzuki, N. 2006, ApJS, 163, 110, doi: 10.1086/499272

Suzuki, N., Tytler, D., Kirkman, D., O'Meara, J. M., & Lubin, D. 2005, ApJ, 618, 592, doi: 10.1086/426062

Temple, M. J., Hewett, P. C., & Banerji, M. 2021, MNRAS, 508, 737, doi: 10.1093/mnras/stab2586

Thompson, T. A., Fabian, A. C., Quataert, E., & Murray, N. 2015, MNRAS, 449, 147, doi: 10.1093/mnras/stv246

Tolea, A., Krolik, J. H., & Tsvetanov, Z. 2002, ApJL, 578, L31, doi: 10.1086/344563

Tombesi, F., Cappi, M., Reeves, J. N., et al. 2010, A&A, 521, A57, doi: 10.1051/0004-6361/200913440

Trammell, G. B., Vanden Berk, D. E., Schneider, D. P., et al. 2007, AJ, 133, 1780, doi: 10.1086/511817

Trump, J. R., Hall, P. B., Reichard, T. A., et al. 2006, ApJS, 165, 1, doi: 10.1086/503834

Urrutia, T., Becker, R. H., White, R. L., et al. 2009, ApJ, 698, 1095, doi: 10.1088/0004-637X/698/2/1095

Urrutia, T., Lacy, M., & Becker, R. H. 2008, ApJ, 674, 80, doi: 10.1086/523959

Urry, C. M., & Padovani, P. 1995, PASP, 107, 803, doi: 10.1086/133630

Vacca, W. D., Cushing, M. C., & Rayner, J. T. 2003, PASP, 115, 389, doi: 10.1086/346193

Vayner, A., Zakamska, N. L., Riffel, R. A., et al. 2021, MNRAS, 504, 4445, doi: 10.1093/mnras/stab1176

Veilleux, S., Trippe, M., Hamann, F., et al. 2013a, ApJ, 764, 15, doi: 10.1088/0004-637X/764/1/15

Veilleux, S., Meléndez, M., Sturm, E., et al. 2013b, ApJ, 776, 27, doi: 10.1088/0004-637X/776/1/27

Véron-Cetty, M.-P., Joly, M., & Véron, P. 2004, A&A, 417, 515, doi: 10.1051/0004-6361:20035714

Villforth, C., Herbst, H., Hamann, F., et al. 2019, MNRAS, 483, 2441, doi: 10.1093/mnras/sty3271

Violino, G., Coppin, K. E. K., Stevens, J. A., et al. 2016, MNRAS, 457, 1371, doi: 10.1093/mnras/stv2937

Vivek, M., Srianand, R., Petitjean, P., et al. 2014, MNRAS, 440, 799, doi: 10.1093/mnras/stu288

—. 2012, MNRAS, 423, 2879, doi: 10.1111/j.1365-2966.2012.21098.x

Voit, G. M., Weymann, R. J., & Korista, K. T. 1993, ApJ, 413, 95, doi: 10.1086/172980

Vollmer, B., Schartmann, M., Burtscher, L., et al. 2018, A&A, 615, A164, doi: 10.1051/0004-6361/201731133

Wampler, E. J., Chugai, N. N., & Petitjean, P. 1995, ApJ, 443, 586, doi: 10.1086/175551

Wang, T., Ferland, G. J., Yang, C., Wang, H., & Zhang, S. 2016, ApJ, 824, 106, doi: 10.3847/0004-637X/824/2/106

Wang, T., Yang, C., Wang, H., & Ferland, G. 2015, ApJ, 814, 150, doi: 10.1088/0004-637X/814/2/150

Waters, T., & Proga, D. 2019, ApJ, 875, 158, doi: 10.3847/1538-4357/ab10e1

Weymann, R. J., Morris, S. L., Foltz, C. B., & Hewett, P. C. 1991, ApJ, 373, 23

White, R. L., Becker, R. H., Gregg, M. D., et al. 2000, ApJS, 126, 133, doi: 10.1086/313300

Wilkes, B. J. 1984, MNRAS, 207, 73, doi: 10.1093/mnras/207.1.73

Wilson, J. C., Henderson, C. P., Herter, T. L., et al. 2004, in Society of Photo-Optical Instrumentation Engineers (SPIE) Conference Series, Vol. 5492, Ground-based Instrumentation for Astronomy, ed. A. F. M. Moorwood & M. Iye, 1295–1305, doi: 10.1117/12.550925

Xu, X., Arav, N., Miller, T., Korista, K. T., & Benn, C. 2021, MNRAS, 506, 2725, doi: 10.1093/mnras/stab1866

Yi, W., Brandt, W. N., Hall, P. B., et al. 2019, ApJS, 242, 28, doi: 10.3847/1538-4365/ab1f90

York, D. G., Adelman, J., Anderson, Jr., J. E., et al. 2000, AJ, 120, 1579, doi: 10.1086/301513

Young, M., Elvis, M., & Risaliti, G. 2009, ApJS, 185, 250, doi: 10.1088/0067-0049/185/1/250

Yuan, S., Strauss, M. A., & Zakamska, N. L. 2016, MNRAS, 462, 1603, doi: 10.1093/mnras/stw1747

Zafar, T., Møller, P., Watson, D., et al. 2015, A&A, 584, A100, doi: 10.1051/0004-6361/201526570

Zakamska, N. L., Hamann, F., Pâris, I., et al. 2016, MNRAS, 459, 3144, doi: 10.1093/mnras/stw718

Zakamska, N. L., Sun, A.-L., Strauss, M. A., et al. 2019, MNRAS, 489, 497, doi: 10.1093/mnras/stz2071

Zhang, N.-X., Brandt, W. N., Ahmed, N. S., et al. 2017, ApJ, 839, 101, doi: 10.3847/1538-4357/aa6842

Zhang, S., Ge, J., Jiang, P., et al. 2015a, ApJ, 802, 92, doi: 10.1088/0004-637X/802/2/92

Zhang, S., Zhou, H., Wang, T., et al. 2015b, ApJ, 803, 58, doi: 10.1088/0004-637X/803/2/58

Zubovas, K. 2018, MNRAS, 473, 3525, doi: 10.1093/mnras/stx2569

Zubovas, K., & King, A. 2012, ApJL, 745, L34, doi: 10.1088/2041-8205/745/2/L34